

Silicon photonic devices and circuits for optical communication applications

Md Ghulam Saber



Department of Electrical & Computer Engineering
McGill University
Montréal, Canada

July 2019

A thesis submitted to McGill University in partial fulfillment of the requirements for the degree of Doctor of Philosophy.

© 2019 Md Ghulam Saber

Abstract

Emerging applications such as cloud-based storage services (e.g., Dropbox, onedrive), high definition streaming services (e.g., Netflix, Amazon prime video), machine-to-machine communications (e.g., Internet of Things), and 5G radio networks are fueling the need for faster and bandwidth-efficient optical networks. The requirements of these applications include increased capacity, and reduced cost, power consumption, footprint, and complexity. Therefore, there is a growing trend in developing integrated optoelectronic devices to meet the above mentioned requirements. Specifically, the silicon-on-insulator (SOI) platform has drawn huge research interest due to its low power operation, dense integration, and low-cost fabrication with relatively high yield using the existing complementary-metal-oxide-semiconductor (CMOS) foundries. Consequently, silicon photonics has recently entered the production phase of the technology development cycle. This thesis presents several silicon photonic devices and circuits for applications in different segments of the optical networks.

In the first part of the thesis, we report several passive silicon photonic devices based on Bragg gratings, interference, and doping. First, two configurations (single-stage and cascaded) of the optical add-drop multiplexers (OADMs) are presented using Bragg gratings in a Mach-Zehnder interferometer. The single-stage and the cascaded OADMs achieved extinction ratios (ERs) of 25 and 51 dB, respectively, and have minimum lithographic feature size within the limitation of the 193 nm deep ultraviolet (DUV) lithography. Second, we present two types of the transversely coupled Fabry-Perot resonators using Bragg gratings and loop mirrors. The Bragg grating based designs offer maximum ER of 37.3 dB and maximum Q-factor of 23642 while the loop mirror based designs offer maximum ER of 18.1 dB and maximum Q-factor of 28086. Third, we demonstrate a 120° optical hybrid using 3×3 multimode interference (MMI) coupler. The hybrid demonstrates measured excess loss of <2.4 dB over 60 nm (1500 nm - 1560 nm) and the deviations in split ratio among the three output ports are <±1 dB over 1500 nm to 1555 nm wavelength range. Phase deviations of ≤5° over 30 nm (1520 nm to 1550 nm) and ≤10° over 80 nm (1500 nm to 1580 nm) bandwidths are also achieved. Finally, we report a hybrid plasmonic waveguide based transverse magnetic (TM)-pass polarizer using highly doped silicon instead of metals. According to our analysis, the proposed TM-pass polarizer achieves an ER of 30.1 dB and an insertion loss (IL) of 3.1 dB with a length of 15 μm near 1550 nm wavelength.

In the last part of the thesis, we present bench-top and integrated solutions for applications in the high-speed passive optical networks (PONs). The standardization process of the physical layers of the high-speed PONs is currently in progress with the IEEE P802.3ca task force and the International Telecommunication Union (ITU) groups. First, we report performance

enhancement of a simplified coherent receiver based on 120° hybrid using 4-level pulse amplitude modulation (PAM-4). This allows the use of low bandwidth optoelectronic components to achieve higher bit rate (e.g., 10G component for 25 Gb/s bit rate). Using the bulk optics based receiver we obtained 25 Gb/s PAM-4 transmission over 21 km of single-mode fiber (SMF) with a receiver sensitivity of -14.5 dBm. Second, we demonstrate a fully-integrated 120° hybrid based simplified coherent receiver on the SOI platform. For the 25 Gb/s 2-level pulse amplitude modulation (PAM-2) signals, a sensitivity of -20.3 dBm is achieved after 21 km of propagation while for the 25 Gb/s (12.5 GBaud) PAM-4 signals, the achievable sensitivity is -9.5 dBm after 21 km of fiber. Third, the performance of the integrated coherent receiver is improved further by using a better transmitter and simple digital signal processing (DSP) at the receiver. We achieved -16.6 dBm of receiver sensitivity with 25 Gb/s (12.5 GBaud) PAM-4 after 21 km without any dispersion compensation and receiver equalizer, and -11.6 dBm of receiver sensitivity with 50 Gb/s (25 GBaud) PAM-4 after 21 km using 31-tap linear feed-forward equalizer (FFE) at the receiver.

Sommaire

Les applications émergentes telles que les services de stockage en nuage (Dropbox, onedrive, par exemple), les services de streaming haute définition (Netflix, Amazon prime video), les communications entre ordinateurs (Internet of Things, par exemple) et les radios pour le réseau 5G sont des nécessitent des réseaux optiques plus rapides et utilisant plus efficacement leur bande passante. Les exigences de ces applications incluent une capacité accrue et une réduction des coûts, de la consommation d'énergie, de l'encombrement et de la complexité des solutions. Par conséquent, il existe une tendance croissante à développer des dispositifs optoélectroniques intégrés pour répondre aux exigences susmentionnées. Plus précisément, la plate-forme silicium sur isolant (SOI) a suscité un intérêt considérable en matière de recherche en raison de son fonctionnement à faible puissance, de son intégration dense et de sa fabrication à faible coût avec un rendement relativement élevé grâce aux fonderies existantes CMOS. En conséquence, la photonique sur silicium a récemment entrée dans la phase de production du cycle de développement technologique. Cette thèse présente plusieurs dispositifs et circuits photoniques en silicium pour des applications dans différents segments des réseaux optiques.

Dans la première partie de cette thèse, nous rapportons plusieurs dispositifs photoniques passifs en silicium basés sur les réseaux de Bragg, interférence et le dopage. Premièrement, deux configurations (à une étape et en cascade) des multiplexeurs optiques add-drop (OADM) sont présentées, utilisant des réseaux de Bragg dans un interféromètre de Mach-Zehnder. Les OADM à une étape et en cascade ont atteint des taux d'extinction (ER) de 25 et 51 dB, respectivement, et ont une taille minimale de caractéristiques lithographiques dans les limites de la lithographie à ultraviolets profonds (DUV) de 193 nm. Deuxièmement, nous présentons deux types de résonateurs Fabry-Perot à couplage transversal utilisant des réseaux de Bragg et des miroirs à boucle. Les conceptions basées sur les réseaux de Bragg offrent un ER maximal de 37,3 dB et un facteur Q maximal de 23642, tandis que les conceptions basées sur des miroirs à boucle offrent un ER maximal de 18,1 dB et un facteur Q maximal de 28086. Troisièmement, nous présentons un hybride optique à 120° utilisant le coupleur multimode par interférence 3×3 (MMI). L'hybride présente une perte en excès mesurée inférieure à 2,4 dB sur 60 nm (1500 nm à 1360 nm) et l'écart du rapport de division entre les trois ports de sortie est $< \pm 1$ dB sur la plage de longueurs d'onde de 1500 nm à 1555 nm. Des déviations de phase de $\leq 5^\circ$ sur 30 nm (1520 nm à 1550 nm) et $\leq 10^\circ$ sur une largeur de bande de 80 nm (1500 nm à 1580 nm) sont également obtenues. Enfin, nous rapportons un polariseur plasmonique hybride passe-transverse magnétique (TM) basé sur un guide d'onde utilisant du silicium hautement dopé au lieu de métaux. Selon notre analyse, le polariseur passe-TM proposé atteint un ER de 30,1 dB et une perte d'insertion (IL) de 3,1 dB avec une longueur de 15 μm à une longueur d'onde de

1550 nm.

Dans la dernière partie de la thèse, nous présentons des solutions intégrées pour des applications dans les réseaux optiques passifs à grande vitesse (PON). Le processus de normalisation des couches physiques du réseau PON à grande vitesse est actuellement en cours avec le groupe de travail IEEE P802.3ca et les groupes de l'Union internationale des télécommunications (ITU). Tout d'abord, nous rapportons l'amélioration des performances d'un récepteur cohérent simplifié basé sur un hybride à 120° utilisant une modulation d'amplitude à 4 niveaux (PAM-4). Cela permet l'utilisation de composants optoélectroniques à faible bande passante pour atteindre un débit plus élevé (par exemple, composant 10G pour un débit de 25 Gb/s). En utilisant le récepteur basé sur les propriétés intrinsèques du matériau, nous avons obtenu une transmission PAM-4 à 25 Gb/s sur 21 km de fibre monomode (SMF) avec une sensibilité de récepteur de -14,5 dBm. Deuxièmement, nous démontrons un récepteur cohérent simplifié basé sur l'hybride à 120° entièrement intégré sur la plate-forme SOI. Pour les signaux PAM-2 à 25 Gb/s, une sensibilité de -15,1 dBm est obtenue après 30 km de propagation, tandis que pour les signaux PAM-4 à 25 Gb/s (12,5 Gb/s), la sensibilité réalisable est de -9,5 dBm après 21 km de la fibre. Troisièmement, les performances du récepteur cohérent intégré sont encore améliorées en utilisant un meilleur émetteur et un simple traitement du signal numérique (DSP) au niveau du récepteur. Nous avons atteint une sensibilité du récepteur de -16,6 dBm avec PAM-4 à 25 Gb/s (12,5 Gbaud) après 21 km sans compensation de dispersion ni égaliseur au niveau du récepteur, et une sensibilité de récepteur de -11,6 dBm avec PAM-4 de 50 Gb/s (25 Gbaud) après 21 km, en utilisant l'égaliseur linéaire à 31-tap de correction avancée (FFE) au niveau du récepteur.

Acknowledgments

First and foremost, I offer gratitude to the Almighty ALLAH (SWT) for giving me the capability to do this work with good health.

I am grateful to my supervisor, *Prof. David V. Plant* for the support and guidance throughout the course of this work. He created a research environment for which I was able to explore many ideas without constraints. I have gained a wealth of knowledge and experience in science and engineering through his direction that is beyond value to my future endeavors. I would like to thank *Prof. Lawrence Chen* and *Prof. Fabrice Labeau* for serving on my supervisory committee and pointing out the imperfections of my work from time to time.

I am grateful to the sponsors who provided financial support throughout the PhD work: R. H. Tomlinson Doctoral Fellowship (McGill), Fonds de Recherche-Nature et Technologies Québec (FRQNT), Natural Sciences and Engineering Research Council of Canada (NSERC), and SPIE Optics and Photonics Education Scholarship. I acknowledge the contribution of Canadian Microelectronics Corporation (CMC) Microsystems, which partly provides the design tools and fabrication costs of the silicon photonic devices presented in this work. I also acknowledge the administrative and computing infrastructure related supports I received from STARaCom (previously SYTACom) staffs *Ms. Maru Basanez*, *Ms. K. Johnson*, and *Mr. Brent Snow*.

I would like to express my gratitude to my colleagues, who offered great help to my research. Many thanks to *Dr. Mathieu Chagnon*, *Dr. Mohamed Osman*, *Dr. David Patel*, *Eslam El-Fiky*, *Dr. Alireza Samani*, *Dr. Yun Wang*, *Dr. Nicolás Abadía*, *Zhenping Xing*, *Md Samiul Alam*, *Kh Arif Shahriar*, *Prof. Ramón Gutiérrez-Castrejón*, *James Skoric*, *Olivier Carpentier*, *Michael Hui*, *Maxime Jacques*, *Luhua Xu*, *Amar Kumar*, *Yannick D'Mello*, *Galib Hakim*, *Dr. Mohamed Sowailem* and *Dr. Meng Qiu*. You have helped me tremendously in this endeavor. In the past four years, I have received countless help from the people in Photonic Systems Group (PSG), who are not mentioned here.

Many thanks to Ericsson who started the collaboration on the PINEAPPLE project. Special thanks to their team *Dr. Gemma Vall-Llosera*, *Dr. Patryk Urban*, *Dr. Boris Dortschy*, *Mr. Fabio Cavaliere*, and *Mr. Stephane Lessard* for their fruitful feedbacks regarding the project.

I would like to express my appreciation and respect to my parents who have always been there for me throughout my whole life. My deepest love and gratefulness go to my wife. She supported me with love, care, and countless emotions throughout all these years after we got married. Thanks a lot for being my life-long companion. Also, I would like to thank my lovely daughter. Your existence changed my life and your smile gives me the positive energy to face the difficulties and cheer for the accomplishments. Many thanks to my grand parents, brother, sister-in-laws, parents-in-law and other family members for their love, support and prayers.

May ALLAH (SWT) grant Jannah (paradise) to my grandmother who passed away six days before my doctoral defence.

A heartfelt thanks goes to all my friends scattered all over the world. Special thanks to my friends in Montreal for their support and making our stay more enjoyable. Finally, I apologize for not being able to mention everyone by name since there are just too many people I am grateful to. I remember you all in my heart and in my prayers.

*Best wishes,
Md Ghulam Saber
July, 2019.*

Statement of originality and contribution of co-authors

This is a manuscript based thesis and therefore, as permitted, contents of this thesis has been published in peer-reviewed publications. References to these publications are provided below. This thesis represents my original research, and it has not been submitted for a degree or diploma at any other institution. The work presented within this thesis is entirely my own, except where references are made. Based on the copyright policies of the Optical Society of America (OSA) and the Institute of Electrical and Electronics Engineers (IEEE), appropriate attributions are maintained and copyright lines appear with every reprinted figure and table from the cited references. The originality and contribution to the existing body of knowledge of the work presented in this thesis is evidenced by the ten peer-reviewed publications that it is based on. This consists of seven journal papers and three conference papers.

Journal articles directly related to this thesis

1. **M. G. Saber**, E. El-Fiky, Z. Xing, M. Osman, D. Patel, A. Samani, M. S. Alam, K. A. Shahriar, L. Xu, G. Vall-Llosera, B. Dortschy, P. J. Urban, F. Cavaliere, S. Lessard, and D. V. Plant, "25 and 50 Gb/s/ λ PAM-4 Transmission Over 43 and 21 km Using A Simplified Coherent Receiver on SOI", *IEEE Photonics Technology Letters*, vol. 31, issue 10, pp. 799-802. [2019]

I conceived the idea, designed the receiver, conducted the experiments and wrote the paper. Other authors contributed by developing the digital signal processing, discussing the idea and revising the manuscript.

2. **M. G. Saber**, M. Osman, D. Patel, A. Samani, E. El-Fiky, M. S. Alam, K. A. Shahriar, Z. Xing, M. Jacques, B. Dortschy, G. Vall-Llosera, P. J. Urban, F. Cavaliere, S. Lessard, and D. V. Plant, "Demonstration of a 120° Hybrid Based Simplified Coherent Receiver on SOI for High Speed PON Applications", *Optics Express*, vol. 26, issue 24, pp. 31222-31232. [2018]

I conceived the idea, performed the design and analysis of the receiver, conducted the experiments and wrote the paper. Other authors contributed by developing the digital signal processing, discussing the idea and revising the manuscript.

3. **M. G. Saber**, M. Morsy-Osman, M. Hui, E. El-Fiky, G. Vall-llosera, B. Dortschy, P. J. Urban, F. Cavaliere, S. Lessard and D. V. Plant, "DSP-free 25 Gbit/s PAM-4 Transmission using 10G Transmitter and Coherent Amplification", *IEEE Photonics Technology Letters*, vol. 30, issue 17, pp. 1547-1550. [2018]

I conceived the idea, conducted the experiments and wrote the paper. Other authors

contributed by developing the digital signal processing, discussing the idea and revising the manuscript.

4. **M. G. Saber**, N. Abadía, and D. V. Plant, "CMOS Compatible All-Silicon TM Pass Polarizer Based on Highly Doped Silicon Waveguide", *Optics Express*, vol. 26, issue 16, pp. 20878-20887. [2018]

I conceived the idea, performed the simulation and analysis of the device and wrote the paper. Other authors contributed by discussing the idea, assisting in the simulation process and revising the manuscript.

5. **M. G. Saber**, N. Abadía, Y. Wang and D. V. Plant, "Fabry-Perot Resonators with Transverse Coupling on SOI Using Loop Mirrors", *Optics Communications*, vol. 415, pp. 121-126, Elsevier. [2018]

I conceived the idea, performed the design and analysis of the devices presented, conducted the experiments and wrote the paper. The other co-authors contributed in editing the paper and discussing the idea.

6. **M. G. Saber**, Y. Wang, E. El-Fiky, D. Patel, Kh. A. Shahriar, M. S. Alam, M. Jacques, Z. Xing, L. Xu, N. Abadía, and D. V. Plant, "Transversely Coupled Fabry-Perot Resonators with Bragg Grating Reflectors", *Optics Letters*, vol. 43, issue 1, pp. 13-16. [2018]

I conceived the idea, performed the simulation and analysis, conducted the experiments and wrote the paper. The co-authors contributed in building the experimental setup and revising the manuscript.

7. **M. G. Saber**, Z. Xing, D. Patel, E. El-Fiky, N. Abadía, Y. Wang, M. Jacques, M. Morsy-Osman, and D. V. Plant, "A CMOS Compatible Ultra-Compact Silicon Photonic Optical Add-Drop Multiplexer with Misaligned Sidewall Bragg Gratings", *IEEE Photonics Journal*, vol. 9, issue 3. [2017]

I conceived the idea, performed the simulation and analysis, and wrote the paper. The measurements were taken using the automated setup at University of British Columbia, Vancouver, BC, Canada. The co-authors contributed in revising the manuscript.

Conference articles directly related to this thesis

8. **M. G. Saber**, E. El-Fiky, D. Patel, M. Morsy-Osman, G. Vall-llosera, P. J. Urban, B. Dortschy and D. V. Plant, "A Silicon-on-Insulator 120° Optical Hybrid Based on 3x3 Multimode Interference Coupler", *Photonics North*, 255-2b-93, Ottawa, Canada, June 6-8. [2017]

I conceived the idea, performed the simulation and analysis, conducted the experiments,

and wrote the paper. The co-authors contributed in discussing the idea and revising the manuscript.

9. **M. G. Saber**, Z. Xing, E. El-Fiky, D. Patel, L. Xu, N. Abadía and D. V. Plant, "Transversely Coupled Fabry-Perot Resonators in SOI", Conference on Lasers and Electro-Optics (CLEO), SM1N.4, San Jose, CA, USA, May 14-19. [2017]

I conceived the idea, performed the simulation and analysis, conducted the experiments and wrote the paper. The co-authors contributed in revising the manuscript.

10. **M. G. Saber**, Z. Xing, D. Patel, E. El-Fiky, N. Abadía, Y. Wang and D. V. Plant, "A Compact Silicon Photonic Add-Drop Multiplexer with Misaligned Sidewall Bragg Gratings in a MZI", Conference on Lasers and Electro-Optics (CLEO), SF1H.2, San Jose, CA, USA, May 14-19. [2017]

I conceived the idea, performed the simulation and analysis, and wrote the paper. The measurements were taken using the automated setup at University of British Columbia, Vancouver, BC, Canada. The co-authors contributed in discussing the idea and revising the manuscript.

Journal articles not directly related to this thesis

11. **M. G. Saber**, L. Xu, R. H. Sagor, Y. Wang, A. Kumar, D. Mao, E. El-Fiky, D. Patel, A. Samani, Z. Xing, M. Jacques, Y. D'Mello, D. V. Plant, and N. Abadía, "Integrated Polarization Handling Devices", IET Optoelectronics. [**Invited**, Under Review]
12. E. El-Fiky, A. Samani, M. Jacques, L. Xu, **M. G. Saber**, and D. V. Plant, "C-band and O-band silicon photonic based low power variable optical attenuators", IEEE Photonics Journal. [2019] [**Accepted**]
13. **M. G. Saber**, G. Vall-Llosera, D. Patel, A. Samani, R. Li, M. Morsy-Osman, M. Chagnon, E. El-Fiky, R. Gutiérrez-Castrejón, P. J. Urban, B. Dortschy, F. Cavaliere, S. Lessard, and D. V. Plant, "Silicon-Based Optical Links Using Novel Direct Detection, Coherent Detection and Dual Polarization Methods for New Generation Transport Architectures", Optics Communications, vol. 450, pp. 48-60. [2019] [**Invited**]
14. L. Xu, Y. Wang, D. Mao, E. El-Fiky, Z. Xing, A. Kumar, **M. G. Saber**, M. Jacques and D. V. Plant, "Broadband 1310/1550-nm Wavelength Demultiplexer Based on Multimode Interference Coupler with Tapered Internal Photonic Crystal for the SOI Platform", Optics Letters, vol. 44, issue 7, pp. 1770-1773. [2019]

-
15. L. Xu, Y. Wang, E. El-Fiky, D. Mao, A. Kumar, Z. Xing, **M. G. Saber**, M. Jacques and D. V. Plant, "Compact Broadband Polarization Beam Splitter Based on Multimode Interference Coupler with Internal Photonic Crystal for the SOI Platform", *IEEE/OSA Journal of Lightwave Technology*, vol. 37, issue 4, pp. 1231-1240. [2019]
 16. E. El-Fiky, A. Samani, M. Sowailem, M. Osman, M. Jacques, D. Patel, **M. G. Saber**, L. Xu, Z. Xing, M. Xiang and D. V. Plant, "Dual Parallel Multi-Electrode Traveling Wave Mach-Zehnder Modulator for 200 Gb/s Intra-datacenter Optical Interconnects", *IEEE Photonics Journal*, vol. 11, issue 1. [2019]
 17. L. Xu, Y. Wang, A. Kumar, E. El-Fiky, D. Mao, H. Tamazin, M. Jacques, Z. Xing, **M. G. Saber** and D. V. Plant, "Compact High-Performance Adiabatic 3-dB Coupler Enabled by Subwavelength Grating Slot in the Silicon-on-Insulator Platform", *Optics Express*, vol. 26, issue 23, pp. 29873-29885. [2018]
 18. N. Abadía, **M. G. Saber**, F. Bello, A. Samani, E. El-Fiky, Y. Wang, J. F. Donegan and D. V. Plant, "CMOS Compatible Multi-Band Plasmonic TE-Pass Polarizer", *Optics Express*, vol. 26, issue 23, pp. 30292-30304. [2018]
 19. Z. Xing, A. Samani, M. Xiang, E. El-Fiky, T. M. Hoang, D. Patel, R. Li, M. Qiu, **M. G. Saber**, M. Morsy-Osman and D. V. Plant, "100 Gb/s PAM4 Transmission System for Datacenter Interconnects Using a SiP ME-MZM Based DAC-Less Transmitter and a VSB Self-Coherent Receiver", *Optics Express*, vol. 26, issue 18, pp. 23969-23979. [2018]
 20. M. Jacques, A. Samani, D. Patel, E. El-Fiky, M. Morsy-Osman, T. Hoang, **M. G. Saber**, L. Xu, J. Sonkoly, M. Ayliffe, and D. V. Plant, "Modulator Material Impact on Chirp, DSP and Performance in Coherent Digital Links: Comparison of Lithium Niobate, Indium Phosphide and Silicon Platforms", *Optics Express*, vol. 26, issue 17, pp. 22471-22490. [2018]
 21. M. Jacques, S. Bouvier, D. Denis, D. Patel, A. Samani, **M. G. Saber**, F. Mounaim, J. Gauthier, and D. V. Plant, "Analysis, Modeling and Mitigation of Parasitic Resonances in Integrated Metallic Seal Rings", *IEEE Transactions on Components, Packaging and Manufacturing Technology*, vol. 8, issue 6, pp. 1082-1091. [2018]
 22. Y. Wang, L. Xu, A. Kumar, Y. D'Mello, D. Patel, Z. Xing, R. Li, **M. G. Saber**, E. El-Fiky and D. V. Plant, "Compact Single-Etched Sub-Wavelength Grating Couplers for O-Band Application", *Optics Express*, vol. 25, issue 24, pp. 30582-30590. [2017]

-
23. E. El-Fiky, M. Osman, M. Sowailem, A. Samani, D. Patel, R. Li, **M. G. Saber**, Y. Wang, N. Abadía, Y. D’Mello and D. V. Plant, “200 Gb/s Transmission Using a Dual Polarization O-Band Silicon Photonic Intensity Modulator for Stokes Vector Direct Detection Applications”, *Optics Express*, vol. 25, issue 24, pp. 30336-30348. [2017]

Conference articles not directly related to this thesis

24. Z. Xing, M. Xiang, E. El-Fiky, X. Li, **M. G. Saber**, L. Xu and D. V. Plant, “600G PAM4 transmission using a 4-lambda CWDM TOSA based on controlled-ISI pulse shaping and Tomlinson-Harashima precoding”, *The 45th European Conference on Optical Communication (ECOC 2019)*, T.3.D, Dublin, Ireland, September 22-26. [2019]
25. **M. G. Saber**, L. Xu, R. H. Sagor, D. V. Plant, and N. Abadía, “Integrated Polarization Handling Devices”, *Semiconductor and Integrated Optoelectronics Conference (SIOE)*, Cardiff, Wales, UK, April 16-18. [2019]
26. Z. Xing, D. Patel, E. El-Fiky, M. Xiang, R. Li, **M. G. Saber**, L. Xu, M. Hui and D. V. Plant, “SiPh Self-Coherent Transmitter Circuit with on-chip CSPR Control Capability based on a Tunable Power Splitter”, *The Optical Networking and Communication Conference (OFC)*, Tu2H.3, San Diego, CA, USA, March 3-7. [2019]
27. E. El-Fiky, Y. D’Mello, Y. Wang, **M. G. Saber**, A. Kumar, J. Skoric, A. Samani, L. Xu, R. Li, D. Patel and D. V. Plant, “Ultra-Broadband and Compact Asymmetrical Beam Splitter Enabled by Angled Sub-Wavelength Grating MMI”, *Conference on Lasers and Electro-Optics (CLEO)*, STh4A.7, San Jose, CA, USA, May 13-18. [2018]
28. N. Abadía, **M. G. Saber**, Q. Lu, W. H. Guo, D. V. Plant and J. Donegan, “Novel Polarization Beam Splitter with High Fabrication Tolerance”, *Conference on Lasers and Electro-Optics (CLEO)*, JW2A.6, Poster Session II, San Jose, CA, USA, May 13-18. [2018]
29. N. Abadía, **M. G. Saber**, Q. Lu, W. Guo, D. V. Plant and J. F. Donegan, “Fabrication Tolerant Polarization Beam Splitter with Easy Calibration”, *International Conference on Nano-photonics and Nano-optoelectronics*, Yokohama, Japan, April 25-27. [2018]
30. Y. Wang, L. Xu, A. Kumar, D. Patel, Z. Xing, R. Li, **M. G. Saber**, Y. D’Mello, E. El-Fiky and D. V. Plant, “O-Band Sub-Wavelength Grating Coupler”, *2017 IEEE Photonics Conference (IPC)*, Orlando, Florida, USA, October 01-05. [2017]

31. Y. Wang, L. Xu, A. Kumar, D. Patel, Z. Xing, R. Li, **M. G. Saber**, Y. D’Mello, E. El-Fiky and D. V. Plant, “Broadband Sub-wavelength Grating Coupler for O-Band Application”, 14th International Conference on Group IV Photonics (GFP), Berlin, Germany, August 23-25. [2017]
32. L. Xu, Y. Wang, D. Patel, E. El-Fiky, Z. Xing, R. Li, **M. G. Saber**, M. Jacques and D. V. Plant, “Polarization Independent Adiabatic 3-dB Coupler for Silicon-on-Insulator”, Conference on Lasers and Electro-Optics (CLEO), SF1I.5, San Jose, CA, USA, May 14-19. [2017]

Contents

Abstract	i
Sommaire	iii
Acknowledgments	v
Statement of originality and contribution of co-authors	vii
Contents	xiii
List of Figures	xvi
List of Tables	xxii
List of Acronyms	xxiii
1 Introduction	1
1.1 Motivation	1
1.1.1 Silicon photonics	2
1.1.2 Optical access networks	5
1.2 State-of-the-art	6
1.2.1 Passive silicon photonic devices	7
1.2.2 Bench-top and integrated solutions for optical access networks	9
1.3 Original contributions	11
1.4 Thesis organization	13
2 Background	14
2.1 Silicon-on-insulator platform and silicon photonic devices	14
2.1.1 Bragg gratings	15

2.1.2	Fabry-Perot Resonator	16
2.1.3	Multimode interference couplers	17
2.1.4	Polarizers	17
2.2	Optical access network	19
2.2.1	Architectures	19
2.2.1.1	TDM PON	19
2.2.1.2	WDM PON	21
2.2.1.3	TWDM PON	21
2.2.1.4	Other types of optical access networks	22
2.2.2	Standardization	22
2.2.2.1	25G-EPON and beyond	23
3	Bragg grating, interference and doping based devices	26
3.1	Optical add-drop multiplexer with misaligned sidewall Bragg gratings	26
3.1.1	Misaligned sidewall gratings	27
3.1.2	Principle of operation	29
3.1.3	Simulation results	31
3.1.4	Experimental results and discussion	34
3.1.5	Conclusions	37
3.2	Transversely coupled Fabry-Perot resonators with Bragg gratings	38
3.2.1	Operating principle	38
3.2.2	Simulation results	41
3.2.3	Experimental results and discussion	44
3.2.4	Conclusions	46
3.3	Transversely coupled Fabry-Perot resonator with loop mirrors	46
3.3.1	Simulations results	48
3.3.2	Experimental results and discussion	48
3.3.3	Conclusions	53
3.4	C-Band 120° optical hybrid using multi-mode interference couplers	53
3.4.1	Device design and simulations	54
3.4.2	Experimental results and discussion	56
3.4.3	Conclusions	59
3.5	All-silicon TM-pass polarizer	59
3.5.1	Theoretical modeling of highly doped silicon and device design	61
3.5.2	Results and discussion	63
3.5.3	Fabrication techniques and tolerance analysis	68

3.5.4	Conclusions	71
4	Simplified coherent receiver using 120° optical hybrid for high speed PONs	72
4.1	25 Gb/s PAM-4 transmission using 10G transmitter and coherent amplification	72
4.1.1	Experimental setup	74
4.1.2	Results and discussion	76
4.1.2.1	Receiver with manual polarization control	76
4.1.2.2	Polarization independent operation	80
4.1.3	Conclusions	83
4.2	Demonstration of a 120° hybrid based integrated coherent receiver	83
4.2.1	Device design and fabrication	84
4.2.2	Transmission experiments	86
4.2.2.1	Experimental setup	86
4.2.2.2	25 Gb/s PAM-2 transmission	88
4.2.2.3	25 Gb/s PAM-4 transmission	92
4.2.3	Conclusion	93
4.3	25 and 50 Gb/s PAM-4 transmission over 43 and 21 km single-mode fiber using integrated coherent receiver	94
4.3.1	Experimental setup	94
4.3.2	Results and Discussion	95
4.3.2.1	25, 40 and 44 Gb/s PAM-4 transmission	95
4.3.2.2	50 Gb/s PAM-4 transmission	101
4.3.3	Conclusions	102
5	Conclusions and Future Works	104
5.1	Thesis highlights	104
5.2	Future research avenues	107
	Appendix	109
	References	115

List of Figures

1.1	Projected increase in global IP traffic by Cisco dated February, 2019. Source: [1] © 2019 Cisco	2
1.2	Global application category traffic share by Sandvine dated October, 2018. Source: [2] © 2018 Sandvine	3
1.3	Silicon photonics market forecast by Yole Développement dated January, 2018. Source: [3] © 2018 Y. Développement	4
1.4	Silicon photonic application range by Yole Développement dated January, 2018. Source: [3] © 2018 Y. Développement	5
1.5	Silicon photonics chip compared to a Canadian 10 cents. Credit: 2019 Md Ghulam Saber	6
1.6	Annual growth of fiber subscription among countries reporting fiber subscription dated December, 2017. Source: [4] © 2018 OECD	7
2.1	Schematic of the cross-section of a silicon-on-insulator wafer [5].	15
2.2	Typical spectral responses of a uniform Bragg grating.	15
2.3	Fabry-Perot resonator in the simplest form.	16
2.4	Scanning electron microscope image of a 2×2 MMI coupler.	17
2.5	Simulated transverse electric field profiles of a 2×2 MMI coupler with excitations at (a) input 1, and (b) input 2.	18
2.6	Schematic of a hybrid plasmonic polarizer (TE/TM).	18
2.7	Architectures of (a) TDM, (b) splitter-based WDM, (c) grating-based WDM, and (d) TWDM PONs. [OLT: optical line terminal, ONU: optical network unit, WDM: wavelength-division-multiplexing.]	20
3.1	Electric field distributions with light injected from the left for gratings with (top): no misalignment, and (bottom): complete misalignment. Source: [6] © 2014 Optical Society of America.	28

3.2	(a) Misaligned sidewall Bragg grating, (b) variation of ΔL . Schematic of the fabricated (c) single-stage OADM configuration, (d) cascaded OADM configuration. Here, $\lambda_4 = \lambda_4'$	29
3.3	Simulated effective refractive index of the 580 nm, n_{eff1} and 420 nm, n_{eff2} silicon waveguides as a function of wavelength.	30
3.4	Simulated transmission responses for the single-stage configuration for (a) different ΔW with NG=400 and $\Delta L=0$ nm, (b) different ΔL with $\Delta W=80$ nm and NG=400, and (c) different NG with $\Delta W=80$ nm and $\Delta L=128$ nm. Simulated transmission responses for the cascaded configuration for (d) different ΔW with NG=400 and $\Delta L=0$ nm, (e) different ΔL with $\Delta W=80$ nm and NG=400, and (f) different NG with $\Delta W=80$ nm and $\Delta L=128$ nm.	32
3.5	FoM as a function of ΔL for different ΔW with NG=400 for the (a) single-stage, and the (b) cascaded configurations.	33
3.6	Simulated coupling coefficients for (a) different ΔW with $\Delta L=0$ nm, and (b) different ΔL with $\Delta W=80$ nm.	34
3.7	SEM images of the fabricated single-stage and cascaded OADMs and misaligned sidewall bragg grating with $\Delta L=128$ nm and $\Delta W=80$ nm.	35
3.8	Measured transmission responses of (a) drop and (b) through port of the single-stage configuration, and (c) drop and (d) through port of the cascaded configuration.	36
3.9	Comparison for the single-stage and cascaded configurations of the OADMs between the simulated and measured (a) ER, and (b) 3-dB bandwidth. Sim. = Simulated and Meas. = Measured.	37
3.10	Schematics of the (a) type I, and the (b) type II TCFPRs, and (c) an all-pass MRR. BG: Bragg Grating	40
3.11	Simulated group index of silicon waveguide with 500 nm \times 220 nm cross-section. Obtained using Lumerical MODE Solutions.	41
3.12	(a) Cavity length sweep of the type I TCFPR with Bragg gratings (color bar indicates the extinction ratio) and simulated transmission response of the (b) type I TCFPR with $L_{eff} = 110 \mu\text{m}$, and the (c) type I TCFPR with $L_{eff} = 943 \mu\text{m}$	42
3.13	Q-factor as a function of κ for both type of TCFPRs.	43
3.14	Effect of variation of κ on the type (a) I, and (b) II TCFPRs' spectral characteristics using simulations.	43
3.15	SEM images of the Bragg grating-based type (a) I, and (b) II TCFPRs, (c) enlarged view of the Bragg grating.	44

3.16	Measured transmission responses of the (a) type I TCFPR with $L_{eff} = 110 \mu\text{m}$, and the (b) type I TCFPR with $L_{eff} = 943 \mu\text{m}$	45
3.17	Variation of the Q-factor and the FSR of the type I and II TCFPRs as a function of L_{eff}	45
3.18	Schematics of the type (a) I, and (b) II TCFPRs with loop mirrors.	47
3.19	(a) Cavity length sweep of the type I TCFPR with loop mirrors (color bar indicates the extinction ratio) and simulated transmission response of the type (b) II TCFPR with $L = 376 \mu\text{m}$ and the type (c) I TCFPR with $L = 1038 \mu\text{m}$	49
3.20	Q-factor as a function of κ for both TCFPRs.	50
3.21	Effect of variation of κ on the (a) type I, and the (b) type II TCFPRs' spectral characteristics using simulations.	50
3.22	SEM images of the type (a) I, and (b) II TCFPRs with loop mirrors, and (c) photograph of the experimental setup.	51
3.23	Measured transmission responses of the (a) type II TCFPR with $L = 376 \mu\text{m}$, and the (b) type I TCFPR with $L = 1038 \mu\text{m}$	52
3.24	Schematic of the 3×3 MMI coupler based 120° optical hybrid.	54
3.25	Variation of length of the 120° optical hybrids for C-band with width = $11 \mu\text{m}$. Here, 1, 2 and 3 are the input ports and 4, 5 and 6 are the output ports as shown in Fig. 3.24. Black dashed circle indicates the optimum length.	55
3.26	Simulated TE field profiles of the 3×3 MMI coupler with excitations at different input ports.	56
3.27	(a) Simulated split ratio of each output ports for light injected at each input ports, and (b) simulated relative phases of the 120° hybrid.	56
3.28	SEM image of the fabricated 120° hybrid.	57
3.29	(a) Measured split ratio of each output ports for light injected at each input ports, and (b) difference of split ratio between each output ports [1 & 2, 1 & 3 and 2 & 3].	57
3.30	(a) Relative phase measurement method, (b) measured relative phases of the 120° optical hybrid, and (c) deviation of the relative phases from the ideal value of 120° and 240°	58
3.31	(a) Real and imaginary parts of the complex permittivity of the highly doped p-silicon as a function of the carrier concentrations at $1.55 \mu\text{m}$ wavelength, (b) real, and (c) imaginary parts of the complex permittivity of the highly doped p-silicon as a function of the wavelength for different carrier concentrations.	62
3.32	(a) Schematic, and (b) cross-section of the proposed TM-pass polarizer.	63

3.33	Extinction ratio (defined in equation 3.13) as a function of the wavelength for different carrier concentrations with $L_{p-si} = 15 \mu\text{m}$, $W_{p-si} = 600 \text{ nm}$, $W_{Si} = 260 \text{ nm}$ and $\text{gap} = 200 \text{ nm}$	64
3.34	Variation of the ER, IL and figure of merit as functions of (a) the L_{p-si} for $W_{p-si} = 600 \text{ nm}$, $W_{Si} = 260 \text{ nm}$, $\text{gap} = 200 \text{ nm}$ and $N = 10 \times 10^{20} \text{ cm}^{-3}$, (b) the W_{p-si} for $L_{p-si} = 15 \mu\text{m}$, $W_{Si} = 260 \text{ nm}$, $\text{gap} = 200 \text{ nm}$ and $N = 10 \times 10^{20} \text{ cm}^{-3}$, (c) the W_{Si} for $L_{p-si} = 15 \mu\text{m}$, $W_{p-si} = 600 \text{ nm}$, $\text{gap} = 200 \text{ nm}$ and $N = 10 \times 10^{20} \text{ cm}^{-3}$, and (d) the gap between the waveguides for $L_{p-si} = 15 \mu\text{m}$, $W_{p-si} = 600 \text{ nm}$, $W_{Si} = 260 \text{ nm}$ and $N = 10 \times 10^{20} \text{ cm}^{-3}$. Figure of merits are shown in the inset of each figure.	65
3.35	ER and IL as a function of the wavelength of the reported TM-pass polarizer for $L_{p-si} = 15 \mu\text{m}$, $W_{p-si} = 600 \text{ nm}$, $W_{Si} = 260 \text{ nm}$, $\text{gap} = 200 \text{ nm}$ and $N = 10 \times 10^{20} \text{ cm}^{-3}$	67
3.36	(a) Schematic showing the mode profiles at different points along the TM-pass polarizer, (b) TM and TE mode propagation through the polarizer. (Electric fields are plotted in both the figures.)	68
3.37	Fabrication tolerance analysis of the proposed TM-pass polarizer	69
4.1	Experimental setup: DAC: digital to analog converter; EML: electroabsorption modulated laser; VOA: variable optical attenuator; VODL: variable optical delay line; SMF: single-mode fiber; PBS: polarization beam splitter; PC: polarization controller; LO: local oscillator; LPF: low-pass filter; TIA: trans-impedance amplifier; BER: bit error rate; RTO: real-time oscilloscope.	74
4.2	EML output power as a function of the bias voltage.	76
4.3	BER as functions of (a) the frequency offset between the incoming signal and the LO, and (b) the LO power.	77
4.4	Receiver sensitivity versus BER for different propagation distances for the single polarization receiver.	78
4.5	PAM-4 eye diagrams (a) in back-to-back (B2B), (b) after 10.5 km, (c) after 20.7 km, (d) after 25.7 km, (e) after 27.7 km, and (f) after 31.2 km of propagation at 25 Gb/s.	79
4.6	BERs and sensitivities for different reach.	80
4.7	(a) BER as functions of the frequency offset between the incoming signal and the LO, and (b) BER statistics for 100 captures with random SOP.	81
4.8	Receiver sensitivity versus BER for different propagation distances for the polarization-independent receiver.	81
4.9	PAM-4 eye diagrams (a) in back-to-back (B2B), (b) after 10.5 km, (c) after 15.5 km, and (d) after 21 km of propagation at 25 Gb/s.	82

4.10	(a) Schematic of the coherent receiver, (b) layout of the coherent receiver, (c) a photograph of the fabricated receiver, and (d) receiver with couplers and probes connected. PSR: Polarization splitter and rotator, PD: Photodetector, MMI: Multimode interference coupler.	85
4.11	25 Gb/s PAM-2 (a) optical eye right after the modulator, and (b) electrical eye after detection using the integrated germanium PD.	86
4.12	(a) Measured split ratio of each output ports for light injected at each input ports, and (b) measured relative phases of the 120° hybrid considering output port 1 as the reference [black dashed lines represent $\pm 10^\circ$ deviation].	87
4.13	Experimental setup. DAC: digital-to-analog converter, SMF: single-mode fiber, EDFA: erbium doped fiber amplifier, VOA: variable optical attenuator, PC: polarization controller, DUT: device under test, LO: local oscillator, RTO: real-time oscilloscope.	88
4.14	(a) BER as functions of the frequency offset between the incoming signal and the LO, and (b) received optical power versus BER for different propagation distances for 25 Gb/s PAM-2 (after subtraction of the losses from the edge coupler).	89
4.15	PAM-2 eye diagrams (a) in back-to-back (B2B), (b) after 21 km, (c) after 26 km, and (d) after 30 km of propagation at 25 Gb/s.	90
4.16	BER statistics for 50 captures with (a) fixed SOP, and (b) random SOP.	91
4.17	Receiver sensitivity versus BER for different propagation distances for 25 Gb/s PAM-4 signal (after subtraction of the losses from the edge coupler).	92
4.18	PAM-4 eye diagrams (a) in back-to-back (B2B), (b) after 10.5 km, and (c) after 21 km of propagation at 25 Gb/s.	93
4.19	Experimental setup. 26 Gbaud PAM-4 optical eye after the modulator is shown inside the green box. DAC: digital-to-analog converter, SMF: single-mode fiber, EDFA: erbium doped fiber amplifier, VOA: variable optical attenuator, PC: polarization controller, DUT: device under test, LO: local oscillator, RTO: real-time oscilloscope.	94
4.20	Receiver sensitivity versus BER for 25 Gb/s PAM-4 (a) over different fiber lengths, and (b) in B2B for different wavelengths [edge coupler loss has been subtracted], and (c) split ratio and phase deviation of the 120° hybrid.	96
4.21	PAM-4 eye diagrams (a) in back-to-back (B2B), (b) after 10.5 km, (c) after 21 km, (d) after 31 km, and (e) after 43 km of propagation at 25 Gb/s.	97
4.22	Receiver sensitivity versus BER for (a) 40 Gb/s, and (b) 44 Gb/s PAM-4 over different fiber lengths. The solid lines indicate without FFE and the dashed lines indicate with 31-tap FFE. Edge coupler loss has been subtracted.	98

4.23	PAM-4 eye diagrams (a) in back-to-back (B2B), (b) after 10.5 km, (c) after 21 km, without FFE and (d) in back-to-back (B2B), (e) after 10.5 km, and (f) after 21 km with 31-tap FFE at 40 Gb/s.	99
4.24	PAM-4 eye diagrams (a) in back-to-back (B2B), (b) after 10.5 km, (c) after 21 km, without FFE and (d) in back-to-back (B2B), (e) after 10.5 km, and (f) after 21 km with 31-tap FFE at 44 Gb/s.	100
4.25	(a) Number of FFE taps versus BER at -3.8 dBm received power in back-to-back (B2B), and (b) receiver sensitivity versus BER for 50 Gb/s PAM-4 over different fiber lengths using different FFE taps [Edge coupler loss has been subtracted]. . .	101
4.26	PAM-4 eye diagrams (a) in back-to-back (B2B), (b) after 10.5 km, and (c) after 21 km at 50 Gb/s with 31-tap FFE.	102
5.1	Summary of the original contributions of the thesis.	105
A1	Schematic of the polarization independent receiver with polarization beam splitter either on the (a) local oscillator (LO) or on the (b) received signal.	109

List of Tables

2.1	Summary of the physical layer properties for different PON standards [7]. [Att.: Attenuation, Diff.: Differential, max.: maximum, Nom.: Nominal]	24
3.1	Measured ER and IL for various cavity lengths.	46
3.2	Measured ER and IL for different cavity lengths.	53
3.3	Comparison with other TM-pass polarizers. ER (Extinction Ratio), IL (Insertion Loss), and Ref. (Reference).	70
4.1	Summary of transmission performance of the integrated simplified coherent receiver.	103

List of Acronyms

AC	Alternating Current
ADC	Analog-to-Digital Converter
ASE	Amplified Spontaneous Emission
B2B	Back-to-Back
BER	Bit Error Rate
BG	Bragg Grating
BW	Bandwidth
BOX	Buried Oxide
CD	Chromatic Dispersion
CMOS	Complementary-Metal-Oxide-Semiconductor
CW	Continuous Wave
DAC	Digital-to-Analog Converter
DSP	Digital Signal Processing
DC	Direct Current
DCA	Digital Communication Analyzer
DFB	Distributed Feed-Back
DOCSIS	Data Over Cable Service Interface Specification
DUT	Device Under Test
EBeam	Electron Beam
ECL	External Cavity Laser
EDB	Electrical Duo-Binary
EDFA	Erbium-Doped Fiber Amplifier
ER	Extinction Ratio
EME	Eigen Mode Expansion
EML	Electroabsorption Modulated Laser
EO	Electro-Optic
ESA	Electrical Spectrum Analyzer
FEC	Forward Error Correction

FFE	Feed-Forward Equalizer
FIR	Finite Impulse Response
FPR	Fabry-Perot Resonator
FR	Footprint Ratio
FSAN	Full Service Access Networks
FSR	Free Spectral Range
FOM	Figure of Merit
FWHM	Full-Width Half-Maximum
GSG	Ground-Signal-Ground
GTI	Gires-Tournois Interferometer
HD-FEC	Hard Decision Forward Error Correction
I/O	Input Output
IL	Insertion Loss
ITU	International Telecommunication Union
IM/DD	Intensity Modulation Direct Detection
IME	Institute of Micro Electronics
ISI	Inter Symbol Interference
LDPC-FEC	Low-Density Parity-Check Forward Error Correction
LMS	Least Mean Squares
LO	Local Oscillator
MMI	Multi Mode Interference
MPW	Multi Project Wafer
MRR	Micro Ring Resonator
MZI	Mach-Zehnder Interferometer
MZM	Mach-Zehnder Modulator
NRZ	Non-Return-to-Zero
OADM	Optical Add Drop Multiplexer
ODB	Optical Duo-Binary
OOK	On-Off Keying
OSA	Optical Spectrum Analyzer
PAM2	2-level Pulse Amplitude Modulation
PAM4	4-level Pulse Amplitude Modulation
PBS	Polarization Beam Splitter
PC	Polarization Controller
PDK	Product Development Kit
PI	Polarization Independent

PIC	Photonic Integrated Circuit
PPG	Pulse Pattern Generator
PON	Passive Optical Network
PSR	Polarization Splitter Rotator
PD	Photo Detector
QAM	Qaudrature Amplitude Modulation
Q-Factor	Quality Factor
RF	Radio Frequency
RMS	Root Mean Square
RTO	Real Time Oscilloscope
SiPh	Silicon Photonics
SMF	Single Mode Fiber
SNR	Signal-to-Noise Ratio
SOI	Silicon-On-Insulator
SOP	State Of Polarization
SPS	Sample Per Symbol
TCFPR	Transversely Coupled Fabry-Perot Resonator
TE	Transverse Electric
TIA	Trans-Impedance Amplifier
TDL	Tunable Delay Line
TDM	Time-Division Multiplexing
TM	Transverse Magnetic
TWDM	Time- and Wavelength- Division Multiplexing
VNA	Vector Network Analyzer
VOA	Variable Optical Attenuator
VODL	Variable Optical Delay Line
WDM	Wavelength-Division Multiplexing

Chapter 1

Introduction

1.1 Motivation

To meet the ever-increasing demand of internet usage by users, the capacity of the communication networks needs a significant increase. It is expected that 60% population of the world will be using the internet by 2022 [1]. The number of connected devices will rise to 28.5 billion in 2022 due to the increase in the number of interconnected devices i.e., Internet of Things. To put things into perspective, this is 3.6 times more than the expected population of the world in 2022 [1]. According to the Cisco report dated February, 2019 (shown in Fig. 1.1), the compound annual growth rate (CAGR) [$\text{CAGR} = (\text{End Val.}/\text{Beg. Val.})^{1/\#\text{years}} - 1$] will be 26% between 2017 and 2022. Global IP traffic will increase threefold over the next five years and the annual global IP traffic will reach 4.8 ZB per year by 2022 [1].

The massive increase in bandwidth demand is fueled by the change in the way we consume media. The emergence of the 4K/8K streaming services are changing the entertainment industry ecosystem. People are moving away from the traditional cable-based broadcast services to the video on-demand services which doubles the data consumption [1,7]. The appearance of the cloud services are redefining the way we compute and store data. Enterprises are moving their computation power to cloud-based servers and people are storing their data on the servers. These applications require high quality internet connections. Gaming is also becoming a significant source of online traffic. The number of downloads are growing on the gaming networks such as, Playstation, Nintendo, and Xbox. Streaming services such as Twitch and professional gaming are going mainstream as well which increase the traffic volume significantly. The advent of cloud gaming services such as 'Google Stadia' will further contribute to the internet traffic share of gaming. A survey on the global application category traffic share by Sandvine dated October, 2018 is shown in Fig. 1.2. According to the report, 58% of the

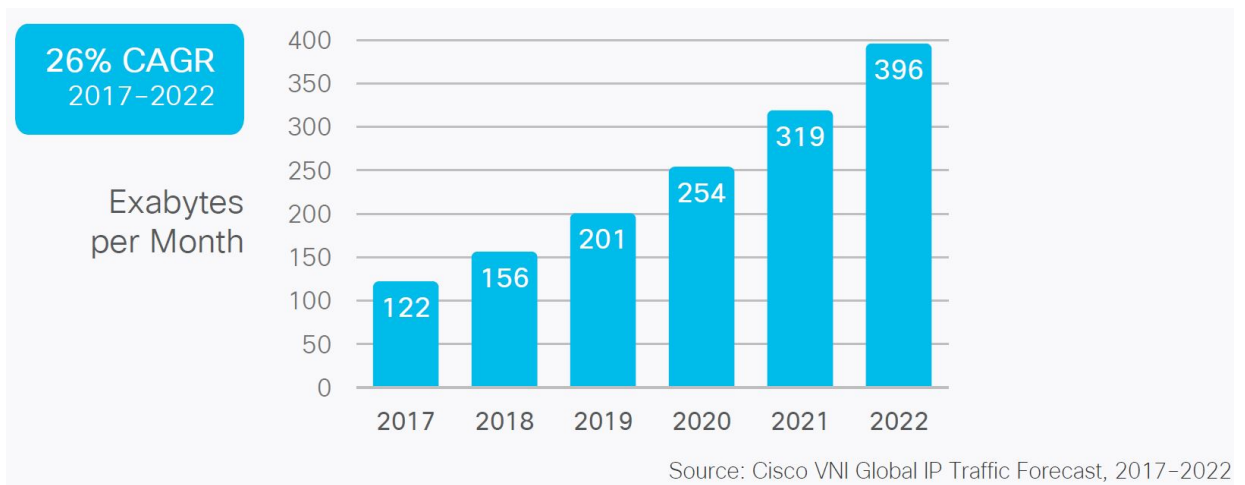


Fig. 1.1 Projected increase in global IP traffic by Cisco dated February, 2019.
Source: [1] © 2019 Cisco

downstream traffic on the internet was video with Netflix having a 15% share [2]. Video was also the top upstream traffic with BitTorrent being second by a small margin. Gaming is third on the list causing 7.78% of the downstream internet traffic [2].

Finally, the fifth generation of mobile networks (5G) is redefining connectivity and services so it includes new market and new industry segments [8]. The requirements of the 5G network includes non-limiting access to data (five nines availability and five nines reliability), peak data rates of 20 Gb/s, and user experience data rates of 10 to 100 Mb/s. We expect 5G to work with latencies of 1 to 10 ms (<1 ms for tactile internet), mobile users at speeds between 50 to 500 km/h, an increase of 3 times the spectral efficiency, a much higher connection density (10k to 1M devices/km²) and a factor of 10 increase in battery life time for small devices. These new capacity trends are imposed on both the telecommunication and data communication networks, and the technology 'per excellence' that can provide large bandwidth is optics. High speed PONs along with mature integrated photonic devices will be required to serve these requirements.

1.1.1 Silicon photonics

Silicon photonics is attracting interest both from academia and industry. Billions of dollars have been invested on the development of silicon photonics to build mature market products [9–12]. According to a report by Yole Développement (shown in Fig. 1.3), silicon photonics will have a market value of \$560 million at chip level and almost \$4 billion at transceiver level in 2025,

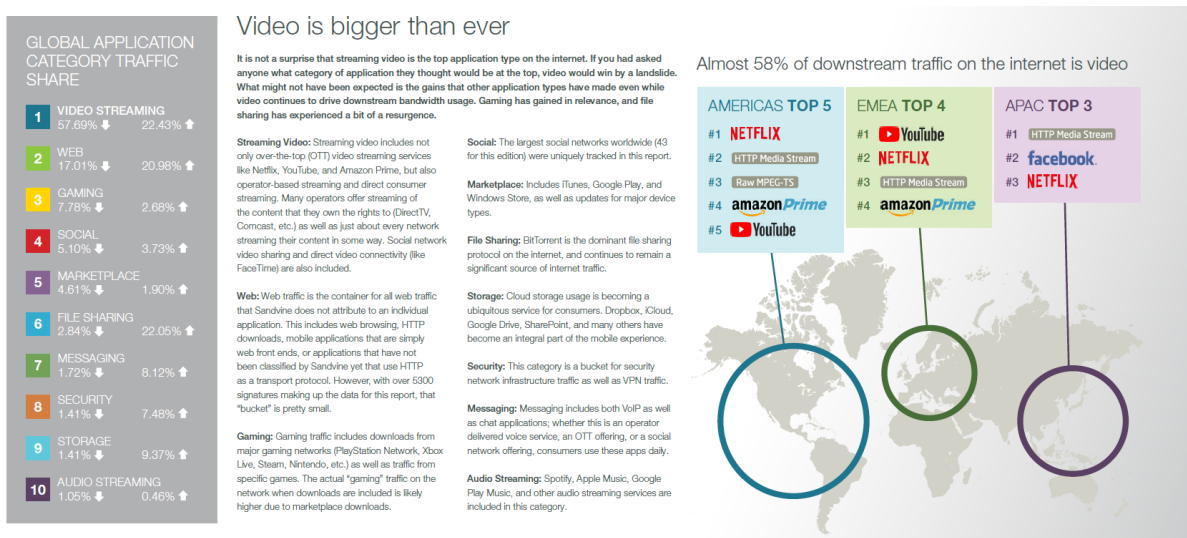


Fig. 1.2 Global application category traffic share by Sandvine dated October, 2018.
Source: [2] © 2018 Sandvine

majority of which will be for intra-data center communication. Apart from data center applications, there are some other interesting applications of silicon photonics. With the emergence of high performance computing to solve critical problems in science, engineering, and business, the performance gridlock has shifted from processors to inter-chip communication due to parallelism. Silicon photonics can solve the future bandwidth scalability issues of high performance computing by offering high bandwidth, low latency and highly integrated optical interconnects. In the telecom sector, silicon photonics modules are attractive in the metropolitan and access networks. As the fiber-to-the-home (FTTH) moves from 10G to 25G, functionality such as wavelength tuning and switching will be required. Companies like Acacia [13] and Aeponyx [14] are developing silicon photonic solution for these network segments. Silicon photonics is also an important platform for biomedical sensing [15] and LiDAR [16] applications. Figure 1.4 shows the different applications of the silicon photonics platform along with the research institutes and companies involved.

One of the major advantages of the silicon photonics platform is the compatibility with the existing CMOS foundries. The fab-less model of silicon photonics has enabled designers and researchers from academia and industry to focus on novel design ideas and applications without worrying about the process development for fabrication of the devices [17]. On the other hand, the CMOS foundries can focus on the fabrication process design fully utilizing the costly fabrication facilities [18,19]. Furthermore, the feasibility to integrate photonic integrated circuits with electronics such as drivers for modulators, trans-impedance amplifiers for photodetectors,

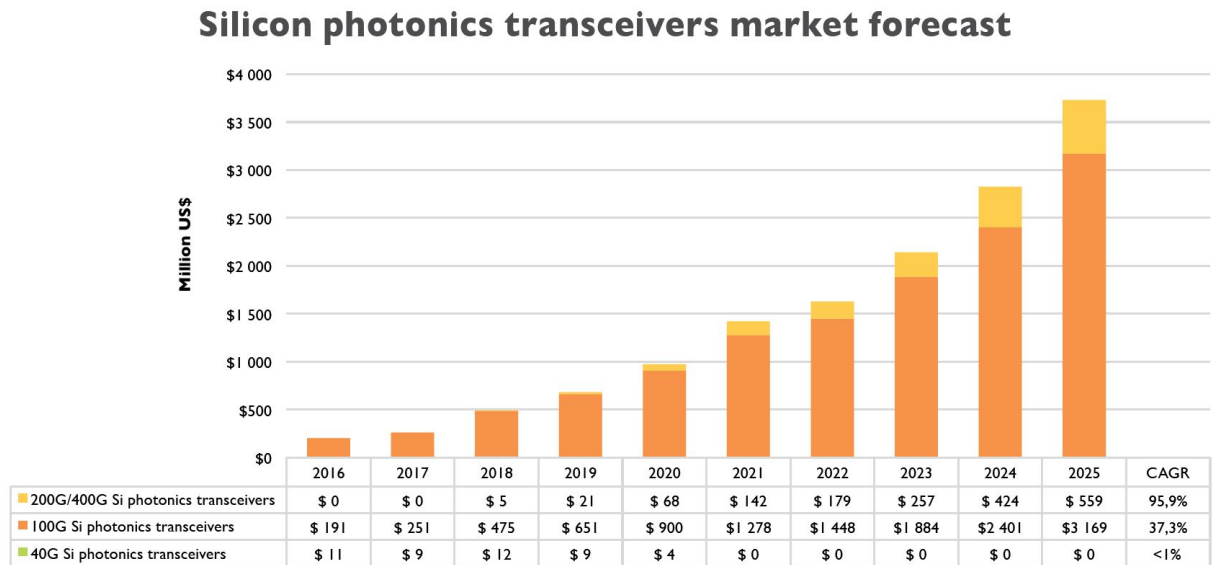


Fig. 1.3 Silicon photonics market forecast by Yole Développement dated January, 2018. Source: [3] © 2018 Y. Développement

and processing of digitized data for high capacity modulation formats [20–22] gives an edge to this platform. Another unique advantage of the silicon photonics platform compared to III-V, LiNbO₃ and silica platforms is the high index contrast between the core and the cladding layers which allows compactness and dense integration. The electrical parasitic loading is reduced as well in electro-optic devices due to the small waveguides which enhances the electro-optic interaction and operating speed [23]. Comparison of dimensions of a Canadian 10 cents with one of our silicon photonic chips fabricated at IME A*, Singapore is shown in Figure 1.5. This chip contains several devices designed by our group.

In spite of the advantages of the silicon photonics platform, there are few challenges that need to be overcome to have competitive edge over other integrated platforms. The sensitivity of the effective index of a silicon waveguide on the fabrication variation results in phase uncertainty of the optical signal propagating through the waveguide. This uncertainty in phase of the optical signal makes the design of wavelength-division-multiplexing (WDM) filters and optical hybrids challenging since precise control of wavelength is necessary in these devices. Another major issue of the silicon photonics platform is the large birefringence. The effective indices of the transverse electric (TE) and transverse magnetic (TM) modes in a typical 500 nm × 220 nm silicon waveguide are 2.45 and 1.77, respectively. Hence, it is challenging to build polarization insensitive devices on the silicon photonics platform.

In this thesis, we demonstrate silicon photonic devices for WDM applications, polarization

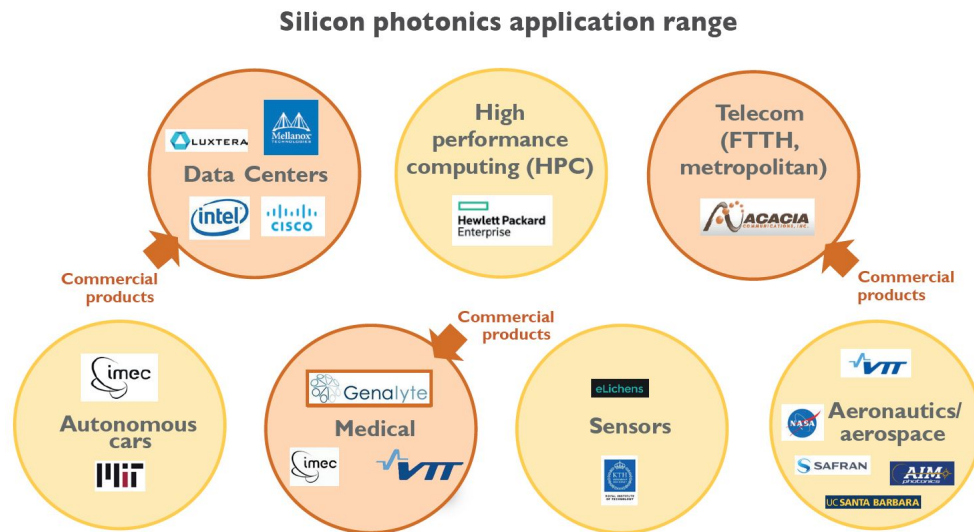


Fig. 1.4 Silicon photonic application range by Yole Développement dated January, 2018. Source: [3] © 2018 Y. Développement

handling devices, and optical hybrids for simplified coherent receivers.

1.1.2 Optical access networks

Access network is the last segment of the network which connects the end-users with the central office of the service provider and hence, often termed as the last-mile network. From the end users' side, access network is the first segment that connects the users to the broader network and can be called the first-mile network [24]. Traditionally, access networks utilized twisted pair copper cables connecting the individual households/enterprises with the central office. However, the bandwidth-distance product of copper cables are very small [25]. A transmission distance of about 100 m is achievable at 100 Mb/s bit rate using sophisticated transmitters [26]. Since single-mode fibers essentially provide unlimited bandwidth and long propagation distances, the copper-based last-mile connections are being gradually replaced by optical fibers. According to a report by the Organization for Economic Co-operation and Development (OECD), fiber-based last-mile connections account for 23.3% of fixed broadband subscriptions with a jump of 15% in the year 2017 [4]. Figure 1.6 shows the annual growth of fiber subscription among countries reporting fiber subscription. The highest growth in fiber occurred in Ireland and Colombia with a growth of 420% and 168%, respectively over the year.

The terminology Fiber-to-the-X (FTTX) covers the broad categories of the fiber-based access networks, i.e., Fiber-to-the-Home (FTTH) when the fiber goes all the way to the single home user, Fiber-to-the-Building (FTTB) in case of the multi-dwelling units, Fiber-to-the-

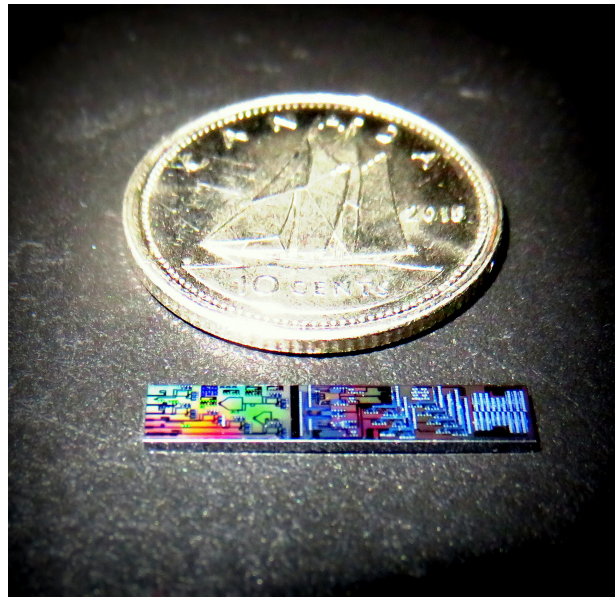


Fig. 1.5 Silicon photonics chip compared to a Canadian 10 cents. Credit: 2019 Md Ghulam Saber

Cabinet (FTTC) and Fiber-to-the-Node (FTTN) when the fiber goes up to a cabinet or node and the rest part is covered by copper cables with lengths of up to 300 m for FTTC and greater than 1 km for FTTN. Asia and the Pacific region have the highest deployment of FTTH with 77% of the worldwide customers [27]. Europe accounts for 15% and North America has 5% of the global FTTH subscribers [27]. Due to the extensive installation of copper-based networks, European and North American providers are reluctant to switch to FTTH/B. Instead, they are more interested in FTTC/N and support the rest of the connection using the copper networks. According to Ovum, FTTH will have a 65% share of the global investment in broadband fixed access equipment in 2021, while the copper-based networks will have the rest 35% share [28].

In this thesis, we report ways to meet the requirements of the emerging high-speed access networks using bench-top and integrated solutions.

1.2 State-of-the-art

In this section, we describe the recent advances in the fields of passive silicon photonic devices and the solutions for optical access networks addressed in the thesis.

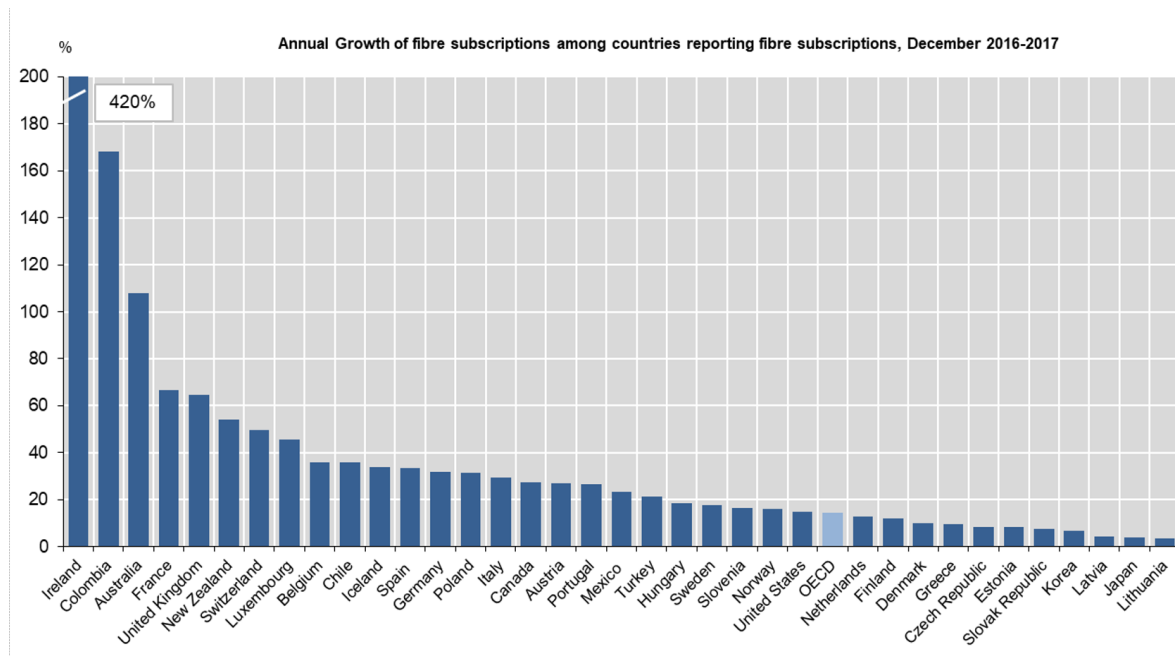


Fig. 1.6 Annual growth of fiber subscription among countries reporting fiber subscription dated December, 2017. Source: [4] © 2018 OECD

1.2.1 Passive silicon photonic devices

Optical add-drop multiplexers

Optical add-drop multiplexers (OADMs) select and route WDM channels. Researchers have been developing OADMs in non-SOI platforms [29–33], and more recently on the SOI platforms [34–40]. In the SOI platform, ring resonator [34–36], grating-assisted contra-directional coupler [38–40], phase-modulated shifted Bragg gratings, multimode antisymmetric waveguide Bragg gratings [41] and sidewall Bragg grating [37, 42] based devices have received much attention. Ring resonators are compact but achieving a flat-top spectral response, and a large free spectral range (FSR) is challenging. Grating-assisted contra-directional coupler based devices are complex in design and large extinction ratio (ER) is difficult to achieve [38, 40, 43]. Bragg grating based devices, on the other hand, offer FSR free operation and several degrees of freedom to achieve desired spectral response [44].

Bragg gratings are reflection-based devices and therefore optical circulators are required in order to use them as multiplexers. Optical circulators are difficult to achieve on SOI since they require non-CMOS compatible materials [45]. Circulators are available as discrete optical components, but increase packaging complexity [46]. One solution to this problem is to incorporate

Bragg gratings in interferometric structures [47]. Bragg gratings in Mach-Zehnder interferometer (MZI) based OADMs on SOI have been reported in the past by several groups. A silicon wire waveguide based Bragg gratings in MZI OADM with a 3-dB bandwidth of 0.7 nm was reported in [42]. But it has a very small ER of 8 dB and a relatively long length of 800 μm . In [37], two OADM configurations based on Bragg gratings in MZIs which offered a 3-dB bandwidth of 3.5 nm and ERs of 40 dB and 45 dB were reported. However, the footprints were 391 $\mu\text{m} \times 1400 \mu\text{m}$ and 391 $\mu\text{m} \times 3600 \mu\text{m}$, respectively, which are excessively large.

In this thesis, we demonstrate ultra-compact, high ER and low insertion loss (IL) OADMs using misaligned sidewall Bragg gratings in MZIs.

Resonators

Resonators [48] are one of the key candidates for WDM applications. Several resonators have been implemented on SOI such as, ring [31,48], racetrack [49], Gires-Turnois [50], Fabry-Perot [51] and Michelson [52]. Among them, the micro ring resonator (MRR) is the most intensively used resonator due to its compact footprint.

Resonators with high Q-factor, low IL, high ER, large FSR and wide tuning range are desired in most applications [53]. In MRR, the critical coupling condition should be conserved to maintain the performance which is often hard to achieve due to fabrication variability. Heaters are used to tune the resonant peaks to the designed wavelengths; however, this increases the power consumption and results in increased complexity of the device. In addition, if the bend radius of the MRR is too small, it becomes difficult to obtain the correct coupling coefficient due to small coupling region.

MRRs can be used as all-pass filters for dispersion compensation applications [54]. Nevertheless, Bragg gratings can be also used as filters for applications like WDM. However, it is hard to obtain repeatable performance using the Bragg grating filters due to serious lithographic distortion [55]. Furthermore, multiple Bragg gratings need to be cascaded to design a filter for multichannel purposes [56]. This increases the IL and the device complexity significantly.

In this thesis, we demonstrate high ER and low IL transversely coupled Fabry-Perot resonators using Bragg gratings and loop mirrors.

Optical hybrids

Optical hybrids are used to mix the received optical signal with the local oscillator and are the central building blocks of the coherent receivers. Stokes vector receivers also utilize optical hybrids [57]. Conventional coherent detection systems use 2×4 90° optical hybrids and utilize the balanced photodetectors to reject unwanted direct detection terms [58]. Integrated 90° hybrids have been demonstrated on the SOI platform [59,60]. Sub-wavelength gratings

(SWG) dispersion-engineered 90° hybrid has been reported as well to reduce the footprint and increase the operation bandwidth [61]. To reduce the complexity of the receiver architecture, single-ended detection based optical front-ends with 120° [62,63] and 180° [64,65] optical hybrids have been reported. Simple integrated 3-dB couplers [66] can be used as 180° hybrids. Indium phosphide based integrated coherent 120° downconverter has been demonstrated in [67]. In [68], an integrated coherent receiver based on 120° hybrids on SOI in the C-band has been reported. However, there is no detail analysis on the design and characterization of the 120° hybrid itself.

In this thesis, we demonstrate broadband and low excess loss 120° hybrid based on 3×3 multimode interference (MMI) coupler using 193 nm deep ultraviolet (DUV) lithography operating in the C-band.

Polarizers

Polarizers are compact and efficient device to suppress the unwanted polarization in an optical signal and retain the desired one. To date, several TM-pass polarizers have been reported in various configurations for different wavelengths of operation [69–72]. Kim et al. [69] demonstrated a TM-pass polarizer using a 1D photonic crystal based on sub-wavelength structure achieving 34 dB of ER and around 1 dB of IL. However, this structure is challenging to fabricate using the 193 nm DUV lithography and it is highly sensitive to fabrication variations. Bai et al. [73] reported a TM-pass polarizer using a hybrid plasmonic grating achieving an ER of 25 dB with a $2.5\ \mu\text{m}$ active length. In this case, silver was used to form the plasmonic waveguide which is not CMOS compatible. Hu et al. [74] proposed a graphene-based TM-pass polarizer having a length of $150\ \mu\text{m}$ which is prohibitive for dense integration. Furthermore, graphene is not suitable for mass production. A TM-pass polarizer based on the insulator-to-metal phase transition of vanadium oxide was proposed by Sanchez et al. [75]. However, a critical temperature of 68°C is required to ensure the phase transition which makes it inefficient in terms of energy consumption compared to passive designs. A sub-wavelength grating (SWG) based TM-pass polarizer was reported in [76] obtaining 27 dB of ER and 0.5 dB of IL. However, this structure is challenging to fabricate using the 193 nm DUV process and is sensitive to tolerance variations. Therefore, most of the reported devices are not CMOS-compatible.

In this thesis, we report a CMOS compatible and high ER TM-pass polarizer using highly doped silicon.

1.2.2 Bench-top and integrated solutions for optical access networks

Bench-top solutions

Due to the increasing bandwidth demand, standardization bodies such as IEEE and ITU-T are

working towards the standardization process of high speed PONs. As such, researchers around the world are looking into ways to cost-effectively increase the capacity of the access networks and maintain the power budget and reach requirements using off-the-shelf components. Several demonstrations of 25 Gb/s transmission on a single λ using different modulation formats (e.g. non-return to zero (NRZ), electrical duo-binary (EDB), optical duo-binary (ODB), PAM-4) have been presented in the past. However, we focus on the PAM-4 format since it is more dispersion tolerant than NRZ and EDB for the same bit rate, requires less bandwidth than NRZ, EDB, and ODB, and does not need dual-drive modulators like ODB [77]. In [78], 25 Gb/s PAM-4 transmission over 20 and 30 km of fiber was demonstrated achieving receiver sensitivities of -23 and -21.5 dBm, respectively, with bit-error-rate (BER) below the hard decision forward error correction (HD-FEC). An external cavity laser (ECL) and a 30 GHz Mach-Zehnder modulator were used at the transmitter and an avalanche photodetector (APD) and electronic dispersion compensation to equalize the PAM-4 eyes were utilized at the receiver.

Zhang et al. [79] demonstrated 30 km PAM-4 transmission at 25 Gb/s with 10G transmitter optical subassembly and receiver optical subassembly achieving -21 dBm of sensitivity below the HD-FEC. This was achieved using APD and feed-forward equalization (FFE) at the receiver to compensate for the bandwidth limitation and the chromatic dispersion (CD). An erbium doped fiber amplifier (EDFA) was utilized as well to improve the power budget. Houtsma et al. [80] reported 25 Gb/s PAM-4 transmission over 20 km distance using 10G optical components and by applying pre-emphasis at the transmitter to compensate for the dispersion and APD at the receiver. A sensitivity of -22 dBm was demonstrated below the HD-FEC level using EDFA as booster for the downstream signal and as pre-amplifier for the upstream signal at the optical line terminal.

An amplifier-less 25 Gb/s PAM-4 transmission over 20 km achieving 29 dB power budget using 10G components was demonstrated in [81]. However, this was achieved by using pre-compensation at the transmitter to alleviate the bandwidth limitation and post-compensation at the receiver to reduce the effect of CD and receiver bandwidth limitation. Moreover, an APD was used at the receiver to increase the sensitivity.

In this thesis, we report digital signal processing (DSP) and dispersion compensation-free 25 Gb/s PAM-4 transmission over 28 km of fiber at a BER below the HD-FEC in the C-band using a 3×3 fiber coupler based simplified coherent receiver and off-the-shelf 10G class electro-absorption modulated laser (EML).

Integrated solutions

The demand for integrated photonic solutions for optical communication applications is increasing due to the advantages of integration in reducing the footprint, cost and energy con-

sumption compared to the discrete architectures [82]. Integrated coherent receivers achieving bit rates of 224 Gb/s using PDM-16-QAM [83] in the C-band and 200 Gb/s using 16-QAM over O, E, S, C and L bands [84] have been reported on the SOI platform. Several other conventional 90° hybrid based integrated coherent receivers have been reported [85–89]. Passive optical networks (PONs) employing bulk optics based coherent detection have been demonstrated as well [90]. However, due to the strict power and cost constraints, coherent receiver architecture developed for the core network cannot be directly transferred to the cost-sensitive segments such as the access network. Single-ended detection based optical front-ends with 120° optical hybrids can be used to simplify the coherent receiver [62, 68, 91, 92]. In [93], a transmitter using hybrid III-V on silicon integrated distributed feedback laser and ring resonator was demonstrated for 25 Gb/s PON applications. However, there has been no demonstration of an integrated coherent receiver for access network applications. In this thesis, we report an integrated simplified coherent receiver on SOI based on 120° hybrid for high speed PON applications.

1.3 Original contributions

The original contributions of this thesis are attested by the design and characterization of the novel silicon photonic devices and circuits. In a chronological order, the key contributions can be summarized as follows:

Bragg grating, interference and doping based devices

- We propose the use of misaligned sidewall Bragg gratings to design OADM. The misalignment of the sidewalls provides another degree of freedom to tune the coupling coefficient of the Bragg grating. By using the misaligned sidewall gratings, we achieved ultra-compact, high ER and narrow bandwidth add-drop multiplexers [94, 95].
- We present two integrated resonators called transversely coupled Fabry-Perot resonators (TCFPRs) using Bragg gratings and loop mirrors. The TCFPRs offer better flexibility to achieve the desired spectral response compared to all-pass MRRs. Furthermore, one variant of the TCFPR features a $\pi/2$ phase shift for each one-way trip through the resonant cavity. In addition, the resonant cavity can be formed using straight waveguides and end reflectors, and hence, the bending losses can be significantly reduced [96–98].
- We present a C-band 120° optical hybrid on SOI for the TE mode using 193 nm optical lithography. The hybrids are based on 3×3 MMI couplers. The optical bandwidth of the MMI is inversely proportional to the number of access waveguides. Therefore, a 3×3 MMI based 120° optical hybrid has intrinsically broader bandwidth than a 90° optical hybrid

based on a 4×4 MMI. Broadband optical hybrids are preferred for colorless detection over wide bandwidth range [99].

- We propose and analyze via simulation a novel approach to implement a CMOS compatible and high ER TM-pass polarizer on the silicon-on-insulator platform with a 340 nm thick silicon core. The TM-pass polarizer utilizes highly doped silicon as the hybrid plasmonic waveguide. The main contribution of our work is the use of highly doped silicon instead of metals to form the hybrid plasmonic waveguide. The real part of the complex relative permittivity of the highly doped silicon approaches a negative value and therefore exhibits metal-like properties. The fabrication process of the proposed TM-pass polarizer is simpler compared to the state-of-the-art since it only uses silicon waveguides and does not require any special material or feature size. The polarizer also offers peak ER selection at different wavelengths by choosing different doping concentrations during fabrication [100].

Simplified coherent receiver based solutions for high speed passive optical networks

- We demonstrate 25 Gb/s PAM-4 transmission over 28 km standard single-mode fiber using off-the-shelf 10 Gb/s EML and 3×3 fiber splitter based simplified coherent receiver in the C-band. No DSP and dispersion compensation have been used either at the transmitter or at the receiver. Furthermore, the use of intensity modulated signal allows to avoid the phase and frequency locking of the local oscillator (LO). We also demonstrate polarization independent operation by slightly modifying the architecture of the simplified coherent receiver and propagate up to 21 km [91]. The receiver architectures were previously demonstrated by other groups using single level on-off-keying (OOK) signal achieving a maximum bit rate of 10 Gb/s [101].
- We report the first simplified coherent receiver using a 120° hybrid on the SOI platform for high speed PON applications. This coherent receiver integrates an inverse taper edge coupler for the received signal, a vertical grating coupler for the local oscillator input, a polarization splitter and rotator (PSR), a 120° hybrid based on a 3×3 MMI coupler, and three germanium photodetectors. The bulk optics based receiver architecture and its operating principle were reported previously with a maximum bit rate of 10 Gb/s. We achieved 25 Gb/s PAM-2 and PAM-4 transmission over 30 and 21 km standard single-mode fiber (SMF) in the C-band without any DSP (e.g., pre-emphasis, pulse shaping, equalization, nonlinearity compensation) and dispersion compensation (e.g., optical or digital) either at the transmitter or at the receiver [102].

- We demonstrate significant performance improvement of the integrated simplified coherent receiver by using a better digital-to-analog converter (DAC) and simple DSP achieving higher bit rates and receiver sensitivities, and longer reach. We achieved 25 and 50 Gb/s PAM-4 transmission over 43 and 21 km SMF, respectively using the 120° hybrid based integrated coherent receiver in the C-band [103].

1.4 Thesis organization

The remainder of the thesis is organized as follows:

In chapter 2, we present the background and theory of the silicon photonic devices such as Bragg gratings, resonators, MMI couplers and polarizers that will be introduced in later chapters. Then, we discuss about the different architectures namely, time-division multiplexing (TDM), wavelength-division multiplexing (WDM), and time and wavelength division multiplexing (TWDM) of the PONs. We also describe the different standards of the PONs that have been already finalized and the progress of the recently initiated 50G EPON standardization process by IEEE P802.3ca task force.

In chapter 3, we report several passive silicon photonic devices using Bragg gratings, interference, and doping. First, two configurations (single-stage and cascaded) of the OADMs are presented using Bragg gratings in a MZI. The detail simulation and experimental results are presented. Second, we present simulation and experimental results of two types of TCFPRs using Bragg gratings and loop mirrors. Third, we demonstrate a 120° optical hybrid using 3×3 MMI coupler for applications in simplified coherent receivers. Finally, we report a hybrid plasmonic waveguide based TM-pass polarizer using highly doped silicon.

In chapter 4, we present bench-top and integrated solutions for the high-speed PONs. First, we report 25 Gb/s PAM-4 transmission using 10G components at the transmitter and a simplified coherent receiver based on 120° hybrid that provides coherent amplification to boost the receiver sensitivity. Second, we demonstrate a fully-integrated 120° hybrid based simplified coherent receiver on the SOI platform for applications in the high-speed PONs. The receiver includes an edge coupler, a grating coupler, a PSR, a 3 × 3 MMI coupler and three germanium photodetectors. No DSP was used in the transmission experiment using the integrated receiver. Third, we report performance improvement of the integrated coherent receiver (achieving twice bit rate) by using a better transmitter and simple DSP at the receiver.

Finally in chapter 5, we summarize the key contributions of the thesis and provide some insights into the future research directions.

Chapter 2

Background

This chapter provides the background and fundamental knowledge of passive silicon photonic devices and optical access network architectures that are pertinent to the research work presented in the thesis. We start with an overview of the SOI platform and discuss the basics of add-drop multiplexers, resonators, optical hybrids and polarizers. We also describe the architectures and standards of the optical access networks along with the recent progress on the high-speed access network standardization process.

2.1 Silicon-on-insulator platform and silicon photonic devices

The SOI platform is an ideal choice to build passive optical interconnects. The silicon wafer offers the highest crystal quality among semiconductor materials and the lowest cost per unit area [10]. The cross-section of an SOI wafer is presented in Fig. 2.1. It comprises a silicon substrate to provide mechanical support, a buried oxide (BOX) layer for insulation, and a thin silicon layer on top of the BOX where the devices are fabricated. A cladding oxide layer is usually grown on top of the top silicon layer for protection; however, some application requires air cladding. The thickness of silicon substrate is about $675\ \mu\text{m}$, the thickness of the BOX layer is between $0.7\ \mu\text{m}$ to $2\ \mu\text{m}$ [5], depending on the application and vendor. The top silicon layer thickness varies based on the application requirements with a range of 0.1 to $0.5\ \mu\text{m}$ [5]. The passive devices reported in the thesis have a $220\ \text{nm}$ thick silicon layer except for the TM-pass polarizer where the thickness is $340\ \text{nm}$. The BOX layer is $2\ \mu\text{m}$ thick and all the devices have a $2.2\ \mu\text{m}$ thick oxide cladding layer [104].

Light can be guided with low-loss in silicon waveguides due to its transparency in the telecommunication window. Hence, plethora of low-cost, compact and high performance passive optical devices have been possible. The fundamentals of the devices reported in the thesis



Fig. 2.1 Schematic of the cross-section of a silicon-on-insulator wafer [5].

are described in the next few sections:

2.1.1 Bragg gratings

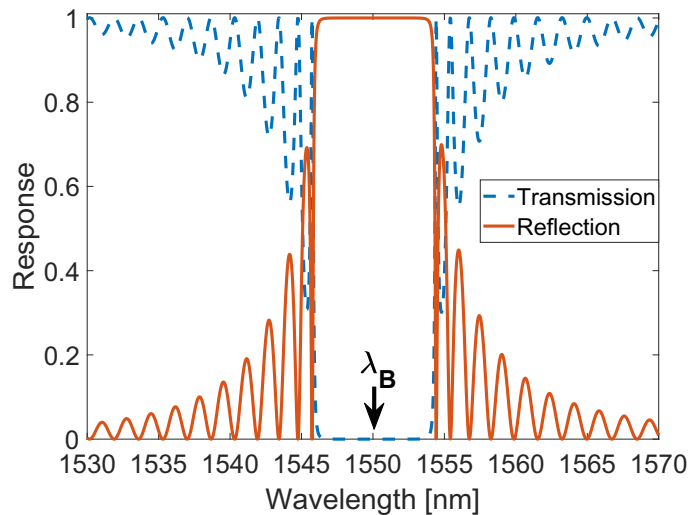


Fig. 2.2 Typical spectral responses of a uniform Bragg grating.

Bragg gratings are filters that reflect light with wavelengths that satisfy the Bragg condition and allow transmission of light in other wavelengths. The basic idea is to modulate the effective index, n_{eff} of the structure periodically in the direction of propagation. This periodic modulation can be obtained by changing the effective index or the physical dimension of the waveguide through the introduction of corrugation. Consequently, distributed and multiple reflections occur and they interfere constructively around the Bragg wavelength where the reflection is the highest. The reflected signals interfere destructively at other wavelengths canceling each other

out. Hence, the light is transmitted through the waveguide. The Bragg wavelength is expressed as:

$$\lambda_{Bragg} = 2n_{eff}\Lambda \quad (2.1)$$

where, n_{eff} is the effective refractive index of the grating structure and Λ is the grating period. Figure 2.2 shows the typical spectral responses of a uniform Bragg grating.

Integrated Bragg gratings are designed by corrugating the waveguides. Other methods to form Bragg gratings in silicon waveguides includes amorphous silicon gratings [105], carrier-induced gratings with p-i-n junction [106] and ion implantation [107]. These approaches are not commonly used due to their complexity in fabrication.

2.1.2 Fabry-Perot Resonator

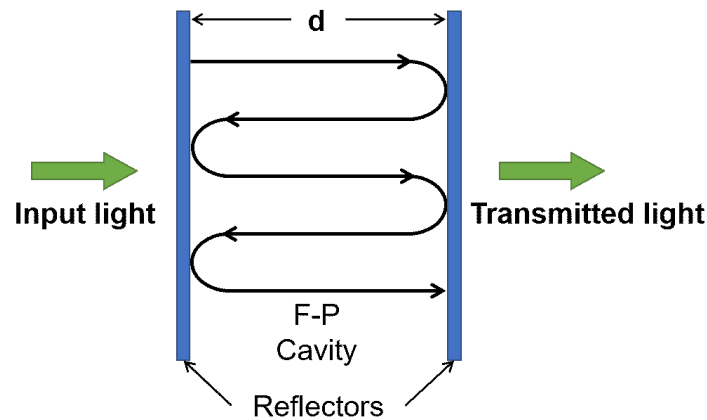


Fig. 2.3 Fabry-Perot resonator in the simplest form.

In the simplest form, a Fabry-Perot resonator comprises two parallel reflectors facing each other with a transparent medium in between as shown in Fig. 2.3. The input light goes through several reflections at the two reflectors before being transmitted through the output. The transmitted light exhibits wavelength dependent periodic variations due to the interferences of the reflected light. Depending on the phase of the reflected light, constructive and destructive interferences occur resulting in maximum and minimum transmissions, respectively. The optical phase difference between two consecutive reflections is given by:

$$\Delta\phi = \frac{4\pi n_{eff}d}{\lambda} \quad (2.2)$$

where, d is the cavity length and n_{eff} is the effective index of the transparent medium. In

the case of integrated Fabry-Perot resonators, n_{eff} denotes the effective index of the waveguide material.

2.1.3 Multimode interference couplers

The MMI coupler is a device that utilizes self-imaging in multimode waveguide [108]. A large number of modes supported by the multimode waveguide interfere at well defined lengths which results in self-imaging. To launch and recover light into and from the multimode waveguide, a number of access waveguides are placed at the input and output of the multimode waveguide. A scanning electron microscope (SEM) image of a 2×2 MMI coupler is provided in Fig. 2.4. The self-imaging length of the MMI is given by [108],

$$3L_{\pi} \simeq \frac{4n_r W_e^2}{\lambda_0} \quad (2.3)$$

Here, L_{π} is the beat length of the two lowest order modes, W_e is the effective MMI width, n_r is the effective index of the MMI slab region and λ_0 is the operating wavelength.

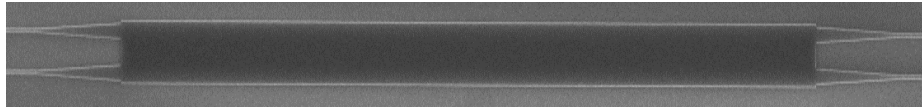


Fig. 2.4 Scanning electron microscope image of a 2×2 MMI coupler.

The fundamental design guidelines of an MMI coupler are provided in [108]. The basic design parameters are the length and width of the multimode waveguide and the positions of the access waveguides. The separation between the access waveguides need to be kept small to minimize the length of the MMI. Typically taper waveguides are used as the access waveguides to ensure the gradual mode evolutions from the connecting single-mode waveguides. Figure 2.5 shows the field evolution of a 2×2 MMI coupler for light launched at both access waveguides at the input.

2.1.4 Polarizers

The high index contrast of the SOI platform allows for compact devices. However, the downside of the high index contrast is large birefringence. Hence, polarization management schemes are required to maintain the performance of silicon photonic devices. Polarizers are simple yet adequate solution to resolve this issue when polarization-division multiplexing (PDM) is not desired. Polarizers eliminate the undesired polarization of the optical signal while retains the useful one. The operating principle of the polarizer is simple: it acts as a good supporter

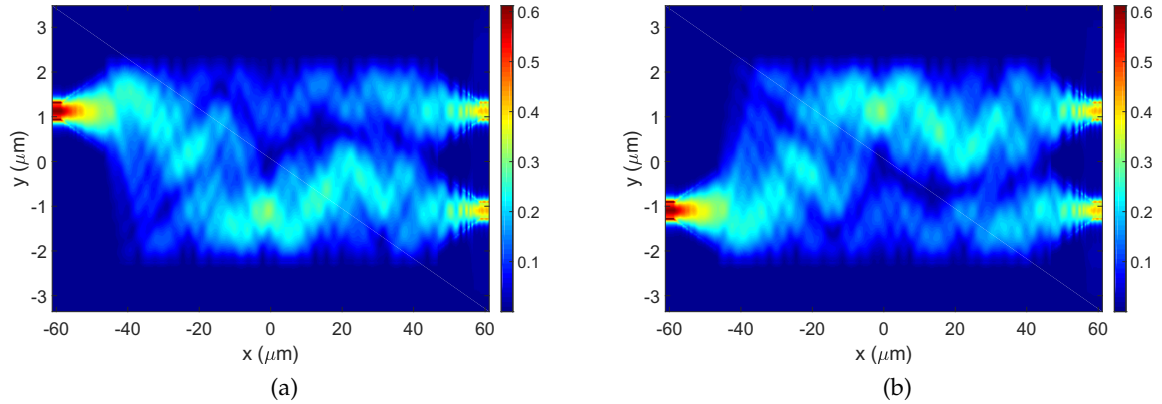


Fig. 2.5 Simulated transverse electric field profiles of a 2×2 MMI coupler with excitations at (a) input 1, and (b) input 2.

for the desired polarization while being cut-off, reflective or absorptive for the undesired one. Figure 2.6 shows the schematic of a hybrid plasmonic polarizer. The light with both TE and TM polarizations are coupled to the silicon waveguide. Depending on the phase matching condition, either TE or TM polarization couples to the other waveguide placed beside the input waveguide. Due to the metal deposited on top of the other waveguide, the polarization that becomes coupled will be absorbed while the remaining polarization that does not couple, will transmit through the input waveguide and can be accessed at the output.

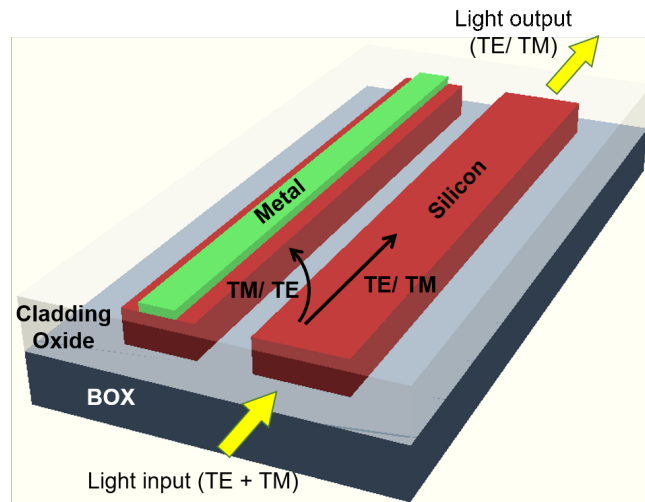


Fig. 2.6 Schematic of a hybrid plasmonic polarizer (TE/TM).

2.2 Optical access network

Optical access network provides connectivity to the end-users of the internet service and are placed in close proximity to the end-users in large volume. Due to different practical reasons, there is a wide variety of access networks that exists today.

2.2.1 Architectures

On a very high level, the access networks can be categorized into three forms: point-to-point, active optical networks and passive optical networks [109].

The point-to-point architecture is the simplest of all forms of access networks. Each end-user is connected with the central office by a dedicated fiber with no additional components in between. Either two different wavelengths are used for upstream and downstream in a single fiber or two different fibers are used for the up/downstream purposes. The advantages of the architecture include security, dedicated bandwidth and easy repair. However, the cost of implementation can be prohibitive.

The active optical network architecture has a single feeder fiber that connects to an active switch at a remote node which further bridges the feeder fiber and the distribution fibers. This way, the cost of implementation is reduced. The bandwidth resource is not shared between end-users allowing them to have dedicated bandwidth. The issue of this architecture is that the active switch located at the remote node requires electrical power which increases the cost of installation and maintenance significantly.

The passive optical network replaces the active switch at the remote node with a passive splitter. Thus, the requirement of electrical power at the remote node is avoided. The feeder fiber is shared by a number of end-users requiring additional protocol for signal multiplexing. Mainly three protocols are used to multiplex the data streams, which are: time-division multiplexing (TDM), wavelength-division multiplexing (WDM) and time- and wavelength-division multiplexing (TWDM) [24, 110]. These multiplexing techniques are briefly described below:

2.2.1.1 TDM PON

A TDM-PON uses a passive power splitter at the remote node to bridge the feeder fiber with the end-users. Each end-user/optical network unit (ONU) receives the data transmitted by the optical line terminal (OLT) in the downstream. The OLT provides a tag on each data frame to allow the ONUs to recognize the data destined to them and ignore the rest. Since the data streams from each end-user are combined passively in the upstream, a time slot is allocated to each ONU to transmit their data to avoid congestion. The OLT coordinates the data

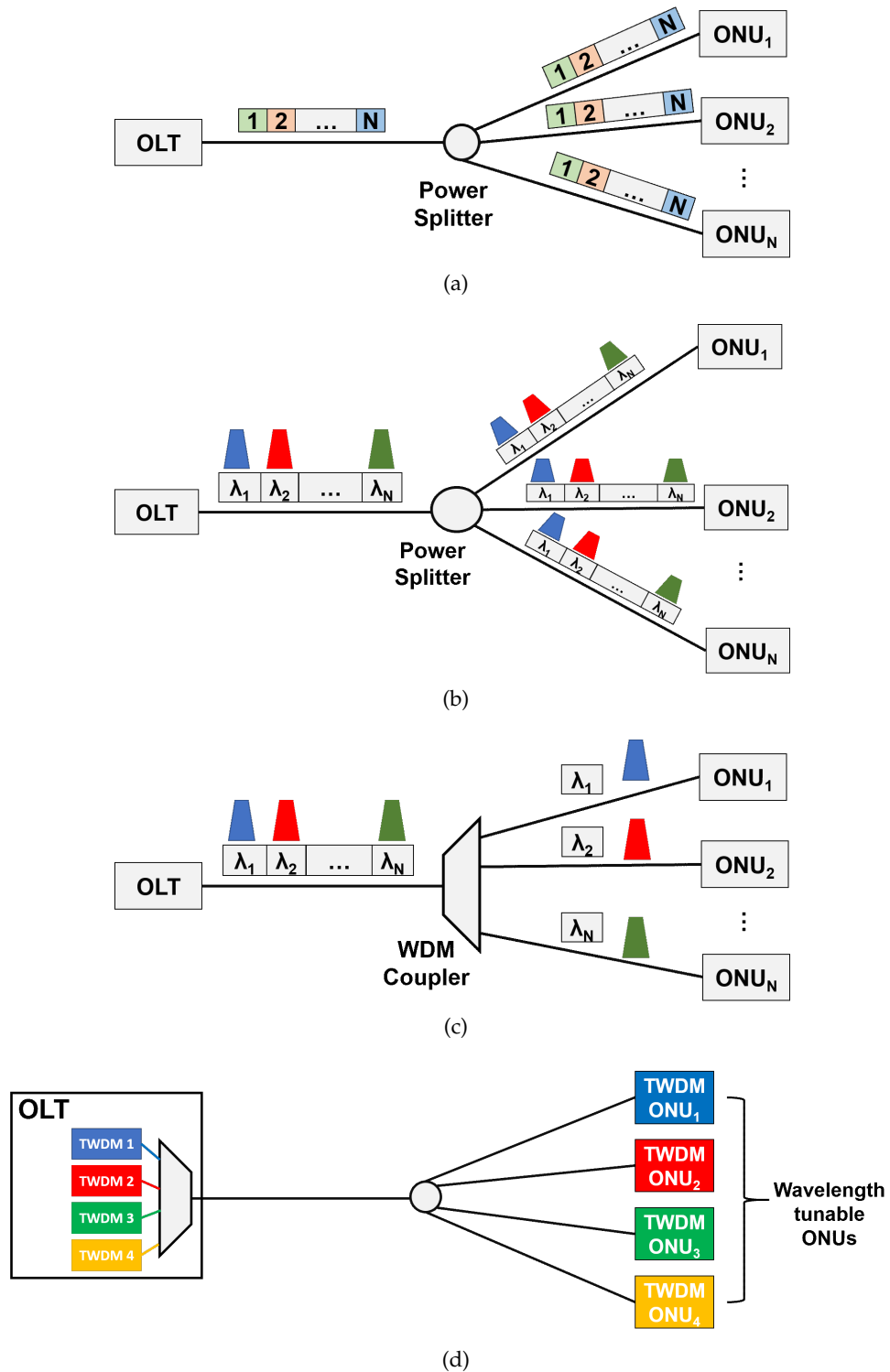


Fig. 2.7 Architectures of (a) TDM, (b) splitter-based WDM, (c) grating-based WDM, and (d) TWDM PONs. [OLT: optical line terminal, ONU: optical network unit, WDM: wavelength-division-multiplexing.]

transmission by each ONU to ensure that the data transmitted by each ONU arrive at the splitter at different times. The upstream of the PONs are unique from other transmission systems due to the fact that all transmitters are facing a single receiver. In addition, each transmission has a different clock phase and power levels which is called the “burst mode problem” [111]. Figure 2.7(a) shows the basic schematic of a TDM-PON. This category of PONs include BPON, G-PON, and EPON.

2.2.1.2 WDM PON

As the name suggests, the WDM PON utilizes different wavelengths to multiplex signals to and from different end-users. There are two major categories of the WDM-PON: splitter-based and grating-based. In splitter-based WDM PON, the remote node has a wavelength transparent passive splitter that sends all the wavelengths to each ONU. The ONU has to tune to their respective wavelengths for upstream and downstream; hence, electronic control is required. In the grating-based architecture, a passive wavelength selective component is located at the remote node which routes one or more wavelengths to the ONUs. The ONU can receive the wavelengths without any tuning. In the upstream, the ONU has to transmit at the correct wavelength to connect to the OLT. The WDM PON has better security and scalability. However, the flexibility is less due to the hard wired wavelength assignments. Since there are many colors/wavelengths (typically 32-64) in a WDM PON, producing a “colorless ONU” is one of the biggest challenges. Instead of creating different ONUs for different colors, it is more practical to produce a ONU with the capability to automatically tune to any color based on the operational requirements. Schematics of the two categories of WDM PONs are provided in Figs. 2.7(b) and 2.7(c).

2.2.1.3 TWDM PON

TWDM PON is the hybrid of TDM and WDM PONs. This is the primary technology selected for NG-PON2 by ITU-T. The TWDM protocol defined for NG-PON2 has 40 Gb/s aggregate capacity using four wavelengths. Each wavelength can deliver up to 10 Gb/s of peak data rate. In the simplest concept, it can be considered as an aggregation of four TDM-PONs using four wavelengths. Figure 2.7(d) shows the schematic of a simple TWDM PON architecture. The ONU uses colorless transceivers that can be tuned to any upstream and downstream wavelengths for ease of inventory management and simplicity of network deployment. Optical amplifiers are used at the OLT side to boost the downstream signals and pre-amplify the upstream signals enabling higher power budget. The TWDM PON is backward compatible with GPON and XGPON allowing the use of the existing infrastructure.

2.2.1.4 Other types of optical access networks

A wide variety of optical access network architectures have been developed over the past decades in addition to the ones discussed in the previous section. One such variant is the Ethernet over fiber which is basically a point-to-point Ethernet built over fiber links. A dedicated fiber connects the end-user to the central office and each end-user requires two transceivers, one of which is located at the end-user premises and the other at the central office. This increases the cost and thus, mostly used for business customers.

Radio Frequency (RF) and Data Over Cable Service Interface Specification (DOCSIS) PONs are two other variants of PON developed mainly for the cable companies. RF PONs are developed to support RF video broadcasting signals over fibers. While DOCSIS PONs are developed to include a DOCSIS service layer interface on top of the PON architecture. Both PONs are developed to support the multi service operators [110].

An alternative multiplexing protocol for PONs is the optical code-division multiplexing (OCDM) [110, 112]. The data streams of each end-user are encoded and decoded to and from optical pulse sequences using the orthogonal codes assigned to them. Although the security is enhanced by asynchronous communication provided by the OCDM, the expensive encoder and decoder limit the market potential of this technique.

Orthogonal frequency division multiplexing (OFDM) is another method to implement optical access network. A high aggregated throughput is achieved by combining multiple sub-carriers each having their own modulation format [113]. The sub-carriers can overlap without interference due to the orthogonality of the sub-carriers which offers high spectral efficiency. The use of aggressive digital signal processing increases the complexity of the transceivers for OFDM which is prohibitive for the wide deployment of OFDM PON.

Finally, the ultra-dense WDM (udWDM) PONs are coherent reception based PONs. Coherent reception techniques provides increased receiver sensitivity, higher spectral efficiency and inherent narrow tunable filtering. Although the coherent reception is pre-dominant in the long-haul transmission segment, the expensive architecture prohibits its application in the access network. Recently, there has been a lot of research effort in simplified coherent receivers to overcome this bottleneck [114]. With the mounting pressure to achieve high speed and higher power budget in the access network, coherent reception seems to be the way forward [115].

2.2.2 Standardization

Early work on the standardization of PONs started in the early 1990s. Standardization of PONs are necessary for cost minimization, risk reduction and successful deployment by ensuring interoperability among vendors and manufacturers. With this goal in mind, seven major

telecommunication service providers from Japan and Europe, and ten international manufacturers formed the Full Service Access Networks (FSAN) in 1995 [116, 117]. The FSAN forms standards for PONs along with ITU-T. A/BPON, GPON, XG(S)-PON, and NG-PON2 are the standards that have been rolled out by these bodies over the years.

IEEE, on the other hand, formed the Ethernet-in-the-first-mile group to put forward Ethernet-based standards for the PONs. Subsequently, the group became a part of the IEEE 802.3 standardization committee and have been rolling out standards such as G-EPON, 10G-EPON and recently initiated 50G-EPON. The EPON is an extension to the local area networks (LAN) in the end-user premises. Due to the extensive use of the Ethernet in the LANs and lower equipment cost, EPON is gaining popularity rapidly.

Since both ITU-T/FSAN and IEEE put forward standards for PONs, efforts are being made to increase collaborations between the two bodies to streamline and combine their efforts [118]. A brief summary of the physical layer properties of the standards drafted by both ITU-T/FSAN and IEEE over the past years are provided in table 2.1 [7].

2.2.2.1 25G-EPON and beyond

Due to the continuous increase in the demand of high-speed data services and with the increasing deployments of 10G PON, the market potential and technology options are being explored to define the PON standards beyond 10G [77]. With such a target, IEEE 802.3ca started the standardization process of 100G-EPON in December, 2015 with an anticipated timeline of August, 2020 [119]. ITU-T/FSAN is also expected to initiate the standardization process of the high speed PONs as indicated in their roadmap released in 2016. However, it has not launched yet due to contradictory visions among the operators [115]. Although the initial target of IEEE 802.3ca task force was to deliver the standards for three different speeds which are 25, 50 and 100 Gb/s, the 100 Gb/s was later removed from the current discussion and the task force was renamed as 50G-EPON [119]. The driving force behind the choice of 25 Gb/s as the base speed is the availability of low-cost 25G components. The rapid development of the data center interconnects drove the maturation of the 25G ecosystem and helped reduce the cost of these optoelectronic components [115, 120]. Due to the insignificant increase in the data rate for 25G-EPON, the task force is also considering 50G-EPON. Both $1\lambda \times 50$ Gb/s and $2\lambda \times 25$ Gb/s are being considered as of this writing.

Significant progress has been made in the standardization process of the 25G-EPON which is summarized in table 2.1. It should be noted that there might be some changes in the future since the standardization is still in progress. Unlike NG-PON2, the 25G-EPON will be based on TDM and therefore, the transceivers will be of fixed wavelength. Both PR30 and PR20 power

Table 2.1 Summary of the physical layer properties for different PON standards [7]. [Att.: Attenuation, Diff.: Differential, max.: maximum, Nom.: Nominal]

	A/BPON ^a (G.983)	GPON (G.984)	G-EPON (802.3ah)	10G-EPON (802.3av)	XG(S)-PON (G.98(0)7)	NG-PON2 (G.989)	25G-EPON ^b (802.3ca)
Network							
Nom. distance [km]	20	20 (LR:60)	10/20	10/20	20	20/40	20
Nom. max. split	32	64	16/64	16/64	64	64	
Att. range [dB]	A: 5-20 B: 10-25 C: 15-30	A: 5-20 B: 10-25 C: 15-30 B+: 13-28 C+: 17-32	PX10: 5-20	PR(X)10: 5-20	N1: 14-29 N2: 16-31	N1: 14-29 N2: 16-31	PR20: 10-24 PR30: 15-29
Diff. path loss [dB]	15	15	14-15	14-15	15	15	
Downstream							
Bit rate [Gb/s]	0.155 0.622 1.244	1.244 2.488	1.25	10.31	9.953	9.953	25
Wavelength [nm] BER before FEC	1480-1580 10^{-10}	1480-1500 10^{-10}	1480-1500 10^{-12}	1575-1580 10^{-12}	1575-1580 10^{-3}	1596-1603 10^{-3}	1356-1360 10^{-2}
Upstream							
Bit rate [Gb/s]	0.155 0.622	1.244 2.488	1.25	1.25 10.31	2.488 9.953	2.488 9.953	10 25
Wavelength [nm] BER before FEC	1260-1360 10^{-10}	1260-1360 10^{-10}	1260-1360 10^{-12}	1260-1280 10^{-12}	1260-1280 10^{-3}	1524-1544 10^{-3}	1260-1280 1290-1310 1532-1540 10^{-2}

^aAPON and BPON are different aliases of the TDM-PON architecture based on the ITU-T G.983 standard.

^bIn progress; will be finalized by August, 2020.

budgets have been chosen and to meet the power budget at 25 Gb/s, a more powerful low-density parity-check FEC (LDPC-FEC) with a pre-FEC BER of 10^{-2} has been selected. Both downstream and upstream will be in the O-band. The standardization of the 50G-EPON is also being discussed. The anticipated application of the 50G-EPON will be the 5G X-hauling (X: front/back/mid). The 50 Gb/s/ λ has been standardized for the 400G Ethernet which is expected to supersede 100G Ethernet in 2020. Therefore, the ecosystem of 50G optoelectronic components will not be mature enough to drive down the cost to be suitable for the PON market until the middle of the next decade. Hence, a lot of research is underway to use high order modulation formats such as PAM-4 along with DSP, to achieve 50 Gb/s/ λ using low bandwidth components [121–123]. Optical amplification is also required to meet the power budget. However, it has been reported in [115] that currently there is no practical solution for 50G PAM-4 that meets the PR30 loss budget. The evolution towards to the 100G-EPON will probably require coherent solutions to meet the power budget requirements. The cost of coherent solutions will reduce if sufficient cost erosion occurs due to the market need, the data center adopts coherent technology in the near future or simplified coherent solutions utilizing intensity modulation becomes mature. However, there are at least five to ten years left before any technology decision needs to be made by the standardization bodies since the commercial market for 100G-EPON is still not big enough.

Chapter 3

Bragg grating, interference and doping based devices

In this chapter, we present passive silicon photonic devices based on Bragg gratings, interference and doping. We start with misaligned sidewall Bragg grating based OADMs. Two configurations of the OADM are demonstrated. Next, we show the simulation and experimental results of two different Fabry-Perot resonators. The resonators are formed using a directional coupler with either Bragg gratings or loop mirrors as the end reflectors. Then, we present the design and measurements of a 3×3 MMI coupler based 120° hybrid. Lastly, we present the design and analysis of a hybrid plasmonic waveguide based TM-pass polarizer using highly doped silicon.

3.1 Optical add-drop multiplexer with misaligned sidewall Bragg gratings

OADMs facilitate flexible addition and extraction of WDM channels and are one of the key components for the implementation of WDM PONs. Thus, the OADMs are widely investigated by the researchers and have been implemented on both non-SOI [29–33], and SOI platforms [34, 40]. On the SOI platform, several schemes have been utilized including ring resonator [34, 36], grating-assisted contra-directional coupler [38, 40], and Bragg grating [37, 42] to build OADMs. While ring resonators have compact footprint, obtaining a flat-top spectral response as well as a large FSR is challenging. The OADMs based on the grating-assisted contra-directional couplers are complex in design and it is difficult to achieve a large ER [38, 40]. Finally, the Bragg grating based devices offer FSR free operation and several degrees of freedom to achieve the desired spectral response.

Recently, a new technique to precisely control the coupling coefficient of silicon waveguide

Bragg gratings by misaligning the sidewall gratings was reported in [6]. This technique significantly alleviates the problem of quantization error during fabrication which occurs because of finite size of the mask grid [6]. In this thesis, we propose ultra-compact OADM in the C-band using misaligned sidewall gratings. We analyze two configurations of the Bragg gratings in MZI-based OADM. We refer to the first design as a single-stage design and the second as a cascaded design. The effect of misalignment variation on the spectral response of both structures was studied numerically and experimentally. The use of misaligned gratings enables a narrow bandwidth with a lower number of periods, thus enabling optimization of the OADM designs for compactness. The organization of this section is as follows. In 3.1.1 the theory of misaligned sidewall grating is described. The principle of operation of the device is presented in 3.1.2, and finally in 3.1.3 and 3.1.4, the simulations and experimental results are discussed, respectively.

3.1.1 Misaligned sidewall gratings

The Bragg condition is given as [124]

$$\lambda_{Bragg} = 2n_{avg}\Lambda \quad (3.1)$$

where λ_{Bragg} is the Bragg wavelength, n_{avg} is the average effective refractive index of the whole grating structure and Λ is the grating period.

Silicon Bragg gratings are normally created by periodic corrugations in the side-wall of a silicon waveguide. Each period of the grating works as a weak reflector due to its index discontinuity. To satisfy the Bragg condition, the grating period, Λ has to be such that all partial reflections add up in phase. In a uniform Bragg grating where the refractive index varies as $n(z) = n_{avg} + \Delta n \cos(2\pi z/\Lambda)$ along the grating longitudinal axis, the grating amplitude reflection coefficient is given as [124]

$$r_g = \frac{i\zeta \sin(qL)}{q \cos(qL) - i\Delta\beta \sin(qL)} \quad (3.2)$$

where, $\zeta = 2\pi\Delta n/\lambda$ is the coupling coefficient which is related to the refractive index modulation depth, $q = \sqrt{\Delta\beta^2 - \zeta^2}$, L is the grating length, $\Delta\beta = \beta - \beta_{Bragg}$ is the propagation constant deviation from the Bragg wavelength and $\beta_{Bragg} = \frac{2\pi n_{avg}}{\lambda_{Bragg}}$. From (3.2), it can be seen that the grating reflection spectrum depends on the refractive index modulation depth and the grating length. Bragg gratings with weak coupling strengths are required to achieve narrow bandwidth which can be designed by reducing the structural corrugation width. The bandwidth is also inversely proportional to the length in such weak Bragg gratings [124]. Therefore, longer grat-

ings are required to obtain narrow bandwidth devices, which increases the device's footprint significantly. Since, achieving a narrow bandwidth (e.g., 1 nm) requires a very small corrugation amplitude, the performance of the Bragg gratings become highly sensitive to variations in the fabrication processes.

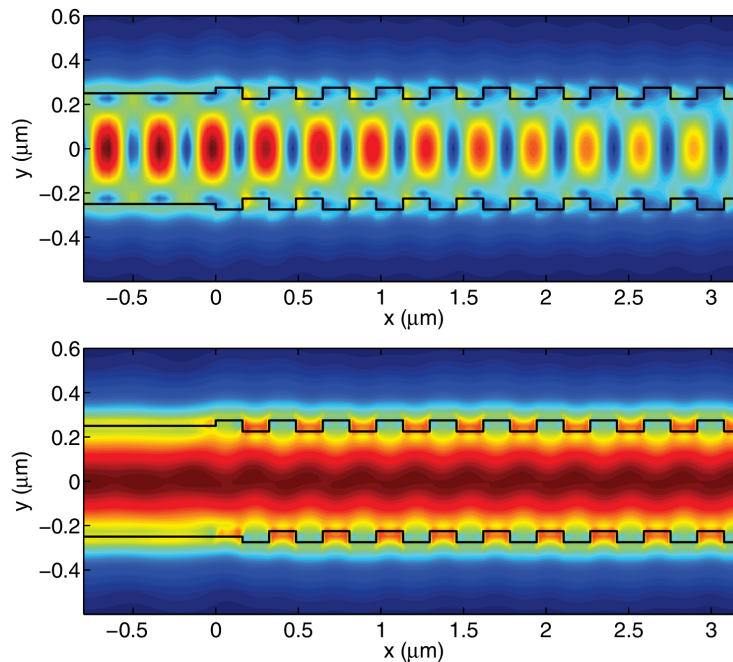


Fig. 3.1 Electric field distributions with light injected from the left for gratings with (top): no misalignment, and (bottom): complete misalignment. Source: [6] © 2014 Optical Society of America.

Wang et al. [6] proposed misaligning the sidewall gratings intentionally to control the grating coupling coefficient. The misaligned grating structure can be broken down into two separate gratings with a phase offset. The effective coupling coefficient of such a grating can be phenomenologically written as [6],

$$\kappa = \left| \frac{\kappa_0}{2} + \frac{\kappa_0}{2} \exp(i.2\pi\Delta L/\Lambda) \right| = \kappa_0 \cos \left(\frac{\pi\Delta L}{\Lambda} \right) \quad (3.3)$$

where κ_0 is the coupling coefficient when there is no misalignment, ΔL is the grating misalignment and $2\pi\Delta L/\Lambda$ is the phase offset. From (3.3), it can be seen that as the misalignment increases, reflections from each grating period interferes less constructively, and thus, weakening the grating strength. Using this technique, narrow bandwidth Bragg gratings can be created with a smaller number of grating periods. When the corrugations on the two sidewalls are completely misaligned, the grating periods interfere destructively, and the structure

no longer reflects light. It is to be noted that Eq. 3.3 is not a rigorous equation and have been derived phenomenologically. The equation provides a coupling coefficient value of zero when there is complete misalignment (i.e., $\Delta L = \Lambda/2$). However, this will not occur practically due to the presence of the perturbations on both sidewalls of the waveguide. The effect of the perturbations can be neglected when the corrugation width is very small. However, it should be taken into consideration for large corrugations widths. Hence, a rigorous model of the coupling coefficient needs to be developed that accounts for the sidewall perturbations. Figure 3.1 shows the electric field distributions in a Bragg grating waveguide with no misalignment (top) and complete misalignment (bottom) [6]. Moreover, this method of weakening the grating strength is less sensitive to fabrication quantization error than reducing the corrugation amplitude [6].

3.1.2 Principle of operation

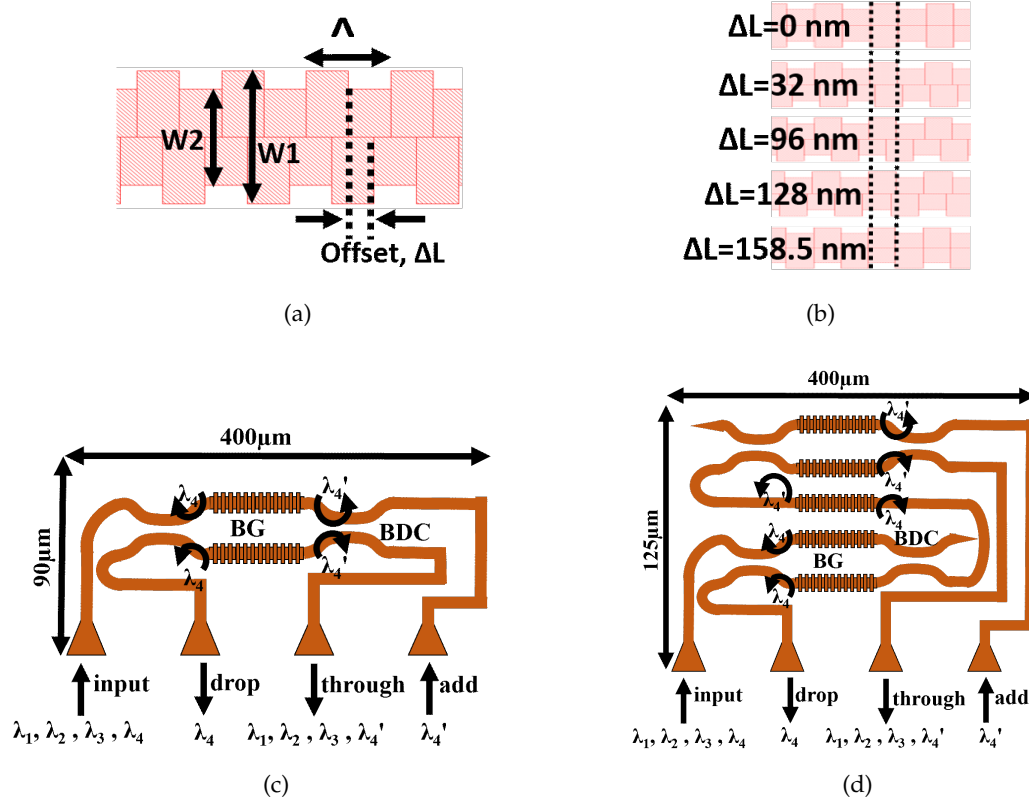


Fig. 3.2 (a) Misaligned sidewall Bragg grating, (b) variation of ΔL . Schematic of the fabricated (c) single-stage OADM configuration, (d) cascaded OADM configuration. Here, $\lambda_4 = \lambda_4'$.

Figure 3.2(a) depicts the Bragg grating corrugation parameters used in our design. Here, $W1$ was chosen to be 580 nm and $W2$ to be 420 nm. Therefore, the corrugation amplitude, ($\Delta W = \frac{W1-W2}{2}$) is 80 nm. The simulated effective refractive index of the 580 nm (n_{eff1}) and 420 nm (n_{eff2}) silicon waveguides as a function of wavelength are shown in Fig. 3.3. At 1542.5 nm wavelength, $n_{eff1}=2.56$ and $n_{eff2}=2.29$; thus, $n_{avg}=2.43$. From the Bragg condition in Eq. 3.1, Λ is found to be 317 nm. Fig. 3.2(b) shows the variation in the offset of the sidewall gratings starting from 0 nm to half of the grating period, i.e., 158.5 nm. At this offset, the two sidewalls are completely out of phase and the structure will not reflect light. The schematics of the two configurations of the OADMs, single-stage and cascaded, are shown in Fig. 3.2(c) and 3.2(d), respectively. All Bragg gratings have been designed to have the same Bragg wavelength. Both arms of the MZI have equal lengths and the Bragg gratings were placed symmetrically within each arm of the MZI. Broadband directional couplers (BDCs) [66] were used as 2×2 power splitter and combiner in the test structures.

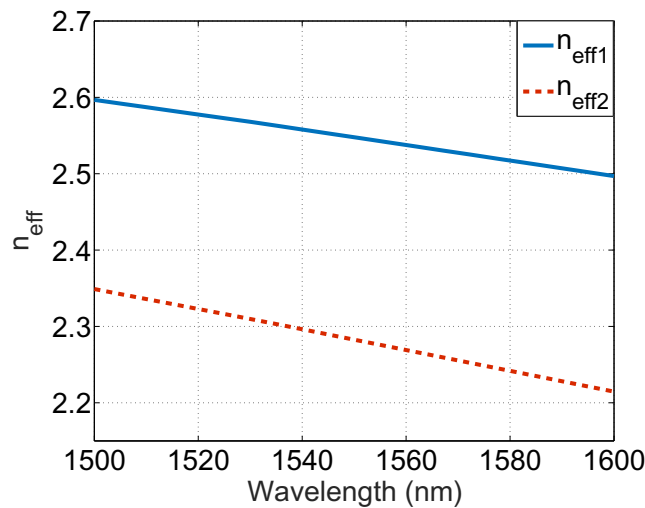


Fig. 3.3 Simulated effective refractive index of the 580 nm, n_{eff1} and 420 nm, n_{eff2} silicon waveguides as a function of wavelength.

Referring to Fig. 3.2(c), light consisting of several wavelengths is launched at the input port of the OADM. Since the Bragg gratings have a Bragg wavelength of λ_4 , light at λ_4 will be reflected. The reflected light exits at the drop port because of the π phase shift induced by the directional coupler during a round trip. The other wavelengths which were outside the reflection bandwidth of the Bragg grating will emerge at the through port, again because of the π phase shift caused by the directional coupler. Since the Bragg gratings in the MZI based OADMs are symmetric, light at λ_4 injected at the add port will get reflected by the Bragg

gratings. The reflected light will exit via the through port, along with other wavelengths that were launched at the input port (except the dropped one).

Referring to Fig. 3.2(d), the cascaded design of the OADM has two identical single-stage OADMs with an additional Bragg grating in the connecting path. The open branches of the single-stage OADMs are terminated with optical terminators. The drop port of the cascaded configuration works on the same principle as the single-stage one. However, the additional Bragg grating in between the OADMs reflects residue light at λ_4 that was not reflected by the Bragg gratings in the first single-stage OADM and prevents it from emerging at the through port. Similarly, if light at λ_4 is launched at the add port, it will be reflected by the Bragg gratings in the second stage of the OADM and exit via the through port. The Bragg grating in between the OADMs will reflect any power that leaked through the second stage of the OADM at this wavelength so that it does not appear at the drop port. With the cascaded configuration, the ER of the OADM can be increased significantly and the cross-talk can be reduced. However, the improved ER and reduced crosstalk come at the expense of additional IL and footprint.

3.1.3 Simulation results

The OADM configurations were first simulated by varying ΔW , ΔL , and the number of grating periods, NG. All the simulations were done in *Lumerical Interconnect* [125] and the *Silicon Electronic-Photonic Integrated Circuits (Si-EPIC)* electron-beam process design kit was utilized [126]. The transmission graphs for the variation of ΔW are shown in Fig. 3.4(a) and 3.4(d), respectively for the single-stage and the cascaded configurations. It can be observed that the ER and bandwidth increases as ΔW is increased. We varied ΔW up to 100 nm since a larger value of ΔW would increase the ER further which can not be measured physically. The lower value of ΔW was chosen based on the minimum fabricated feature size that has been reported in the literature. ΔL was varied from 0 nm to 158.5 nm (half the grating period) and the results are shown in Fig. 3.4(b) and 3.4(e) for the single-stage and the cascaded configurations, respectively. The ER and bandwidth exhibits a decreasing nature as ΔL is increased. The results for the variation of NG is provided in Fig. 3.4(c) and 3.4(f) for the single-stage and the cascaded configuration, respectively. The ER decreases but the bandwidth remains constant if NG is decreased as can be seen from the figures. The upper value of NG was chosen because a higher value would increase the ER further which can not be measured physically. Furthermore, it would increase the footprint and IL of the device. The cascaded configuration achieves significantly larger ER for both ΔW and ΔL variation. The sensitivity of the power meter in the simulation software was set to -100 dB and is why clipping can be observed in Fig. 3.4. We chose this value for power meter sensitivity because a ER value of less than -100 dB cannot

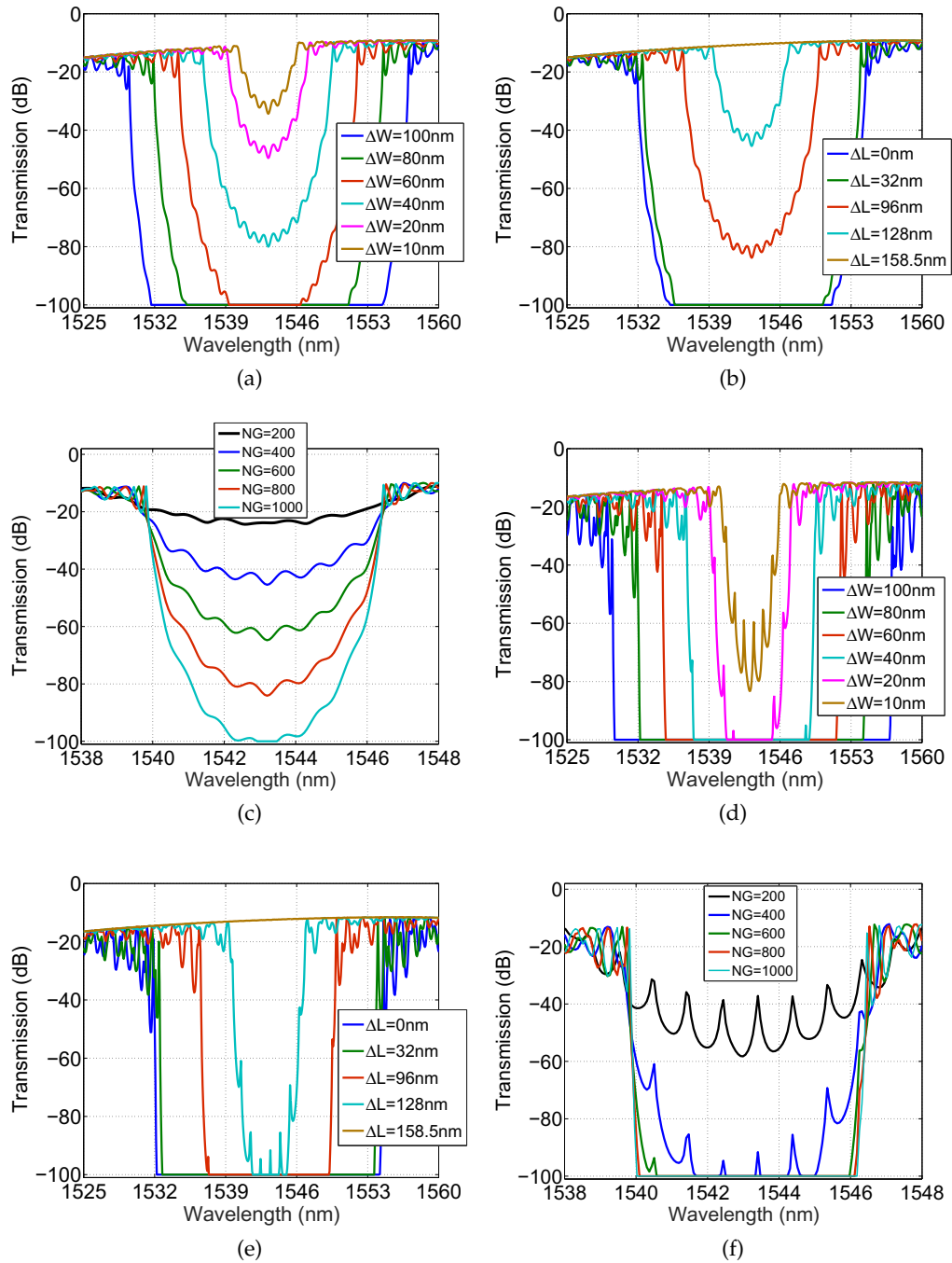


Fig. 3.4 Simulated transmission responses for the single-stage configuration for (a) different ΔW with $NG=400$ and $\Delta L=0$ nm, (b) different ΔL with $\Delta W=80$ nm and $NG=400$, and (c) different NG with $\Delta W=80$ nm and $\Delta L=128$ nm. Simulated transmission responses for the cascaded configuration for (d) different ΔW with $NG=400$ and $\Delta L=0$ nm, (e) different ΔL with $\Delta W=80$ nm and $NG=400$, and (f) different NG with $\Delta W=80$ nm and $\Delta L=128$ nm.

be measured physically. The clipping phenomenon indicates that the OADMs have higher ER than what we can observe.

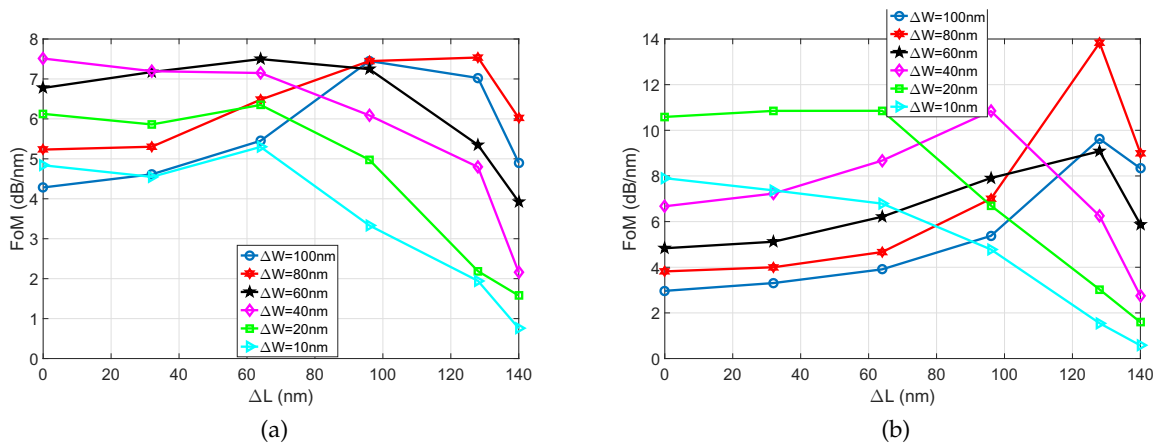


Fig. 3.5 FoM as a function of ΔL for different ΔW with $NG=400$ for the (a) single-stage, and the (b) cascaded configurations.

From the results presented in Fig. 3.4, we will choose ΔW , ΔL , and NG by balancing ER, bandwidth and device compactness. For $NG=200$, the ERs are only 12 dB and 26 dB for the single-stage and the cascaded configurations, respectively whereas for $NG=400$, the ERs are 35.5 dB and 85.85 dB, respectively. Since increasing NG to 600 does not provide significant improvement of ER for the cascaded configuration, we chose $NG=400$ to make the device compact. We have derived a figure of merit (FoM) parameter from the ER, 3-dB bandwidth and footprint to determine the value of ΔW and ΔL . The FoM has been defined as follows (3.4): (a) the footprint of the cascaded configuration is considered as the standard. The footprint of both configurations is divided by the footprint of the cascaded configuration; this is designated as the footprint ratio (FR), (b) the FR is multiplied with the 3-dB bandwidth, and (c) the ER is divided by this product.

$$FoM = \frac{ER}{BW(3dB) \times FR} \quad (3.4)$$

The FoMs for the single-stage and the cascaded configurations as a function of ΔL for different values of ΔW are presented in Fig. 3.5. It can be seen that the highest value of FoM for the single-stage and the cascaded configurations are 7.54 dB/nm and 13.83 dB/nm, respectively which are obtained at $\Delta W=80$ nm and $\Delta L=128$ nm. Therefore, we have used these values for our fabrication.

In order to evaluate the effectiveness of misaligned sidewall Bragg gratings compared to typical aligned sidewall gratings, we study the effect of increasing ΔL versus decreasing ΔW

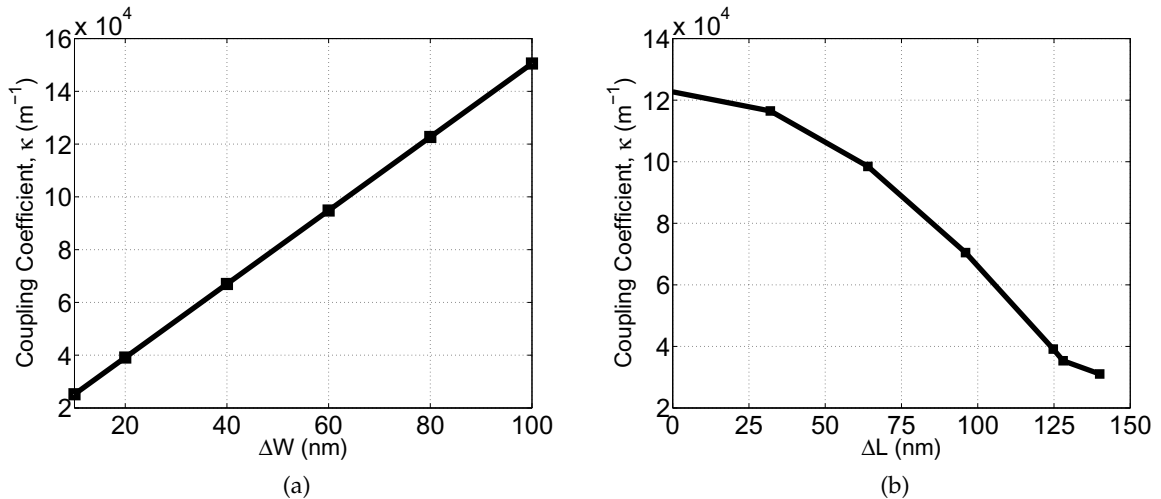


Fig. 3.6 Simulated coupling coefficients for (a) different ΔW with $\Delta L=0$ nm, and (b) different ΔL with $\Delta W=80$ nm.

on the coupling coefficients. The coupling coefficients of the Bragg gratings for different ΔW with ΔL fixed at zero, and with the ΔW constant at 80 nm for different ΔL are calculated and presented in Fig. 3.6. As can be seen in Fig. 3.6, the coupling coefficient decreases as ΔW is reduced or ΔL is increased. In terms of practical implementations, varying ΔL to achieve different coupling coefficients is more resistant to fabrication errors as shown in [6]. This can also be attributed to the fact that fabricating small feature size is difficult. For example, from Fig. 3.6, it can be seen that a coupling coefficient of $3.9 \times 10^4 \text{ m}^{-1}$ is obtained at $\Delta W=20$ nm with $\Delta L=0$ nm (Fig. 3.6(a)) which can also be obtained with $\Delta W=80$ nm and $\Delta L=124.7$ nm (Fig. 3.6(b)). The 80 nm feature size will resolve better during fabrication compared to the 20 nm features. The larger ΔW also allowed us to use a smaller number of grating periods and reduce the device footprint.

3.1.4 Experimental results and discussion

The devices were fabricated with a single-etch process using electron beam lithography [127]. The waveguides have a $500 \text{ nm} \times 220 \text{ nm}$ cross-section with a $3 \mu\text{m}$ buried oxide and native oxide cladding. Fully-etched sub-wavelength grating couplers were used for coupling light in and out of the OADMs [128]. Calibration grating coupler pairs, with one input grating coupler and one output grating coupler, were used to calibrate the ILs of the grating couplers from the test structures. The scanning electron microscope (SEM) images of the fabricated OADMs and misaligned Bragg grating with $\Delta L=128$ nm and $\Delta W=80$ nm are shown in Fig. 3.7. Transmission

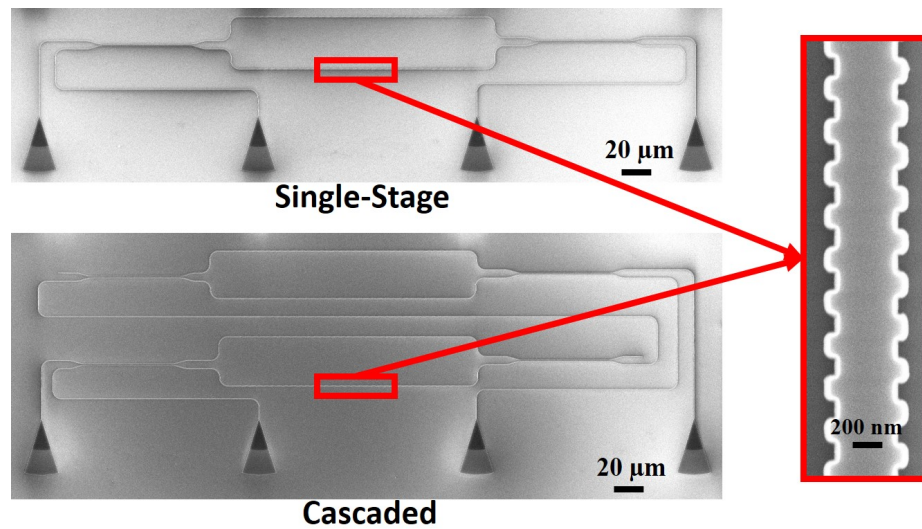


Fig. 3.7 SEM images of the fabricated single-stage and cascaded OADM and misaligned sidewall bragg grating with $\Delta L=128$ nm and $\Delta W=80$ nm.

spectra were measured by sweeping an external cavity laser over the wavelength of interest and recording the output power from various ports of the device with a power meter. The results for both the single-stage and cascaded configurations are presented in Fig. 3.8. ΔL was varied from 0 nm to half of the grating period, Λ . As can be seen from Fig. 3.8, for both configurations, the bandwidth reduces as ΔL is increased. This occurs because the reflection from each grating period interferes less constructively as the grating misalignment increases.

In case of the single-stage configuration, the ER remains almost constant at 51 dB for up to $\Delta L=96$ nm and decreases to 25 dB at $\Delta L=128$ nm. For the case of the cascaded configuration, the ER remains constant at around 51 dB until $\Delta L=128$ nm. This can be explained from the fact that the cascaded configuration has an intermediate Bragg grating, which reflects the residue light that leaks from the first stage, thus achieving a higher ER even at $\Delta L=128$ nm. At $\Delta L=158.5$ nm, there is no reflection as demonstrated by the solid brown line in the input-to-through plot of Fig. 3.8. The measured ILs from the input-to-drop port and the input-to-through port are 2 dB and 4.1 dB, respectively for the single-stage configuration, and 2 dB and 8.5 dB, respectively for the cascaded configuration. The additional loss in the through port of the cascaded configuration emerges because of the extra path and Bragg gratings that the light needs to travel to reach the through port compared to the single-stage configuration. Part of the light also leaks through the add port which is another reason for the increased IL at the through port.

The simulated and measured ERs and 3-dB bandwidths are compared in Fig. 3.9. Regarding the ER, the difference between the simulated and measured results is large as observed in

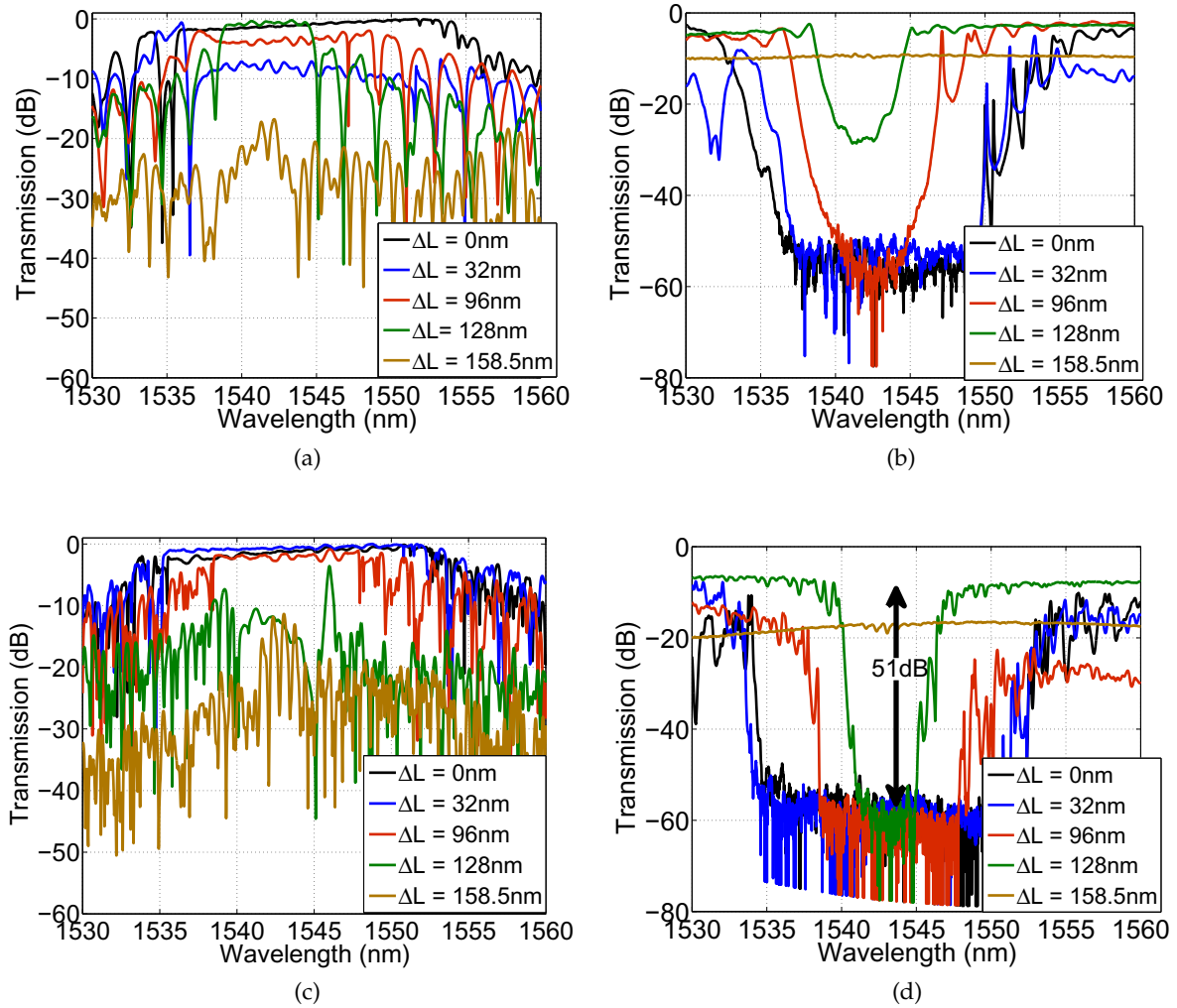


Fig. 3.8 Measured transmission responses of (a) drop and (b) through port of the single-stage configuration, and (c) drop and (d) through port of the cascaded configuration.

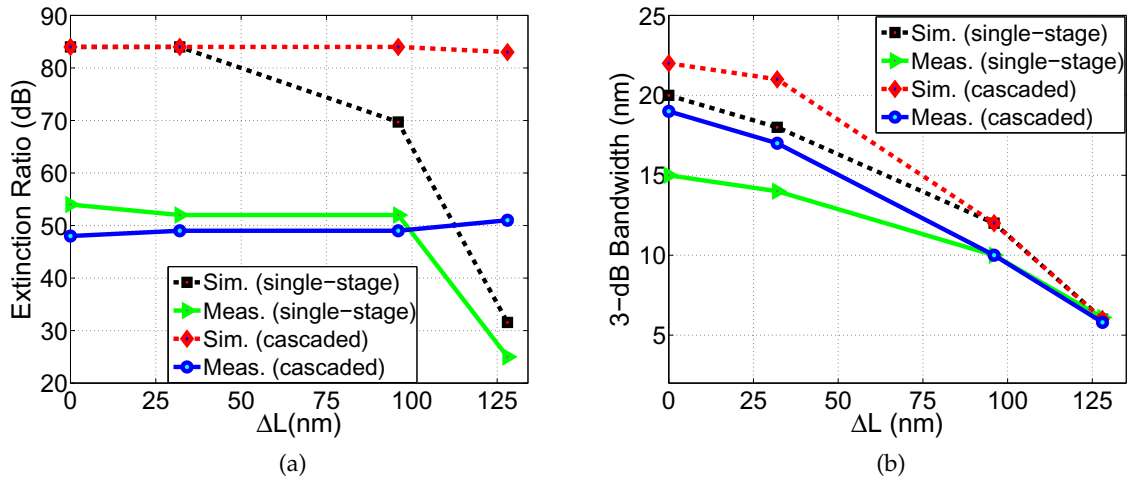


Fig. 3.9 Comparison for the single-stage and cascaded configurations of the OADMs between the simulated and measured (a) ER, and (b) 3-dB bandwidth. Sim. = Simulated and Meas. = Measured.

Fig. 3.9(a). This is attributed to the -80 dBm sensitivity limit of the power meter used in the experiment. The fact that the ER remains constant with the increase in ΔL (even at 128 nm for the cascaded configuration) provides further evidence that the devices have higher ER than measurable with our equipment. Another evidence is that the simulated and measured ERs start to agree for $\Delta L > 100$ nm when the simulated ER become < 50 dB which is within the sensitivity capabilities of the power meter used in the experiment. For the 3-dB bandwidth parameter, the agreement between simulations and measurements is good and the deviations between the simulated and measured values decrease as ΔL is increased as shown in Fig. 3.9(b).

3.1.5 Conclusions

We present two configurations of the OADM utilizing misaligned sidewall Bragg gratings and obtained ERs of 25 and 51 dB with a footprint of only $400 \mu\text{m} \times 90 \mu\text{m}$ and $400 \mu\text{m} \times 125 \mu\text{m}$, respectively. In future designs, the sidelobes can be reduced by apodizing the gratings [129]. The misalignment technique to vary the grating strength profile for apodization is more resilient to fabrication errors compared to changing the corrugation amplitude to vary the grating strength profile [6]. Thus, our proposed designs not only provide good performance but also relax fabrication tolerances. Furthermore, the feature size used in the designs can be fabricated using 193 nm DUV lithography.

3.2 Transversely coupled Fabry-Perot resonators with Bragg gratings

One of the most intensively used components in SOI are resonators, which have applications in WDM, optical sensors, laser cavities and all optical signal processing [130,131]. While a high Q-factor is required for applications like sensing [132] and lasing [131]; WDM applications necessitate resonators with low IL, high ER, and a wide tuning range [133].

Various kinds of resonators have been implemented on the SOI platform in the past including ring [31,48], racetrack [49], Gires-Turnois [50], Fabry-Perot [51] and Michelson [52]. Out of all the variations, the micro ring resonator (MRR) is the most heavily used because of its compact footprint. MRRs [48] are one of the key candidates for WDM applications. However, to obtain a high ER using MRRs, multi-stage configurations are used which leads to an increased device complexity [134]. Furthermore, the critical coupling condition needs to be maintained which is difficult to achieve. MRRs with a small bend radius are required to obtain a large FSR, but if the bend radius is too small, the bending loss becomes too high and achieving the required coupling coefficient becomes difficult due to the small coupling length.

The concept and experimental demonstration of fiber based transversely coupled Fabry-Perot resonators (TCFPR) was first reported in [135,136]. In this thesis, we report a detailed study of the design, fabrication, and characterization of integrated TCFPRs with Bragg gratings on SOI. The proposed resonator structure merge the advantages of both ring resonators and Bragg gratings enabling the variation of more design parameters to tune the spectral characteristics.

3.2.1 Operating principle

As shown in Fig. 3.10, the TCFPRs consist of a directional coupler, two Bragg gratings and waveguide cavities. Depending on which two ends of the waveguide cavities are terminated with Bragg gratings, we refer to the TCFPRs as type I and type II, as presented in Fig. 3.10(a) and 3.10(b), respectively. The key difference between them is that a $\pi/2$ phase shift occurs in every transit inside the waveguide cavity in the case of the type II TCFPR. TCFPRs with Bragg gratings combine the benefits of both ring resonators and Bragg gratings allowing for more flexibility in tuning the spectral characteristics. Unlike MRRs, TCFPRs do not have any critical coupling condition. Furthermore, a single TCFPR can be used to drop multiple channels similar to MRR add-drop filters, but not limited by the FSR as is the case for the MRR add-drop filters because the implementation of the Bragg gratings act as a channel filter.

The spectral characteristics of an all-pass MRR can be tuned by putting heaters either on the coupling region to tune the coupling coefficient or on the ring itself to vary the optical path length as shown in Fig. 3.10(c). Whereas, TCFPRs with Bragg gratings provide the freedom of

tuning the spectral characteristics of the Bragg gratings, in addition to the possibility of tuning the coupling coefficient and the optical path length. The physical parameters set the reflectivity and bandwidth of the Bragg grating, which then determines the ER and the number of channels of the TCFPR. By increasing or decreasing the bandwidth of the Bragg grating, resonant peaks can be added or removed; which in turn increases or decreases the number of channels that can be dropped using the TCFPR. In addition, the resonant cavity of the TCFPRs can be made to be straight waveguide to alleviate bending losses. Type I and II TCFPRs can be cascaded to make compound resonators with tunable spectral mode suppression capability [137] which have applications in laser linewidth narrowing, filtering and spectral analysis. The $\pi/2$ phase shift offered by the type II TCFPR is required for such applications, a feature which is absent in all-pass MRRs. It should be noted that the devices presented in sections 3.2 and 3.3 do not include the heaters. We only discussed the possibility of tuning the characteristics of the devices using heaters.

Referring to Fig. 3.10(a) and 3.10(b), in the type I and II TCFPRs, two ports of the directional coupler are connected to the input and output grating couplers while the other two ports are connected to the Bragg gratings via straight waveguides. In the type I TCFPR, the Bragg gratings are connected to the waveguide ends such that no phase shift occurs during each transit within the cavity, while in the type II TCFPR, the Bragg gratings are connected in a manner that causes a $\pi/2$ phase shift for each transit through the cavity. The output intensities can be expressed as following for the type I and II TCFPRs, respectively [136, 138],

$$I_I = [(1 - \kappa)^{1/2} E^{in}]^2 [1 - (R_1 R_2 + R'_1 R'_2)]^2 \times \left\{ \frac{1 + \frac{4(R_1 R_2 + R'_1 R'_2) \sin^2[\beta(l_1 + l_2)]}{[1 - (R_1 R_2 + R'_1 R'_2)]^2}}{\left\{ 1 + \frac{4R_1 R_2}{(1 - R_1 R_2)^2} \sin^2[\beta(l_1 + l_2)] \right\} (1 - R_1 R_2)^2} \right\} \quad (3.5)$$

$$I_{II} = [\kappa^{1/2} E^{in}]^2 [1 + R_4 R_3 + R'_4 R'_3]^2 \times \left\{ \frac{1 - \frac{4(R_4 R_3 + R'_4 R'_3) \sin^2[\beta(l_4 + l_3)]}{[1 + R_4 R_3 + R'_4 R'_3]^2}}{\left\{ 1 - \frac{4R'_4 R'_3}{(1 + R'_4 R'_3)^2} \sin^2[\beta(l_4 + l_3)] \right\} (1 + R'_4 R'_3)^2} \right\} \quad (3.6)$$

where, $R_j = r_j(1 - \kappa)^{1/2}(1 - \gamma)^{1/2} \exp(-2\alpha l_j)$; $j = 1, 2, 3, 4$,
 $R'_j = r_j \kappa^{1/2}(1 - \gamma)^{1/2} \exp(-2\alpha l_j)$; $j = 1, 2, 3, 4$.

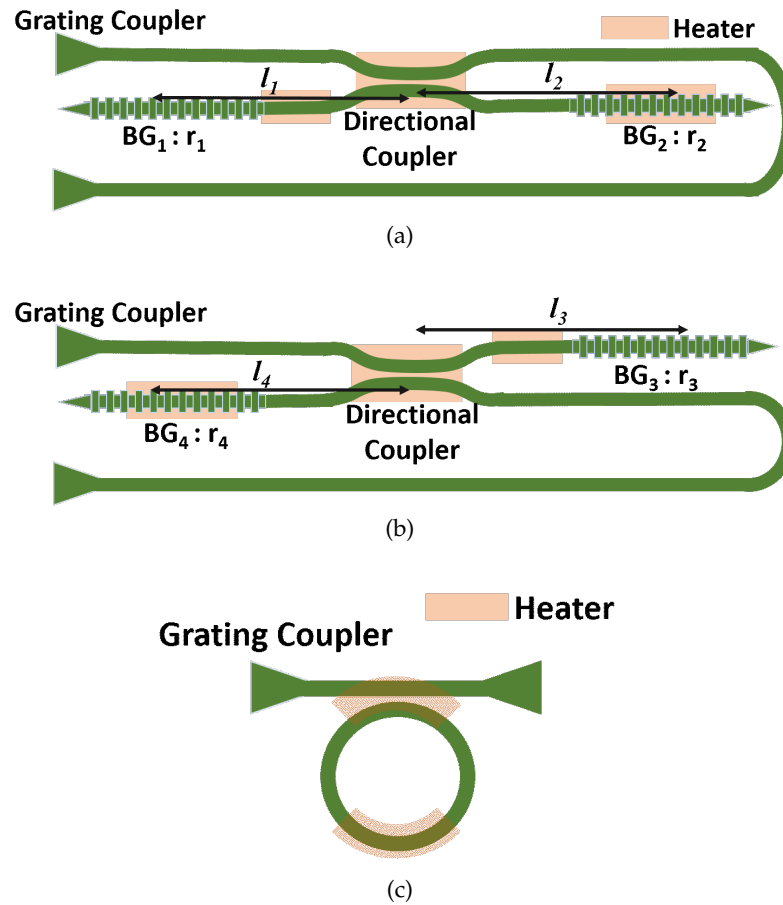


Fig. 3.10 Schematics of the (a) type I, and the (b) type II TCFPRs, and (c) an all-pass MRR. BG: Bragg Grating

E^{in} is the input electric field, α is the amplitude loss, $\beta = \frac{2\pi}{\lambda}n_{eff}$ is the propagation constant, n_{eff} is the effective index, κ is the directional coupler coupling coefficient, γ is the excess loss of the directional coupler, r_1 , r_2 , r_3 and r_4 are the reflectivities of BG₁, BG₂, BG₃ and BG₄, respectively, and l_1 , l_2 , l_3 and l_4 are the waveguide cavity lengths as depicted in both Fig. 3.10(a) and 3.10(b).

The light penetrates into the Bragg gratings to some extent and gets fully reflected before traveling through the entire length of the Bragg grating. Thus, we use the term effective cavity length, L_{eff} to express the resonant cavity length which includes the length of the waveguide cavities on both sides of the directional coupler, the length of the directional coupler and the length up to which light penetrates into the Bragg grating. This length is smaller than the total length if we consider the entire length of the Bragg gratings. We calculate L_{eff} by measuring the FSR (either from simulation results or from measurements) and using the relation provided

below [138],

$$L_{eff} = \frac{c}{2n_g \times FSR} \quad (3.7)$$

where, c is the speed of light and n_g is the group index. It is to be noted that the FSR in the above equation is in terms of frequency difference. The simulated n_g as a function of wavelength for the waveguide used in our design is shown in Fig. 3.11. In [138], n_{eff} was used instead of the n_g for the fiber-based TCFPR. However, due to non-negligible dispersion in SOI waveguides we have used n_g , which takes the dispersion into account.

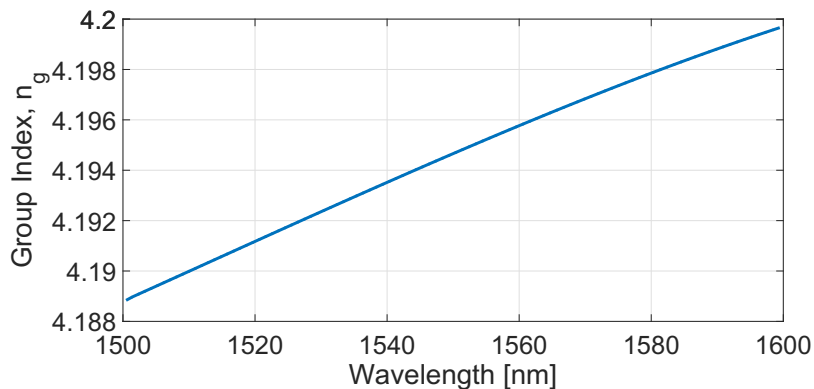


Fig. 3.11 Simulated group index of silicon waveguide with $500 \text{ nm} \times 220 \text{ nm}$ cross-section. Obtained using Lumerical MODE Solutions.

3.2.2 Simulation results

The effect of varying the cavity length and κ on the spectral characteristics of the TCFPRs have been studied using simulations. All the simulations have been done in *Lumerical Interconnect* [125] and the *Si-EPIC* electron-beam process design kit has been utilized [126]. Fig. 3.12(a) shows the effect of varying the cavity length on the FSR of the TCFPRs. The color bar indicates the ER of the resonant peaks. It can be seen that the FSR can be tuned from a few nanometers to fractions of a nanometer by changing the cavity length.

Transmission responses of the TCFPRs with effective cavity lengths of $110 \mu\text{m}$ and $943 \mu\text{m}$ are presented in Fig 3.12(b) and 3.12(c), respectively. Bragg gratings with corrugation width of 100 nm , grating period of 320 nm and 1500 periods are used as the mirrors. The TCFPR with $L_{eff} = 110 \mu\text{m}$ achieved Q-factor, ER and FSR values of 2765 , 39 dB and 2.75 nm , respectively, while the TCFPR with $L_{eff} = 943 \mu\text{m}$ exhibits Q-factor, ER and FSR values of 22687 , 21 dB and 0.31 nm , respectively.

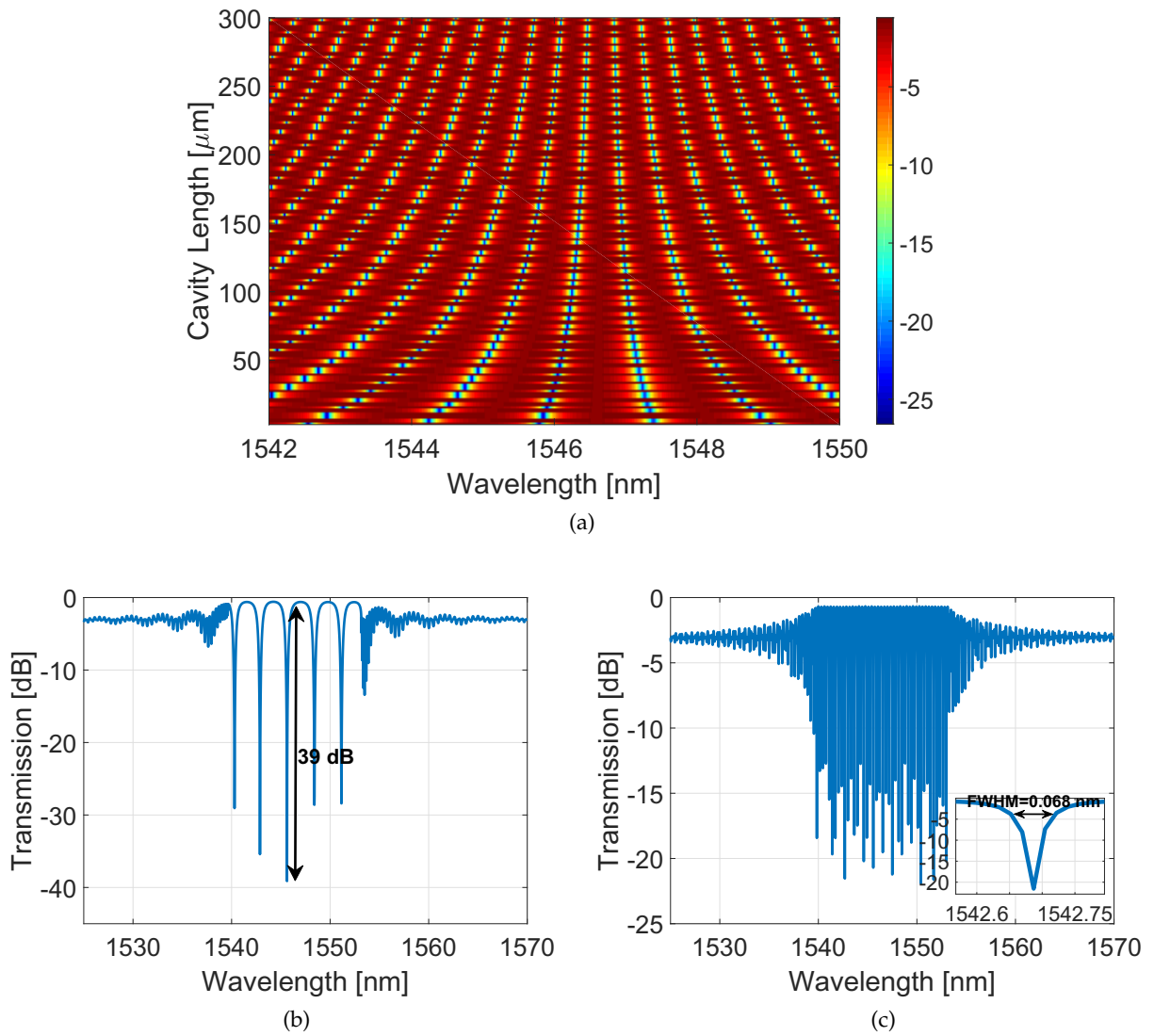


Fig. 3.12 (a) Cavity length sweep of the type I TCFPR with Bragg gratings (color bar indicates the extinction ratio) and simulated transmission response of the (b) type I TCFPR with $L_{eff} = 110 \mu\text{m}$, and the (c) type I TCFPR with $L_{eff} = 943 \mu\text{m}$.

The behavior of the Q-factor as κ is varied, is depicted in Fig. 3.13. A high Q-factor is obtained in the case of the type I TCFPR when κ is small and in the case of the type II TCFPR when κ is large. The opposite responses of the type I and II TCFPRs come from the fact that only an amplitude change takes place inside the cavity of the type I device while both an amplitude change and a $\pi/2$ phase shift occur inside the type II TCFPR cavity.

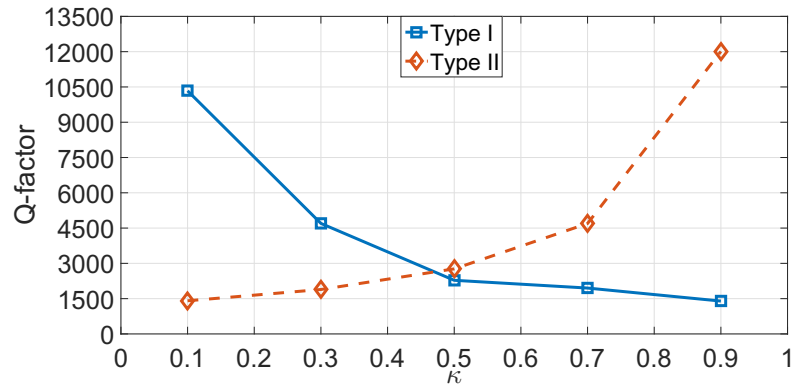


Fig. 3.13 Q-factor as a function of κ for both type of TCFPRs.

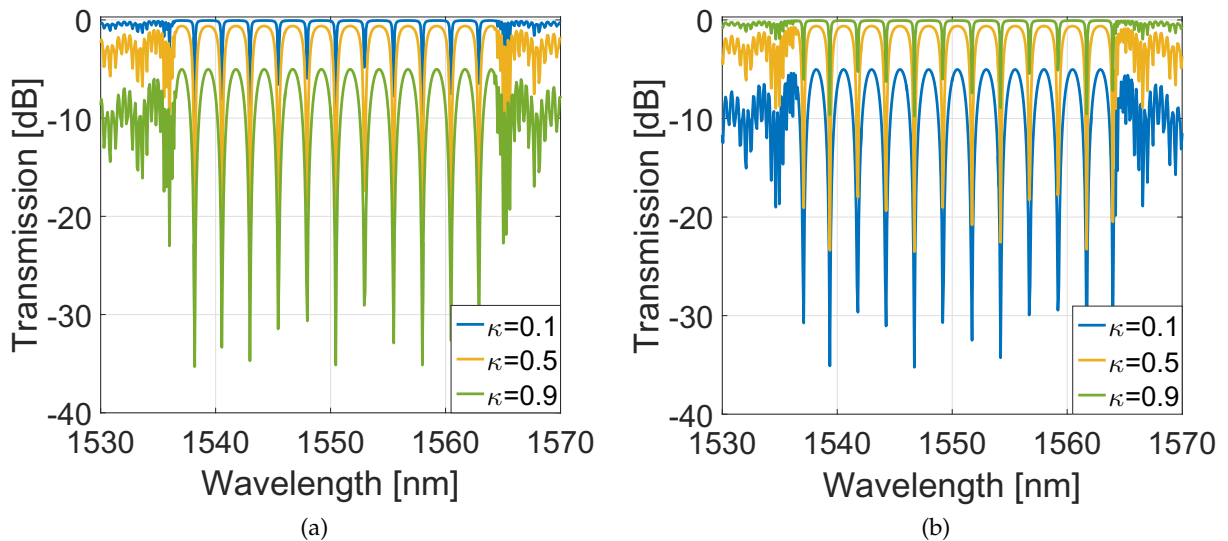


Fig. 3.14 Effect of variation of κ on the type (a) I, and (b) II TCFPRs' spectral characteristics using simulations.

Figure 3.14(a) and 3.14(b) present the simulated effect of the variation of κ on the spectral characteristics of the type I and II TCFPRs, respectively. To obtain a flattop passband, κ should be small in the case of the type I TCFPR and large for the type II TCFPR. However, the ER gets

smaller as the flatness of the passband increases in both cases; i.e., κ is decreased for the type I TCFPR and increased for the type II TCFPR. As shown in [139], high Q-factor and high ER are conflicting requirements and there is a trade-off between these two performance parameters. Therefore, with increasing κ , the Q-factor is decreased and the ER is increased for the type I TCFPR and the reverse is observed in the case of the type II TCFPR.

3.2.3 Experimental results and discussion

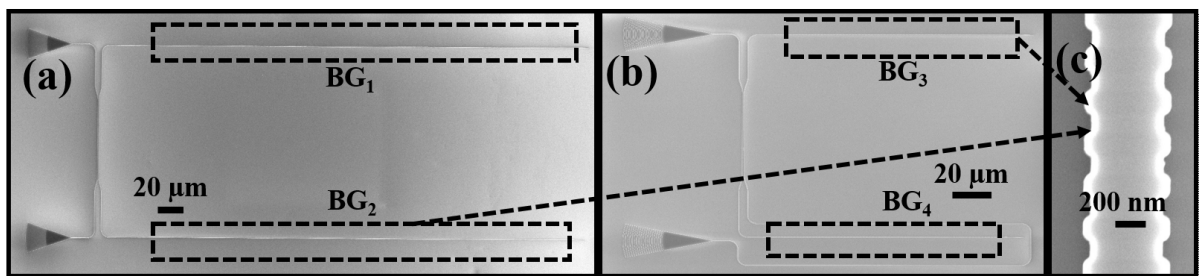


Fig. 3.15 SEM images of the Bragg grating-based type (a) I, and (b) II TCFPRs, (c) enlarged view of the Bragg grating.

The devices were fabricated using electron beam lithography on a SOI wafer with 220 nm silicon layer thickness. The wafer has a 2 μm buried oxide layer and 2.2 μm thick silica has been deposited over the silicon layer after the etching step was completed. Fig. 3.15 presents the SEM images of the fabricated devices. Broadband sub-wavelength grating couplers with 90 nm 1-dB bandwidths [140] were used to couple light into and out of the devices and calibration grating couplers were used to calibrate the ILs of the grating couplers from the devices under test. A broadband directional coupler [141] with a 1-dB bandwidth in excess of 100 nm was used as the 3-dB directional coupler. Sidewall Bragg gratings with 100 nm corrugation widths, 320 nm grating period and 1500 periods resulting in a length of 480 μm were utilized as the mirrors to form the resonant waveguide cavity.

A custom-built setup using a Yenista TUNICS C-band laser and a CT400 passive optical component tester is used to perform the measurements. The measured transmission spectra of the type I TCFPRs with $L_{eff} = 110 \mu\text{m}$ and $943 \mu\text{m}$ are depicted in Fig. 3.16(a) and 3.16(b), respectively. As can be seen from the figures, the TCFPR with $L_{eff} = 110 \mu\text{m}$ achieves an ER of 37.28 dB. This TCFPR has an IL of 2.48 dB, an FSR of 2.58 nm and a Q-factor of 3356; whereas, the TCFPR with $L_{eff} = 943 \mu\text{m}$ achieves a Q-factor of 23642, an IL of 1.48 dB, an FSR of 0.3 nm and an ER of 8.6 dB. The measurements matches well with the simulation results presented in Fig. 3.12(b) and 3.12(c) except for the fact that the resonant peaks appear over a different wavelength range. Since Bragg gratings are sensitive to fabrication variations, the

Bragg wavelength differs from the simulation results although the same grating period is used during fabrication. As a result, the range of wavelength over which the resonant peaks appear are different from the simulations.

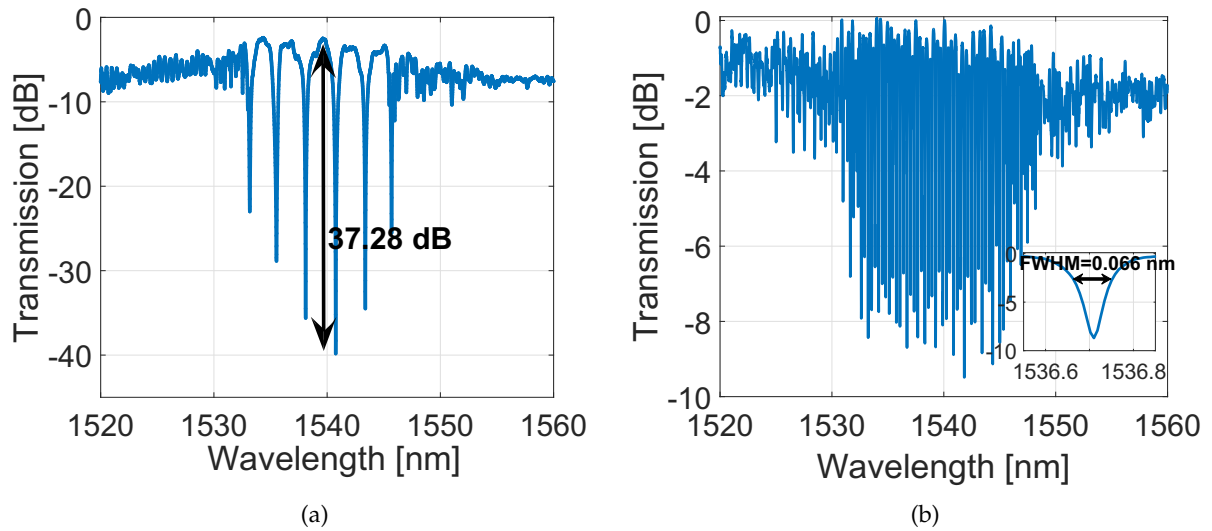


Fig. 3.16 Measured transmission responses of the (a) type I TCFPR with $L_{eff} = 110 \mu\text{m}$, and the (b) type I TCFPR with $L_{eff} = 943 \mu\text{m}$.

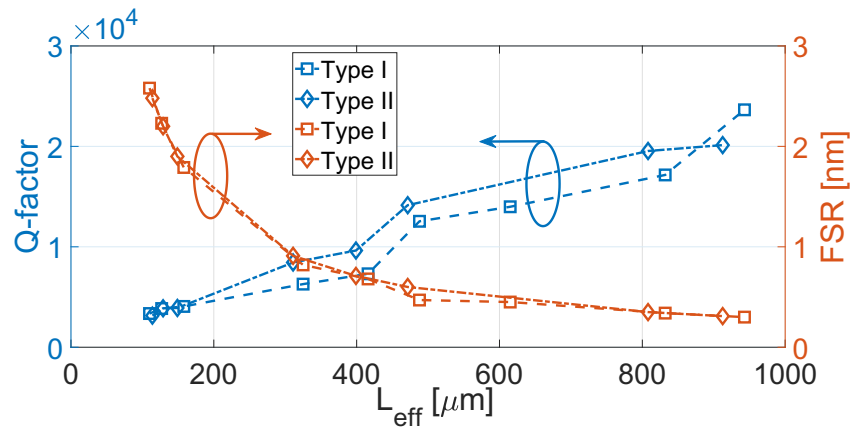


Fig. 3.17 Variation of the Q-factor and the FSR of the type I and II TCFPRs as a function of L_{eff} .

The Q-factor can be written as [48],

$$Q - factor = \frac{\lambda_{res}}{FWHM} = \frac{\pi n_g L_{eff} \sqrt{r_{1,4} r_{2,3}}}{\lambda_{res} (1 - r_{1,4} r_{2,3})} \quad (3.8)$$

where, λ_{res} is the resonant wavelength and $FWHM$ is the full-width half-maximum. Variation of the Q-factor and the FSR as a function of L_{eff} for both type I and II TCFPRs are presented in Fig. 3.17. Both type of TCFPRs show similar FSRs for a certain L_{eff} as shown in Fig. 3.17. The Q-factor increases with the increase of L_{eff} for both of the TCFPRs as suggested by Eq. 3.8. Although at smaller L_{eff} , the type II TCFPRs exhibit slightly higher Q-factor than the type I TCFPRs, the highest Q-factor is achieved by the type I TCFPR at $L_{eff} = 943 \mu\text{m}$. The achieved ERs and ILs for various values of L_{eff} for type I and II TCFPRs are reported in Table 3.1. A decreasing trend of the ERs can be observed with the increase of L_{eff} . The ER can be related to the resonator losses [142]. Since increasing the L_{eff} increases the propagation loss, the ER is decreased. However, the ILs do not exhibit any such trend.

Table 3.1 Measured ER and IL for various cavity lengths.

L_{eff} [μm]	Type I		Type II	
	ER [dB]	IL [dB]	ER [dB]	IL [dB]
110	37.28	2.48	27.56	2.41
158	27.68	2.4	24.33	2.39
325	17.68	2.2	15.64	2.13
416	17.65	1.8	15.09	1.73
488	11.6	2.1	13.26	2
832	10.43	1.7	11.23	2
943	8.69	1.43	11.14	3.08

3.2.4 Conclusions

In summary, we have demonstrated novel TCFPRs on the SOI platform. The TCFPRs offer better flexibility to achieve the desired spectral response compared to all-pass MRRs. Furthermore, one variant of the TCFPR features a $\pi/2$ phase shift for each one-way trip through the resonant cavity. Since the resonant cavity can be formed using straight waveguides and BGs as the end reflectors, bending losses can be eliminated in the TCFPRs. The effect of varying the cavity length is studied experimentally for both types of TCFPRs. The impact of tuning the κ on the spectral response of the TCFPRs is also investigated in simulation. In future designs, the spectral range can be increased by using chirped gratings.

3.3 Transversely coupled Fabry-Perot resonator with loop mirrors

In this section, we present the simulation and experimental results of loop mirror based TCFPRs. The operating principle of this version of the TCFPR is same as the Bragg grating based design. Since Bragg gratings have small reflection bandwidths, TCFPRs utilizing Bragg gratings

exhibit resonant peaks over smaller bandwidths, therefore, limiting device applications where a broadband resonant spectrum is required. Loop mirror based TCFPRs, on the other hand, exhibit resonant peaks over a broader range of wavelengths. A silicon photonic interleaver based on an interfering loop had been demonstrated in [143] achieving boxlike spectral response over 60 nm bandwidth. The interfering loop contained a Fabry-Perot cavity formed by two Sagnac loops.

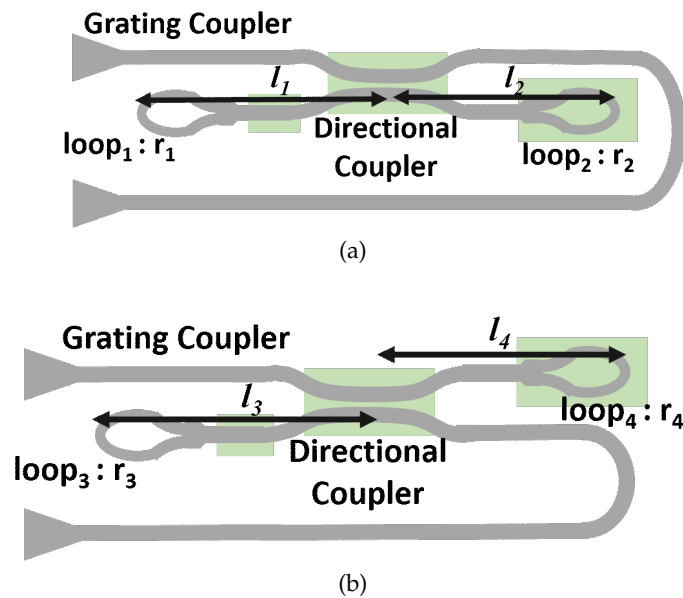


Fig. 3.18 Schematics of the type (a) I, and (b) II TCFPRs with loop mirrors.

Two different configurations of the resonators have been obtained by connecting the loop mirrors to two different sets of ports of the directional coupler which are referred to as type I and type II as shown in Fig. 3.18(a) and 3.18(b), respectively. TCFPRs using loop mirrors offer tuning the properties of the loop mirrors to achieve the desired response, in addition to the coupling coefficient of the directional coupler and the optical path length of the waveguide cavities. The reflectivity of the loop mirrors can be tuned by tailoring the Y-branch and length of the loop. In [144], the variation of Y-branch to obtain different reflectivities have been investigated thoroughly via simulation and experiment. The reflectivity of the loop reflector can be maximized by optimizing the Y-branch waveguide dimensions. The reflectivity can be varied by changing the power splitting ratio at the Y-junction and the transmission loss at the half-ring arc [144]. A larger imbalance in the splitting ratio of the Y-junction and a higher loss at the half-ring arc will reduce the reflectivity and vice-versa. A high reflectivity is desired to obtain a large Q-factor.

3.3.1 Simulations results

The effects of varying the waveguide cavity length and the coupling coefficient of the directional coupler, κ on the spectral characteristics of the TCFPRs are simulated first.

Figure 3.19(a) depicts the variation of FSR as a function of the cavity length of the TCFPRs with loop mirrors. The color bar indicates the ER of the resonant peaks. The FSR can be varied from a few nanometers to fractions of a nanometer by tailoring the cavity length.

Transmission responses of the type II TCFPR with a cavity length of $376 \mu\text{m}$ and the type I TCFPR with a cavity length of $1038 \mu\text{m}$ are presented in Fig 3.19(b) and 3.19(c), respectively. The former achieved Q-factor, ER and FSR values of 5760, 23.62 dB and 1.19 nm, respectively, while the latter exhibits Q-factor, ER and FSR values of 27046, 18.5 dB and 0.32 nm, respectively.

Variation of the Q-factor as a function of κ is depicted in Fig. 3.20. As κ decreases, the Q-factor of the type I TCFPRs increases and for the type II TCFPRs high Q-factors are obtained for larger values of κ . Since a $\pi/2$ phase shift takes place inside the cavity of the type II device which does not occur in the type I TCFPRs, we observe the opposite responses.

The effects of variation of κ on the resonant spectrum of the type I and II TCFPRs are presented in Fig. 3.21(a) and 3.21(b), respectively. As can be seen from the figures, flattop passbands are obtained when κ is small in case of the type I TCFPRs and is large for the type II TCFPRs. A flattop passband is desired in WDM applications to ensure that the filters do not introduce any distortions in the signal that passes through it. However, there is a trade-off between the ER and the flatness of the passband. As κ is decreased, the ER becomes smaller for the type I TCFPRs and the opposite happens for the type II TCFPRs. This can be explained from the fact that high Q-factor and high ER cannot be obtained simultaneously and there is a trade-off between them [139].

3.3.2 Experimental results and discussion

Figure 3.22(a) and 3.22(b) depict the SEM images of the type I and II TCFPRs, respectively. Electron beam lithography is used to fabricate the devices with a single etch step. The SOI wafers have a $2 \mu\text{m}$ buried oxide layer and a 220 nm silicon layer on top of the buried oxide layer. After etching, a silica layer with a thickness of $2.2 \mu\text{m}$ was deposited over the silicon layer.

The measurements were taken using a custom-built setup with a Yenista TUNICS C-band laser and a CT400 passive optical component tester. A polarization maintaining fiber array with a pitch of $127 \mu\text{m}$ was used to test the device. A photograph of the experimental setup is shown in Fig. 3.22(c). Vertical grating couplers with a 90 nm 1-dB bandwidth [140] were used to inject and extract the light to and from the device. Calibration grating coupler pairs connected by straight waveguides were used to calibrate the ILs of the grating couplers from

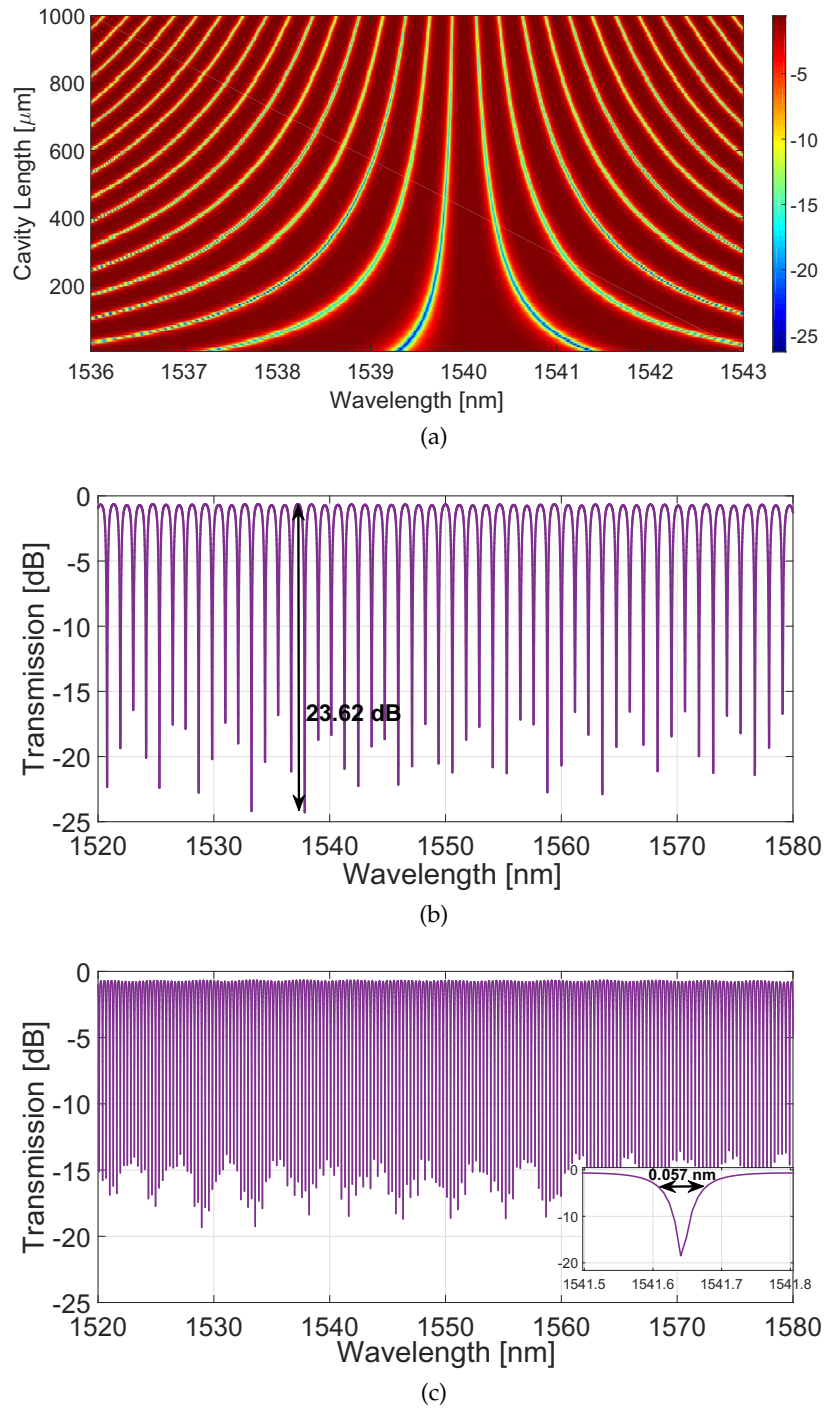


Fig. 3.19 (a) Cavity length sweep of the type I TCFPR with loop mirrors (color bar indicates the extinction ratio) and simulated transmission response of the type (b) II TCFPR with $L = 376 \mu\text{m}$ and the type (c) I TCFPR with $L = 1038 \mu\text{m}$.

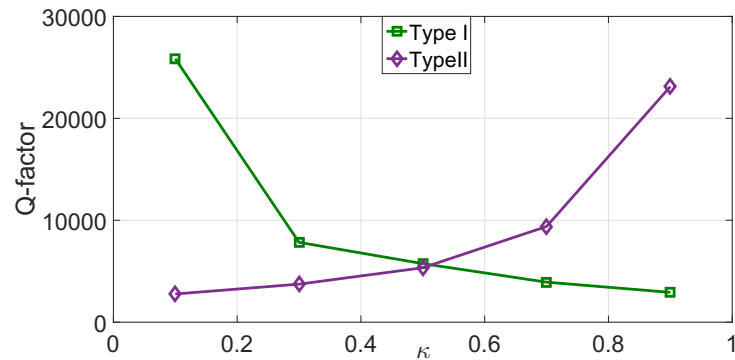
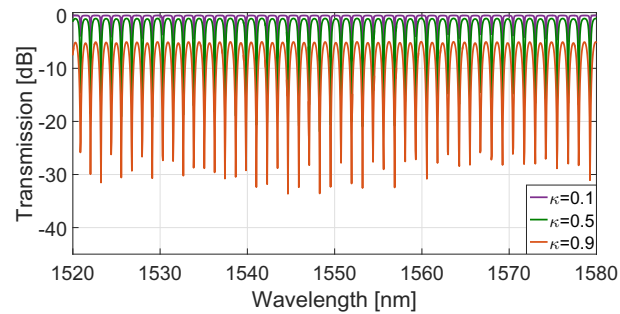
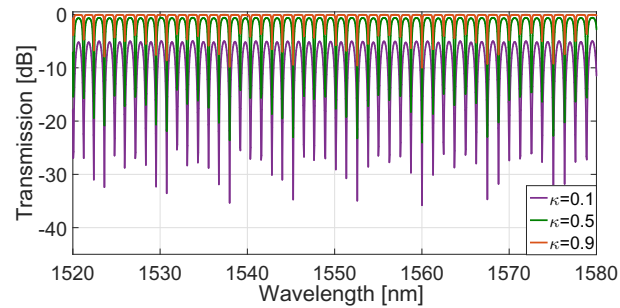


Fig. 3.20 Q-factor as a function of κ for both TCFPRs.



(a)



(b)

Fig. 3.21 Effect of variation of κ on the (a) type I, and the (b) type II TCFPRs' spectral characteristics using simulations.

the transmission response of the TCFPRs. The directional coupler used in the device has a 1-dB bandwidth in excess of 100 nm [141] and has a gap of 200 nm. The loop mirrors are designed using a Y-branch and by connecting the two ports of the Y-branch with a strip waveguide. The waveguides have a cross-section of 500 nm \times 220 nm and the loop has a radius of 14 μ m.

Figure 3.23(a) and 3.23(b) present the measured transmission responses of the type II TCFPR

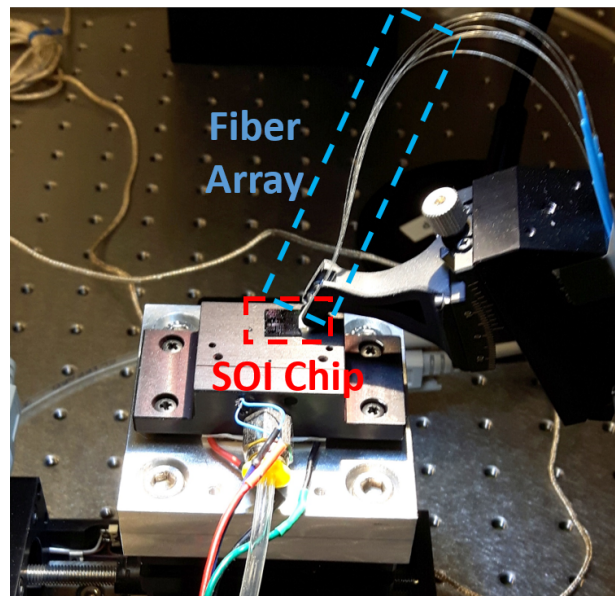
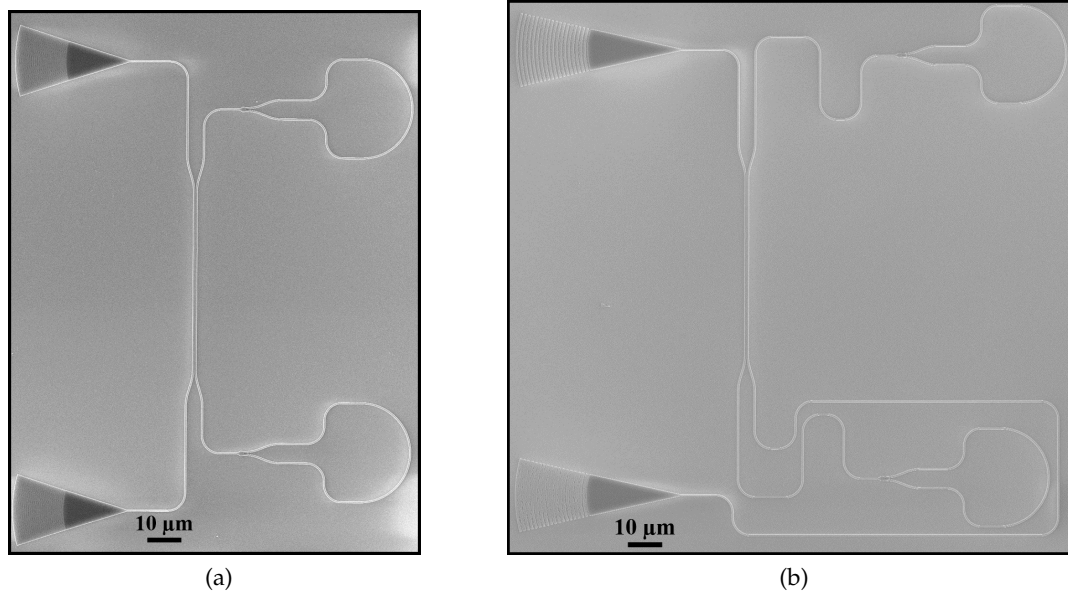


Fig. 3.22 SEM images of the type (a) I, and (b) II TCFPRs with loop mirrors, and (c) photograph of the experimental setup.

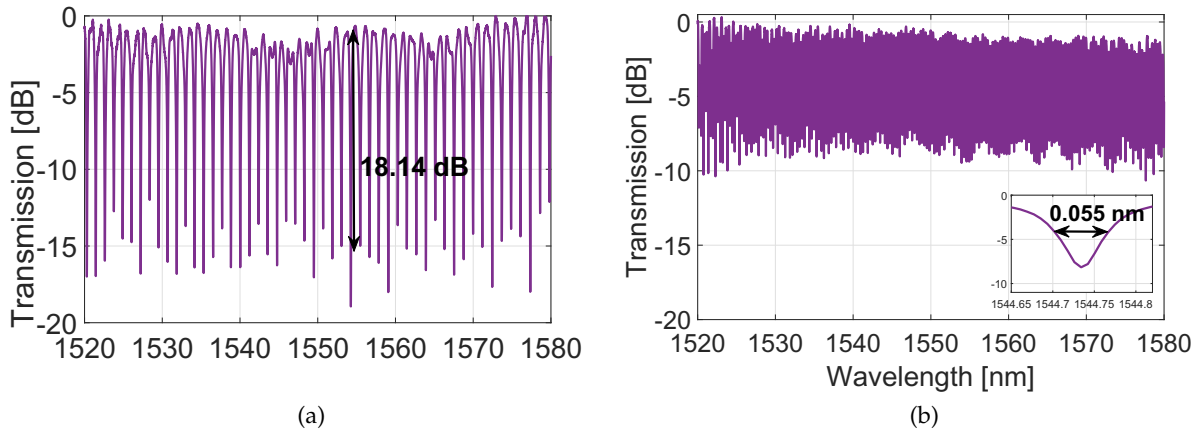


Fig. 3.23 Measured transmission responses of the (a) type II TCFPR with $L = 376 \mu\text{m}$, and the (b) type I TCFPR with $L = 1038 \mu\text{m}$.

with a $376 \mu\text{m}$ cavity length and the type I TCFPR with a $1038 \mu\text{m}$ cavity length. It can be seen that, the type II TCFPR with $L = 376 \mu\text{m}$ achieves an ER of 18.14 dB, an FSR of 1.22 nm, a Q-factor of 5120 and an IL of 2.12 dB. The type I TCFPR with $L = 1038 \mu\text{m}$ achieves a Q-factor of 28086 with an ER of 10.04 dB, an FSR of 0.32 nm and an IL of 1.9 dB. The measurements agree well with the simulations presented in Fig. 3.19(b) and 3.19(c).

As shown in [144], the reflectivity of the loop mirror varies with wavelength in a periodic manner which is attributed to the unsymmetrical branching of the Y-branch. As a consequence, the IL of the TCFPR varies with the wavelength as can be observed from Fig. 3.23. The resonance ER in Fig 3.23(a) and 3.23(b) varies approximately sinusoidally with the variation of the wavelength. This phenomena can be attributed to the fact that the self-coupling coefficient of a resonator with a directional coupler exhibit a sinusoidal variation with wavelength as shown in [145,146]. Hence, the resonance ER exhibits a similar sinusoidal pattern as a function of the wavelength.

The measured ER and the ILs of both types of TCFPRs with different cavity lengths are presented in table 3.2. The same directional coupler has been used in all these variations of the TCFPR to ensure that the loss due to the directional coupler is fixed. It can be observed that as the cavity length increases, the ER decreases. As mentioned in [142], the ER is related to the resonator losses. Thus, with the increase of the cavity length, the propagation loss increases and as a consequence the ER decreases. The measured propagation losses of the waveguides used in the reported devices are 2.2 dB/cm for the straight waveguides and 6.2 dB/cm for the curved waveguides [147].

Table 3.2 Measured ER and IL for different cavity lengths.

L [μm]	Type I		Type II	
	ER [dB]	IL [dB]	ER [dB]	IL [dB]
376	17.62	1.75	18.14	2.12
413	16.05	1.54	14.74	1.43
536	13	1.37	13.96	2.7
641	12.72	1.93	12.66	1.95
738	12.5	1.61	12.63	1.8
838	11.04	1.97	12.17	2.14
938	10.41	1.78	11.6	2.45
1038	10.04	1.9	11.45	2.8

3.3.3 Conclusions

We present two configurations of TCFPRs using the loop mirror reflectors. We achieved a Q-factor of 28086 and an ER of 10.04 dB for a 1038 μm cavity length and an ER of 18.14 dB and a Q-factor of 5120 for a cavity length of 376 μm . The reported TCFPRs offer better design flexibility compared to the all-pass MRRs.

3.4 C-Band 120° optical hybrid using multi-mode interference couplers

Coherent detection techniques facilitate the linear mapping of the in-phase and quadrature components of optical fields to the electrical domain which allows the use of DSP [148]. DSP is the key enabler to implement spectrally efficient modulation formats and mitigate the transmission impairments [149]. Moreover, coherent detection system allows convergence to the limits of spectral efficiency [150].

Coherent optical detection systems have already been deployed in long-haul, metro and inter-data center networks. Passive optical networks employing coherent detection have been demonstrated as well [90]. In the intra-data center segment, multilevel intensity modulation and direct detection is used to achieve bit rates up to 100 Gb/s per λ [151]. However, this approach offers limited optical power efficiency which is challenging to scale further. Recently, several research groups have suggested to use coherent detection for high-speed intra-data center applications to exploit all four dimensions of the optical field and to increase the receiver sensitivity [151, 152]. However, due to the strict power and cost constraints of this segment, coherent detection systems with simpler front-end are required. The expensive receiver architecture developed for the core network cannot be directly transferred to the cost-sensitive segments such as intra-data center and access networks.

Conventional coherent detection systems use 2×4 90° optical hybrid to mix the received op-

tical signal with the local oscillator and utilize balanced photodetectors to reject the unwanted direct detection terms [58]. Although balanced detection using 90° optical hybrids is favored in long-haul communication systems due to its superior performance in suppressing different noise sources, single-ended detection is less expensive due to simpler trans-impedance amplifiers and less number of required RF connections. To reduce the complexity of the receiver architecture, single-ended detection based optical front-ends with 120° optical hybrids applicable for colorless reception have been reported in [62, 153]. In [68], an integrated coherent receiver based on 120° hybrid in SOI in the C-band has been reported. However, there is no detail analysis on the design and characterization of the 120° hybrid itself. In [92], polarization-independent coherent receivers based on 120° optical hybrid have been demonstrated for intensity modulated signals with applications in the access networks. 120° optical hybrids have broader bandwidth and larger fabrication tolerance compared to 90° hybrids [153] based on 4×4 MMI couplers.

In this thesis, we present a C-band 120° optical hybrid on SOI with silicon thickness of 220 nm for the TE mode using 193 nm DUV lithography. The hybrid is based on 3×3 MMI couplers. As seen in [154], the optical bandwidth of an MMI is inversely proportional to the number of access waveguides. Therefore, a 3×3 MMI based 120° optical hybrid has intrinsically broader bandwidth than a 90° optical hybrid based on a 4×4 MMI. Broadband optical hybrids are preferred for colorless detection over wide bandwidth range.

3.4.1 Device design and simulations

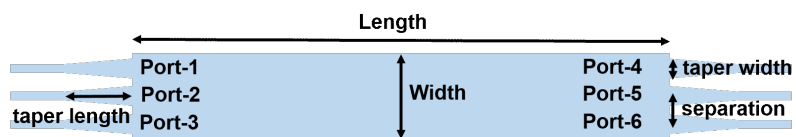


Fig. 3.24 Schematic of the 3×3 MMI coupler based 120° optical hybrid.

The 120° optical hybrid is a 6-port device with 3 input and 3 output ports. The hybrid provides linear combinations of the input fields at the 3 output ports with mutual relative phase offsets of 120° and 240° . The schematic of the reported 120° optical hybrid based on 3×3 MMI coupler is shown in Fig. 3.24. MMI coupler is a photonic device that utilizes self-imaging in multimode waveguide [108]. A large number of modes supported by the multimode waveguide interfere at well defined lengths which results in self-imaging. To launch light into the waveguide and recover it from the waveguide, a number of access waveguides are placed at the input and output of the multimode waveguide. The self-imaging length of the MMI is

given by [108],

$$3L_{\pi} \simeq \frac{4n_r W_e^2}{\lambda_0} \quad (3.9)$$

Here, L_{π} is the beat length of the two lowest order modes, W_e is the effective MMI width, n_r is the effective index of the MMI slab region and λ_0 is the operating wavelength.

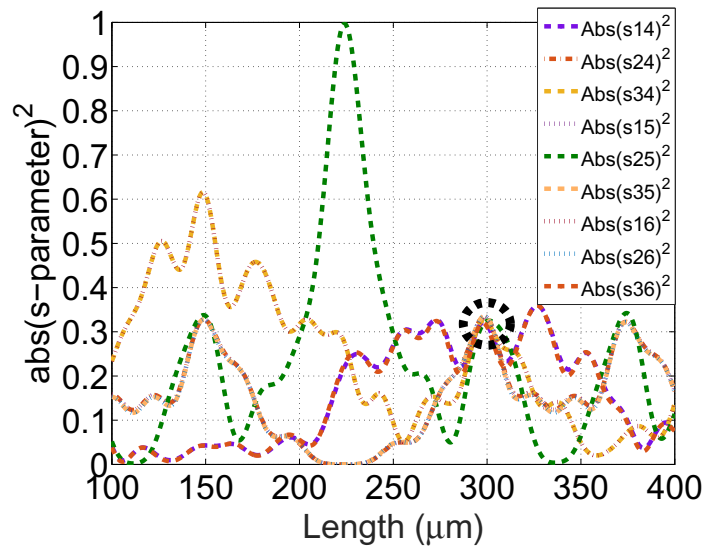


Fig. 3.25 Variation of length of the 120° optical hybrids for C-band with width = $11 \mu\text{m}$. Here, 1, 2 and 3 are the input ports and 4, 5 and 6 are the output ports as shown in Fig. 3.24. Black dashed circle indicates the optimum length.

The fundamental design guidelines of an MMI coupler are provided in [108]. The basic design parameters are the length and width of the multimode waveguide and the positions of the access waveguides. The simulations were carried out using *Lumerical MODE eigenmode expansion solver* [155]. It has been shown in [60] that the excess loss of an MMI decreases with an increase in the width of the multimode waveguide. Initially the width of the multimode waveguide was chosen based on the results which were reported in [60]. After running simulations we found the optimum width to be $11 \mu\text{m}$. Since the 3×3 MMI coupler should have a split ratio of $1/3$ of the input at each output port, the access waveguides need to be placed symmetrically around the center axis on both sides of the multimode waveguide. The gap among the access waveguides also need to be chosen carefully. Tapered waveguides were used to ensure the gradual evolution of the optical modes from waveguide width of $0.5 \mu\text{m}$ to $2.5 \mu\text{m}$. Finally the length of the MMI was varied to find the sweet spot where the split ratio is $1/3$ of the input at each output port and relative phase differences are 120° and 240° with respect to a reference port. The variation of the absolute squared scattering parameters of different ports with the

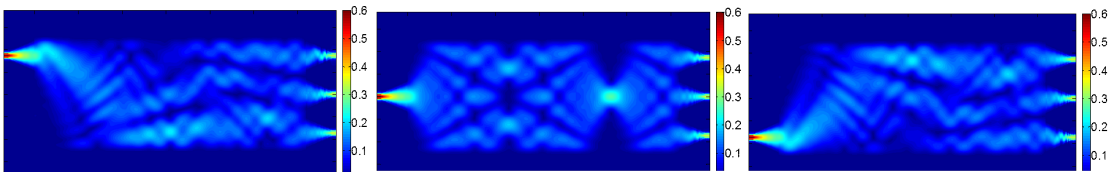


Fig. 3.26 Simulated TE field profiles of the 3×3 MMI coupler with excitations at different input ports.

variation of MMI length are shown in Fig. 3.25. It can be observed that the optimum length is $298 \mu\text{m}$. The TE field profiles of the 3×3 MMI coupler with excitations at different input ports are shown in Fig. 3.26. With light injected at any input port, the hybrid divides it equally at the 3 output ports acting like a $1/3$ power splitter.

The simulated split ratio and phase deviations at each output port for light launched at different input ports with the variation of wavelengths are presented in Fig. 3.27(a) and 3.27(b), respectively. Maximum excess loss of 2.65 dB and phase deviation of $\leq 5^\circ$ are achieved over 65 nm (1520 nm - 1585 nm) bandwidth.

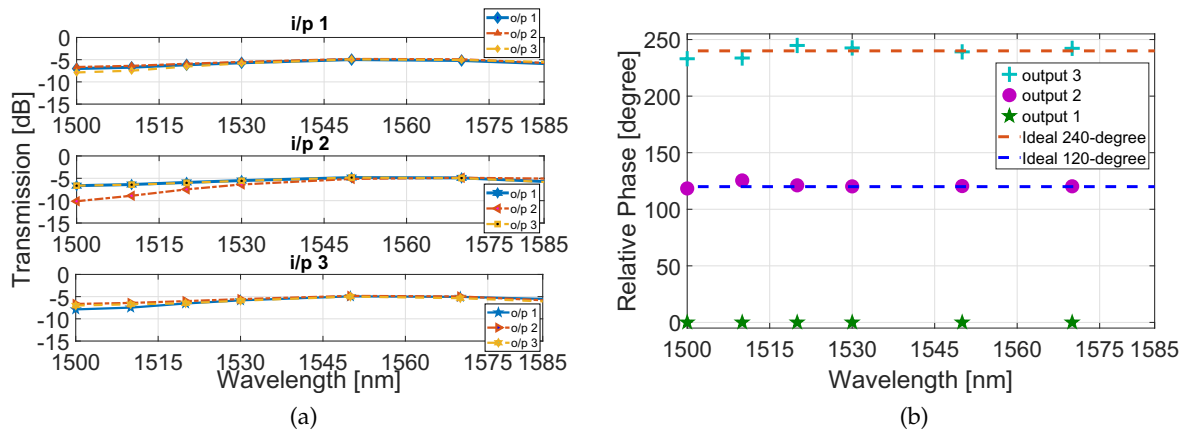


Fig. 3.27 (a) Simulated split ratio of each output ports for light injected at each input ports, and (b) simulated relative phases of the 120° hybrid.

3.4.2 Experimental results and discussion

Electron beam lithography with a single-etch step has been used to fabricate the devices. The channel waveguides have a cross-section of $500 \text{ nm} \times 220 \text{ nm}$ to maintain the single-mode profile. The devices have $2 \mu\text{m}$ buried oxide layer and $2.2 \mu\text{m}$ oxide cladding. Vertical grating couplers were used to couple light into and out of the 3×3 MMI couplers and calibration grating couplers were used to calibrate the ILs of the grating couplers from the device under test.

Fig. 3.28 presents the SEM image of the fabricated 120° optical hybrid with device dimensions.

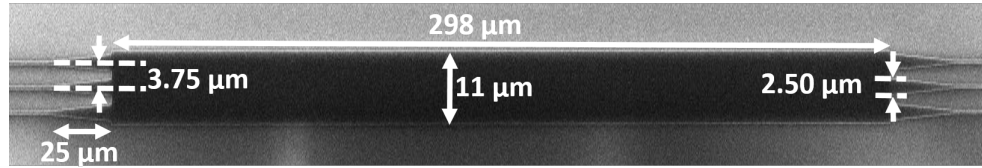


Fig. 3.28 SEM image of the fabricated 120° hybrid.

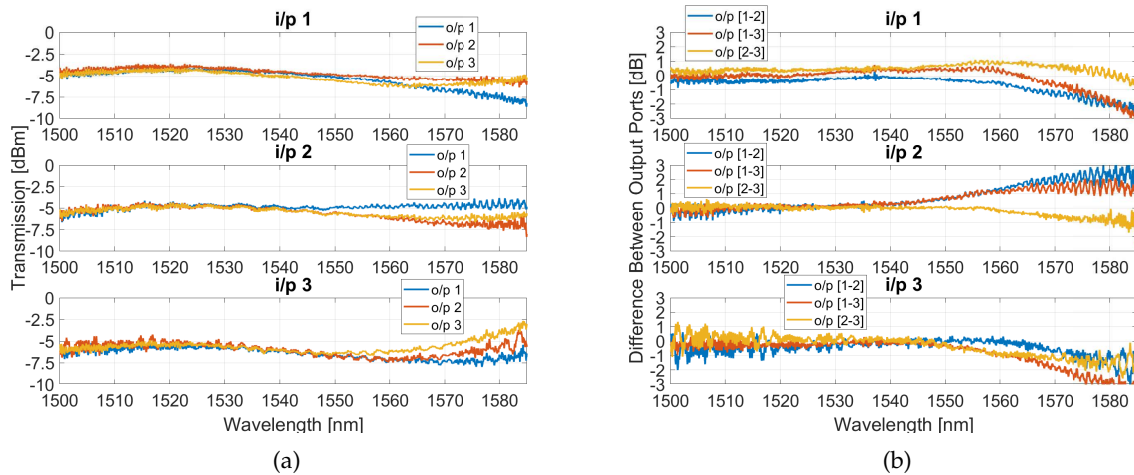


Fig. 3.29 (a) Measured split ratio of each output ports for light injected at each input ports, and (b) difference of split ratio between each output ports [1 & 2, 1 & 3 and 2 & 3].

The measurements have been performed using Yenista TUNICS C-band lasers and CT400 passive optical component tester. To measure the split ratio of the C-band hybrids, the laser was swept from 1500 nm to 1585 nm with a step size of 10 picometer. Polarization maintaining fiber array with a pitch of $127 \mu\text{m}$ was used to test the device. The 3×3 MMI coupler is designed to provide $1/3$ of the input power at each output ports which translates to -4.82 dB . The measured transmission spectra at different output ports for light launched at different input ports are shown in Fig. 3.29(a). Within the 1500 nm to 1560 nm range, the hybrid exhibits $<2.4 \text{ dB}$ of excess loss. The differences among different output ports are shown in Fig. 3.29(b). The deviation in split ratio is $<\pm 1 \text{ dB}$ over 1500 nm to 1555 nm.

The relative phase measurement method is presented in Fig. 3.30(a). Light launched at the input grating coupler is split using a Y-branch. The two output ports of the Y-branch are connected to the two input ports of the 120° hybrids with a path difference of about $250 \mu\text{m}$ to

implement a MZI structure. This results in a MZI behavior at the 3 output ports of the hybrid. The FSR is a distinctive feature of a MZI which is defined by a phase difference of 2π . From this FSR characteristics the relative phases can be calculated using the following relation and considering one of the output ports as reference.

$$\frac{\Delta\phi}{\Delta\lambda} = \frac{2\pi}{FSR} \quad (3.10)$$

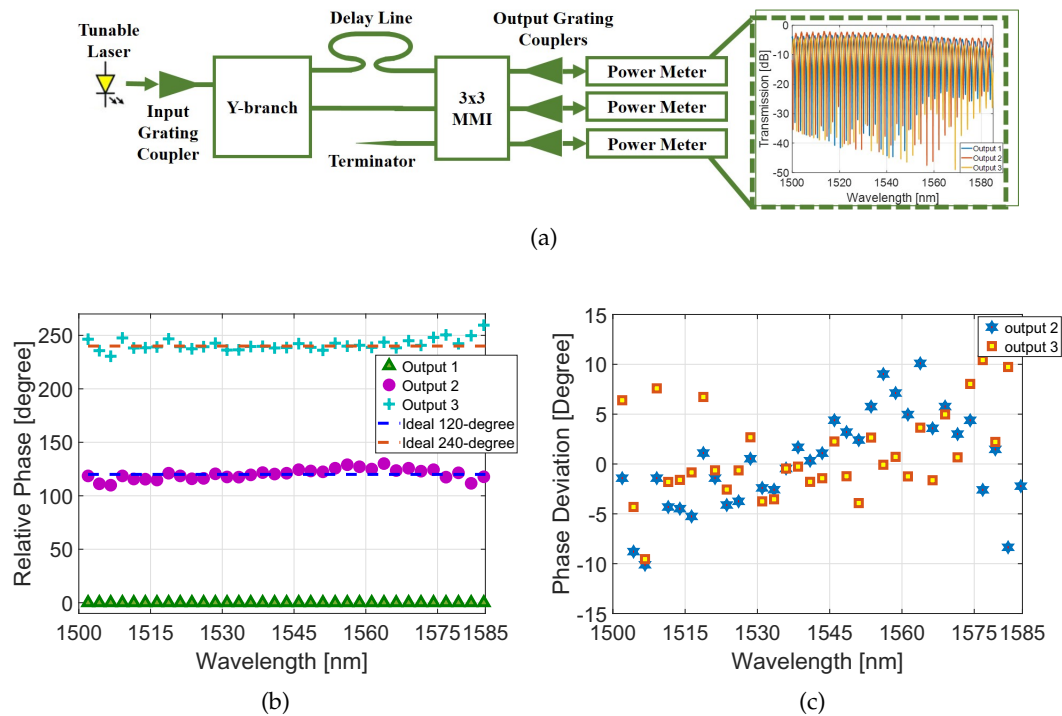


Fig. 3.30 (a) Relative phase measurement method, (b) measured relative phases of the 120° optical hybrid, and (c) deviation of the relative phases from the ideal value of 120° and 240° .

Here, $\Delta\phi$ is the relative phase difference, FSR is the free spectral range of the reference output and $\Delta\lambda$ is the distance of minima for different output ports with respect to the minima of the reference port. The calculated relative phases of the 120° optical hybrid with the variation of the wavelength are shown in Fig. 3.30(b). The two dashed straight lines indicate the ideal 120° and 240° relative phases. Figure 3.30(c) shows the deviation of the relative phases from the ideal values of 120° and 240° . The hybrid demonstrates phase deviations of $\leq 5^\circ$ over 30 nm (1520 nm to 1550 nm) and $\leq 10^\circ$ over 80 nm (1500 nm to 1580 nm) bandwidths, respectively. It has been shown in [156] by means of rigorous numerical simulations that in an amplitude

phase shift keying phase diversity receiver, the phase deviation of the 3 output ports should be less than $\pm 10^\circ$ to have < 1 dB penalty compared to the ideal case.

3.4.3 Conclusions

In conclusion, we present the experimental demonstration of a 120° optical hybrid based on 3×3 MMI in the C-band using 193 nm optical lithography on the SOI platform. The hybrid shows < 2.4 dB of excess loss and $\leq 10^\circ$ phase deviation over 60 nm and 80 nm wavelength range, respectively.

3.5 All-silicon TM-pass polarizer

Silicon photonics has been recognized as a key technology to fabricate compact optical components and systems [95,97,157]. The large difference in refractive index between silicon and its native oxide silica enables high-density integration of photonic components. However, this also makes the SOI platform highly polarization dependant which greatly limits the large-scale application of the SOI based photonic integrated circuits (PICs) [158]. Hence, polarization management is one of the key requirements in silicon photonics in order to avoid performance degradation [158]. Oftentimes, a polarization diversity scheme [159] is used to avoid this issue. Polarization beam splitters [160,161] and rotators [162] are required to implement a polarization diversity scheme which increases the complexity and footprint of the overall PIC. Unless a polarization division multiplexing (PDM) scheme is required, a simple solution will be to use a polarizer which suppresses the undesired mode and passes the desired one.

There are three key features of a polarizer that need to be achieved including a high ER, a low IL and a compact footprint. In the past, researchers have proposed and demonstrated several TE-pass and TM-pass polarizers based on CMOS compatible [71,76,163] and non-CMOS compatible materials [72,164,165]. Since one of the most attractive features of silicon photonics is the compatibility with the CMOS process which enables low-cost mass volume production, it is desirable to design polarizers using CMOS compatible materials and processes. Dai et al. [166] proposed a TE-pass polarizer with 20 dB ER using shallowly-etched SOI ridge optical waveguides with a length of 1 mm which is too long from the integration perspective. SWG based TE- and TM-pass polarizers have also been demonstrated in [167] and [76], respectively, where the grating acts as a Bragg reflector for one mode and as a sub-wavelength waveguide for the other mode. However, SWGs require feature sizes which can not be fabricated using 193 nm DUV lithography. Polarizers using special materials like graphene and vanadium oxide have been demonstrated in [74,168] and [75], respectively. However, fabricating these structures is challenging. Furthermore, the design proposed by [74] has a length of $150 \mu\text{m}$, which is

excessively long and the performance of the vanadium oxide based design depends on the insulator-to-metal phase transitions with a critical temperature of 68°C which increases the energy consumption [75] with respect to passive devices. Due to the ability to manipulate light at dimensions beyond the diffraction limit [169], surface plasmon polariton based devices have received increased attention in the recent years [170]. Several hybrid plasmonic waveguide based polarizers have been demonstrated as well in the past [73, 164, 171] in an attempt to increase the integration density of the PICs. Bai et al. [73] demonstrated a TM-pass polarizer based on hybrid plasmonic grating achieving an ER over 25 dB with a 2.5 μm active length. However, silver was used as the metal which is not CMOS compatible.

Herein, we report a CMOS compatible hybrid plasmonic TM-pass polarizer on the SOI platform with a silicon layer thickness of 340 nm. Although, SOI wafers with 220 nm thick silicon layers are one of the most widely used platforms, it is a suboptimal option for many on-chip components [172]. Peak directionalities of 84% and 71% were obtained for the TE and the TM modes, respectively for grating couplers with silicon layer thicknesses of ~ 350 nm and ~ 330 nm, respectively in [172]. Silicon carrier-depletion modulators based on a 340 nm thick silicon layer have been reported in [173] to achieve better light-carrier overlap by improving the mode confinement. Frequently, a thicker silicon layer is used in hybrid III-V/SOI lasers to achieve better mode coupling [174]. Several polarization beam splitters [175–177], polarizers [73] and multimode interference couplers [178] have been demonstrated as well on 340 nm SOI wafers. Thus, there is a growing interest in developing passive and active devices on the 340 nm thick SOI platform.

In this thesis, we demonstrate a TM-pass polarizer using highly doped silicon waveguide. The main contribution of our work is the use of highly doped silicon instead of metals to form the hybrid plasmonic waveguide. The real part of the complex relative permittivity of the highly doped silicon approaches a negative value and therefore, exhibits metal-like properties. Silver and gold are the two most widely used metals in plasmonics [179]. However, these two metals are not CMOS compatible. Utilizing highly doped silicon instead of metal enables our proposed polarizer to be fabricated using the CMOS process. Furthermore, the fabrication process gets simpler due to our all-silicon approach since no other material such as graphene, vanadium oxide, indium tin oxide or metals needs to be deposited. According to our analysis, the proposed TM-pass polarizer achieves an ER of 30.1 dB and an IL of 3.1 dB with a length of 15 μm near 1550 nm wavelength. The reported polarizer is also highly fabrication tolerant and offers peak ER selection at different wavelengths by choosing different doping concentrations during fabrication.

3.5.1 Theoretical modeling of highly doped silicon and device design

The highly doped silicon is assumed to be doped with boron with a resulting carrier concentration in the range of 10^{20} to 10^{21} cm^{-3} . Active carrier concentration of $1.08 \times 10^{21} \text{ cm}^{-3}$ had been demonstrated experimentally in the past by Linaschke et al. [180]. The empirical relations on the variation of the refractive index of the doped silicon provided by Soref et al. [181] are applicable in the case of low doping concentrations. Nevertheless, the complex relative permittivity of the highly doped p-silicon¹ at telecom wavelengths can be modeled using the Lorentz-Drude model [182],

$$\varepsilon(\omega) = \varepsilon_{\infty} - \frac{\omega_p^2}{\omega^2 (1 + i \frac{1}{\omega\tau})} = \left(\varepsilon_{\infty} - \frac{\omega_p^2 \tau^2}{1 + \omega^2 \tau^2} \right) + i \frac{\omega_p^2 \tau}{\omega (1 + \omega^2 \tau^2)} \quad (3.11)$$

where, ω_p is the plasma frequency, ε_{∞} is the infinite frequency relative permittivity, τ is the electron/hole relaxation time, $\omega = \frac{2\pi c}{\lambda}$ is the angular frequency, c is the speed of light in vacuum and i is the imaginary unit. In the case of the highly doped degenerate intrinsic semiconductors, $\omega_p^2 = \frac{Ne^2}{\varepsilon_0 m_{eff}}$ and $\tau = \frac{\mu m_{eff}}{e}$; where, N is the free carrier concentration, μ is the electron/hole's drift mobility and m_{eff} is the averaged electron/hole effective mass. Usually, the angular frequency $\omega \gg \omega_p$ and $\omega\tau \gg 1$ [183]. Thus, equation 3.11 can be expressed as following,

$$\varepsilon(\omega) = \left(\varepsilon_{\infty} - \frac{\sigma}{\omega^2 \varepsilon_0 \tau} \right) + i \frac{\sigma}{\omega^3 \tau^2 \varepsilon_0} \quad (3.12)$$

where, $\sigma \approx eN\mu$ is the conductivity of the doped silicon and e is the charge of an electron and ε_0 is the free space permittivity. The dielectric-like property of highly doped p-silicon is decreased due to high carrier concentration and the infinite frequency relative permittivity, ε_{∞} approaches 1. The real and the imaginary parts of the complex relative permittivity of the p-silicon as a function of the carrier concentration at 1550 nm wavelength are shown in Fig. 3.31(a). Here, $\mu = 50 \text{ cm}^2 / (\text{V.s})$ and $m_{eff} \approx m_0$, where, m_0 is the mass of the electron [183]. The real part of the permittivity becomes negative when the carrier concentration goes beyond $4.55 \times 10^{20} \text{ cm}^{-3}$. Therefore, p-silicon behaves like a metal after this carrier concentration. The real and the imaginary parts of the permittivity as a function of the wavelength for different carrier concentrations are shown as well in Fig. 3.31(b) and 3.31(c), respectively. A small linear wavelength dependence can be observed.

In hybrid plasmonic based polarizers (both TE- and TM-pass) the metals are used to support the hybrid plasmonic mode and act as absorbers to attenuate the undesired mode [171]. In principal, the metals can absorb both TE and TM modes depending on which mode is coupled

¹It is being called p-silicon due to boron doping (3 valence electrons)

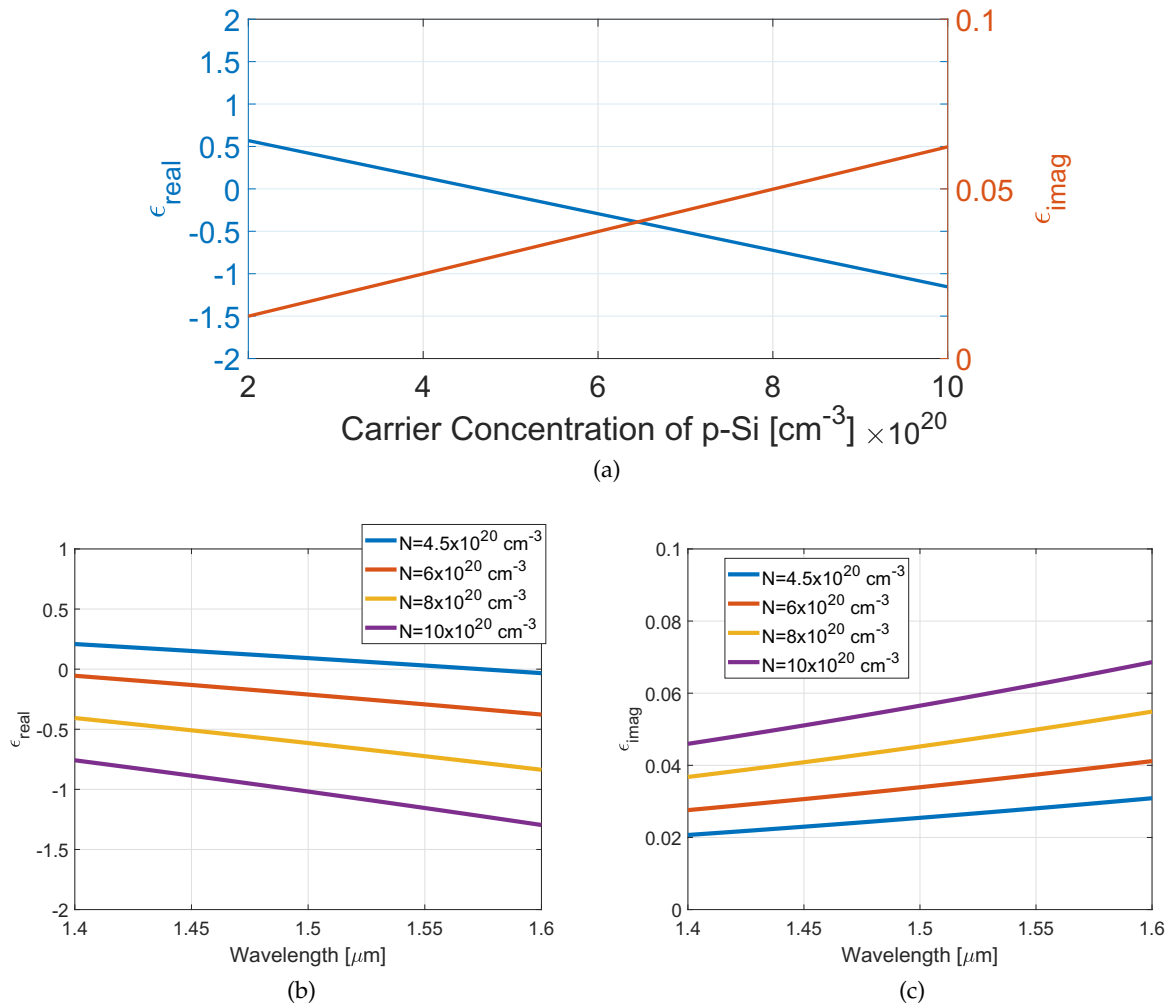


Fig. 3.31 (a) Real and imaginary parts of the complex permittivity of the highly doped p-silicon as a function of the carrier concentrations at $1.55 \mu\text{m}$ wavelength, (b) real, and (c) imaginary parts of the complex permittivity of the highly doped p-silicon as a function of the wavelength for different carrier concentrations.

to the metallic waveguide. The geometry of the waveguides determines which mode is coupled to the metallic waveguide and which mode passes through the dielectric waveguide with minimum interference from the metallic waveguide.

The schematic and the cross-section of the proposed TM-pass polarizer are presented in Fig. 3.32(a) and 3.32(b), respectively. The polarizer consists of a regular silicon waveguide and a highly doped silicon waveguide which behaves like a metal. The upper cladding layer is made of silica. The highly doped p-silicon waveguide is the key part of the device which is placed by the side of the silicon waveguide with a certain gap to suppress the TE mode significantly through absorption and let the TM mode pass with minimum attenuation. The silicon waveguide has a width of W_{Si} and the p-silicon waveguide has a width of W_{p-Si} and a length of L_{p-Si} . As mentioned before, the device is designed for the SOI platform with a silicon layer thickness, $h = 340$ nm. The refractive indices of silicon and silica have been obtained from [184] and for the highly doped p-silicon we utilized the Lorentz-Drude model to obtain the refractive indices as shown in Fig. 3.31.

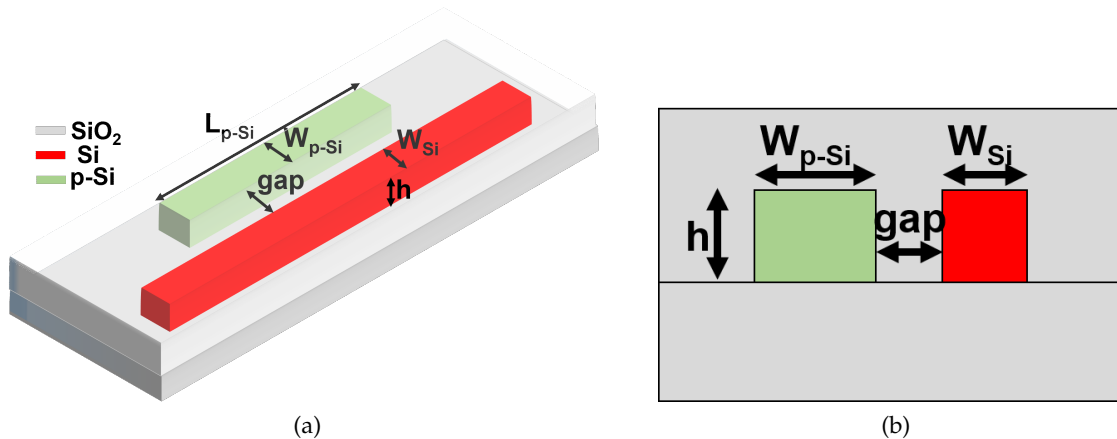


Fig. 3.32 (a) Schematic, and (b) cross-section of the proposed TM-pass polarizer.

3.5.2 Results and discussion

The TM-pass polarizer has been analyzed first by varying the different design parameters such as the carrier concentration, N , the L_{p-Si} , the W_{p-Si} , the W_{Si} and the gap between the two waveguides. All the simulations have been performed using a three-dimensional finite-difference time-domain (FDTD) based solver from Lumerical [185]. The mode source [186] with a Gaussian envelope and a wavelength span of $1.5 \mu\text{m}$ to $1.6 \mu\text{m}$ was pumped in the device.

The effect of changing the carrier concentration of the highly-doped p-silicon on the spectral response of the TM-pass polarizer is presented in Fig. 3.33. It can be observed that the ER peak

exhibits a blue shift as the carrier concentration is increased. As shown earlier in Fig. 3.31, the real and the imaginary parts of the complex relative permittivity changes with the variation of the carrier concentration. The zero-crossing wavelength for the real part of the complex relative permittivity shifts towards smaller wavelengths with the increase of the carrier concentration. Since the absorption of the p-silicon is wavelength dependent and it depends on both the real and the imaginary parts of the complex relative permittivity, the peak changes as the carrier concentration is varied. This enables the selection of the ER peak through the variation of the carrier concentration during fabrication. Our target wavelength of operation for the TM-pass polarizer is the C-band (1.530 μm to 1.565 μm). Thus we chose a carrier concentration for which the ER is maximized in the C-band. For a carrier concentration of $9 \times 10^{20} \text{ cm}^{-3}$, the maximum ER is 37.9 dB which occurs at 1.595 μm wavelength which is far beyond the C-band. Therefore, we chose a carrier concentration of $10 \times 10^{20} \text{ cm}^{-3}$ for which the ER is maximum in the C-band (near 1.545 μm).

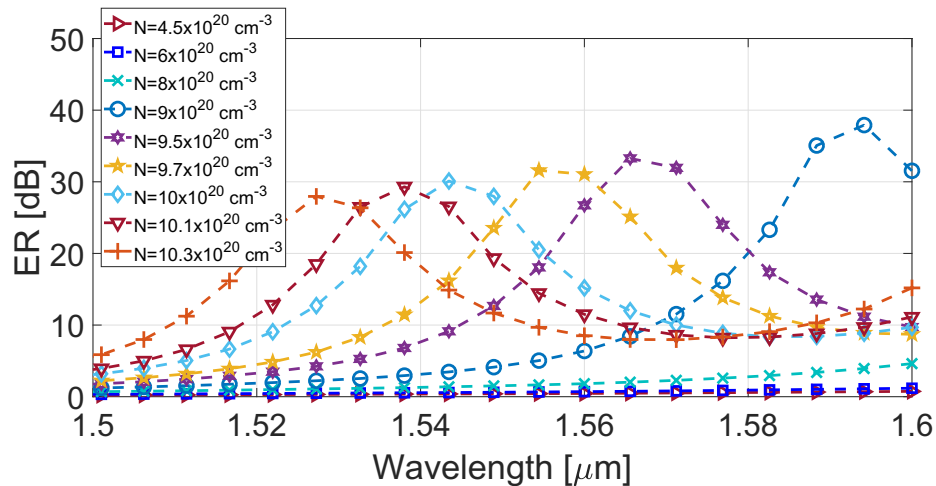


Fig. 3.33 Extinction ratio (defined in equation 3.13) as a function of the wavelength for different carrier concentrations with $L_{p-Si} = 15 \mu\text{m}$, $W_{p-Si} = 600 \text{ nm}$, $W_{Si} = 260 \text{ nm}$ and gap = 200 nm.

The two most important features that a polarizer should have are high ER and low IL and their definitions can be expressed as,

$$ER = 10 \log_{10} \frac{P_{TM}^{output}}{P_{TE}^{output}} \quad (3.13)$$

where, P_{TM}^{output} is the output power of the TM mode at the end of the silicon waveguide and

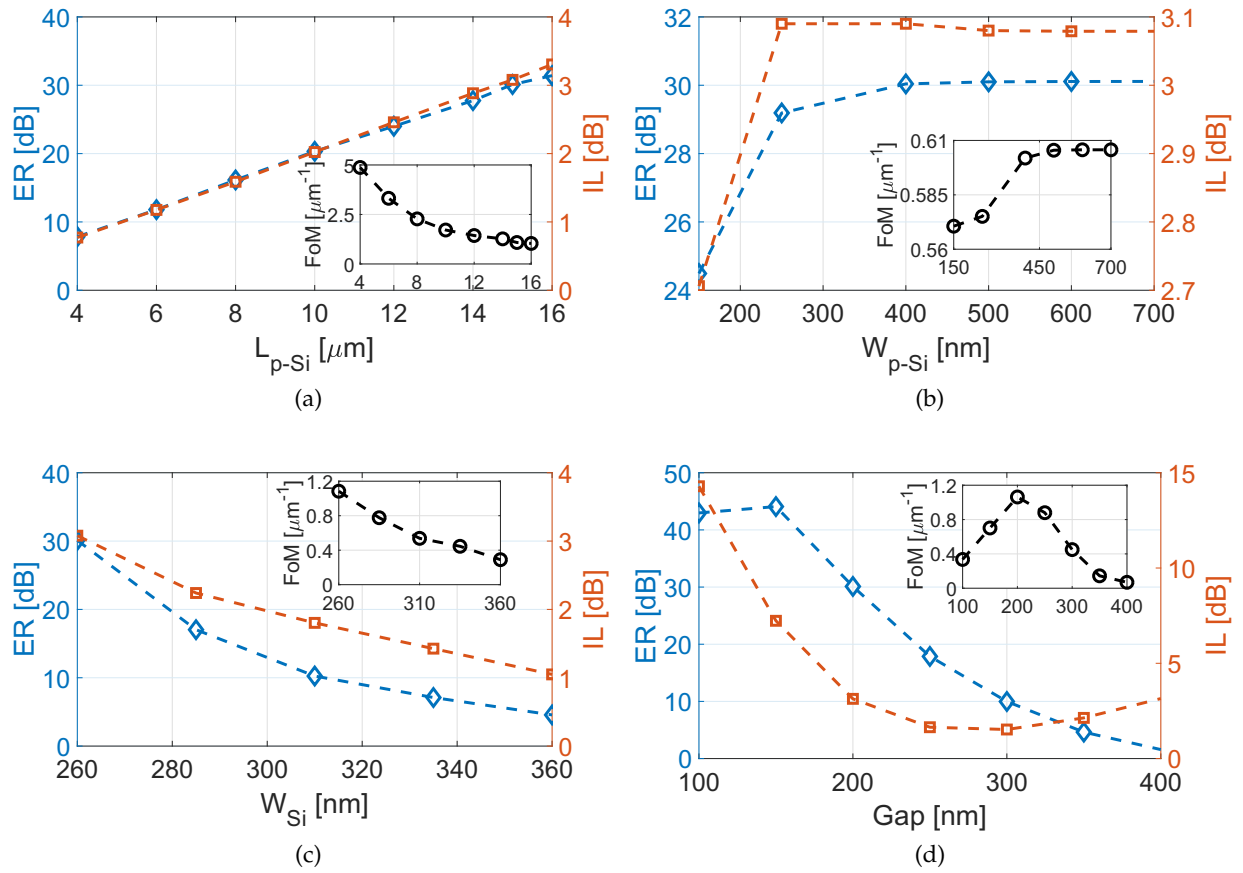


Fig. 3.34 Variation of the ER, IL and figure of merit as functions of (a) the L_{p-Si} for $W_{p-Si} = 600$ nm, $W_{Si} = 260$ nm, gap = 200 nm and $N = 10 \times 10^{20} \text{ cm}^{-3}$, (b) the W_{p-Si} for $L_{p-Si} = 15 \mu\text{m}$, $W_{Si} = 260$ nm, gap = 200 nm and $N = 10 \times 10^{20} \text{ cm}^{-3}$, (c) the W_{Si} for $L_{p-Si} = 15 \mu\text{m}$, $W_{p-Si} = 600$ nm, gap = 200 nm and $N = 10 \times 10^{20} \text{ cm}^{-3}$, and (d) the gap between the waveguides for $L_{p-Si} = 15 \mu\text{m}$, $W_{p-Si} = 600$ nm, $W_{Si} = 260$ nm and $N = 10 \times 10^{20} \text{ cm}^{-3}$. Figure of merits are shown in the inset of each figure.

P_{TE}^{output} is the output power of the TE mode at the end of the silicon waveguide.

$$IL = 10 \log_{10} \frac{P_{TM}^{output}}{P_{TM}^{input}} \quad (3.14)$$

where, P_{TM}^{input} is the power of the TM mode at the input of the silicon waveguide.

The length of the polarizer should be small too to ensure its dense integrability. We have derived a figure of merit (FoM) based on these three metrics to optimize the design parameters of the proposed TM-pass polarizer.

$$FoM = \frac{ER}{IL \times L} \quad (3.15)$$

Figure 3.34(a) presents the variation of the ER and the IL as a function of the L_{p-si} . As we increase the length of the p-silicon waveguide, both the ER and the IL increase. The figure of merit is also presented in the inset of the figure. The design target is to obtain an ER greater than 20 dB [187] which is achieved for $L_{p-si} > 10 \mu\text{m}$. For our device, we choose the $L_{p-si} = 15 \mu\text{m}$ for which an ER of 30.1 dB and an IL of 3.1 dB are observed. Although the figure of merit decreases with the increasing L_{p-si} , it exhibits a saturation tendency at larger values of the L_{p-si} . Since our target is to maximize the ER and minimize the device footprint and the IL, we did not consider L_{p-si} larger than $15 \mu\text{m}$ since the IL and footprint go up if we do so. The effects of changing the W_{p-si} on the ER and the IL of the polarizer are shown in Fig. 3.34(b). The ER and the IL increase with the increasing W_{p-si} . Since our goal is to design a CMOS compatible polarizer, the minimum W_{p-si} is chosen to be 150 nm, which is larger than the minimum feature size of the 193 nm DUV lithography [188]. As we increase the W_{p-si} , the figure of merit increases and saturates around $W_{p-si} = 600 \text{ nm}$. Therefore, we choose the W_{p-si} to be 600 nm.

In [189], a detailed analysis is provided on the modal characteristics of silicon waveguides for different heights and widths in the C-band. It is observed that for a height of 340 nm, the width of the silicon waveguide needs to be between $\sim 260 \text{ nm}$ and $\sim 360 \text{ nm}$ to maintain the single-mode condition for both the TE and the TM modes. Thus, we vary the W_{Si} from 260 nm to 360 nm as shown in Fig. 3.34(c). Both the ER and IL are decreased with increasing W_{Si} and the best figure of merit is obtained for a width of 260 nm. For a thinner waveguide, the TE mode is less confined within the waveguide and hence it gets more attenuated (due to absorption) resulting in a higher ER of the polarizer.

The variations of the ER and the IL as a function of the gap between the p-silicon and the silicon waveguides are presented in Fig. 3.34(d). The gap is varied from 100 nm to 400 nm. The ER and the IL decrease with the increase of the gap; however, the IL start to increase when the

gap increases beyond 300 nm. From the inset figure, it can be observed that the highest figure of merit is obtained for a gap of 200 nm.

The wavelength dependence of the ER and the IL is shown in Fig. 3.35. With $L_{p-Si} = 15 \mu\text{m}$, $W_{p-Si} = 600 \text{ nm}$, $W_{Si} = 260 \text{ nm}$, gap = 200 nm and carrier concentration of $10 \times 10^{20} \text{ cm}^{-3}$, an ER of 30.1 dB and an IL of 3.1 dB have been obtained. The bandwidths over which the TM-pass polarizer maintains 20 dB and 10 dB ERs are 21.05 nm and 48 nm, respectively.

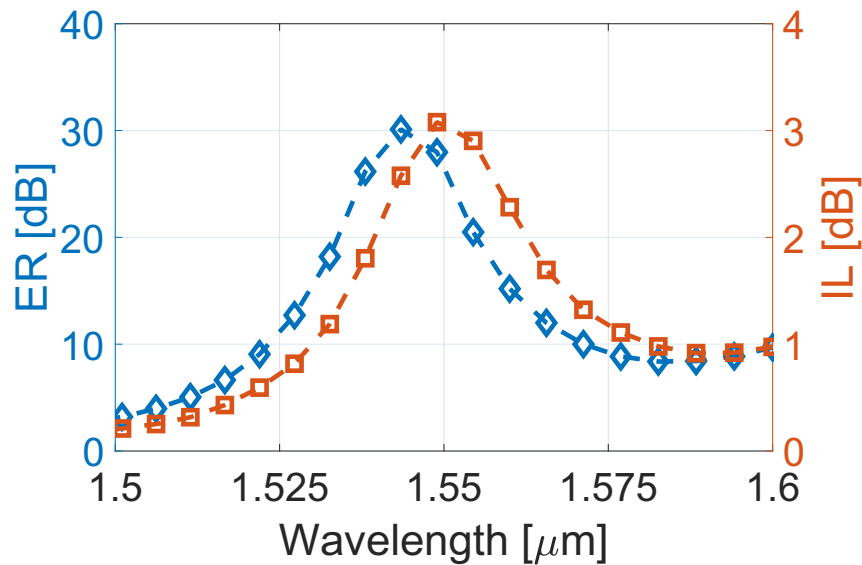


Fig. 3.35 ER and IL as a function of the wavelength of the reported TM-pass polarizer for $L_{p-Si} = 15 \mu\text{m}$, $W_{p-Si} = 600 \text{ nm}$, $W_{Si} = 260 \text{ nm}$, gap = 200 nm and $N = 10 \times 10^{20} \text{ cm}^{-3}$.

The evolution of the TE and the TM modes at different points of the polarizer are shown in Fig. 3.36(a). The amplitudes of the electric field profiles throughout the polarizer are shown as well in Fig. 3.36(b) for both the TE and the TM modes. It can be observed that the TM mode passes through the polarizer with insignificant attenuation while the TE mode is attenuated significantly.

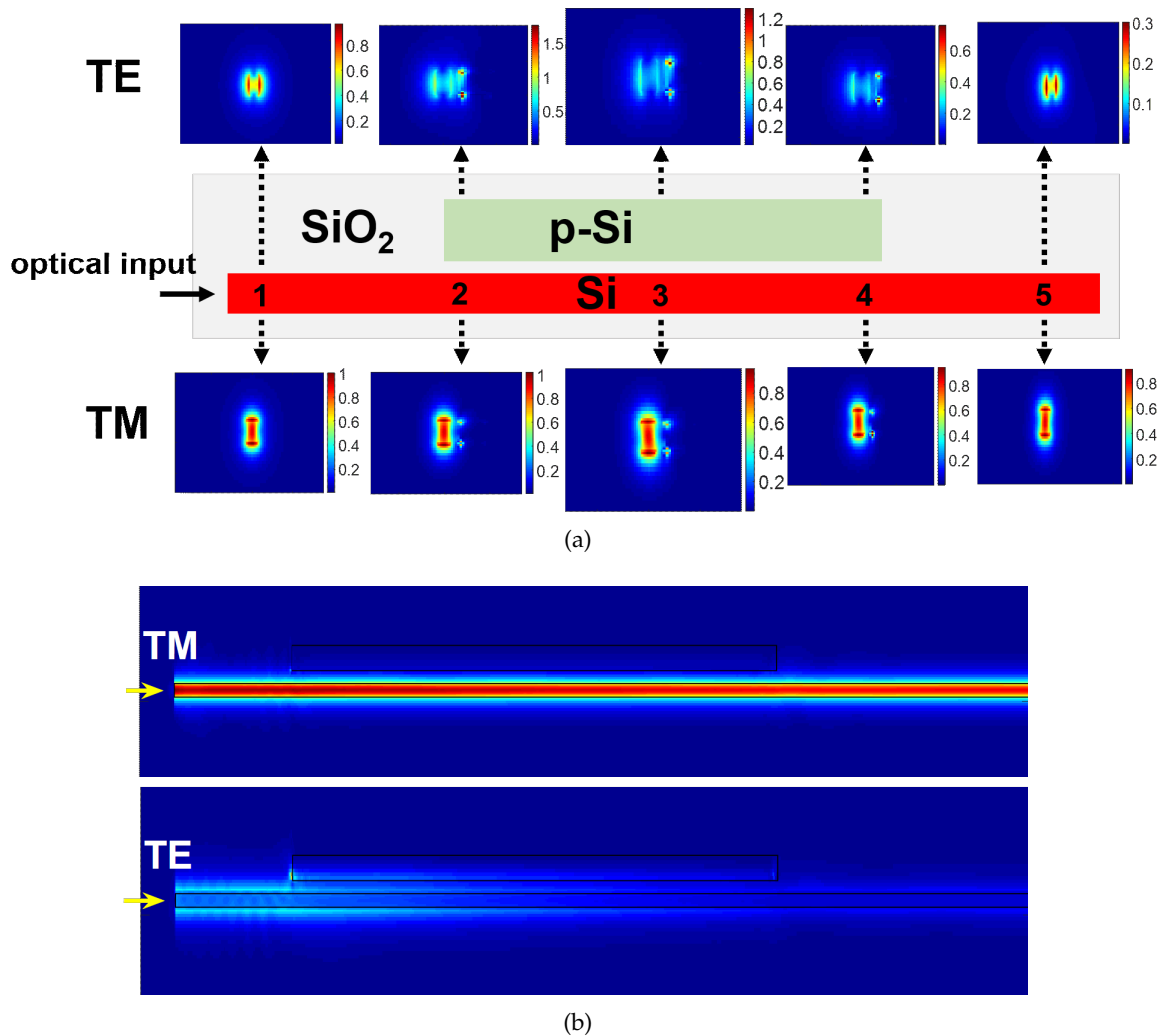


Fig. 3.36 (a) Schematic showing the mode profiles at different points along the TM-pass polarizer, (b) TM and TE mode propagation through the polarizer. (Electric fields are plotted in both the figures.)

3.5.3 Fabrication techniques and tolerance analysis

The proposed TM-pass polarizer can be fabricated on a SOI wafer with a 340 nm thick silicon core. The devices can be patterned using both electron beam and 193 nm DUV lithography processes and the reactive ion etching technique can be used to form the waveguides. Finally, the silicon waveguide can be doped with boron using the ion implantation method and a layer of silica can be deposited over the silicon layer as the cladding. Typically, the multi-project wafer (MPW) runs at IME, Singapore offer 220 nm silicon platform and a doping concentration of about 10^{20} cm^{-3} [190]. Hence, a customized process will be required to fabricate the TM-

pass polarizer. As mentioned in the introduction of this section, there is a growing interest in fabricating devices on the 340 nm platform [73, 175–178]. Furthermore, doping concentration of $1.08 \times 10^{21} \text{ cm}^{-3}$ has been experimentally achieved [180]. Therefore, the proposed TM-pass polarizer can be fabricated without any issue.

The 200 mm SOI wafers used in MPW runs offer a silicon layer thickness non-uniformity with a 3σ of ± 6 nm [191]. However, for 300 mm wafers a non-uniformity with a 3σ of ± 1 nm [192] has been achieved. In 193 nm DUV lithography process, the linewidth uniformity is controlled with a 3σ of ± 8 nm [172, 193], although a size deviation of up to ± 10 nm can be found very often [172]. These variations during the fabrication process causes performance variations of the device. Thus, analyzing the tolerance to the key design parameters of the device is necessary.

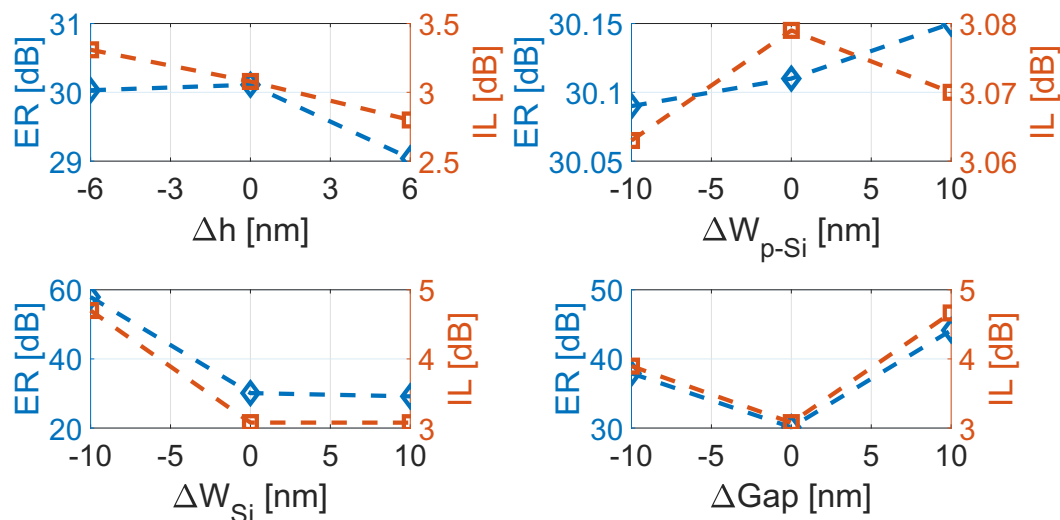


Fig. 3.37 Fabrication tolerance analysis of the proposed TM-pass polarizer .

Figure 3.37 presents the effects of varying the h , the W_{p-Si} , the W_{Si} and the gap between the waveguides on the ER and the IL of the device. We varied the height by ± 6 nm and the other parameters by ± 10 nm in order to analyze the fabrication tolerance of the proposed device. It can be observed from Fig. 3.37 that the ER and the IL are almost constant with the variation of the h and the W_{p-Si} . When the W_{Si} is increased by 10 nm, the ER and the IL are almost constant; however, when the W_{p-Si} is decreased by 10 nm, the ER is increased by 27.8 dB while the IL is increased by 1.62 dB. As mentioned before, for a height of 340 nm, the silicon waveguide will maintain the single-mode condition for both the TE and the TM modes for a width between 260

nm and 360 nm. When the width is less than 260 nm, the waveguide maintains single-mode condition for the TM mode but enters the cut-off regime for the TE mode. In case of the 250 nm width of the silicon waveguide, the waveguide is almost on the edge of cut-off regime and the TE mode is less confined in the silicon waveguide. As a result, the TE mode gets easily absorbed by the p-silicon waveguide. Thus, the sudden jump in ER occurs when we reduce the W_{Si} to 250 nm while IL exhibit insignificant increase in comparison to the ER. It should be noted that such high ER cannot be achieved by only reducing the silicon waveguide width to 250 nm and entering the edge of the cut-off regime. It is the combined effect of both the p-silicon waveguide that absorbs the TE mode and the thinner silicon waveguide that enables the easier absorption. The ERs are increased by 7.8 dB and 14 dB when we change the gap by -10 nm and +10 nm, respectively. The ILs increase as well for both the cases.

Table 3.3 Comparison with other TM-pass polarizers. ER (Extinction Ratio), IL (Insertion Loss), and Ref. (Reference).

Ref. (Year)	ER [dB]	IL [dB]	Footprint	CMOS	Type of work
This work (2018)	30.1	3.1	15 μm	Yes	Simulation
[69] (2016)	34	1	4 μm	Yes	Experimental
[71] (2012)	11.5	Not mentioned	0.1 μm	Yes	Simulation
[72] (2013)	15.2	0.84	3.9 μm	No	Simulation
[73] (2017)	25	0.088	2.5 μm	No	Simulation
[74] (2017)	40	3	150 μm	No	Simulation
[75] (2015)	15	3	1 μm	No	Simulation
[76] (2014)	27	0.5	9 μm	Yes	Experimental
[194] (2014)	45	1	7.5 μm	No	Simulation
[195] (2015)	20	0.15	1.31 μm	Yes	Simulation
[196] (2016)	20	1	2.84 μm	Yes	Simulation
[197] (2018)	24	0.97	12 μm	Yes	Simulation
[198] (2019)	22	0.11	1 μm	Yes	Simulation

Finally in table 3.3, we compare the performance of our reported TM-pass polarizer with the state-of-the-art. The key parameters, such as the ER, IL, footprint and CMOS-compatibility are compared and presented.

The TM-pass polarizer designs reported in [72–75, 194] use non-CMOS compatible materials like silver, graphene and vanadium oxide. On the other hand, the work in [69, 76, 197] utilized sub-wavelength structures which are challenging to fabricate using the 193 nm DUV lithography and are sensitive to fabrication variations. The device proposed in [195] has a buried silicon layer and the one in [196] and [198] require deposition of titanium nitride and aluminum-doped zinc oxide, respectively adjacent to silicon dioxide with no gap in between. Both of these structures pose fabrication challenges.

3.5.4 Conclusions

We present a TM-pass polarizer with an ER of 30.1 dB, an IL of 3.1 dB and a length of 15 μm . The proposed TM-pass polarizer offers better fabrication tolerances by incorporating feature sizes above the minimum required size for the fabrication process. Since the polarizer design is based on the highly-doped silicon waveguide, tunability of the ER can be achieved by varying the carrier concentration during fabrication.

Chapter 4

Simplified coherent receiver using 120° optical hybrid for high speed PONs

In this chapter, we present the 120° optical hybrid based bench-top and integrated solutions for the next generation PON applications. We start by the demonstration of a simplified bench-top coherent receiver using 120° optical hybrid achieving 25 Gb/s PAM-4 transmission over 21 km using 10G transmitter. Then, we demonstrate a fully-integrated 120° optical hybrid based simplified coherent receiver and report 25 Gb/s PAM-2 transmission over 30 km and 25 Gb/s PAM-4 transmission over 21 km without any DSP. Finally, we present performance enhancement of the integrated simplified coherent receiver using a better digital-to-analog converter (DAC) and report 50 Gb/s PAM-4 transmission over 21 km using 31-tap linear feed-forward equalizer (FFE).

4.1 25 Gb/s PAM-4 transmission using 10G transmitter and coherent amplification

Emerging internet applications such as cloud, high definition streaming and the increase in required data rates for 5G radio networks are pushing the need for faster and high spectral efficiency optical access networks. With the increasing deployments of 10G PONs, service providers are looking into the possibility of extending the PON beyond 10G [77]. Full-Service Access Networks (FSAN) started discussion about the smooth evolution of the 10G base XGS-PON and NG-PON2 standards to higher line rate, longer reach and better flexibility in its roadmap and refer to it as XGS-PON+ [199]. The IEEE P802.3ca 50G-EPON Task Force also started to standardize 25/50G PON based on a 25 Gb/s line rate in 2016 [119] with an anticipated timeframe of second quarter of 2020. The market for symmetrical 25G services is mostly driven by 5G fronthaul and backhaul applications while the increasing trend to store contents

on the cloud drives the asymmetrical 10/25G services [120].

Since there are already many PONs deployed, it is expected that the next generation PON will be able to coexist on the same optical distribution network and support similar power budgets and reach requirements of at least the last generation of deployed PON. However, increasing the line rate beyond 10G is challenging with NRZ signals due to the reduction in chromatic dispersion (CD) tolerance and signal-to-noise ratio and requirement of higher bandwidth components. This increases the overall cost of the system. Advanced modulation formats like PAM-4, discrete multi-tone and optical duobinary (ODB) and electrical duobinary (EDB) are being investigated for future PONs [77] to resolve this issue.

Since the access network is very sensitive to cost, it will evolve to 25 Gb/s line rate in the coming years by leveraging the industry ecosystem developing around 25G components for data center applications. However, the photodetectors used in the data center are usually P-type-Intrinsic-N-type (PIN) diodes which indicates that high-speed avalanche photodiode (APD) development will lag significantly [120]. Thus, either the 10G APDs or the high-speed PIN photodetectors have to be used in the near-medium term. But the PIN photodetectors have smaller sensitivity compared to the APDs which makes it difficult to achieve higher power budget. One solution might be using coherent amplification at the receiver [101,200]. The receiver sensitivity can be improved to the theoretical shot noise limit by using the local oscillator (LO) power to amplify the incoming signal [200]. Although coherent detection systems have already been deployed in long-haul, metro and inter-data center networks, due to the power and cost sensitivity of the access segment, simpler coherent detection systems are required. The expensive receiver architecture developed for the long-haul segment cannot be directly implemented in the access networks. To reduce the complexity of the receiver architecture, single-ended detection based optical front-ends with 120° optical hybrids can be utilized [101,200]. While the advantages of using coherent detection in the core network is to be able to achieve higher spectral efficiency and to compensate for distortions like CD, the main attractions for using coherent detection in the access segment are the increased receiver sensitivity and frequency selectivity (for WDM PONs).

In the past, different research groups have demonstrated 25 Gb/s transmission on a single λ using different modulation formats (e.g. NRZ, PAM-4, EDB, ODB) [78–81]. These demonstrations utilized DSP to compensate for impairments like bandwidth limitation and CD, APDs to obtain higher sensitivity and EDFAs to improve the power budget.

In this thesis, we present 25 Gb/s PAM-4 transmission over 28 km of fiber at a BER below the HD-FEC in the C-band using a 3×3 fiber coupler based simplified coherent receiver. Off-the-shelf 10G class EML is used at the transmitter and PIN photodetectors are used at the receiver. Unlike the previous demonstrations, we did not use any DSP (responsible for 70% of

energy consumption in a 100 Gb/s transponder with 40 nm CMOS electronics [201]) both at the transmitter and the receiver, any form of dispersion compensation and EDFA to keep the cost to a minimum. Receiver sensitivities of -18.5, -17 and -13.5 dBm and power budgets of 21, 19.5 and 16 dB are achieved in back-to-back, after 20 and 28 km, respectively which can be increased further by using higher LO power. We also demonstrate polarization independent (PI) operation by slightly modifying the architecture of the simplified coherent receiver. For the PI demonstration of 25 Gb/s PAM-4 transmission, we achieved receiver sensitivities of -17 and -14.5 dBm and power budgets of 19.5 and 17 dB in back-to-back and after 21 km, respectively. Although the receiver architectures and their operating principle have been presented in [92,202], those demonstrations are based on single level signals and at much lower bit rate (maximum 10 Gb/s) than this work. We demonstrate DSP- and dispersion compensation-free 25 Gb/s PAM-4 transmission at BERs below the HD-FEC with 10G transmitters and simplified coherent receivers. This will allow to satisfy the increasing operators demand for supporting new services requiring high bandwidth and low latency (e.g. 25 Gb/s fronthaul services based on CPRI or eCPRI) on the installed optical access infrastructure.

4.1.1 Experimental setup

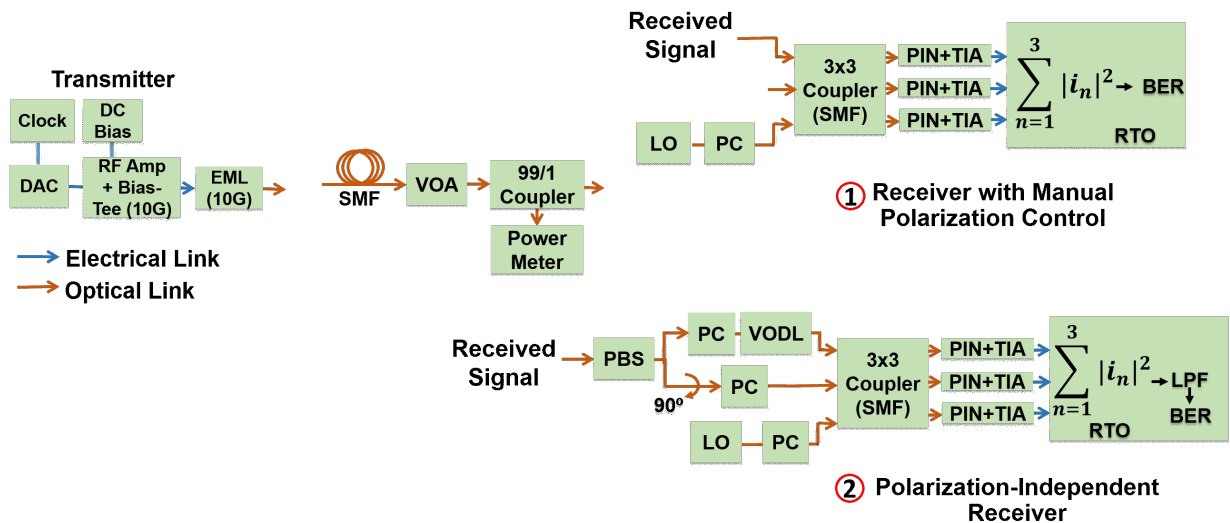


Fig. 4.1 Experimental setup: DAC: digital to analog converter; EML: electroabsorption modulated laser; VOA: variable optical attenuator; VODL: variable optical delay line; SMF: single-mode fiber; PBS: polarization beam splitter; PC: polarization controller; LO: local oscillator; LPF: low-pass filter; TIA: trans-impedance amplifier; BER: bit error rate; RTO: real-time oscilloscope.

The experimental setup is shown in Fig. 4.1. A 6-bit DAC (Micram VEGA DAC II, 17 GHz bandwidth and maximum 34 GSa/s sampling rate) together with an FPGA board is utilized to generate PAM-4 signals with periodic 2^{18} random bit sequences. A sampling rate of 25 GSa/s is used to generate the 12.5 GBaud (25 Gb/s) PAM-4 signal. Since we do not use any pre-compensation, the 6-bit DAC can be replaced by a two-bit DAC realized by two pattern generator channels producing two binary signals with unequal amplitudes that are later combined using RF combiners to generate the PAM-4 signal. After a RF amplifier (Picosecond 5866, 10 GHz bandwidth) and a bias-tee (Picosecond), the electrical signal is applied to modulate a commercial C-band EML (Cyoptics E4560) with 11 GHz 3-dB bandwidth which consists of a distributed feedback (DFB) laser and an electro-absorption modulator. The EML is operated at 1°C temperature and 98.5 mA current. The emission wavelength of the EML is 1547.48 nm at these settings. Figure 4.2 illustrates the measured output power of the EML as a function of the bias voltage. A bias voltage of -1.35 V is found to be optimum for our case and is therefore used throughout the experiment. The modulated signal is then propagated through SMF (0.20 dB/km attenuation and 18 ps/nm/km CD coefficient) of different lengths (31.2 km maximum).

After SMF transmission, the optical signal is first attenuated by a variable optical attenuator (VOA), and then enters into a 99/1 coupler to facilitate the received optical power measurement. It should be noted that no optical amplifier has been used in the experiment. The transmitted signal is then connected to one port of the commercial fused-fiber 3×3 coupler. An ECL is used as the LO which is connected to a second input port of the 3×3 coupler through a polarization controller (PC). The PC is used to manually align the polarization of the LO to that of the received signal. To resolve the issue of manual polarization control, a polarization independent (PI) scheme had been demonstrated in [202] using the 3×3 coupler.

The frequency and phase of the LO and the received signal do not need to be matched perfectly since we are using intensity modulated signal. Thus, the ECL can be replaced by a DFB laser with temperature controller [92]. The three output ports of the 3×3 coupler is connected to three AC-coupled PIN photodetectors with trans-impedance amplifiers (TIAs) (Picometrix, 35 GHz bandwidth).

A real-time oscilloscope (RTO) (Keysight) with 40 GSa/s sampling rate and 16 GHz analog bandwidth is employed to digitize the three received signals. Although the photodetectors have 35 GHz bandwidth, the effective receiver bandwidth is 16 GHz due to the RTO and no signal information is available beyond 16 GHz when we process the data after digitizing. The three digitized signals on the three channels of the RTO are then squared and added to recover the received signal. It should be noted that the processing of the three signals can be done using analog electronic components as shown in [92] provided that the components have enough bandwidth. Finally, the BER is computed by comparing the received bit sequence with the

transmitted ones. We want reiterate here that no DSP is performed offline on the digitized waveforms apart from squaring and summing the three waveforms and BER counting.

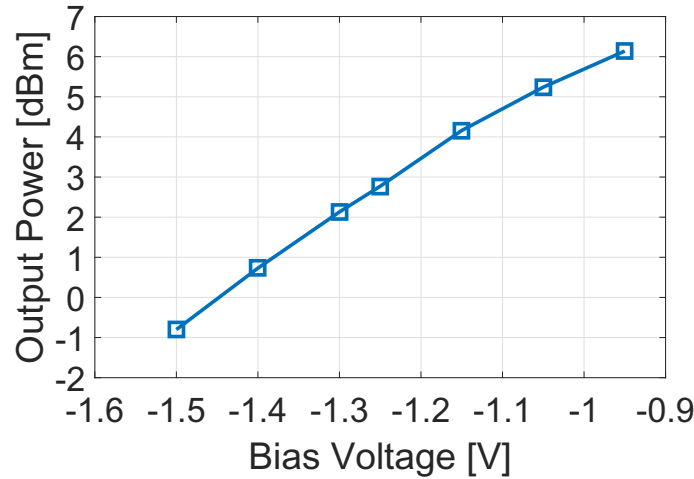


Fig. 4.2 EML output power as a function of the bias voltage.

For the PI demonstration, we used the receiver proposed in [202]. The received signal is split into two orthogonal components using a polarization beam splitter (PBS). After rotating one of the two orthogonal components by 90° , the two output ports of the PBS are connected to the two input ports of the 3×3 coupler. The LO enters the third port of the coupler. Since the 3×3 coupler used in the experiment is not polarization-maintaining (PM), PCs were utilized to make sure that the polarizations on the 3 input ports of the 3×3 coupler are aligned. As demonstrated in [92,101], the PCs will not be necessary if a PM 3×3 coupler is used. A variable optical delay line (VODL) is also used in one of the input ports to equalize the delays between the two input ports of the 3×3 coupler where the received signals are connected. We used an RTO with 80 GSa/s sampling rate and 33 GHz bandwidth for the PI receiver measurements since higher receiver bandwidth is required due to the heterodyne nature of the utilized PI architecture. A low-pass filtering (4th order Bessel filter) step is added after squaring and summing the three digitized signals during offline processing. All other parts and steps are similar to the receiver with manual polarization control.

4.1.2 Results and discussion

4.1.2.1 Receiver with manual polarization control

The receiver architecture used here offers minimum receiver bandwidth like the homodyne receiver and does not have any strict requirement of frequency and phase control of the LO

like the heterodyne receiver. We investigated the tolerance of the receiver to frequency offset between the incoming signal and the LO by measuring the BER in back-to-back at a fixed received power. As can be seen in Fig. 4.3(a), insignificant penalty occurs for a frequency offset of 6 GHz. This offset value is much greater than the emission frequency fluctuations (~ 100 MHz [101]) and the typical frequency deviation during lifetime (~ 2.5 GHz) of common DFB lasers. This characteristic reduces the complexity and cost of practical receiver implementation.

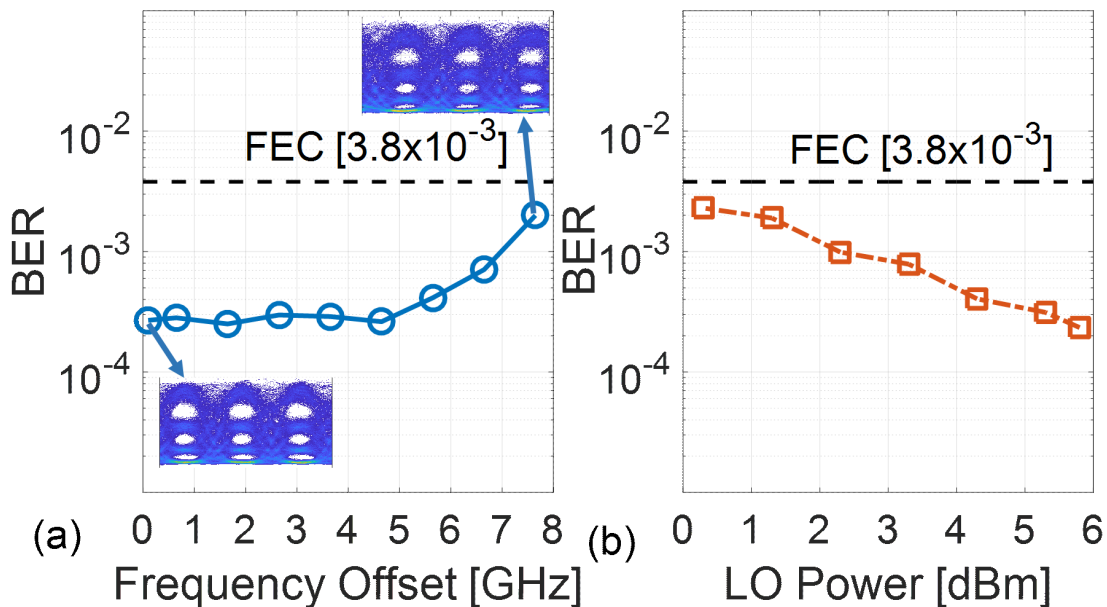


Fig. 4.3 BER as functions of (a) the frequency offset between the incoming signal and the LO, and (b) the LO power.

Figure 4.3(b), presents the BER as a function of the LO power at a fixed received optical power in back-to-back. The BER improves as we increase the LO power. Although the LO we used in the experiment can provide up to 15 dBm of optical power, we could only use up to 5.8 dBm to stay below the overload limit of the photodetector. We anticipate that better BER and receiver sensitivity can be obtained by further increasing the LO power as shown in [203] and [200], where, 10 dBm and 12 dBm of LO power were used, respectively to achieve better BERs.

The BERs as a function of the received optical power for different propagation distances are presented in Fig. 4.4. Receiver sensitivities of -18.5, -17.5, -17, -15.2 and -13.5 dBm are obtained for back-to-back, and after 10.5, 20.7, 25.7 and 27.7 km of fiber propagation. We want to reiterate here that the sensitivities can be further improved by increasing the LO power. Receiver sensitivity of -39 dBm was achieved for 40 km transmission of 10 Gb/s NRZ signal using a similar detection method [101]. Error floors can be observed at higher received optical power in

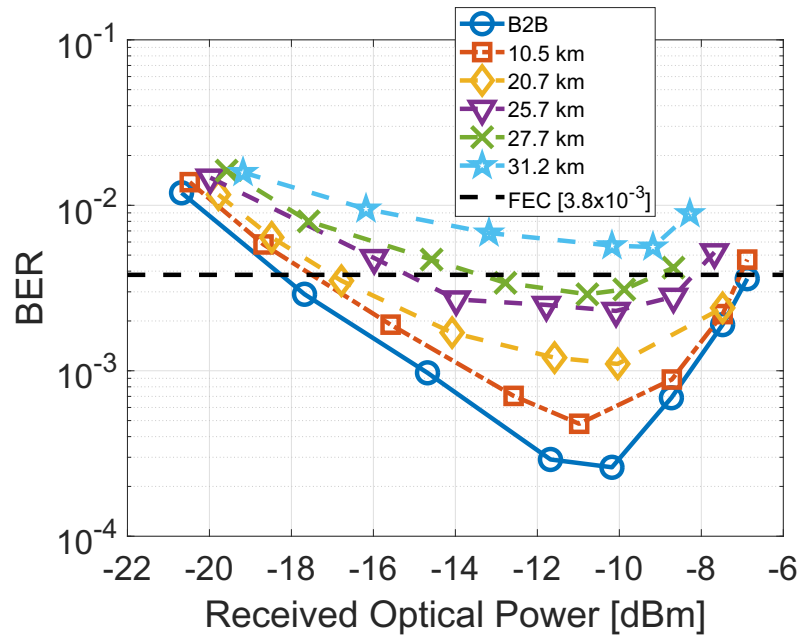


Fig. 4.4 Receiver sensitivity versus BER for different propagation distances for the single polarization receiver.

Fig. 4.4. This happens because the TIAs in the photodetectors start to saturate at higher optical powers distorting the PAM-4 signal. Receiver thermal noise is another reason for the increased BER at higher received power. Another source of sensitivity penalty is the non-ideal behavior of the 3×3 coupler. It has been shown in [156] by means of rigorous numerical simulations that the gain imbalance on the 3 channels should be below 5% and the angle mismatch should be below $\pm 10^\circ$ (which translates to a 20% deviation of the splitting ratio from the ideal value of $1/3$) to have less than 1 dB of penalty from the ideal case. The 3×3 coupler used in the experiment exhibits about 11% of deviation of the splitting ratio from the ideal value of $1/3$ which is higher than the maximum allowable deviation to have smaller penalty. Therefore, we believe that higher receiver sensitivity can be achieved by using a better 3×3 coupler.

Figure 4.5 presents the eye diagrams after different propagation distances. As can be seen, the top level of the eye is noisier than the bottom level which was observed in previous demonstrations as well for NRZ signals [92, 202]. We have deliberately squeezed the bottom eye of the PAM-4 signal by tuning the bias level of the EML to provide enough space for the top eye so that the BER can be reduced. Clear open eye diagrams are observed in back-to-back and after 10 km of propagation where the impact of CD is negligible. As we keep increasing the fiber length, the eyes start to get noisier due to the CD and get almost closed after 31.2 km of propagation. It should be noted that no dispersion compensation has been used either optically

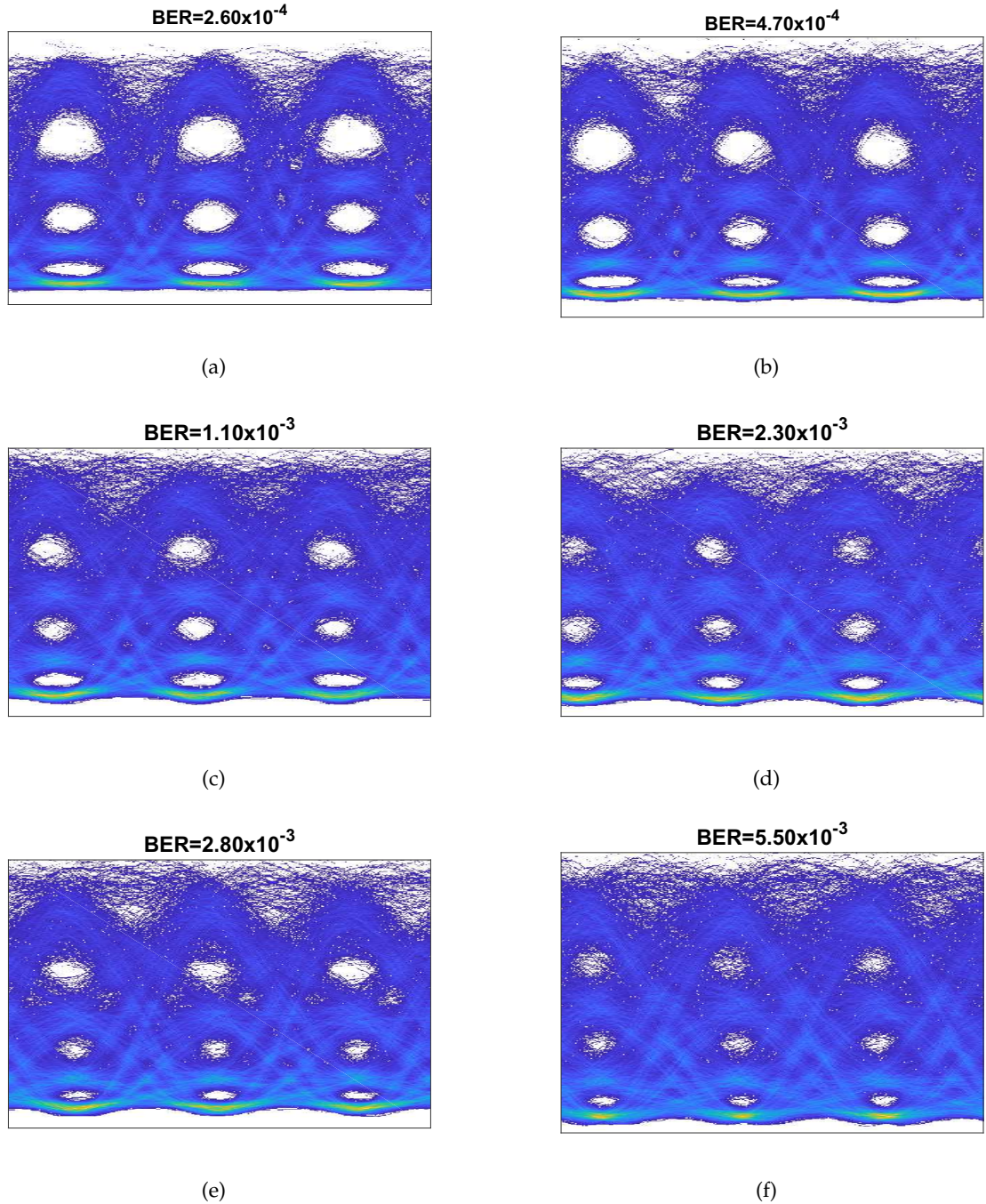


Fig. 4.5 PAM-4 eye diagrams (a) in back-to-back (B2B), (b) after 10.5 km, (c) after 20.7 km, (d) after 25.7 km, (e) after 27.7 km, and (f) after 31.2 km of propagation at 25 Gb/s.

or digitally.

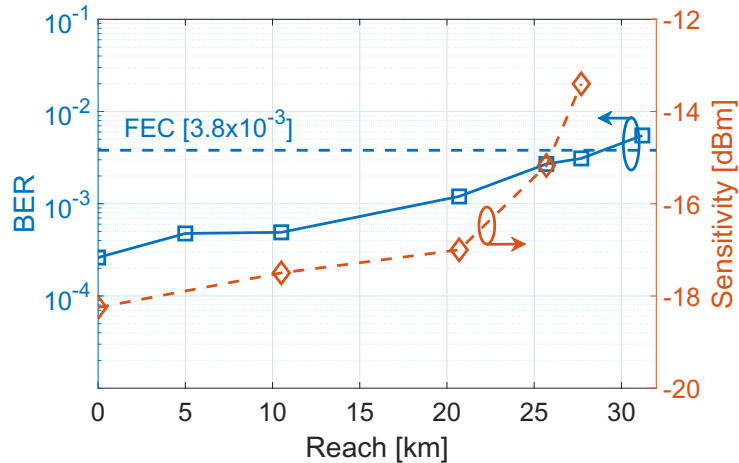


Fig. 4.6 BERs and sensitivities for different reach.

In Fig. 4.6, the BER performance at different reach is presented along with the achieved sensitivities at every distance. As expected, the BER performance degrades with the increased reach and after 29 km of propagation it goes above the HD-FEC level. As mentioned before, we could not use higher LO power due to the overload limit of the photodetectors. Longer reach is anticipated if higher LO power is used.

4.1.2.2 Polarization independent operation

According to the operating principle of the PI receiver shown in [202], after squaring and summing, the received signal becomes,

$$S(t) = \frac{2}{3}R^2E_{LO}^2r^2(t) \left[1 - \left\{ \sin(2\varphi) \times \sin\left(\frac{\pi}{6} - 4\pi\Delta\nu t - \psi\right) \right\} \right] \quad (4.1)$$

where, R is the photodiode responsivity, $\Delta\nu$ is the frequency offset between the incoming signal and the LO, E_{LO}^2 is the power of the LO, $r(t)$ is the modulated signal, ψ is the SOP ellipticity angle and φ is the orientation of the main axis of the polarization ellipse. The first term in $S(t)$ is the correct demodulated signal at the baseband and the second term is the polarization dependent spurious copy centered around $2\Delta\nu$ which needs to be filtered using the low pass filter (LPF). The detail derivation can be found in the appendix.

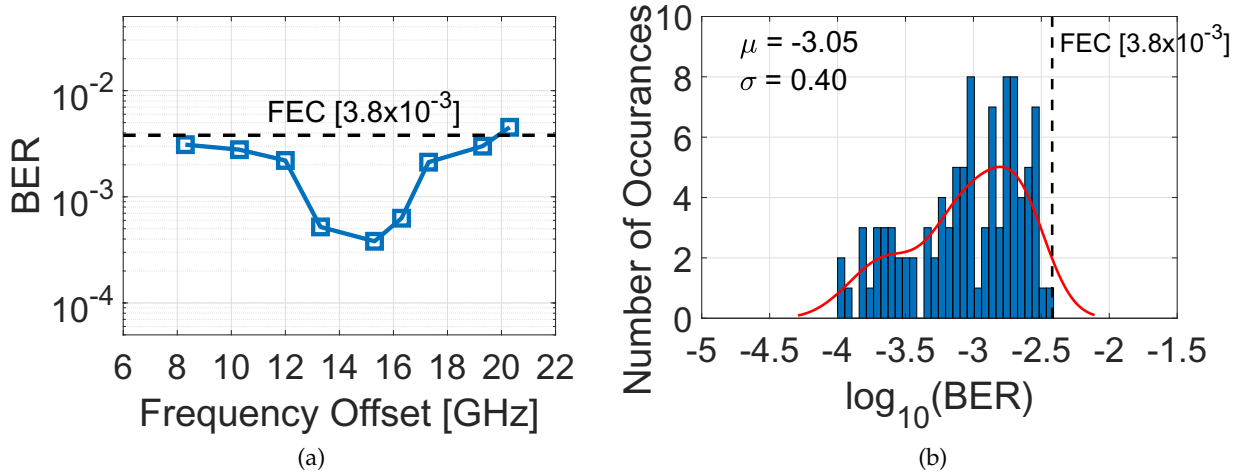


Fig. 4.7 (a) BER as functions of the frequency offset between the incoming signal and the LO, and (b) BER statistics for 100 captures with random SOP.

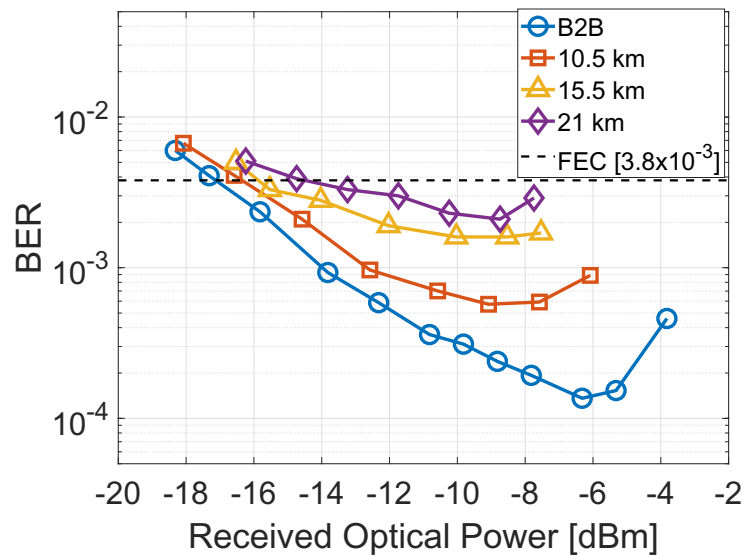


Fig. 4.8 Receiver sensitivity versus BER for different propagation distances for the polarization-independent receiver.

As shown in [92,202], the PI receiver needs to have a frequency offset between the signal and the LO to ensure that the polarization dependent spurious copy does not overlap with the information carrying signal at the baseband. The offset needs to be large enough to move the spurious copy beyond the cut-off of the LPF used during offline processing; however, the PD

and the RTO need to have enough bandwidth to recover the whole heterodyne signal.

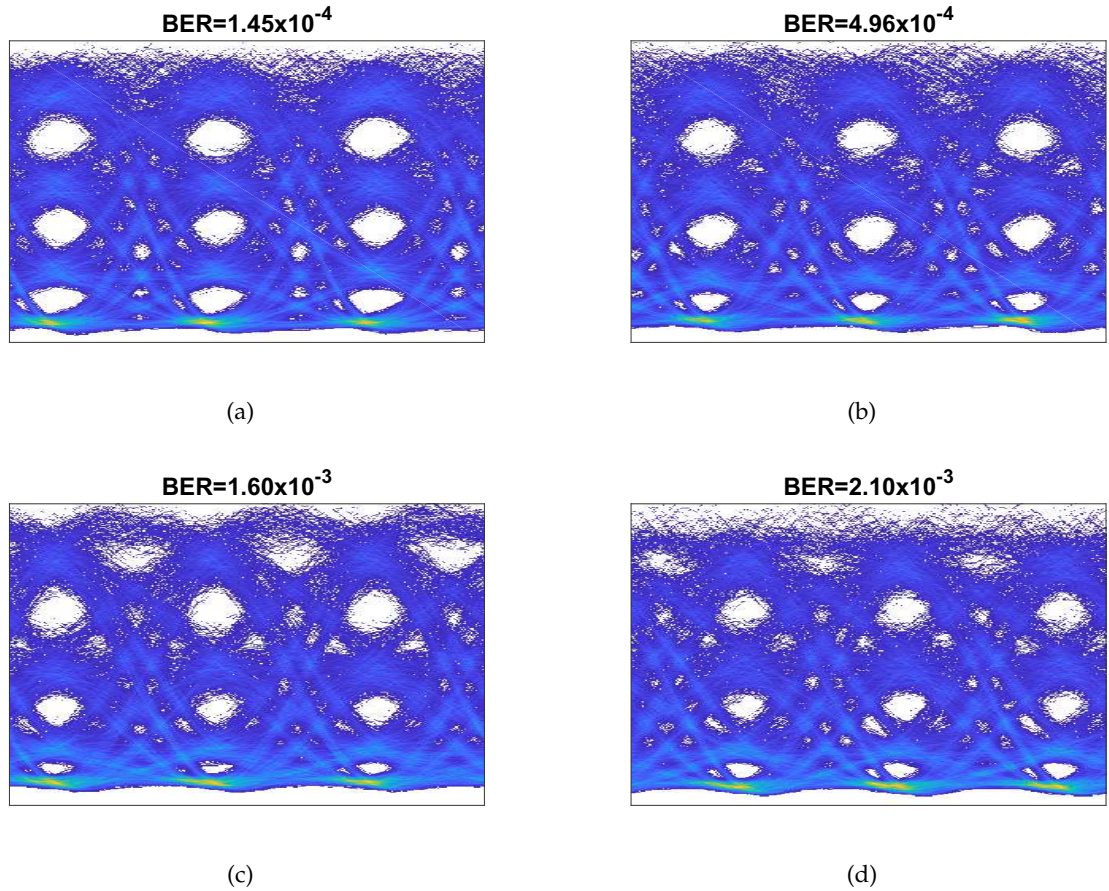


Fig. 4.9 PAM-4 eye diagrams (a) in back-to-back (B2B), (b) after 10.5 km, (c) after 15.5 km, and (d) after 21 km of propagation at 25 Gb/s.

To find the best operating conditions, the performance of the PI receiver is investigated first by varying the frequency offset between the signal and the LO at a fixed received power. It can be seen from Fig. 4.7(a) that the minimum BER occurs between 13 GHz and 16 GHz offset. We then assessed the PI operation of the receiver by randomly varying the state of polarization (SOP) of the received signal using a PC and measuring the BER 100 times in back-to-back. The received power was fixed at -9.8 dBm to obtain a mean $\log_{10}(\text{BER})$ of -3.36 (4.35×10^{-4}) when the SOP was fixed. Figure 4.7(b) presents the statistics of the 100 BER measurements for random SOP. A mean of -3.05 (8.9×10^{-4}) is obtained with a standard deviation of 0.40. This corresponds to a mean power penalty of about 2.34 dB in terms of receiver sensitivity compared to the fixed SOP case.

Finally the PI receiver performance is investigated in terms of BER versus received optical power for different propagation distances which is presented in Fig. 4.8. Receiver sensitivities of -17.1, -16.5, -16 and -14.5 dBm and power budgets of 19.5, 18.6, 18 and 17 dB are obtained in back-to-back and after 10.5, 15.5 and 21 km propagation, respectively. The PI receiver suffers from a sensitivity penalty of about 1.2 dB compared to the manual polarization control case. This can be attributed to the increased IL of the additional components such as, PBS, PC, mating sleeves and the non-ideal ER of the PBS. The eye diagrams after different propagation distances for the PI receiver are shown in Fig. 4.9.

4.1.3 Conclusions

We have reported, 25 Gb/s PAM-4 transmission using commercial 10G-class transmitter, PIN PDs and simplified coherent receiver over 28 km (receiver with manual polarization control) and 20 km (PI receiver) of fiber. Any form of DSP (e.g. pre-emphasis, equalization, pulse shaping etc.), optical amplification and dispersion compensation (e.g. optical or digital) were not applied throughout the whole system. In addition, no frequency or phase control of the LO is required due to the use of intensity modulated signal. For the polarization sensitive receiver, a sensitivity of -17 dBm is achieved after 21 km of propagation with BER below the HD-FEC. Furthermore, it has been shown that 29 km of propagation at 25 Gb/s can be obtained with BER below the HD-FEC. Finally, for the PI operation receiver sensitivity of -14.5 dBm is obtained after 21 km of propagation.

4.2 Demonstration of a 120° hybrid based integrated coherent receiver

As articulated in the previous section, 120° hybrid based optical front-ends with single-ended detection can be used to reduce the complexity of the traditional coherent receiver to suit the requirements of the access networks [200,202]. Coherent detection provides increased receiver sensitivity and frequency selectivity (allowing to get rid of tunable optical filters) in the access networks. As described in the last section, several groups have demonstrated 25 Gb/s and higher bit rate signal transmission in the C- and O-bands using different modulation formats (e.g., PAM-2, PAM-4, EDB, and ODB) based on bulk optics [78,79,81,204–206]. Integrated coherent receivers with conventional 90° hybrid based architectures achieving bit rate of 224 Gb/s using PDM-16-QAM [83] in the C-band and 200 Gb/s using 16-QAM over O, E, S, C and L bands [84] have been reported on the SOI platform. However, there has been no demonstration of an integrated coherent receiver with simplified architecture for access network applications. Integrated solutions are preferred since they offer a reduction in size, cost, and power consumption compared to bulk optics solutions [207]. In particular, the SOI platform has garnered

much attention recently to build high performance, compact, and high yield components and systems [208] due to its high index contrast and CMOS compatibility.

In this thesis, we present an integrated simplified coherent receiver on the SOI platform for C-band operation consisting of an edge coupler, a vertical grating coupler, a PSR, a 3×3 MMI coupler based 120° hybrid and three germanium photodetectors. The bulk optics based PI receiver architecture and operating principle was demonstrated in [92, 202] with a maximum bit rate of 10 Gb/s. Herein, we report the first demonstration of DSP- and dispersion compensation-free 25 Gb/s PAM-2 transmission over 30 km SMF in the C-band using the simplified integrated coherent receiver. We also demonstrate 25 Gb/s PAM-4 transmission over 21 km below the HD-FEC.

The rest of the section is organized as follows. In subsection 4.2.1, the design and fabrication of the components and the circuit of the integrated receiver are described. Transmission experiments using the integrated coherent receiver are presented in subsection 4.2.2. The concluding remarks are provided in subsection 4.2.3.

4.2.1 Device design and fabrication

The receiver has been fabricated in a MPW run at IME A*STAR (currently Advanced Micro Foundry Pte Ltd, Singapore) on a SOI wafer with a 220 nm thick top silicon layer and a $2\ \mu\text{m}$ thick buried oxide layer using 193 nm DUV lithography.

The schematic and layout of the integrated coherent receiver, photograph of the fabricated circuit with couplers and probes are shown in Fig. 4.10. The incoming signal is coupled to the chip using the edge coupler. The received signal is then split and rotated to TE polarization using the PSR [209]. The two output ports of the PSR are connected to the two input ports of the 3×3 MMI coupler [99]. These two paths were carefully designed to have equal lengths to ensure that the two signals after splitting reach the MMI at the same time. A grating coupler is used to couple the LO with TE polarization which is then connected to the third input port of the 3×3 MMI. Finally, the three output ports of the 3×3 MMI are connected to three germanium photodetectors [210]. It should be noted that no TIA has been used.

The PSR used in the receiver is $490\ \mu\text{m}$ long and has <-12 dB of polarization crosstalk at 1530 nm [209]. The PDs have a responsivity of about 0.75 A/W and a dark current of $6.5\ \mu\text{A}$ at 2 V reverse bias voltage [210]. Figures 4.11(a) and 4.11(b) show the eye diagram of 25 Gb/s PAM-2 signal right after the modulator and after detection using the integrated germanium PD, respectively. The 3×3 MMI based 120° hybrid was designed for TE polarization and has a length and width of $298\ \mu\text{m}$ and $11\ \mu\text{m}$, respectively [99]. The detail simulation and experimental results of the 3×3 MMI are presented in section 3.4 of the previous chapter. Figures 4.12(a)

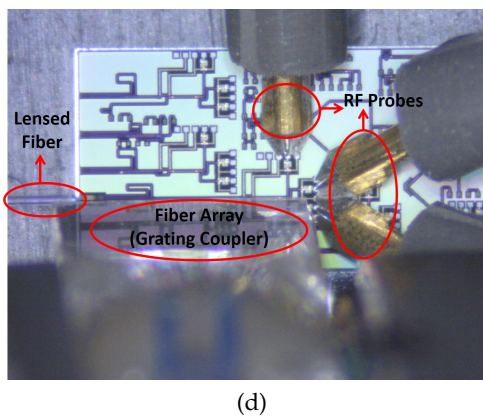
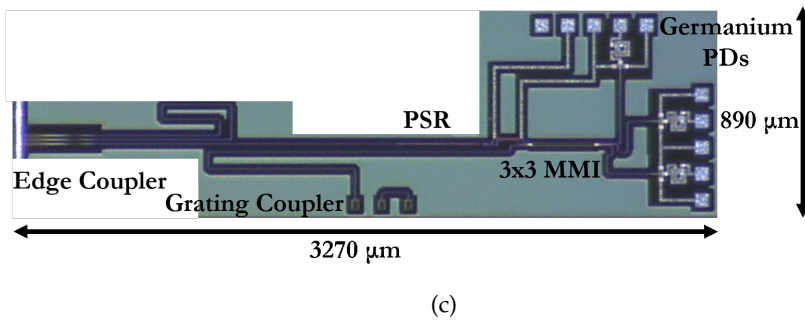
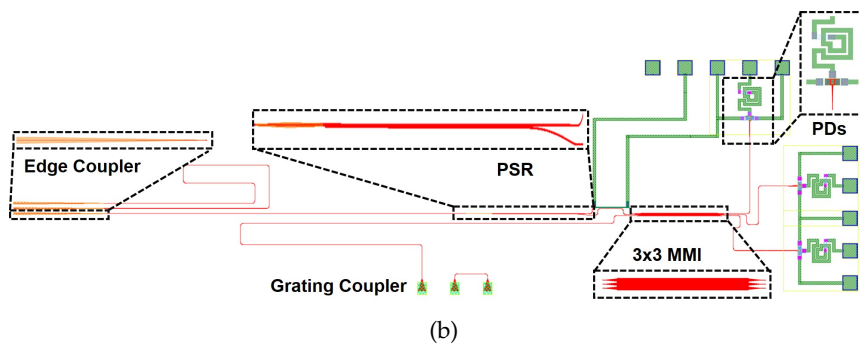
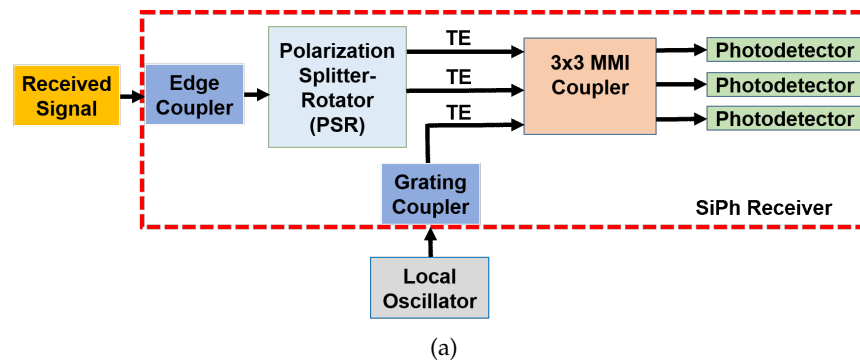


Fig. 4.10 (a) Schematic of the coherent receiver, (b) layout of the coherent receiver, (c) a photograph of the fabricated receiver, and (d) receiver with couplers and probes connected. PSR: Polarization splitter and rotator, PD: Photodetector, MMI: Multimode interference coupler.

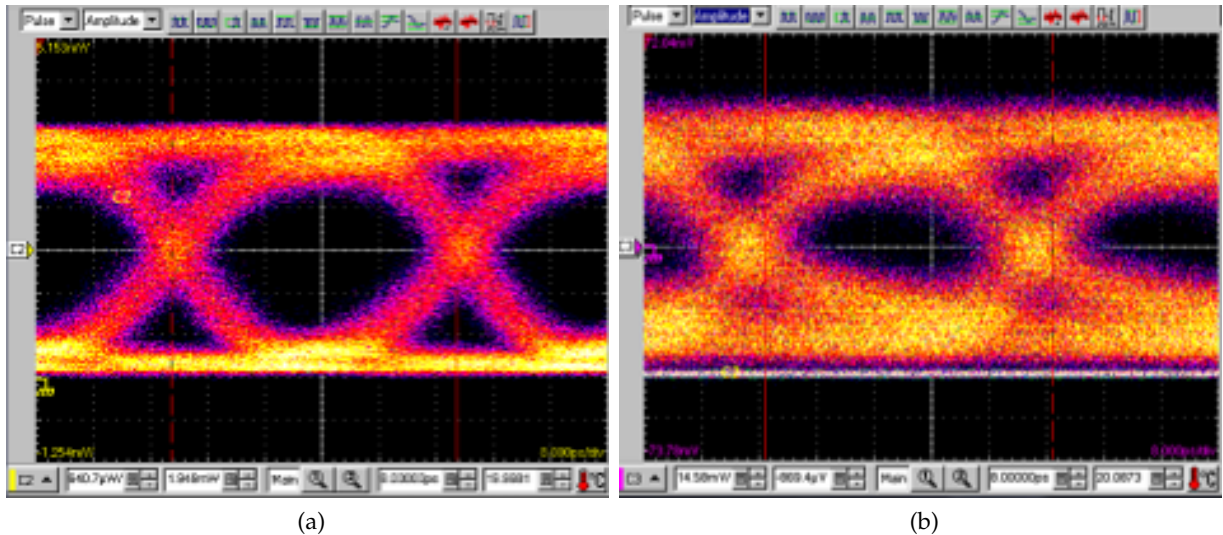


Fig. 4.11 25 Gb/s PAM-2 (a) optical eye right after the modulator, and (b) electrical eye after detection using the integrated germanium PD.

and 4.12(b) show the split ratio of the three output ports of the hybrid for light injected at each input port and relative phases of the three output ports of the 120° hybrid, respectively. The hybrid demonstrates measured excess loss of <2.4 dB over 60 nm (1500 nm - 1560 nm) and the deviations in split ratio among the three output ports are $<\pm 1$ dB over 1500 nm to 1555 nm wavelength range. Phase deviations of $\leq 5^\circ$ over 30 nm (1520 nm to 1550 nm) and $\leq 10^\circ$ over 80 nm (1500 nm to 1580 nm) bandwidths are also achieved.

4.2.2 Transmission experiments

4.2.2.1 Experimental setup

The experimental setup is shown in Fig. 4.13. A 6-bit DAC (Micram VEGA DAC II, with a 17 GHz analog bandwidth and maximum sampling rate of 34 GSa/s) is used to generate PAM-2 and PAM-4 signals with periodic 2^{18} random bit sequences. A sampling rate of 25 GSa/s is used to generate the 25 Gb/s PAM-2 and 25 Gb/s (12.5 Gbaud) PAM-4 signals. Since no pre-compensation has been used, the 6-bit DAC can be replaced by a pattern generator for the PAM-2 case and two binary pattern generators and a 2-bit DAC for the PAM-4 case. After a RF amplifier (SHF 810), the electrical signal is applied to modulate a commercial C-band lithium niobate Mach-Zehnder modulator (Avanex SD40) with a 30 GHz 3-dB bandwidth. The modulator is biased at the quadrature point and an external cavity laser (ECL) emitting CW light at 1530 nm wavelength is used as the light source. The modulated signal is then propagated

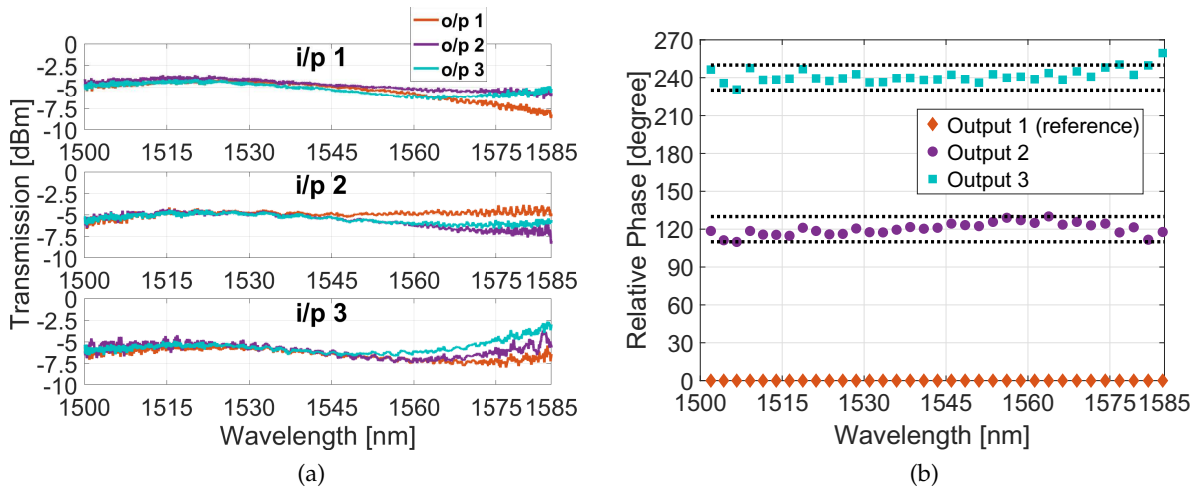


Fig. 4.12 (a) Measured split ratio of each output ports for light injected at each input ports, and (b) measured relative phases of the 120° hybrid considering output port 1 as the reference [black dashed lines represent $\pm 10^\circ$ deviation].

through standard SMF of different lengths. After SMF transmission, the optical signal is first amplified using an EDFA, then attenuated by a VOA to sweep the received optical power followed by a PC. The EDFA has been used to compensate for the high coupling loss (around 10 dB) of the edge coupler due to a sub-optimal design and coupling setup. By replacing the current edge coupler with designs having very low coupling loss [211] (around 0.5 dB) and modifying the setup to achieve better coupling, we can get rid of the EDFA. Finally, the signal is coupled to the chip using a lensed fiber. Another ECL is used as the LO which is coupled to the chip using a fiber array. Since the frequency and phase of the LO do not need to be aligned perfectly, a DFB laser can be used instead of the ECL. The RF signals from the three integrated germanium PDs are collected using three RF probes. The PDs are also biased using the RF probes with reverse bias voltage of 2 V. Three bias-tees are used for the purpose of biasing the PDs and collecting the RF signals from the PDs. The RF end of the bias-tees are connected to three channels of a RTO with 80 GSa/s sampling rate and 33 GHz analog bandwidth. The bias-tees also serve as DC-blocks since no DC goes through the RF end when we capture the signals using the RTO.

An offset of about 75% to 80% of the baud rate need to be maintained between the incoming signal and the LO to move the polarization dependent spurious copy away from the information carrying signal at the baseband. As a consequence, the signals at the three output ports of the 120° hybrid are intra/heterodyne in nature which require the PDs and the RTO to have enough bandwidth to recover the whole intra/heterodyne signal. The PDs used in the inte-

grated coherent receiver are rated for 60 GHz bandwidth [210] but the RTO has only 33 GHz bandwidth. Thus, the effective receiver bandwidth is 33 GHz since no information beyond this frequency is available after digitizing the three signals. To recover the transmitted signal, the three digitized signals are squared, added, and then low-pass filtered (4th order Bessel filter). Finally, the bit-error-rate (BER) is calculated by comparing the received and the transmitted bit sequences.

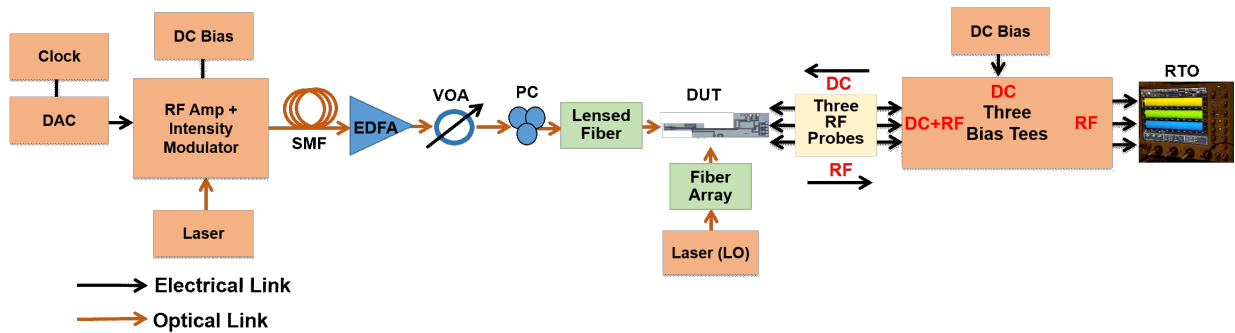


Fig. 4.13 Experimental setup. DAC: digital-to-analog converter, SMF: single-mode fiber, EDFA: erbium doped fiber amplifier, VOA: variable optical attenuator, PC: polarization controller, DUT: device under test, LO: local oscillator, RTO: real-time oscilloscope.

4.2.2.2 25 Gb/s PAM-2 transmission

As mentioned above, the PI operation of the receiver requires about $(0.75 \text{ to } 0.8 \times \text{baud rate})$ of frequency offset between the incoming signal and the LO. To find the optimum offset that results in the best BER, the receiver performance by varying the frequency offset is first investigated. From Fig. 4.14(a), it can be seen that the minimum BER is found around 10.50 GHz offset (only 42% of the baud rate). Although this offset is not 75% of the baud rate, we cannot go further due to the bandwidth limit of the RTO. When we increase the offset, the received signal becomes a passband signal after beating with the LO in the 120° hybrid and the required receiver bandwidth is increased to $BW_{req} = B + \Delta\nu$ (where, BW_{req} is the required bandwidth and B is the signal baud rate) to recover the signal fully. In our case, the baud rate is 25 Gbaud while the RTO bandwidth is 33 GHz. Thus, if we increase the offset by 10.50 GHz, the required bandwidth becomes about 35.50 GHz. Therefore, after digitizing the signal using the RTO, the whole passband signal cannot be obtained and consequently the baseband signal cannot be recovered properly after squaring, summing, and low-pass filtering. Hence, the BER increases as we increase the offset. We anticipate that the BER can be reduced further by increasing the fre-

quency offset if a higher bandwidth RTO is used. The system will be less sensitive to frequency drift as well since the signal can be recovered fully even with higher frequency offset.

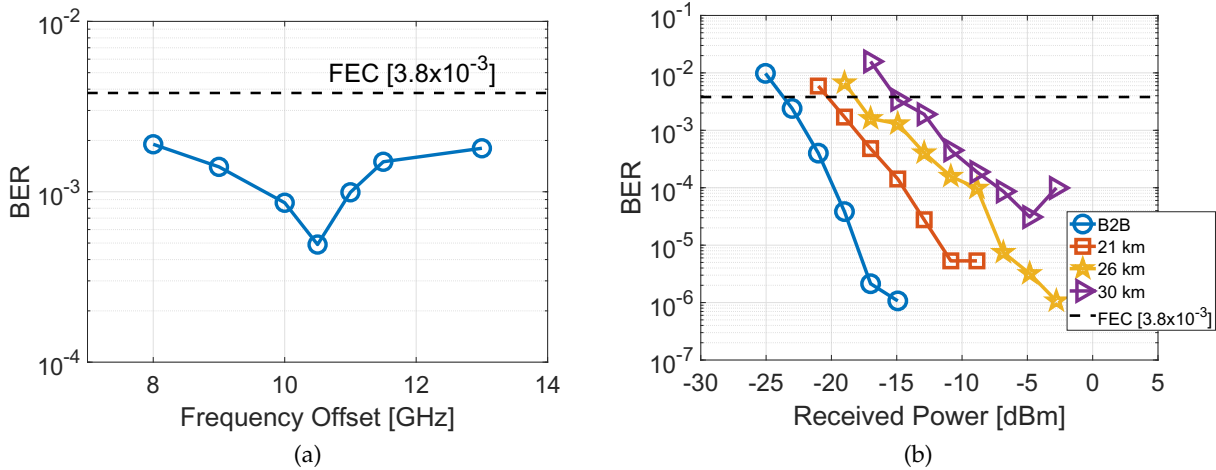


Fig. 4.14 (a) BER as functions of the frequency offset between the incoming signal and the LO, and (b) received optical power versus BER for different propagation distances for 25 Gb/s PAM-2 (after subtraction of the losses from the edge coupler).

The BERs as a function of the received power (edge coupler loss has been subtracted which is around 10 dB) for propagation over different lengths of fiber are presented in Fig. 4.14(b). It can be observed that the receiver sensitivities are -23.7, -20.3, -18.2, and -15.1 dBm below the HD-FEC threshold in back-to-back, after 21, 26, and 30 km, respectively. The LO power going into the chip is fixed at 8 dBm (excluding the grating coupler loss) for these measurements. The germanium layer gets saturated at higher received power and cannot absorb more photons to generate photocurrent. As a result, error floor occurs at higher received power. We also suspect receiver thermal noise to be another reason for the increased BER at higher received power. The eye diagrams in back-to-back and after different propagation distances are provided in Fig. 4.15. Clear open eye diagrams can be observed in back-to-back. The eyes start to get closed as we propagate over longer spans of fiber due to the impact of CD. We want to reiterate here that no dispersion compensation has been used either optically or digitally.

Finally, the performance of the receiver is assessed for PI operation. We capture the signals after the integrated PDs 50 times when the SOP is fixed and another 50 times by randomly varying the SOP of the received signal using a PC in back-to-back configuration. The received optical power is kept fixed at -21 dBm while capturing the signals using the RTO. Figures 4.16(a) and 4.16(b) present the statistics of the 50 BER measurements for the fixed and the random SOP cases, respectively. A mean $\log_{10}(\text{BER})$ of -3.5529 (2.80×10^{-4}) and standard deviation of

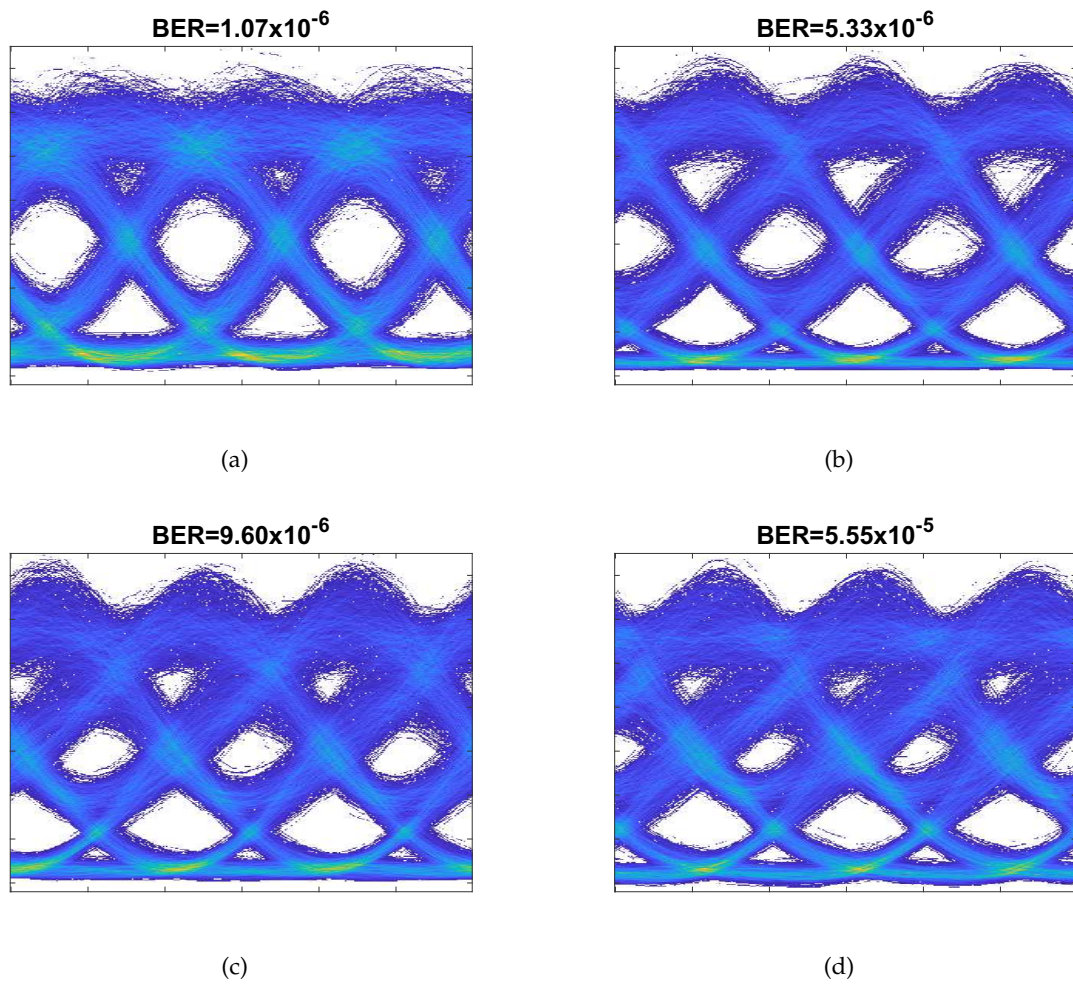


Fig. 4.15 PAM-2 eye diagrams (a) in back-to-back (B2B), (b) after 21 km, (c) after 26 km, and (d) after 30 km of propagation at 25 Gb/s.

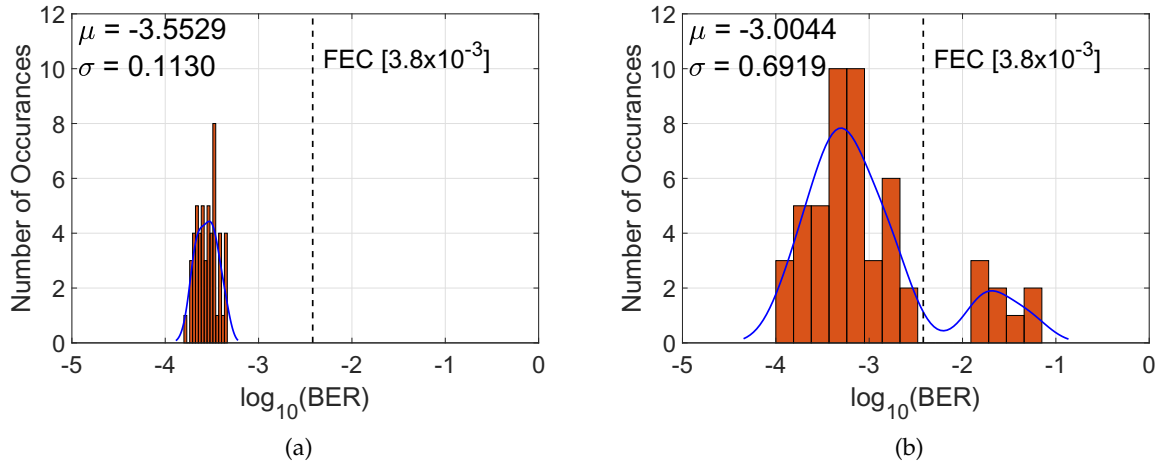


Fig. 4.16 BER statistics for 50 captures with (a) fixed SOP, and (b) random SOP.

0.1130 are obtained when the SOP is fixed. The mean and standard deviations are increased to -3.0044 (9.90×10^{-4}) and 0.69 , respectively for the random SOP case. This increase in mean BER corresponds to a power penalty of about 1.28 dB in terms of receiver sensitivity. It can also be observed in Fig. 4.16(b) that for some SOPs the BER goes beyond the HD-FEC limit which suggests that the receiver is polarization sensitive. This polarization sensitivity is coming from the high polarization dependent coupling loss of the edge coupler and low ER of the PSR. The amount of light coupled to the integrated receiver is reduced when the signal SOP is aligned more towards the TM polarization. The PSR has a polarization crosstalk of only < -12 dBm [209] at the wavelength we are operating. Thus, the TM polarization that gets coupled to the chip does not get converted to the TE mode fully. The polarization of the LO is TE and the 3×3 MMI is designed for the TE mode. The residue TM mode that gets through the PSR and goes into the 3×3 MMI does not contribute to the actual signal since the LO signal coming into the MMI is TE. Besides, the imaging length of the MMI for TM polarization is different from TE and hence, the MMI will not behave as a 120° hybrid for the TM mode. Part of the penalty also comes from the non-ideal behavior of the MMI (deviations from the ideal 120° and 240° relative phases). The performance of the receiver in terms of the SOP sensitivity can be improved by using edge coupler designs with lower polarization dependent loss [211] and PSR with better polarization crosstalk [162].

4.2.2.3 25 Gb/s PAM-4 transmission

In this section, we demonstrate the 25 Gb/s (12.5 Gbaud) PAM-4 transmission performance. Use of PAM-4 signal allows the use of low bandwidth components both at the transmitter and the receiver as shown in [91] which reduces the overall cost of the system. Although this advantage comes at the cost of reduced receiver sensitivity since PAM-4 signals require higher SNR than PAM-2 signals.

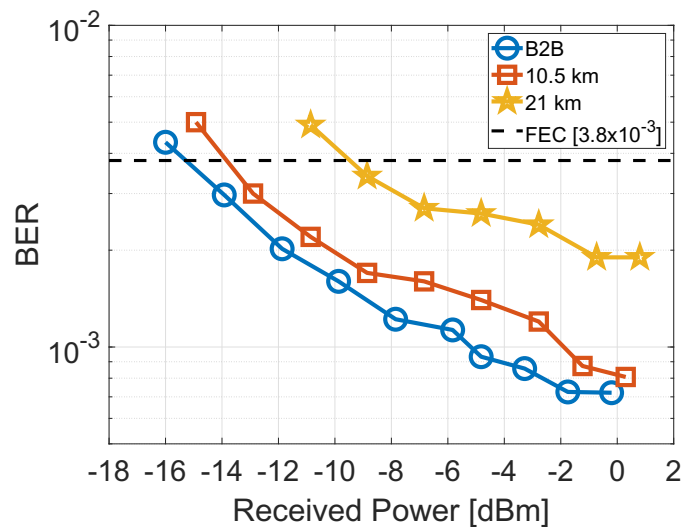


Fig. 4.17 Receiver sensitivity versus BER for different propagation distances for 25 Gb/s PAM-4 signal (after subtraction of the losses from the edge coupler).

We set the frequency offset between the incoming signal and the LO to be 10 GHz (80% of the baud rate) and the local oscillator power to be 8 dBm. The RTO bandwidth does not put any limitation on the usable frequency offset value for the 25 Gb/s PAM-4 case, since the baud rate is only 12.5 Gbaud. Figure 4.17 presents the received optical power versus BER curves for different propagation distances. Receiver sensitivities are found to be -15.3, -14, and -9.5 dBm below the HD-FEC threshold in back-to-back, after 10.5, and 21 km, respectively.

Finally, in Fig. 4.18 we present the 25 Gb/s PAM-4 eye diagrams in back-to-back, after 10.5 and 21 km. The eyes are open in back-to-back and become distorted due to the impact of CD after 21 km propagation. As can be observed from Fig. 4.18, the top level of the eyes have more noise than the bottom levels which was observed in previous demonstration [91] as well. Hence, we squeeze the bottom levels of the PAM-4 signal by tuning the bias level of the modulator to give more space to the top levels which ultimately results in reduced BER.

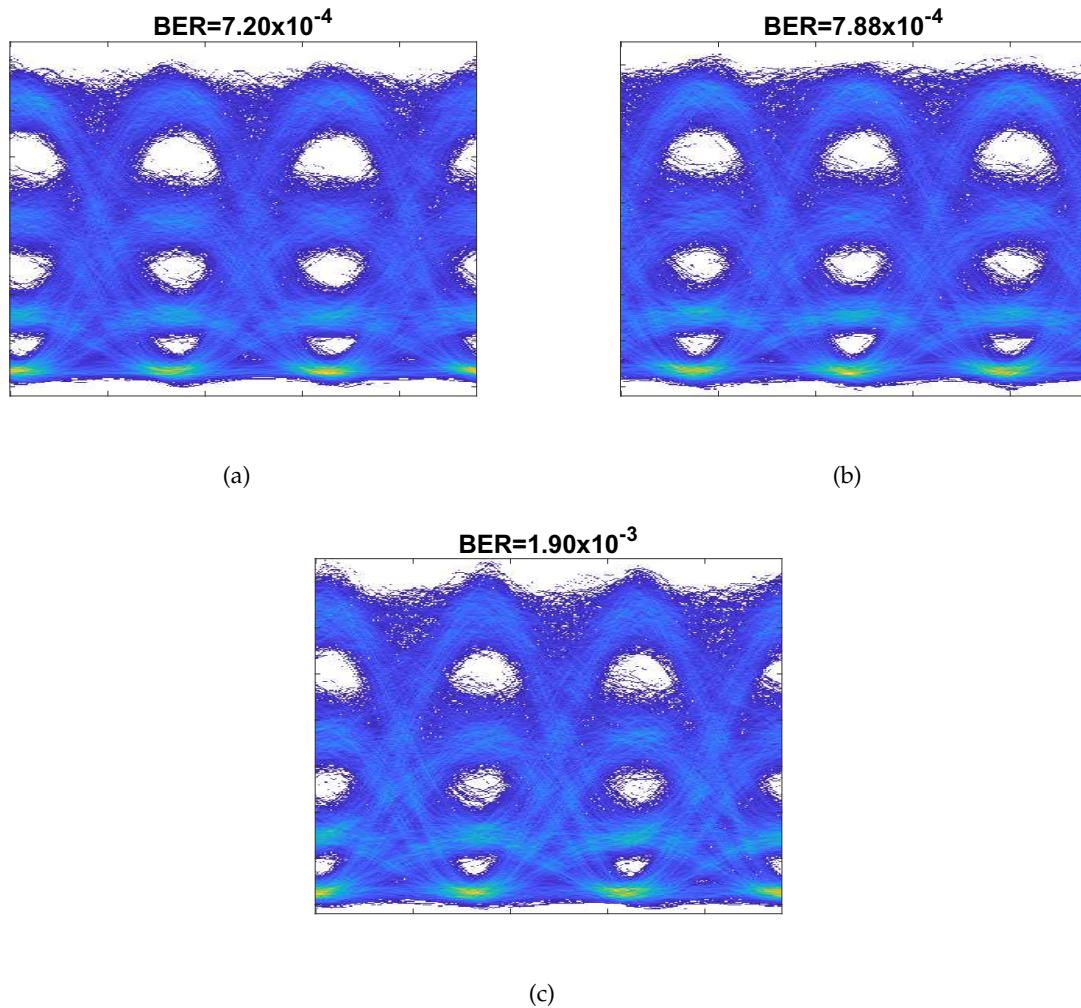


Fig. 4.18 PAM-4 eye diagrams (a) in back-to-back (B2B), (b) after 10.5 km, and (c) after 21 km of propagation at 25 Gb/s.

4.2.3 Conclusion

We report an integrated simplified coherent receiver on the SOI platform that achieves 25 Gb/s PAM-2 transmission over 30 km and 25 Gb/s PAM-4 transmission over 21 km. No form of DSP (e.g., pre-emphasis, equalization, pulse shaping etc.) apart from squaring, summing, and low-pass filtering the three waveforms and no dispersion compensation (e.g., optical or digital) were applied throughout the whole system. In addition, no frequency or phase control of the LO was required due to the use of intensity modulated signal. For the PAM-2 signals, a sensitivity of -15.10 dBm is achieved after 30 km of propagation while for the PAM-4 signals, the achievable

sensitivity is -9.50 dBm after 21 km of fiber. The results presented here will lead the path for simpler and lower cost implementation of 120° hybrid based simplified integrated coherent receiver for the emerging 5G X-haul, metro and access network applications. Although we present the performance of a C-band integrated coherent receiver, similar integrated receiver can be fabricated for O-band operation by redesigning some components, such as the PSR and the 120° hybrid which is a topic of further experimentation and beyond the scope of the thesis.

4.3 25 and 50 Gb/s PAM-4 transmission over 43 and 21 km single-mode fiber using integrated coherent receiver

In the previous section, we reported the integrated version of the PI receiver [202] on the SOI platform achieving 25 Gb/s/ λ PAM-4 transmission over 21 km with a receiver sensitivity of -9.5 dBm below the HD-FEC. In this section, we demonstrate significant performance improvement of the integrated receiver by using a better DAC and simple DSP achieving higher bit rates and receiver sensitivities, and longer reach.

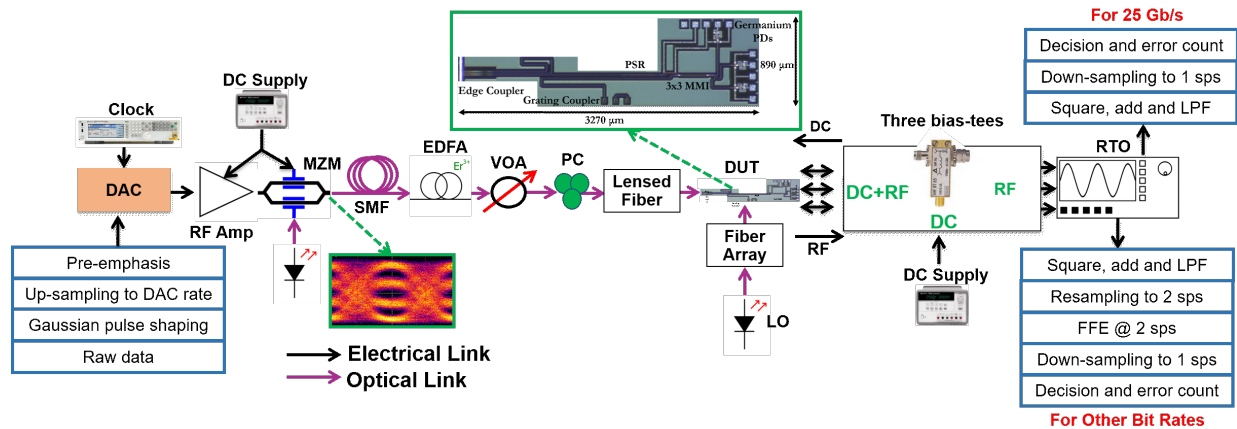


Fig. 4.19 Experimental setup. 26 Gbaud PAM-4 optical eye after the modulator is shown inside the green box. DAC: digital-to-analog converter, SMF: single-mode fiber, EDFA: erbium doped fiber amplifier, VOA: variable optical attenuator, PC: polarization controller, DUT: device under test, LO: local oscillator, RTO: real-time oscilloscope.

4.3.1 Experimental setup

The experimental testbed is shown in Fig. 4.19. An 8-bit DAC is used to generate PAM-4 signals at a sampling rate of 60 GSa/s. Pre-emphasis is used to compensate only for the DAC channel. The pre-emphasis is a real-valued finite impulse response filter. The DAC output is

connected to a RF amplifier which then drives a lithium niobate Mach-Zehnder modulator. The modulator is driven at the quadrature point. We achieved an optical modulation amplitude (OMA) of about 3.5 mW at 25 GBaud. An ECL emitting light at 1530 nm is used as the CW source. A PAM-4 optical eye at 26 GBaud right after the modulator is shown in Fig. 4.19. We used a Gaussian pulse with a factor of 0.8. After transmission over different lengths of fiber, the signal is amplified using an EDFA, followed by attenuation using a VOA to facilitate the received optical power sweep. As mentioned in the last section 4.2.2, the EDFA can be removed by improving the edge coupler design and the coupling setup to achieve better light coupling. The optical signal then goes through a PC before being coupled to the chip through the edge coupler. A micrograph of the fabricated receiver and the DSP blocks are shown in Fig. 4.19. The details of the integrated receiver can be found in the previous section 4.2.1 and detail design parameters of the PSR, the germanium PDs and the 120° hybrid can be found in [209], [210], and [99], respectively. The rest of the setup and processing is similar to the previous section 4.2.1. A linear FFE step running at 2 samples/symbol is added for the 40, 44 and 50 Gb/s PAM-4 transmission cases during offline processing..

4.3.2 Results and Discussion

4.3.2.1 25, 40 and 44 Gb/s PAM-4 transmission

For the 25 Gb/s PAM-4 transmission, a frequency offset of 10 GHz (80% of the baud rate) is used. Since the baud rate is only 12.5 Gbaud in this case, the transmitter can be replaced by 10G components as shown in [91] which will reduce the overall system cost. The BER versus received optical power curves for different lengths of fiber are presented in Fig. 4.20(a). The LO power was set at 8 dBm for all these measurements. Receiver sensitivities of -18, -17.5, -16.6, -14.50, and -9.8 dBm in back-to-back and after 10.5, 21, 31, and 43 km, respectively are obtained at a BER below the HD-FEC. The low density parity check FEC (LDPC-FEC) line (at a BER of 1×10^{-2}) is shown as well for reference purpose, which has been recently approved as the FEC for 25/50G EPON [212].

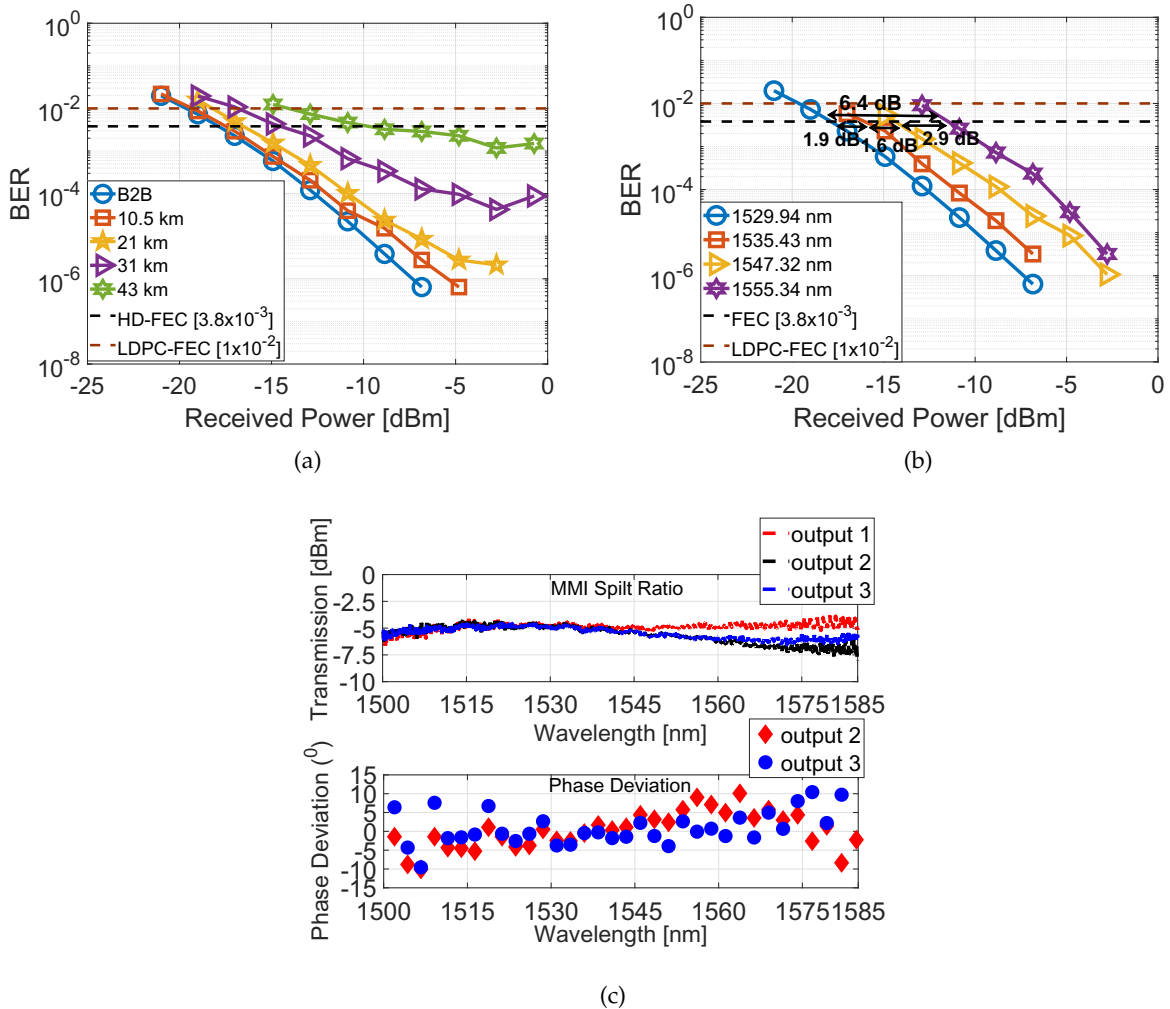


Fig. 4.20 Receiver sensitivity versus BER for 25 Gb/s PAM-4 (a) over different fiber lengths, and (b) in B2B for different wavelengths [edge coupler loss has been subtracted], and (c) split ratio and phase deviation of the 120° hybrid.

A few corresponding eye diagrams for different fiber lengths are shown in Fig. 4.21. The eye diagrams are quite open even after propagating over 31 km of fiber. It should be noted that no dispersion compensation (either digital or optical) and receiver equalization have been used.

The performance of the receiver at different wavelengths within the C-band in back-to-back for 25 Gb/s PAM-4 transmission is presented in Fig. 4.20(b). It can be observed that the performance degrades as we increase the wavelength. This can be attributed to two factors. First, the split ratio and the phase deviation of the 120° hybrid worsen as we increase the wavelength (shown in Fig. 4.20(c)) which results in penalty since the hybrid deviates from the

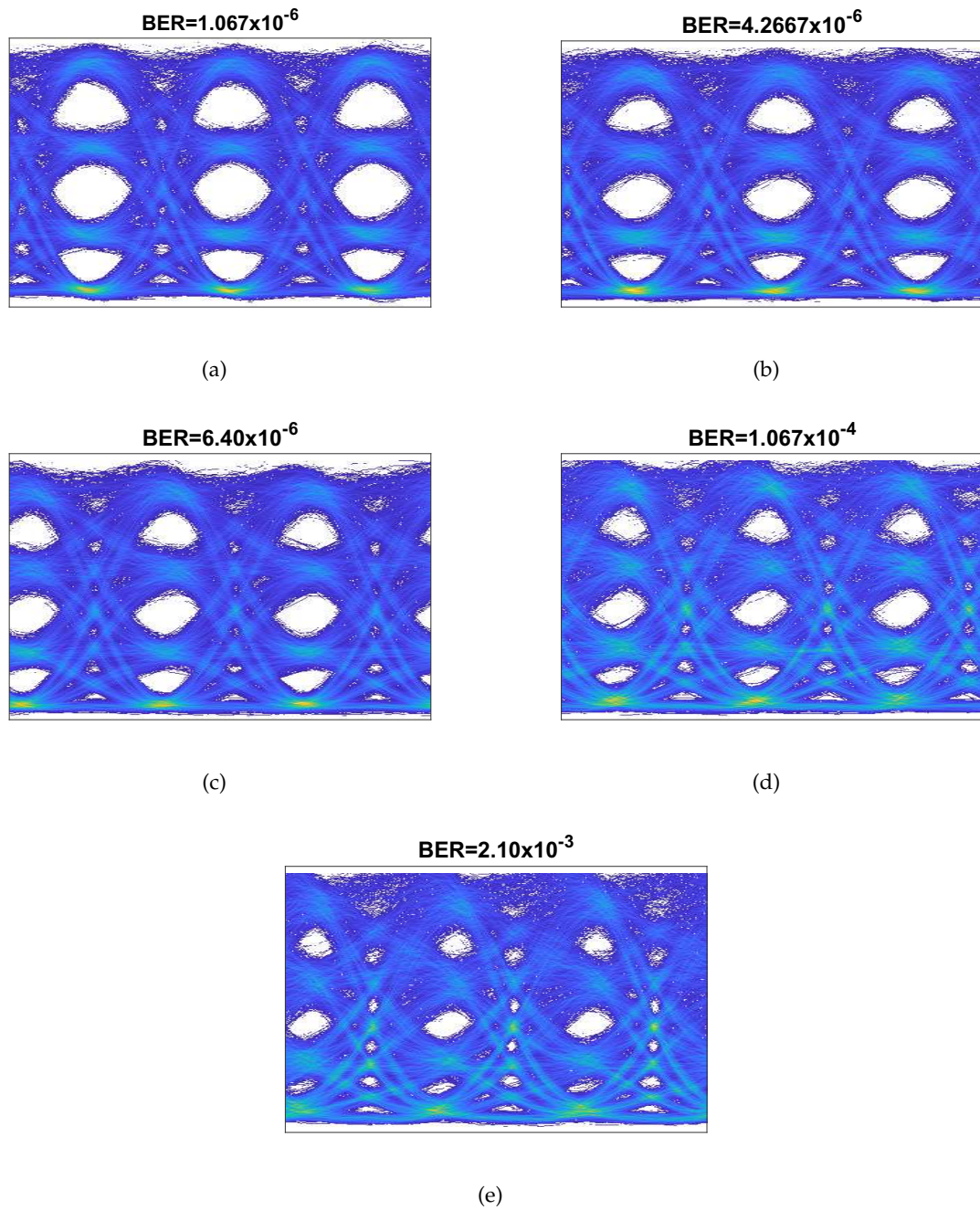


Fig. 4.21 PAM-4 eye diagrams (a) in back-to-back (B2B), (b) after 10.5 km, (c) after 21 km, (d) after 31 km, and (e) after 43 km of propagation at 25 Gb/s.

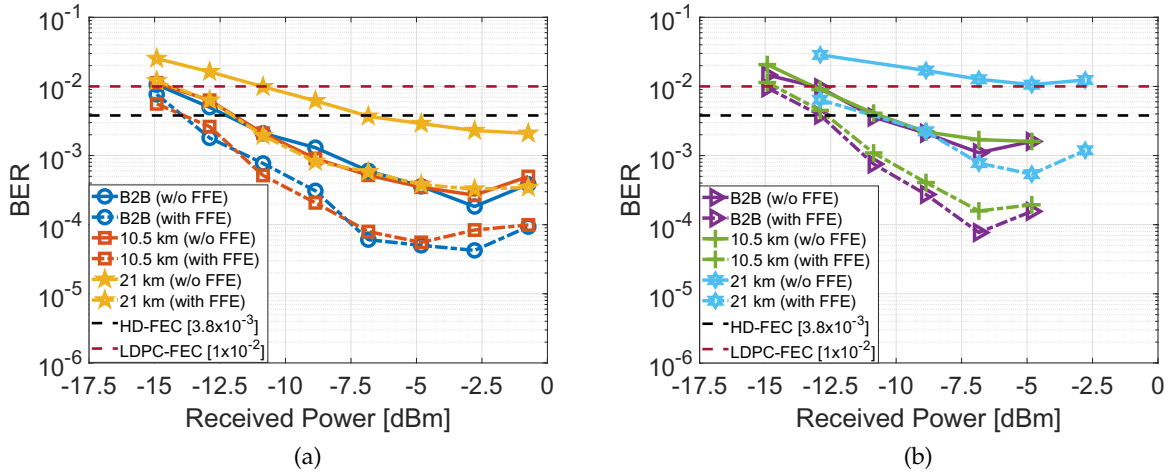


Fig. 4.22 Receiver sensitivity versus BER for (a) 40 Gb/s, and (b) 44 Gb/s PAM-4 over different fiber lengths. The solid lines indicate without FFE and the dashed lines indicate with 31-tap FFE. Edge coupler loss has been subtracted.

ideal 120° behavior. The other reason is the rapid decrease in the absorption coefficient of the germanium layer at higher wavelengths [213,214]. As a result, more light is required to generate the same photocurrent which reduces the receiver sensitivity.

For the 40 and 44 Gb/s PAM-4 transmission, 10.5 GHz frequency offset is used. Although it is not 75% of the baud rate, we could not use higher offset values due to the 33 GHz bandwidth limit of the RTO. Figure 4.22 presents the BER performance of 40 and 44 Gb/s PAM-4 transmission for different fiber lengths. The receiver sensitivities are -12.3, -12, and -7 dBm in back-to-back and after 10.5, and 21 km, respectively for 40 Gb/s PAM-4, and -11 and -10.5 dBm in back-to-back and after 10.5 km, respectively for 44 Gb/s PAM-4 without applying any form of dispersion compensation and receiver equalization. The BER is above the HD-FEC for 21 km propagation of 44 Gb/s PAM-4. When 31-tap FFE is applied at the receiver, the receiver sensitivities become -14, -13.9, and -12 dBm for 40 Gb/s and -13, -12.7, and -11 dBm for 44 Gb/s in back-to-back, and after 10.5 and 21 km, respectively. The FFE compensates for distortions arising from both the bandwidth limitation and the suboptimal frequency offset between the signal and the LO. The eye diagrams with and without the FFE for different distances are shown in Fig. 4.23 and 4.24 for 40 and 44 Gb/s PAM-4 transmission, respectively. As explained in the previous section (4.2.2.2), the integrated receiver is polarization sensitive.

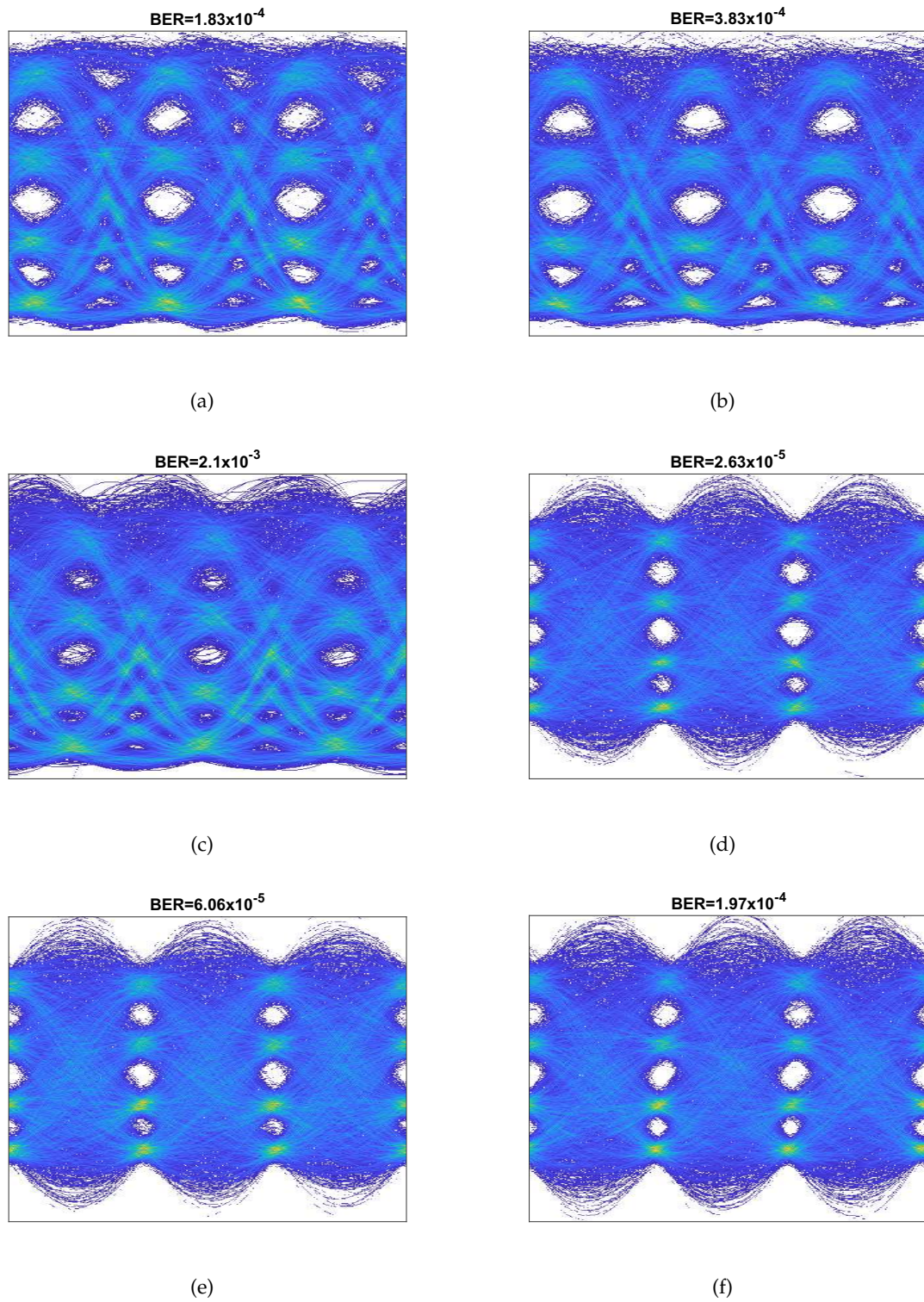


Fig. 4.23 PAM-4 eye diagrams (a) in back-to-back (B2B), (b) after 10.5 km, (c) after 21 km, without FEC and (d) in back-to-back (B2B), (e) after 10.5 km, and (f) after 21 km with 31-tap FEC at 40 Gb/s.

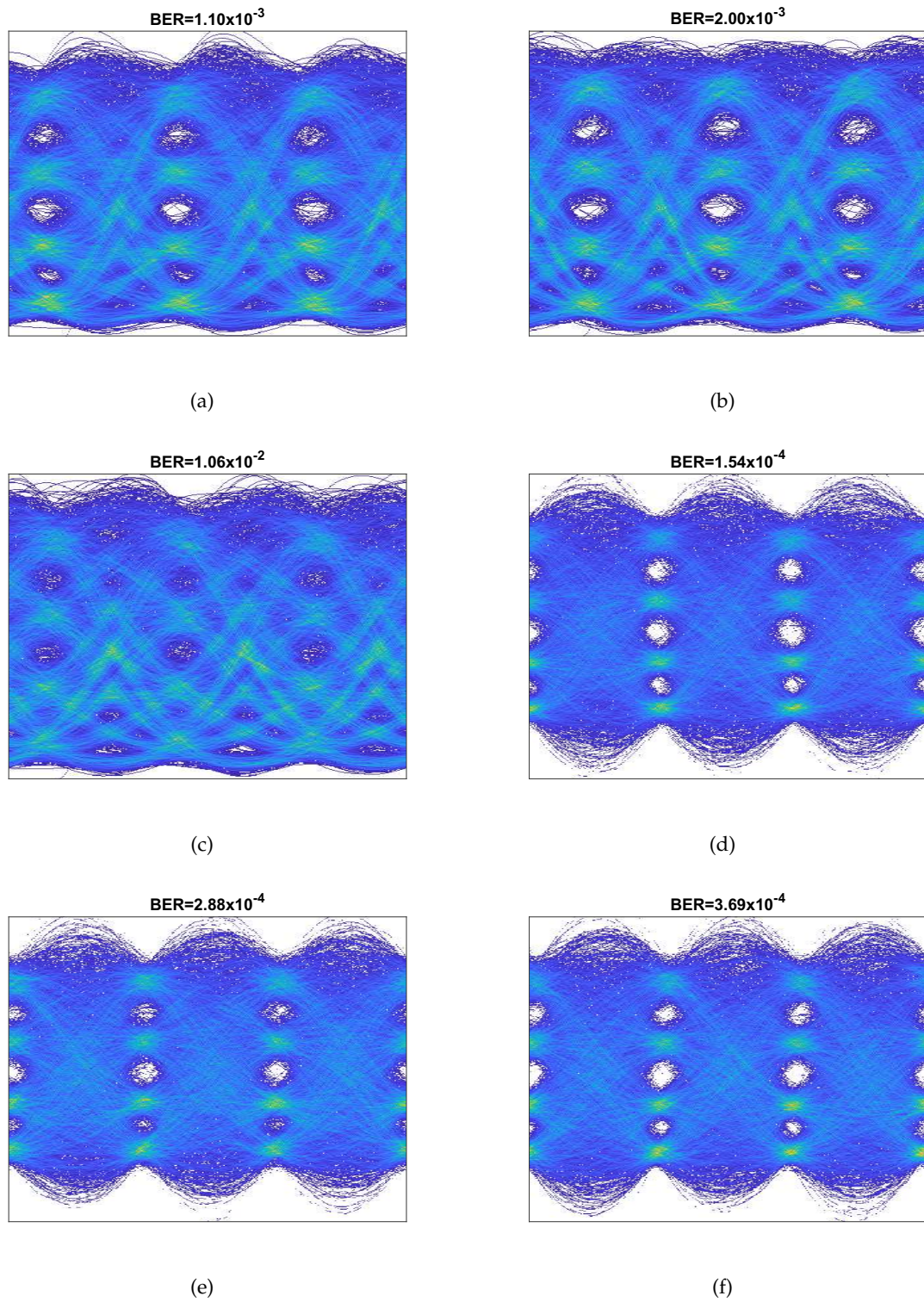


Fig. 4.24 PAM-4 eye diagrams (a) in back-to-back (B2B), (b) after 10.5 km, (c) after 21 km, without FFE and (d) in back-to-back (B2B), (e) after 10.5 km, and (f) after 21 km with 31-tap FFE at 44 Gb/s.

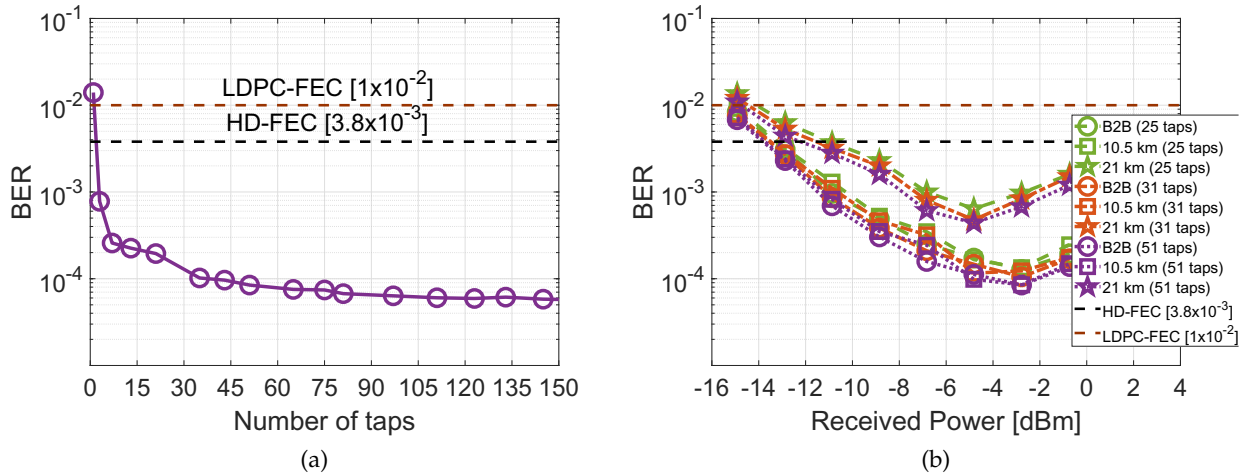


Fig. 4.25 (a) Number of FFE taps versus BER at -3.8 dBm received power in back-to-back (B2B), and (b) receiver sensitivity versus BER for 50 Gb/s PAM-4 over different fiber lengths using different FFE taps [Edge coupler loss has been subtracted].

4.3.2.2 50 Gb/s PAM-4 transmission

Single wavelength 50 Gb/s PAM-4 transmission is more attractive compared to channel bonding two 25 Gb/s wavelengths to achieve 50 Gb/s since reduction in required optoelectronic components, wavelength resources and overall system cost can be achieved. IEEE 802.3bs has already standardized the 50 Gb/s lanes for 200G and 400G Ethernet. It is expected that the 50 Gb/s lane based 200G and 400G will start replacing 100G in data centers around 2020. Hence, a lot of research is underway to commoditize the 50G optoelectronic components, an ecosystem which the access segment can leverage.

Due to the RTO bandwidth limit we could use 10.5 GHz frequency offset between the signal and the LO which is only 42% of the baud rate. We could not achieve BERs below the HD-FEC without using the linear FFE at the receiver for 50 Gb/s PAM-4 transmission. Figure 4.25(a) shows the BER for different number of filter taps in back-to-back at -3.8 dBm of received power. The BER does not improve much after 31 FFE taps. The BER versus the received power curves for 25, 31, and 51 taps are shown in Fig. 4.25(b). We achieved receiver sensitivities of -13.3 dBm in back-to-back, -13.2, and -11 dBm after 10.5 and 21 km for 25 taps, -13.6 dBm in back-to-back, -13.5, and -11.6 dBm after 10.5 and 21 km for 31 taps, and -13.8 dBm in back-to-back, -13.7, and -12.2 dBm after 10.5 and 21 km for 51 taps. Figure 4.26 shows the eye diagrams for different propagation distances using 31-tap FFE.

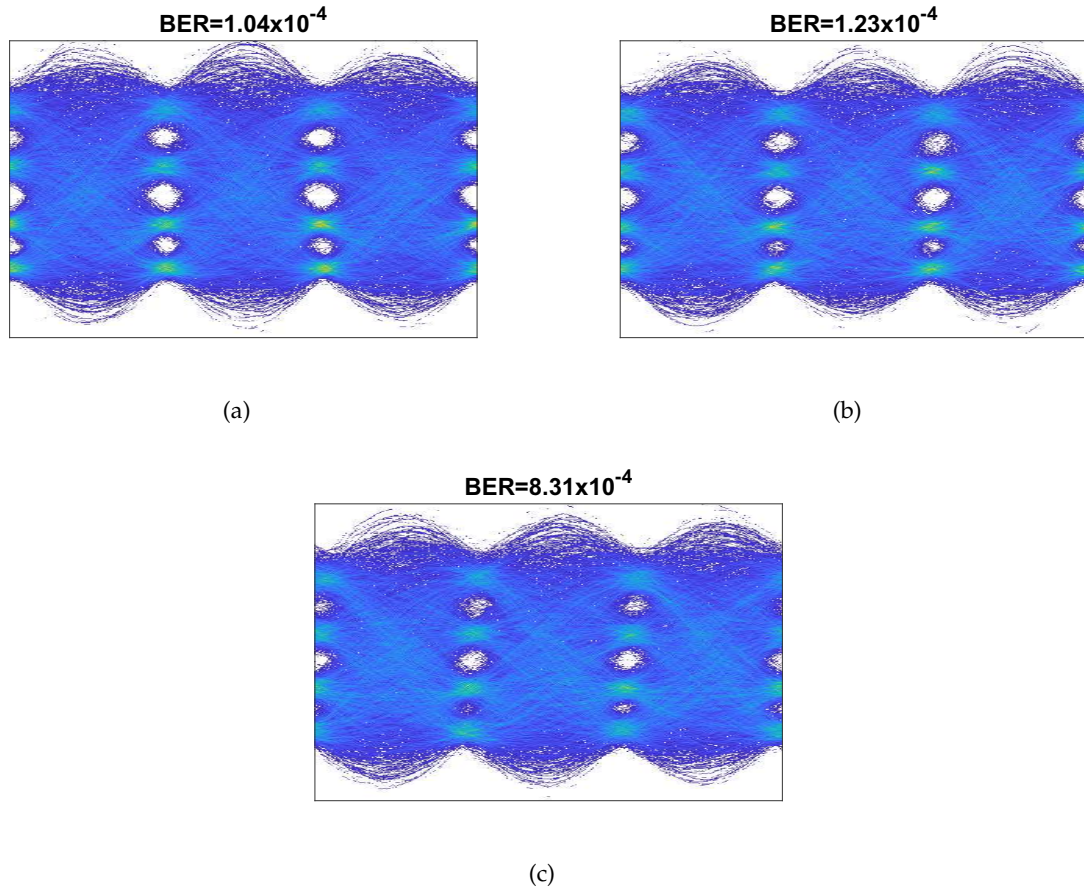


Fig. 4.26 PAM-4 eye diagrams (a) in back-to-back (B2B), (b) after 10.5 km, and (c) after 21 km at 50 Gb/s with 31-tap FFE.

4.3.3 Conclusions

We present 25 and 50 Gb/s PAM-4 transmission over 43 and 21 km, respectively below the HD-FEC limit in the C-band using the integrated simplified coherent receiver on SOI. We achieved -16.6 dBm of receiver sensitivity at 25 Gb/s after 21 km without any dispersion compensation and receiver equalizer, and -11.6 dBm at 50 Gb/s after 21 km using 31-tap linear FFE at the receiver. A summary of the receiver sensitivities achieved using the integrated simplified coherent receiver (presented in sections 4.2 and 4.3) at various distances for different modulation formats are provided in table 4.1.

Table 4.1 Summary of transmission performance of the integrated simplified coherent receiver.

Modulation Format	Bit Rate [Gb/s]	Fiber Length [km]	Sensitivity @ HD-FEC [dBm]	DAC Type	DSP
PAM-2	25	B2B	-23.7	6-bit	No
		21	-20.3	6-bit	No
		26	-18.2	6-bit	No
		30	-15.1	6-bit	No
PAM-4	25	B2B	-15.3	6-bit	No
		10.5	-14	6-bit	No
		21	-9.5	6-bit	No
PAM-4	25	B2B	-18	8-bit	DAC equalization
		10.5	-17.5	8-bit	DAC equalization
		21	-16.6	8-bit	DAC equalization
		31	-14.5	8-bit	DAC equalization
		43	-9.8	8-bit	DAC equalization
PAM-4	50	B2B	-13.6	8-bit	DAC equalization & 31-tap FFE
		10.5	-13.5	8-bit	DAC equalization & 31-tap FFE
		21	-11.6	8-bit	DAC equalization & 31-tap FFE

Chapter 5

Conclusions and Future Works

New business and technology drivers, such as cloud, high definition video streaming and 5G radio networks combined with requirements like low latency, scalability, and flexibility are propelling the advancement of the high-speed fiber optical networks. On both ends of the optical fiber, silicon photonics-based transceivers have left the research institutes to become a mature market product [9–12]. Silicon photonics offers larger wafer size, power and cost reductions compared to existing III-V materials. By being the same material as the electronic circuitry industry it eliminates potential problems arising from differing coefficients of expansion in thermally varying environments. The maturity of passives like waveguides, grating couplers, tapers, microring filters, optical hybrids [97,215,216] and actives such as modulators and photodetectors [215,217–219], in silicon photonics is also another sign of the readiness of this technology.

5.1 Thesis highlights

In this thesis, we explored different silicon photonic devices and systems, and bench-top solution for optical communication applications. The major contributions of this work are shown in Fig. 5.1.

In chapter 3, we report various passive silicon photonic devices based on Bragg gratings, interference, and doping of silicon waveguide. The key findings are listed below along with the publications produced:

- We demonstrate ultra-compact OADMs in the C-band using misaligned sidewall gratings. We analyze two configurations of the Bragg gratings in MZI-based OADMs. The effect of misalignment variation on the spectral response of both structures was studied numerically and experimentally. The use of misaligned gratings enables a narrow bandwidth

Silicon Photonic Components and Systems for Optical Communication Applications

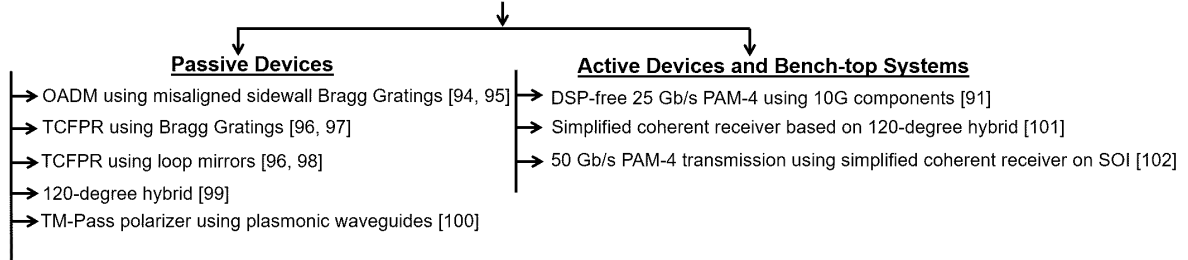


Fig. 5.1 Summary of the original contributions of the thesis.

with a lower number of periods, thus enabling optimization of the OADM designs for compactness. We experimentally measured 3-dB bandwidths of 6 nm and 6.2 nm and ERs of 25 dB and 51 dB with device footprints of $400 \mu\text{m} \times 90 \mu\text{m}$ and $400 \mu\text{m} \times 125 \mu\text{m}$, respectively for the single-stage and the cascaded configurations. Furthermore, the OADMs are designed with 193 nm DUV lithography compatible minimum feature size [94,95].

- We report novel Fabry-Perot resonators with transverse coupling on the SOI platform. The TCFPRs offer better flexibility to achieve the desired spectral response compared to all-pass MRRs. Furthermore, one variant of the TCFPR features a $\pi/2$ phase shift for each one-way trip through the resonant cavity. Since the resonant cavity can be formed using straight waveguides and Bragg gratings as the end reflectors, bending losses can be eliminated in the TCFPRs. The effect of varying the cavity length is studied experimentally for both types of TCFPRs. The impact of tuning the κ on the spectral response of the TCFPRs is also investigated. Our reported devices exhibit ER, FSR, Q-factor and IL values of 37.28 dB, 2.58 nm, 3356 and 2.48 dB, respectively for an effective cavity length of $110 \mu\text{m}$ and of 8.69 dB, 0.3 nm, 23642 and 1.43 dB, respectively for a $943 \mu\text{m}$ effective cavity length [96,97].
- We present the detail simulation, fabrication and characterization of the loop mirror-based TCFPRs. In our work, we experimentally obtained Q-factor, ER and FSR values of 28086, 10.04 dB and 0.32 nm respectively for a $1038 \mu\text{m}$ cavity length and of 5120, 18.14 dB and 1.22 nm, respectively for a cavity length of $376 \mu\text{m}$. Finally, the resonators have footprints of less than $128.5 \mu\text{m} \times 156 \mu\text{m}$ [96,98].
- We demonstrate a 120° optical hybrid based on 3×3 MMI in the C-band using 193 nm optical lithography on the SOI platform. Via simulation, a maximum excess loss of 2.65 dB and phase deviation of $\leq 5^\circ$ are achieved over 65 nm (1520 nm - 1585 nm). The hybrid

shows measured excess loss of <2.4 dB over 60 nm (1500 nm - 1560 nm), and phase deviations of $\leq 5^\circ$ over 30 nm (1520 nm to 1550 nm) and $\leq 10^\circ$ over 80 nm (1500 nm - 1580 nm) wavelength range, respectively [99].

- We present a hybrid plasmonic TM-pass polarizer using highly doped silicon instead of metal to form the plasmonic waveguide. The design parameters such as the width and length of the silicon and highly doped silicon waveguides, carrier concentration of the highly doped silicon, and the gap between the waveguides have been optimized to obtain the highest figure of merit and maintain the fabrication limitations simultaneously. According to our analysis, the proposed TM-pass polarizer achieves an ER of 30.1 dB and an IL of 3.1 dB with a length of 15 μm near 1550 nm wavelength. The reported polarizer is also highly fabrication tolerant and offers peak ER selection at different wavelengths by choosing different doping concentrations during fabrication. [100].

In chapter 4, we present bench-top and integrated solutions for the high-speed PONs. The summary of the key results and the resulted publications are provided below:

- We present 25 Gb/s PAM-4 transmission over 28 km of fiber at a BER below the HD-FEC in the C-band using a 3×3 fiber coupler based simplified coherent receiver. Off-the-shelf 10G class EML is used at the transmitter and PIN PDs are used at the receiver. Receiver sensitivities of -18.5, -17 and -13.5 dBm and power budgets of 20.80, 19.6 and 16 dB are achieved at a bit error rate (BER) below the HD-FEC threshold (i.e., 3.8×10^{-3}) in back-to-back, after 20.7 and 28 km, respectively which can be increased further by using higher LO power. For the polarization independent demonstration of 25 Gb/s PAM-4 transmission, we achieved receiver sensitivities of -17.10 and -14.5 dBm and power budgets of 19.5 and 17 dB in back-to-back and after 21 km, respectively. [91].
- We report an integrated simplified coherent receiver on the SOI platform consisting of an inverse taper edge coupler for the received signal, a vertical grating coupler for the local oscillator input, a PSR, a 120° hybrid based on a 3×3 MMI coupler, and three germanium photodetectors. We did not apply any DSP (e.g., pre-emphasis, equalization, pulse shaping etc.) apart from squaring, summing, and low-pass filtering the three waveforms and dispersion compensation (e.g., optical or digital) throughout the whole system. Receiver sensitivities of -23.7, -20.5, and -15.1 dBm are achieved in back-to-back, after 21 and 30 km, respectively. We also demonstrate 25 Gb/s PAM-4 transmission achieving receiver sensitivities of -15.3, -14, and -9.5 dBm below the HD-FEC threshold in back-to-back, after 10.5 and 21 km, respectively. Although the receiver architecture is meant to be insensitive to the SOP of the incoming signal based on the operating principle [202], it exhibits

polarization dependence when tested by varying the SOP of the incoming signal using a polarization controller. The polarization dependence on the SOP can be attributed to the polarization dependence of the edge coupler and small ER (only 12 dB at 1530 nm) of the PSR [209], which can be improved by using a better edge coupler and PSR [102].

- We present 25 and 50 Gb/s PAM-4 transmission over 43 and 21 km, respectively below the HD-FEC limit in the C-band using an integrated simplified coherent receiver on SOI and enabled by simple DSP and a better DAC. We obtained receiver sensitivities of -18, -17.5, -16.6, -14.5, and -10 dBm in back-to-back, and after 10.5, 21, 31, and 43 km, respectively for 25 Gb/s PAM-4, -12.3 -12 and -7 dBm in back-to-back and after 10.5, and 21 km, respectively for 40 Gb/s PAM-4, and -11 and -10.5 dBm in back-to-back and after 10.5 km, respectively for 44 Gb/s PAM-4 without any receiver equalizer. The integrated receiver is characterized using different wavelengths within the C-band. We also achieved 50 Gb/s PAM-4 transmission with receiver sensitivities of -13.6 dBm in back-to-back, -13.5 and -11.6 dBm after 10.5 and 21 km using 31-tap linear FFE [103].

5.2 Future research avenues

While the research objectives of this thesis have been accomplished, a number of interesting research avenues related to the work presented in the thesis still exist that can be pursued in the future. In this section, we list some of potential research ideas originated from the topics covered in the thesis.

- The OADMs presented in chapter 3 are capable of adding/dropping a single wavelength. It will be interesting to extend the design by cascading multiple OADMs to obtain a multi-wavelength OADM [56]. The design can be further extended by adding heaters on top of the Bragg gratings to achieve tunability of the Bragg wavelength resulting in a reconfigurable OADM [220]. In future designs, the sidelobes can be reduced by apodizing the gratings (altering the amplitude of the effective index modulation along the length of the grating) [129].
- The TCFPRs using both Bragg gratings and loop mirrors can be extended to design dispersion compensating filter like the one presented in [221] by substituting the MZIs with the TCFPRs. Another interesting extension of the TCFPRs will be to design optical delay lines [222]. The dispersion compensating filters and the delay lines can later be used in optical transmission experiments.

- The 120° optical hybrid is designed for the TE mode and has a quite large footprint. Further work may include using sub-wavelength gratings to optimize the design to obtain footprint reduction, operating bandwidth extension and achieving dual-polarization (both TE and TM) operation [223]. Although the fabrication tolerance of the device will be reduced if sub-wavelength gratings are used.
- The TM-pass polarizer presented in this thesis has a large footprint and small bandwidth over which the ER is >20 dB. Design optimizations can be done including introduction of plasmonic bend waveguides to reduce the footprint and enhance the overall performance. Furthermore, hybrid plasmonic TE-pass polarizers can be designed using the highly doped silicon replacing the metals.
- The bench-top solution-based 25 Gb/s PAM-4 transmission using 10G transmitter work can be extended to higher bit rates such as 50 Gb/s or 100 Gb/s per λ to meet the increasing bandwidth demand in the access networks. Using $1\lambda \times 50$ Gb/s or $1\lambda \times 100$ Gb/s instead of $2\lambda \times 25$ Gb/s or $4\lambda \times 25$ Gb/s can save wavelength resources which is scarce due to a wide variety of applications occupying different bands. Although achieving higher bit rates will require DSP to some extent which will increase the complexity of the system. The architecture of the simplified coherent receiver can be modified to capture phase information instead of detecting only the envelope. This will enable the use of other high order modulation formats with better spectral efficiency. Another research direction might be the use of multilevel user-interleaving concept to reduce the system complexity at the user side.
- The integrated simplified coherent receiver presented in the thesis is designed for the C-band and is sensitive to polarization of the incoming signal. Since the IEEE 802.3ca 50G-EPON standards have chosen O-band for both upstream and downstream, the receiver can be redesigned for operation in the O-band. Furthermore, the polarization dependency can be overcome by using better edge couplers and PSRs. Design optimizations can be done to improve the performance of the photodetectors used in the receiver since it has high dark current. Packaging the receiver to include TIAs can be another step towards the maturation of the receiver.

Appendix

The derivation of the operating principle of the simplified coherent receiver are presented here. As shown in [202], both configurations of Fig. A1 provide similar results. Although we performed the experiments using the configuration presented in Fig. A1(b), we will show the derivation of the configuration shown in Fig. A1(a).

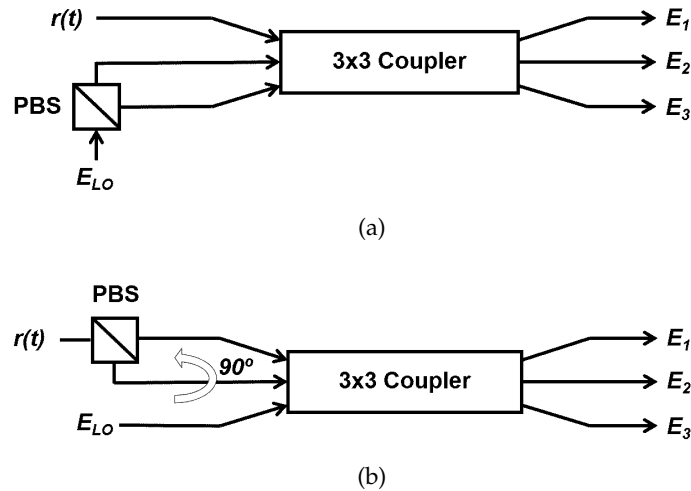


Fig. A1 Schematic of the polarization independent receiver with polarization beam splitter either on the (a) local oscillator (LO) or on the (b) received signal.

We assume a frequency difference of $\Delta\nu$ between the signal and the LO. The polarization of the signal can be random and thus, the Jones vector can be expressed as,

$$U(t) = \begin{bmatrix} r(t)e^{j(2\pi\Delta\nu t)} \cos \phi \\ r(t)e^{j(2\pi\Delta\nu t + \psi)} \sin \phi \end{bmatrix}$$

where, $r(t)$ is the modulated signal, ϕ is the main axis orientation of the polarization ellipse and ψ is the angle of ellipticity (for linear polarization $\psi = 0$).

Let us assume [202],

$$x = 2\pi\Delta\nu t$$

$$y = 2\pi\Delta\nu t + \psi$$

$$E_x^{in} = r(t)e^{jx} \cos \phi$$

$$E_y^{in} = r(t)e^{jy} \sin \phi$$

The three outputs of the coupler are given by [62, 202, 224],

$$\begin{bmatrix} E_{1,j} \\ E_{2,j} \\ E_{3,j} \end{bmatrix} = \begin{bmatrix} a & b & b \\ b & a & b \\ b & b & a \end{bmatrix} \begin{bmatrix} E_x & E_y \\ E_{LO} & 0 \\ 0 & E_{LO} \end{bmatrix}$$

where, $j = x$ or y polarization.

$$a = \frac{2}{3} \exp(jkl) + \frac{1}{3} \exp(-j2kl)$$

$$b = \frac{1}{3} \exp(-j2kl) - \frac{1}{3} \exp(jkl)$$

For a symmetric 1:1:1 coupler, $kl = \frac{2\pi}{9}$ [62].

$$\begin{aligned} |a|^2 &= aa^* \\ &= \left[\frac{2}{3} \exp(jkl) + \frac{1}{3} \exp(-j2kl) \right] \left[\frac{2}{3} \exp(-jkl) + \frac{1}{3} \exp(j2kl) \right] \\ &= \left[\frac{2}{3} \exp(j\frac{2\pi}{9}) + \frac{1}{3} \exp(-j\frac{4\pi}{9}) \right] \left[\frac{2}{3} \exp(-j\frac{2\pi}{9}) + \frac{1}{3} \exp(j\frac{4\pi}{9}) \right] \\ &= \frac{4}{9} + \frac{1}{9} + \frac{2}{9} \exp(j\frac{2\pi}{3}) + \frac{2}{9} \exp(-j\frac{2\pi}{3}) \\ &= \frac{5}{9} + \frac{4}{9} \cos\left(\frac{2\pi}{3}\right) \\ &= \frac{5}{9} + \frac{4}{9} \left(-\frac{1}{2}\right) \\ &= \frac{1}{3} \end{aligned}$$

$$\begin{aligned} |b|^2 &= bb^* \\ &= \left[\frac{1}{3} \exp(-j\frac{4\pi}{9}) - \frac{1}{3} \exp(j\frac{2\pi}{9}) \right] \left[\frac{1}{3} \exp(j\frac{4\pi}{9}) - \frac{1}{3} \exp(-j\frac{2\pi}{9}) \right] \\ &= \frac{1}{9} + \frac{1}{9} - \frac{1}{9} \exp(-j\frac{2\pi}{3}) - \frac{1}{9} \exp(j\frac{2\pi}{3}) \\ &= \frac{2}{9} - \frac{2}{9} \cos\left(\frac{2\pi}{3}\right) \\ &= \frac{2}{9} - \frac{2}{9} \left(-\frac{1}{2}\right) \\ &= \frac{1}{3} \end{aligned}$$

$$\begin{aligned} ab^* &= \left[\frac{2}{3} \exp(j\frac{2\pi}{9}) + \frac{1}{3} \exp(-j\frac{4\pi}{9}) \right] \left[\frac{1}{3} \exp(j\frac{4\pi}{9}) - \frac{1}{3} \exp(-j\frac{2\pi}{9}) \right] \\ &= -\frac{2}{9} + \frac{1}{9} + \frac{2}{9} \exp(j\frac{2\pi}{3}) - \frac{1}{9} \exp(-j\frac{2\pi}{3}) \\ &= -\frac{1}{9} + \frac{1}{9} \left[2 \exp(j\frac{2\pi}{3}) - \exp(-j\frac{2\pi}{3}) \right] \\ &= -\frac{1}{9} + \frac{1}{9} \left[2 \left[\cos\left(\frac{2\pi}{3}\right) + j \sin\left(\frac{2\pi}{3}\right) \right] - \left[\cos\left(\frac{2\pi}{3}\right) - j \sin\left(\frac{2\pi}{3}\right) \right] \right] \\ &= -\frac{1}{9} + \frac{1}{9} \left[2 \left[-\frac{1}{2} + j\frac{\sqrt{3}}{2} \right] - \left[-\frac{1}{2} - j\frac{\sqrt{3}}{2} \right] \right] \\ &= -\frac{1}{9} - \frac{1}{18} + j\frac{1}{2\sqrt{3}} \\ &= -\frac{1}{6} + j\frac{1}{2\sqrt{3}} \end{aligned}$$

$$|r| = \sqrt{a^2 + b^2} = \sqrt{\left(-\frac{1}{6}\right)^2 + \left(\frac{1}{2\sqrt{3}}\right)^2} = \frac{1}{3}$$

$$\theta = \tan^{-1}\left(\frac{-6}{2\sqrt{3}}\right) = \frac{2\pi}{3}$$

$$\begin{aligned}
a^*b &= \left[\frac{2}{3} \exp(-j\frac{2\pi}{9}) + \frac{1}{3} \exp(j\frac{4\pi}{9}) \right] \left[\frac{1}{3} \exp(-j\frac{4\pi}{9}) - \frac{1}{3} \exp(j\frac{2\pi}{9}) \right] \\
&= -\frac{2}{9} + \frac{1}{9} + \frac{2}{9} \exp(-j\frac{2\pi}{3}) - \frac{1}{9} \exp(j\frac{2\pi}{3}) \\
&= -\frac{1}{9} + \frac{1}{9} \left[2 \exp(-j\frac{2\pi}{3}) - \exp(j\frac{2\pi}{3}) \right] \\
&= -\frac{1}{9} + \frac{1}{9} \left[2 \left[\cos\left(\frac{2\pi}{3}\right) - j \sin\left(\frac{2\pi}{3}\right) \right] - \left[\cos\left(\frac{2\pi}{3}\right) + j \sin\left(\frac{2\pi}{3}\right) \right] \right] \\
&= -\frac{1}{9} + \frac{1}{9} \left[2 \left[-\frac{1}{2} - j\frac{\sqrt{3}}{2} \right] - \left[-\frac{1}{2} + j\frac{\sqrt{3}}{2} \right] \right] \\
&= -\frac{1}{9} - \frac{1}{18} - j\frac{1}{2\sqrt{3}} \\
&= -\frac{1}{6} - j\frac{1}{2\sqrt{3}} \\
|r| &= \sqrt{a^2 + b^2} = \sqrt{\left(-\frac{1}{6}\right)^2 + \left(-\frac{1}{2\sqrt{3}}\right)^2} = \frac{1}{3} \\
\theta &= \tan^{-1}\left(\frac{6}{2\sqrt{3}}\right) = \frac{4\pi}{3} = -\frac{2\pi}{3}
\end{aligned}$$

As mentioned before,

$$\begin{bmatrix} E_{1,j} \\ E_{2,j} \\ E_{3,j} \end{bmatrix} = \begin{bmatrix} a & b & b \\ b & a & b \\ b & b & a \end{bmatrix} \begin{bmatrix} E_x & E_y \\ E_{LO} & 0 \\ 0 & E_{LO} \end{bmatrix}$$

$$E_{1x}^{out} = ar(t)e^{jx} \cos \phi + bE_{LO}$$

$$E_{1y}^{out} = ar(t)e^{jy} \sin \phi + bE_{LO}$$

$$\begin{aligned}
|E_{1x}^{out}|^2 &= (ar(t)e^{jx} \cos \phi + bE_{LO}) (a^*r(t)e^{-jx} \cos \phi + b^*E_{LO}) \\
&= |a|^2 r^2(t) \cos^2 \phi + |b|^2 E_{LO}^2 + ab^*r(t)E_{LO} \cos \phi e^{jx} + a^*br(t)E_{LO} \cos \phi e^{-jx} \\
&= m_1 + n_1 + \frac{1}{3}r(t)E_{LO} \cos \phi e^{jx} e^{j\frac{2\pi}{3}} + \frac{1}{3}r(t)E_{LO} \cos \phi e^{-jx} e^{-j\frac{2\pi}{3}} \\
&= m_1 + n_1 + \frac{1}{3}r(t)E_{LO} \cos \phi 2 \cos\left(x + \frac{2\pi}{3}\right) \\
&= m_1 + n_1 + \frac{2}{3}r(t)E_{LO} \cos \phi \cos\left(x + \frac{2\pi}{3}\right)
\end{aligned}$$

$$\begin{aligned}
|E_{1y}^{out}|^2 &= (ar(t)e^{jy} \sin \phi + bE_{LO}) (a^*r(t)e^{-jy} \sin \phi + b^*E_{LO}) \\
&= |a|^2 r^2(t) \sin^2 \phi + |b|^2 E_{LO}^2 + ab^*r(t)E_{LO} \sin \phi e^{jy} + a^*br(t)E_{LO} \sin \phi e^{-jy} \\
&= m_1 + n_1 + \frac{1}{3}r(t)E_{LO} \sin \phi e^{jy} e^{j\frac{2\pi}{3}} + \frac{1}{3}r(t)E_{LO} \sin \phi e^{-jy} e^{-j\frac{2\pi}{3}} \\
&= m_1 + n_1 + \frac{1}{3}r(t)E_{LO} \sin \phi 2 \cos\left(y + \frac{2\pi}{3}\right) \\
&= m_1 + n_1 + \frac{2}{3}r(t)E_{LO} \sin \phi \cos\left(y + \frac{2\pi}{3}\right)
\end{aligned}$$

$$\begin{aligned}
i_1 &= R \left(|E_{1x}^{out}|^2 + |E_{1y}^{out}|^2 \right) \\
&= \frac{2}{3} R E_{LO} r(t) \left[\cos \phi \cos\left(x + \frac{2\pi}{3}\right) + \sin \phi \cos\left(y + \frac{2\pi}{3}\right) \right]
\end{aligned}$$

Here, $m_1 = |a|^2 r^2(t) \cos^2 \phi$ or $|a|^2 r^2(t) \sin^2 \phi$ and $n_1 = |b|^2 E_{LO}^2$. n_1 is a DC-term which will be blocked by the DC-block and m_1 is a much smaller direct-detection term and hence, neglected.

$$\begin{aligned}
E_{2x}^{out} &= br(t)e^{jx} \cos \phi + aE_{LO} \\
E_{2y}^{out} &= br(t)e^{jy} \sin \phi + bE_{LO} \\
|E_{2x}^{out}|^2 &= (br(t)e^{jx} \cos \phi + aE_{LO}) (b^*r(t)e^{-jx} \cos \phi + a^*E_{LO}) \\
&= |b|^2r^2(t)\cos^2\phi + |a|^2E_{LO}^2 + a^*br(t)E_{LO} \cos \phi e^{jx} + ab^*r(t)E_{LO} \cos \phi e^{-jx} \\
&= m_2 + n_2 + \frac{1}{3}r(t)E_{LO} \cos \phi e^{jx} e^{-j\frac{2\pi}{3}} + \frac{1}{3}r(t)E_{LO} \cos \phi e^{-jx} e^{j\frac{2\pi}{3}} \\
&= m_2 + n_2 + \frac{1}{3}r(t)E_{LO} \cos \phi 2 \cos \left(x - \frac{2\pi}{3}\right) \\
&= m_2 + n_2 + \frac{2}{3}r(t)E_{LO} \cos \phi \cos \left(x - \frac{2\pi}{3}\right) \\
|E_{2y}^{out}|^2 &= (br(t)e^{jy} \sin \phi + bE_{LO}) (b^*r(t)e^{-jy} \sin \phi + b^*E_{LO}) \\
&= |b|^2r^2(t)\sin^2\phi + |b|^2E_{LO}^2 + bb^*r(t)E_{LO} \sin \phi e^{jy} + b^*br(t)E_{LO} \sin \phi e^{-jy} \\
&= m_2 + n_2 + \frac{2}{3}r(t)E_{LO} \sin \phi \cos y \\
i_2 &= R \left(|E_{2x}^{out}|^2 + |E_{2y}^{out}|^2 \right) \\
&= \frac{2}{3}RE_{LO}r(t) \left[\cos \phi \cos \left(x - \frac{2\pi}{3}\right) + \sin \phi \cos y \right]
\end{aligned}$$

Here, $m_2=|b|^2r^2(t)\cos^2\phi$ or $|b|^2r^2(t)\sin^2\phi$ and $n_2=|a|^2E_{LO}^2$ or $|b|^2E_{LO}^2$. n_2 is a DC-term which will be blocked by the DC-block and m_2 is a much smaller direct-detection term and hence, neglected.

$$\begin{aligned}
E_{3x}^{out} &= br(t)e^{jx} \cos \phi + bE_{LO} \\
E_{3y}^{out} &= br(t)e^{jy} \sin \phi + aE_{LO} \\
|E_{3x}^{out}|^2 &= (br(t)e^{jx} \cos \phi + bE_{LO}) (b^*r(t)e^{-jx} \cos \phi + b^*E_{LO}) \\
&= |b|^2r^2(t)\cos^2\phi + |b|^2E_{LO}^2 + bb^*r(t)E_{LO} \cos \phi e^{jx} + b^*br(t)E_{LO} \cos \phi e^{-jx} \\
&= m_3 + n_3 + \frac{2}{3}r(t)E_{LO} \cos \phi \cos x \\
|E_{3y}^{out}|^2 &= (br(t)e^{jy} \sin \phi + aE_{LO}) (b^*r(t)e^{-jy} \sin \phi + a^*E_{LO}) \\
&= |b|^2r^2(t)\sin^2\phi + |a|^2E_{LO}^2 + a^*br(t)E_{LO} \sin \phi e^{jy} + ab^*r(t)E_{LO} \sin \phi e^{-jy} \\
&= m_3 + n_3 + \frac{2}{3}r(t)E_{LO} \sin \phi \cos \left(y - \frac{2\pi}{3}\right) \\
i_3 &= R \left(|E_{3x}^{out}|^2 + |E_{3y}^{out}|^2 \right) \\
&= \frac{2}{3}RE_{LO}r(t) \left[\cos \phi \cos x + \sin \phi \cos \left(y - \frac{2\pi}{3}\right) \right]
\end{aligned}$$

Here, $m_3=|b|^2r^2(t)\cos^2\phi$ or $|b|^2r^2(t)\sin^2\phi$ and $n_3=|a|^2E_{LO}^2$ or $|b|^2E_{LO}^2$. n_3 is a DC-term which will be blocked by the DC-block and m_3 is a much smaller direct-detection term and hence, neglected.

Derivation of k : The term k will be useful in the derivation of $S(t)$ afterwards.

$$\begin{aligned}
k &= \frac{1}{2}\cos^2\phi \cos\left(2x + \frac{4\pi}{3}\right) + \frac{1}{2}\sin^2\phi \cos\left(2y + \frac{4\pi}{3}\right) + \frac{1}{2}\cos^2\phi \cos\left(2x - \frac{4\pi}{3}\right) + \\
&\frac{1}{2}\sin^2\phi \cos 2y + \frac{1}{2}\cos^2\phi \cos 2x + \frac{1}{2}\sin^2\phi \cos\left(2y - \frac{4\pi}{3}\right) \\
&= \frac{1}{2}\cos^2\phi \left(\cos 2x \cos \frac{4\pi}{3} - \sin 2x \sin \frac{4\pi}{3}\right) + \frac{1}{2}\sin^2\phi \left(\cos 2y \cos \frac{4\pi}{3} - \sin 2y \sin \frac{4\pi}{3}\right) + \\
&\frac{1}{2}\cos^2\phi \left(\cos 2x \cos \frac{4\pi}{3} + \sin 2x \sin \frac{4\pi}{3}\right) + \frac{1}{2}\sin^2\phi \cos 2y + \frac{1}{2}\cos^2\phi \cos 2x + \\
&\frac{1}{2}\sin^2\phi \left(\cos 2y \cos \frac{4\pi}{3} + \sin 2y \sin \frac{4\pi}{3}\right) \\
&= \frac{1}{2}\cos^2\phi \left(-\frac{1}{2}\cos 2x + \frac{\sqrt{3}}{2}\sin 2x\right) + \frac{1}{2}\sin^2\phi \left(-\frac{1}{2}\cos 2y + \frac{\sqrt{3}}{2}\sin 2y\right) + \\
&\frac{1}{2}\cos^2\phi \left(-\frac{1}{2}\cos 2x - \frac{\sqrt{3}}{2}\sin 2x\right) + \frac{1}{2}\sin^2\phi \cos 2y + \frac{1}{2}\cos^2\phi \cos 2x + \\
&\frac{1}{2}\sin^2\phi \left(-\frac{1}{2}\cos 2y + \frac{\sqrt{3}}{2}\sin 2y\right) \\
&= -\frac{1}{4}\cos^2\phi \cos 2x + \frac{\sqrt{3}}{4}\cos^2\phi \sin 2x - \frac{1}{4}\sin^2\phi \cos 2y + \frac{\sqrt{3}}{4}\sin^2\phi \sin 2y + \\
&-\frac{1}{4}\cos^2\phi \cos 2x - \frac{\sqrt{3}}{4}\cos^2\phi \sin 2x + \frac{1}{2}\sin^2\phi \cos 2y + \frac{1}{2}\cos^2\phi \cos 2x \\
&-\frac{1}{4}\sin^2\phi \cos 2y - \frac{\sqrt{3}}{4}\sin^2\phi \sin 2y \\
&= 0
\end{aligned}$$

Finally,

$$\begin{aligned}
S(t) &= i_1^2 + i_2^2 + i_3^2 \\
&= \frac{4}{9}R^2E_{LO}^2r^2(t) \left[\begin{aligned} &\left\{ \cos\phi \cos\left(x + \frac{2\pi}{3}\right) + \sin\phi \cos\left(y + \frac{2\pi}{3}\right) \right\}^2 + \\ &\left\{ \cos\phi \cos\left(x - \frac{2\pi}{3}\right) + \sin\phi \cos y \right\}^2 + \\ &\left\{ \cos\phi \cos x + \sin\phi \cos\left(y - \frac{2\pi}{3}\right) \right\}^2 \end{aligned} \right] \\
&= \frac{4}{9}R^2E_{LO}^2r^2(t) \left[\begin{aligned} &\cos^2\phi \cos^2\left(x + \frac{2\pi}{3}\right) + \sin^2\phi \cos^2\left(y + \frac{2\pi}{3}\right) + \\ &2\cos\phi \cos\left(x + \frac{2\pi}{3}\right) \sin\phi \cos\left(y + \frac{2\pi}{3}\right) + \cos^2\phi \cos^2\left(x - \frac{2\pi}{3}\right) + \\ &\sin^2\phi \cos^2 y + 2\cos\phi \cos\left(x - \frac{2\pi}{3}\right) \sin\phi \cos y + \cos^2\phi \cos^2 x + \\ &\sin^2\phi \cos^2\left(y - \frac{2\pi}{3}\right) + 2\cos\phi \cos x \sin\phi \cos\left(y - \frac{2\pi}{3}\right) \end{aligned} \right] \\
&= \frac{4}{9}R^2E_{LO}^2r^2(t) \left[\begin{aligned} &\frac{1}{2}\cos^2\phi \{1 + \cos(2x + \frac{4\pi}{3})\} + \frac{1}{2}\sin^2\phi \{1 + \cos(2y + \frac{4\pi}{3})\} + \\ &\sin 2\phi \cos\left(x + \frac{2\pi}{3}\right) \cos\left(y + \frac{2\pi}{3}\right) + \frac{1}{2}\cos^2\phi \{1 + \cos(2x - \frac{4\pi}{3})\} + \\ &\frac{1}{2}\sin^2\phi \{1 + \cos 2y\} + \sin 2\phi \cos\left(x - \frac{2\pi}{3}\right) \cos y + \\ &\frac{1}{2}\cos^2\phi \{1 + \cos 2x\} + \frac{1}{2}\sin^2\phi \{1 + \cos(2y - \frac{4\pi}{3})\} \\ &+ \sin 2\phi \cos x \cos\left(y - \frac{2\pi}{3}\right) \end{aligned} \right] \\
&= \frac{4}{9}R^2E_{LO}^2r^2(t) \left[\begin{aligned} &\frac{1}{2}\cos^2\phi + \frac{1}{2}\cos^2\phi \cos(2x + \frac{4\pi}{3}) + \frac{1}{2}\sin^2\phi + \frac{1}{2}\sin^2\phi \cos(2y + \frac{4\pi}{3}) + \\ &\sin 2\phi \cos\left(x + \frac{2\pi}{3}\right) \cos\left(y + \frac{2\pi}{3}\right) + \frac{1}{2}\cos^2\phi + \frac{1}{2}\cos^2\phi \cos(2x - \frac{4\pi}{3}) + \\ &\frac{1}{2}\sin^2\phi + \frac{1}{2}\sin^2\phi \cos 2y + \sin 2\phi \cos\left(x - \frac{2\pi}{3}\right) \cos y + \\ &\frac{1}{2}\cos^2\phi + \frac{1}{2}\cos^2\phi \cos 2x + \frac{1}{2}\sin^2\phi + \frac{1}{2}\sin^2\phi \cos(2y - \frac{4\pi}{3}) \\ &+ \sin 2\phi \cos x \cos\left(y - \frac{2\pi}{3}\right) \end{aligned} \right]
\end{aligned}$$

$$\begin{aligned}
&= \frac{4}{9}R^2E_{LO}^2r^2(t) \left[\begin{aligned} &\frac{3}{2} + \frac{1}{2}\cos^2\phi \cos(2x + \frac{4\pi}{3}) + \frac{1}{2}\sin^2\phi \cos(2y + \frac{4\pi}{3}) + \\ &+ \frac{1}{2}\cos^2\phi \cos(2x - \frac{4\pi}{3}) + \frac{1}{2}\sin^2\phi \cos 2y + \frac{1}{2}\cos^2\phi \cos 2x + \\ &\frac{1}{2}\sin^2\phi \cos(2y - \frac{4\pi}{3}) + \sin 2\phi \cos(x - \frac{2\pi}{3}) \cos y + \\ &\sin 2\phi \cos(x + \frac{2\pi}{3}) \cos(y + \frac{2\pi}{3}) + \sin 2\phi \cos x \cos(y - \frac{2\pi}{3}) \end{aligned} \right] \\
&= \frac{4}{9}R^2E_{LO}^2r^2(t) \left[\frac{3}{2} + k + \sin 2\phi \left\{ \begin{aligned} &(\cos x \cos \frac{2\pi}{3} - \sin x \sin \frac{2\pi}{3})(\cos y \cos \frac{2\pi}{3} - \sin y \sin \frac{2\pi}{3}) + \\ &\cos x (\cos y \cos \frac{2\pi}{3} + \sin y \sin \frac{2\pi}{3}) + \\ &\cos y (\cos x \cos \frac{2\pi}{3} + \sin x \sin \frac{2\pi}{3}) \end{aligned} \right\} \right] \\
&= \frac{4}{9}R^2E_{LO}^2r^2(t) \left[\frac{3}{2} + \sin 2\phi \left\{ \begin{aligned} &(\cos x \cos \frac{2\pi}{3} - \sin x \sin \frac{2\pi}{3})(\cos y \cos \frac{2\pi}{3} - \sin y \sin \frac{2\pi}{3}) + \\ &\cos x (\cos y \cos \frac{2\pi}{3} + \sin y \sin \frac{2\pi}{3}) + \\ &\cos y (\cos x \cos \frac{2\pi}{3} + \sin x \sin \frac{2\pi}{3}) \end{aligned} \right\} \right] \\
&= \frac{4}{9}R^2E_{LO}^2r^2(t) \left[\frac{3}{2} + \sin 2\phi \left\{ \begin{aligned} &(-\frac{1}{2}\cos x - \frac{\sqrt{3}}{2}\sin x)(-\frac{1}{2}\cos y - \frac{\sqrt{3}}{2}\sin y) + \\ &\cos x (-\frac{1}{2}\cos y + \frac{\sqrt{3}}{2}\sin y) + \\ &\cos y (-\frac{1}{2}\cos x + \frac{\sqrt{3}}{2}\sin x) \end{aligned} \right\} \right] \\
&= \frac{4}{9}R^2E_{LO}^2r^2(t) \left[\frac{3}{2} + \sin 2\phi \left\{ \begin{aligned} &\frac{1}{4}\cos x \cos y + \frac{\sqrt{3}}{4}\cos x \sin y + \frac{\sqrt{3}}{4}\sin x \cos y + \\ &\frac{3}{4}\sin x \sin y - \frac{1}{2}\cos x \cos y + \frac{\sqrt{3}}{2}\cos x \sin y \\ &-\frac{1}{2}\cos x \cos y + \frac{\sqrt{3}}{2}\cos y \sin x \end{aligned} \right\} \right] \\
&= \frac{4}{9}R^2E_{LO}^2r^2(t) \left[\frac{3}{2} + \sin 2\phi \left\{ \begin{aligned} &-\frac{3}{4}\cos x \cos y + \frac{3\sqrt{3}}{4}\cos x \sin y + \\ &\frac{3\sqrt{3}}{4}\sin x \cos y + \frac{3}{4}\sin x \sin y \end{aligned} \right\} \right] \\
&= \frac{4}{9}R^2E_{LO}^2r^2(t) \left[\frac{3}{2} + \sin 2\phi \left\{ \begin{aligned} &-\frac{3}{8}\{\cos(x+y) + \cos(x-y)\} + \\ &\frac{3\sqrt{3}}{8}\{\sin(x+y) - \sin(x-y)\} + \\ &\frac{3\sqrt{3}}{8}\{\sin(y+x) - \sin(y-x)\} + \\ &\frac{3}{8}\{\cos(x-y) - \cos(x+y)\} \end{aligned} \right\} \right] \\
&= \frac{4}{9}R^2E_{LO}^2r^2(t) \left[\frac{3}{2} + \sin 2\phi \left\{ -\frac{3}{4}\cos(x+y) + \frac{3\sqrt{3}}{4}\sin(x+y) \right\} \right] \\
&= \frac{4}{9}R^2E_{LO}^2r^2(t) \left[\frac{3}{2} - \frac{3}{2}\sin 2\phi \left\{ \frac{1}{2}\cos(x+y) - \frac{\sqrt{3}}{2}\sin(x+y) \right\} \right] \\
&= \frac{4}{9}R^2E_{LO}^2r^2(t) \left[\frac{3}{2} - \frac{3}{2}\sin 2\phi \left\{ \sin \frac{\pi}{6} \cos(x+y) - \cos \frac{\pi}{6} \sin(x+y) \right\} \right] \\
&= \frac{2}{3}R^2E_{LO}^2r^2(t) \left[1 - \sin 2\phi \sin\left(\frac{\pi}{6} - x - y\right) \right] \\
&= \frac{2}{3}R^2E_{LO}^2r^2(t) \left[1 - \sin 2\phi \sin\left(\frac{\pi}{6} - 4\pi\Delta vt - \psi\right) \right]
\end{aligned}$$

References

- [1] “Cisco Visual Networking Index: Forecast and Trends, 2017 - 2022,” <https://www.cisco.com/c/en/us/solutions/collateral/service-provider/visual-networking-index-vni/white-paper-c11-741490.html>, Tech. Rep., February, 2019.
- [2] “2018 Global Internet Phenomena Report,” <https://www.sandvine.com/hubfs/downloads/phenomena/2018-phenomena-report.pdf>, Tech. Rep., October, 2018.
- [3] “Yole Développement: Silicon Photonics 2018,” <https://www.i-micronews.com/report/product/silicon-photonics-2018.html#description>, Tech. Rep., January, 2018.
- [4] “OECD broadband statistics update,” <http://www.oecd.org/internet/broadband/broadband-statistics-update.htm>, June, 2018.
- [5] “SOITEC photonics SOI,” <https://www.soitec.com/en/products/photonics-soi>, 2018.
- [6] X. Wang, Y. Wang, J. Flueckiger, R. Bojko, A. Liu, A. Reid, J. Pond, N. A. Jaeger, and L. Chrostowski, “Precise control of the coupling coefficient through destructive interference in silicon waveguide Bragg gratings,” *Optics Letters*, vol. 39, no. 19, pp. 5519–5522, 2014.
- [7] R. van der Linden, “Adaptive modulation techniques for passive optical networks,” *Ph. D. Dissertation, Technische Universiteit Eindhoven*, 2018.
- [8] “Ericsson White Paper, 5G Systems, January, 2015.”
- [9] C. Gunn, “CMOS photonics technology overview,” in *Compound Semiconductor Integrated Circuit Symposium, 2006. CSIC 2006. IEEE*. IEEE, 2006, pp. 139–140.
- [10] B. Jalali and S. Fathpour, “Silicon photonics,” *Journal of Lightwave Technology*, vol. 24, no. 12, pp. 4600–4615, 2006.
- [11] “Mellanox,” <http://www.mellanox.com/blog/category/silicon-photonics/>, 2016.

-
- [12] “Finisar,” <http://investor.finisar.com/releaseDetail.cfm?ReleaseID=871808>, 2016.
- [13] “Acacia Communications,” <https://acacia-inc.com/>, 2018.
- [14] “AEPONYX,” <http://www.aeponyx.com/about/>, 2018.
- [15] “Genalyte,” <https://www.genalyte.com/>, 2018.
- [16] “Analog Photonics,” <http://www.analogphotonics.com/about/>, 2018.
- [17] M. Hochberg and T. Baehr-Jones, “Towards fabless silicon photonics,” *Nature Photonics*, vol. 4, no. 8, p. 492, 2010.
- [18] A. E. Lim, T.-Y. Liow, J. Song, C. Li, Q. Fang, X. Tu, N. Duan, K. K. Chen, R. P. C. Tern, C. Peng, B. W. Mun, M. N. Islam, J. S. Park, C. Subbu, and G.-Q. Lo, “Path to silicon photonics commercialization: 25 Gb/s platform development in a CMOS manufacturing foundry line,” in *Optical Fiber Communication Conference*. Optical Society of America, 2014, pp. Th2A–51.
- [19] A. E.-J. Lim, J. Song, Q. Fang, C. Li, X. Tu, N. Duan, K. K. Chen, R. P.-C. Tern, and T.-Y. Liow, “Review of silicon photonics foundry efforts,” *IEEE Journal of Selected Topics in Quantum Electronics*, vol. 20, no. 4, pp. 405–416, 2014.
- [20] A. Narasimha, B. Analui, Y. Liang, T. J. Sleboda, and C. Gunn, “A fully integrated 4×10Gb/s DWDM optoelectronic transceiver in a standard 0.13 μm CMOS SOI,” in *Solid-State Circuits Conference, 2007. ISSCC 2007. Digest of Technical Papers. IEEE International*. IEEE, 2007, pp. 42–586.
- [21] T. Pinguet, B. Analui, G. Masini, V. Sadagopan, and S. Gloeckner, “40-Gbps monolithically integrated transceivers in CMOS photonics,” in *Silicon Photonics III*, vol. 6898. International Society for Optics and Photonics, 2008, p. 689805.
- [22] D. M. Gill, C. Xiong, J. Proesel, J. Rosenberg, J. Ellis-Monaghan, J. Orcutt, M. Khater, D. Viens, Y. A. Vlasov, W. Haensch, and W. M. J. Green, “Demonstration of error free operation up to 32 Gb/s from a CMOS integrated monolithic nano-photonics transmitter,” in *CLEO: Science and Innovations*. Optical Society of America, 2015, pp. STu4F–3.
- [23] P. Dong, “Silicon photonic integrated circuits for wavelength-division multiplexing applications,” *IEEE Journal of Selected Topics in Quantum Electronics*, vol. 22, no. 6, pp. 370–378, 2016.
- [24] C. F. Lam, *Passive Optical Networks: Principles and Practice*. Elsevier, 2011.

-
- [25] C.-H. Lee, W. V. Sorin, and B. Y. Kim, "Fiber to the home using a PON infrastructure," *Journal of Lightwave Technology*, vol. 24, no. 12, pp. 4568–4583, 2006.
- [26] D. Chrissan, "Uni-DSL: One DSL for universal service," *Texas Instruments White Paper (Spay018)*, 2004.
- [27] "FTTH Global perspective by IDATE DigiWorld," <http://www.cercle-credo.com/docs/evenements/idateftthglobalperspective010617public.pdf>, Tech. Rep., June, 2017.
- [28] "Transformation of Wireline Access Networks," <https://ovum.informa.com/resources/product-content/white-paper-transformation-of-wireline-access-networks-requires-smarter-solution>, Tech. Rep., September, 2016.
- [29] S. T. Chu, B. E. Little, W. Pan, T. Kaneko, S. Sato, and Y. Kokubun, "An eight-channel add-drop filter using vertically coupled microring resonators over a cross grid," *IEEE Photonics Technology Letters*, vol. 11, no. 6, pp. 691–693, 1999.
- [30] K. Kintaka, J. Nishii, S. Murata, and S. Ura, "Eight-channel WDM intraboard optical interconnect device by integration of add/drop multiplexers in thin-film waveguide," *Journal of Lightwave Technology*, vol. 28, no. 9, pp. 1398–1403, 2010.
- [31] B. Little, S. Chu, P. Absil, J. Hryniewicz, F. Johnson, F. Seiferth, D. Gill, V. Van, O. King, and M. Trakalo, "Very high-order microring resonator filters for WDM applications," *IEEE Photonics Technology Letters*, vol. 16, no. 10, pp. 2263–2265, 2004.
- [32] C. R. Giles and M. Spector, "The wavelength add/drop multiplexer for lightwave communication networks," *Bell Labs Technical Journal*, vol. 4, no. 1, pp. 207–229, 1999.
- [33] Y. Chen, C. Hu, C. Lee, K. Feng, M. Lu, C.-H. Chang, Y. Tu, and S. Tzeng, "Low-crosstalk and compact optical add-drop multiplexer using a multiport circulator and fiber Bragg gratings," *IEEE Photonics Technology Letters*, vol. 12, no. 10, pp. 1394–1396, 2000.
- [34] D. Wu, Y. Wu, Y. Wang, J. An, and X. Hu, "Four-channel optical add-drop multiplexer based on dual racetrack micro-ring resonators," *Optics Communications*, vol. 354, pp. 386–391, 2015.
- [35] L. Yangyang, T. Yonghui, and Y. Lin, "Integrated reconfigurable optical add-drop multiplexers based on cascaded microring resonators," *Journal of Semiconductors*, vol. 34, no. 9, p. 094012, 2013.

-
- [36] A. Vorckel, M. Monster, W. Henschel, P. H. Bolivar, and H. Kurz, "Asymmetrically coupled silicon-on-insulator microring resonators for compact add-drop multiplexers," *IEEE Photonics Technology Letters*, vol. 15, no. 7, pp. 921–923, 2003.
- [37] J. Wang and L. R. Chen, "Low crosstalk Bragg grating/Mach-Zehnder interferometer optical add-drop multiplexer in silicon photonics," *Optics Express*, vol. 23, no. 20, pp. 26 450–26 459, 2015.
- [38] M. Caverley, R. Boeck, L. Chrostowski, and N. A. Jaeger, "High-speed data transmission through silicon contra-directional grating coupler optical add-drop multiplexers," in *CLEO: QELS Fundamental Science*. Optical Society of America, 2015, pp. JTh2A–41.
- [39] H. Qiu, G. Jiang, T. Hu, H. Shao, P. Yu, J. Yang, and X. Jiang, "FSR-free add-drop filter based on silicon grating-assisted contradirectional couplers," *Optics Letters*, vol. 38, no. 1, pp. 1–3, 2013.
- [40] B. Naghdi and L. R. Chen, "Silicon photonic contradirectional couplers using subwavelength grating waveguides," *Optics Express*, vol. 24, no. 20, pp. 23 429–23 438, 2016.
- [41] J. Jiang, H. Qiu, G. Wang, Y. Li, T. Dai, X. Wang, H. Yu, J. Yang, and X. Jiang, "Broadband tunable filter based on the loop of multimode Bragg grating," *Optics Express*, vol. 26, no. 1, pp. 559–566, 2018.
- [42] H. Yamada, T. Chu, S. Ishida, and Y. Arakawa, "Optical add-drop multiplexers based on Si-wire waveguides," *Applied Physics Letters*, vol. 86, no. 19, p. 191107, 2005.
- [43] W. Shi, H. Yun, C. Lin, M. Greenberg, X. Wang, Y. Wang, S. T. Fard, J. Flueckiger, N. A. Jaeger, and L. Chrostowski, "Ultra-compact, flat-top demultiplexer using anti-reflection contra-directional couplers for CWDM networks on silicon," *Optics Express*, vol. 21, no. 6, pp. 6733–6738, 2013.
- [44] A. D. Simard and S. LaRochelle, "Complex apodized Bragg grating filters without circulators in silicon-on-insulator," *Optics Express*, vol. 23, no. 13, pp. 16 662–16 675, 2015.
- [45] K. Mitsuya, Y. Shoji, and T. Mizumoto, "Demonstration of a silicon waveguide optical circulator," *IEEE Photonics Technology Letters*, vol. 25, no. 8, pp. 721–723, 2013.
- [46] S. Ghosh, S. Keyvaninia, W. Van Roy, T. Mizumoto, G. Roelkens, and R. Baets, "Adhesively bonded Ce: YIG/SOI integrated optical circulator," *Optics Letters*, vol. 38, no. 6, pp. 965–967, 2013.

-
- [47] T. Mizuochi, T. Kitayama, K. Shimizu, and K. Ito, "Interferometric crosstalk-free optical add/drop multiplexer using mach-zehnder-based fiber gratings," *Journal of Lightwave Technology*, vol. 16, no. 2, pp. 265–276, 1998.
- [48] W. Bogaerts, P. De Heyn, T. Van Vaerenbergh, K. De Vos, S. Kumar Selvaraja, T. Claes, P. Dumon, P. Bienstman, D. Van Thourhout, and R. Baets, "Silicon microring resonators," *Laser & Photonics Reviews*, vol. 6, no. 1, pp. 47–73, 2012.
- [49] M. Mirshafiei, R. Brunner, S. Lessard, and D. V. Plant, "A silicon photonic broken race-track resonator for large-scale tuning of FSR," *IEEE Photonics Technology Letters*, vol. 28, no. 5, pp. 565–568, 2016.
- [50] P. D. Morin and L. Chen, "Gires-Tournois interferometers with sidewall Bragg gratings in SOI," in *CLEO: Science and Innovations*. Optical Society of America, 2016, pp. STh4E–8.
- [51] C. A. Barrios, V. Almeida, R. Panepucci, B. Schmidt, and M. Lipson, "Compact silicon tunable Fabry-Perot resonator with low power consumption," *IEEE Photonics Technology Letters*, vol. 16, no. 2, pp. 506–508, 2004.
- [52] J. Song, Q. Fang, S. Tao, T. Liow, M. Yu, G. Lo, and D. Kwong, "Fast and low power Michelson interferometer thermo-optical switch on SOI," *Optics Express*, vol. 16, no. 20, pp. 15304–15311, 2008.
- [53] A. Li, Q. Huang, and W. Bogaerts, "Design of a single all-silicon ring resonator with a 150 nm free spectral range and a 100 nm tuning range around 1550 nm," *Photonics Research*, vol. 4, no. 2, pp. 84–92, 2016.
- [54] C. Madsen, G. Lenz, A. Bruce, M. Cappuzzo, L. Gomez, and R. Scotti, "Integrated all-pass filters for tunable dispersion and dispersion slope compensation," *IEEE Photonics Technology Letters*, vol. 11, no. 12, pp. 1623–1625, 1999.
- [55] L. Chrostowski and K. Iniewski, *High-speed photonics interconnects*. CRC Press, 2013.
- [56] J. Wang and L. Chen, "Multichannel OADM using cascaded Bragg grating/Mach-Zehnder interferometers in SOI," *Electronics Letters*, vol. 51, no. 18, pp. 1431–1433, 2015.
- [57] M. Morsy-Osman, M. Chagnon, M. Poulin, S. Lessard, and D. V. Plant, "224-Gb/s 10-km transmission of PDM PAM-4 at 1.3 μm using a single intensity-modulated laser and a direct-detection MIMO DSP-based receiver," *Journal of Lightwave Technology*, vol. 33, no. 7, pp. 1417–1424, 2015.

-
- [58] Y. Painchaud, M. Poulin, M. Morin, and M. Têtu, "Performance of balanced detection in a coherent receiver," *Optics Express*, vol. 17, no. 5, pp. 3659–3672, 2009.
- [59] M. S. Hai, M. N. Sakib, and O. Liboiron-Ladouceur, "A compact silicon-on-insulator optical hybrid for low loss integration with balanced photodetectors," in *Optical Communication (ECOC 2013), 39th European Conference and Exhibition on*. IET, 2013, pp. 1–3.
- [60] K. Voigt, L. Zimmermann, G. Winzer, H. Tian, B. Tillack, and K. Petermann, "C-band optical 90-degree hybrids in silicon nanowaveguide technology," *IEEE Photonics Technology Letters*, vol. 23, no. 23, pp. 1769–1771, 2011.
- [61] L. Xu, Y. Wang, D. Patel, M. Morsy-Osman, R. Li, M. Hui, M. Parvizi, N. Ben-Hamida, and D. V. Plant, "Ultra-broadband and ultra-compact optical 90° hybrid based on 2×4 MMI coupler with subwavelength gratings on silicon-on-insulator," in *Optical Fiber Communication Conference*. Optical Society of America, 2018, pp. M3I–7.
- [62] C. Xie, P. J. Winzer, G. Raybon, A. H. Gnauck, B. Zhu, T. Geisler, and B. Edvold, "Colorless coherent receiver using 3×3 coupler hybrids and single-ended detection," *Optics Express*, vol. 20, no. 2, pp. 1164–1171, 2012.
- [63] P. Reyes-Iglesias, A. Ortega-Moñux, and I. Molina-Fernández, "Colorless monolithically integrated 120° downconverter," *Optics Express*, vol. 21, no. 20, pp. 23 048–23 057, 2013.
- [64] I. N. Cano, A. Lerín, V. Polo, and J. Prat, "Polarization independent single-PD coherent ONU receiver with centralized scrambling in udWDM-PONs," in *Optical Communication (ECOC), 2014 European Conference on*. IEEE, 2014, pp. 1–3.
- [65] J. A. Altabas, G. S. Valdecasa, M. Didriksen, J. A. Lazaro, I. Garces, I. T. Monroy, and J. B. Jensen, "Real-time 10Gbps polarization independent quasicohherent receiver for NG-PON2 access networks," in *Optical Fiber Communication Conference*. Optical Society of America, 2018, pp. Th1A–3.
- [66] Z. Lu, D. Celo, P. Dumais, E. Bernier, and L. Chrostowski, "Comparison of photonic 2×2 3-dB couplers for 220 nm silicon-on-insulator platforms," in *2015 IEEE 12th International Conference on Group IV Photonics (GFP)*. IEEE, 2015, pp. 57–58.
- [67] P. Reyes-Iglesias, A. Ortega-Moñux, and I. Molina-Fernández, "Enhanced monolithically integrated coherent 120° downconverter with high fabrication yield," *Optics Express*, vol. 20, no. 21, pp. 23 013–23 018, 2012.

-
- [68] P. Dong, C. Xie, and L. L. Buhl, "Monolithic polarization diversity coherent receiver based on 120-degree optical hybrids on silicon," *Optics Express*, vol. 22, no. 2, pp. 2119–2125, 2014.
- [69] D. W. Kim, M. H. Lee, Y. Kim, and K. H. Kim, "Ultracompact transverse magnetic mode-pass filter based on one-dimensional photonic crystals with subwavelength structures," *Optics Express*, vol. 24, no. 19, pp. 21 560–21 565, 2016.
- [70] J. Chi, H. Liu, N. Huang, and Z. Wang, "High-performance transverse magnetic mode-pass polarizer based on silicon nitride–silicon subwavelength grating waveguide for mid-infrared wavelengths," *Applied Physics Express*, vol. 11, no. 4, p. 042005, 2018.
- [71] T. K. Ng, M. Z. M. Khan, A. Al-Jabr, and B. S. Ooi, "Analysis of CMOS compatible Cu-based TM-pass optical polarizer," *IEEE Photonics Technology Letters*, vol. 24, no. 9, pp. 724–726, 2012.
- [72] X. Guan, P. Xu, Y. Shi, and D. Dai, "Ultra-compact broadband TM-pass polarizer using a silicon hybrid plasmonic waveguide grating," in *Asia Communications and Photonics Conference*. Optical Society of America, 2013, pp. ATH4A–2.
- [73] B. Bai, L. Liu, R. Chen, and Z. Zhou, "Low loss, compact TM-pass polarizer based on hybrid plasmonic grating," *IEEE Photonics Technology Letters*, vol. 29, no. 7, pp. 607–610, 2017.
- [74] X. Hu and J. Wang, "Ultrabroadband compact graphene–silicon TM-pass polarizer," *IEEE Photonics Journal*, vol. 9, no. 2, pp. 1–10, 2017.
- [75] L. Sánchez, S. Lechago, and P. Sanchis, "Ultra-compact TE and TM pass polarizers based on vanadium dioxide on silicon," *Optics Letters*, vol. 40, no. 7, pp. 1452–1455, 2015.
- [76] X. Guan, P. Chen, S. Chen, P. Xu, Y. Shi, and D. Dai, "Low-loss ultracompact transverse-magnetic-pass polarizer with a silicon subwavelength grating waveguide," *Optics Letters*, vol. 39, no. 15, pp. 4514–4517, 2014.
- [77] V. Houtsma and D. van Veen, "A study of options for high-speed TDM-PON beyond 10G," *Journal of Lightwave Technology*, vol. 35, no. 4, pp. 1059–1066, 2017.
- [78] D. van Veen, V. Houtsma, and H. Chow, "Demonstration of symmetrical 25 Gbps Quaternary PAM/Duobinary TDM-PON with multilevel interleaving of users," in *Optical Communication (ECOC), 2015 European Conference on*. IEEE, 2015, pp. 1–3.

-
- [79] H. Zhang, S. Fu, J. Man, W. Chen, X. Song, and L. Zeng, "30km downstream transmission using $4 \times 25\text{Gb/s}$ 4-PAM modulation with commercial 10Gbps TOSA and ROSA for 100Gb/s-PON," in *Optical Fiber Communications Conference and Exhibition (OFC)*, 2014. IEEE, 2014, pp. 1–3.
- [80] V. Houtsma and D. van Veen, "Demonstration of symmetrical 25 Gbps TDM-PON with 31.5 dB optical power budget using only 10 Gbps optical components," in *Optical Communication (ECOC), 2015 European Conference on*. IEEE, 2015, pp. 1–3.
- [81] J. Gao, "Demonstration of the first 29dB power budget of 25-Gb/s 4-PAM system without optical amplifier for next generation access network," in *Optical Fiber Communications Conference and Exhibition (OFC)*, 2016. IEEE, 2016, pp. 1–3.
- [82] D. Thomson, A. Zilkie, J. E. Bowers, T. Komljenovic, G. T. Reed, L. Vivien, D. Marris-Morini, E. Cassan, L. Viro, J.-M. Fédéli, J.-M. Hartmann, J. H. Schmid, D.-X. Xu, F. Boeuf, P. O'Brien, G. Z. Mashanovich, and M. Nedeljkovic, "Roadmap on silicon photonics," *Journal of Optics*, vol. 18, no. 7, p. 073003, 2016.
- [83] P. Dong, X. Liu, S. Chandrasekhar, L. L. Buhl, R. Aroca, Y. Baeyens, and Y.-K. Chen, "224-Gb/s PDM-16-QAM modulator and receiver based on silicon photonic integrated circuits," in *Optical Fiber Communication Conference and Exposition and the National Fiber Optic Engineers Conference (OFC/NFOEC)*, 2013. IEEE, 2013, pp. 1–3.
- [84] C. Doerr, L. Chen, T. Nielsen, R. Aroca, L. Chen, M. Banaee, S. Azemati, G. McBrien, S. Y. Park, J. Geyer, B. Guan, B. Mikkelsen, C. Ramussen, M. Givehchi, Z. Wang, B. Potsaid, H. C. Lee, E. Swanson, and J. G. Fujimoto, "O, E, S, C, and L band silicon photonics coherent modulator/receiver," in *Optical Fiber Communications Conference and Exhibition (OFC)*, 2016. IEEE, 2016, pp. 1–3.
- [85] L. Chen, C. Doerr, R. Aroca, S. Park, J. Geyer, T. Nielsen, C. Rasmussen, and B. Mikkelsen, "Silicon photonics for 100G-and-beyond coherent transmissions," in *Optical Fiber Communications Conference and Exhibition (OFC)*, 2016. OSA, 2016, pp. 1–3.
- [86] M. Morsy-Osman, M. Chagnon, X. Xu, Q. Zhuge, M. Poulin, Y. Painchaud, M. Pelletier, C. Paquet, and D. V. Plant, "Analytical and experimental performance evaluation of an integrated Si-photonic balanced coherent receiver in a colorless scenario," *Optics Express*, vol. 22, no. 5, pp. 5693–5730, 2014.
- [87] Y. Painchaud, M. Pelletier, M. Poulin, F. Pelletier, C. Latrasse, G. Robidoux, S. Savard, J.-F. Gagné, V. Trudel, M.-J. Picard *et al.*, "Ultra-compact coherent receiver based on hybrid

-
- integration on silicon," in *Optical Fiber Communication Conference and Exposition and the National Fiber Optic Engineers Conference (OFC/NFOEC)*, 2013. IEEE, 2013, pp. 1–3.
- [88] C. R. Doerr, P. J. Winzer, Y.-K. Chen, S. Chandrasekhar, M. S. Rasras, L. Chen, T.-Y. Liow, K.-W. Ang, and G.-Q. Lo, "Monolithic polarization and phase diversity coherent receiver in silicon," *Journal of Lightwave Technology*, vol. 28, no. 4, pp. 520–525, 2010.
- [89] S. Gudyriev, C. Kress, H. Zwickel, J. N. Kemal, S. Lischke, Z. Lars, C. Koos, and C. Scheytt, "Coherent ePIC receiver for 64 GBaud QPSK in 0.25 μm photonic BiCMOS technology," *Journal of Lightwave Technology*, 2018.
- [90] J. B. Jensen, R. Rodes, A. Caballero, N. Cheng, D. Zibar, and I. T. Monroy, "VCSEL based coherent PONs," *Journal of Lightwave Technology*, vol. 32, no. 8, pp. 1423–1433, 2014.
- [91] M. G. Saber, M. Morsy-Osman, M. Hui, E. El-Fiky, G. Vall-Llosera, B. Dortschy, P. J. Urban, F. Cavaliere, S. Lessard, and D. V. Plant, "DSP-free 25 Gbit/s PAM-4 transmission using 10G transmitter and coherent amplification," *IEEE Photonics Technology Letters*, vol. 30, no. 17, pp. 1547–1550, 2018.
- [92] M. Artiglia, M. Presi, F. Bottoni, M. Rannello, and E. Ciaramella, "Polarization-independent coherent real-time analog receiver for PON access systems," *Journal of Lightwave Technology*, vol. 34, no. 8, pp. 2027–2033, 2016.
- [93] A. Gallet, G. Levaufre, A. Accard, D. Make, J.-G. Provost, R. Brenot, A. Shen, N. Lagay, J. Decobert, S. Malhouitre, S. Olivier, and G.-H. Duan, "Hybrid III-V on silicon integrated distributed feedback laser and ring resonator for 25 Gb/s future access networks," *Journal of Lightwave Technology*, vol. 36, no. 8, pp. 1498–1502, 2018.
- [94] M. G. Saber, Z. Xing, D. Patel, E. El-Fiky, N. Abadía, Y. Wang, and D. V. Plant, "A compact silicon photonic add-drop multiplexer with misaligned sidewall Bragg gratings in a MZI," in *2017 Conference on Lasers and Electro-Optics (CLEO)*. IEEE, 2017, pp. 1–2.
- [95] M. G. Saber, Z. Xing, D. Patel, E. El-Fiky, N. Abadia, Y. Wang, M. Jacques, M. Morsy-Osman, and D. V. Plant, "A CMOS compatible ultra-compact silicon photonic optical add-drop multiplexer with misaligned sidewall Bragg gratings," *IEEE Photonics Journal*, vol. 9, no. 3, pp. 1–10, 2017.
- [96] M. G. Saber, Z. Xing, E. El-Fiky, D. Patel, L. Xu, N. Abadía, and D. V. Plant, "Transversely coupled Fabry-Perot resonators in SOI," in *CLEO: Science and Innovations*. Optical Society of America, 2017, pp. SM1N–4.

-
- [97] M. G. Saber, Y. Wang, E. El-Fiky, D. Patel, K. A. Shahriar, M. S. Alam, M. Jacques, Z. Xing, L. Xu, N. Abadía, and D. Plant, "Transversely coupled Fabry-Perot resonators with Bragg grating reflectors," *Optics Letters*, vol. 43, no. 1, pp. 13–16, 2018.
- [98] M. G. Saber, N. Abadía, Y. Wang, and D. V. Plant, "Fabry-Perot resonators with transverse coupling on SOI using loop mirrors," *Optics Communications*, vol. 415, pp. 121–126, 2018.
- [99] M. G. Saber, E. El-Fiky, D. Patel, M. Morsy-Osman, D. V. Plant, G. Vall-llosera, P. J. Urban, and B. Dortschy, "A silicon-on-insulator 120° optical hybrid based on 3×3 multimode interference coupler," in *Photonics North (PN), 2017*. IEEE, 2017, pp. 1–1.
- [100] M. G. Saber, N. Abadía, and D. V. Plant, "CMOS compatible all-silicon TM pass polarizer based on highly doped silicon waveguide," *Optics Express*, vol. 26, no. 16, pp. 20 878–20 887, 2018.
- [101] M. Artiglia, R. Corsini, M. Presi, F. Bottoni, G. Cossu, and E. Ciaramella, "Coherent systems for low-cost 10 Gb/s optical access networks," *Journal of Lightwave Technology*, vol. 33, no. 15, pp. 3338–3344, 2015.
- [102] M. G. Saber, M. Osman, D. Patel, A. Samani, E. El-Fiky, M. S. Alam, K. A. Shahriar, Z. Xing, M. Jacques, B. Dortschy, G. Vall-Llosera, P. J. Urban, F. Cavaliere, S. Lessard, and D. V. Plant, "Demonstration of a 120° hybrid based simplified coherent receiver on SOI for high speed PON applications," *Optics Express*, vol. 26, no. 24, pp. 31 222–31 232, 2018.
- [103] M. G. Saber, E. El-Fiky, Z. Xing, M. Morsy-Osman, D. Patel, A. Samani, M. S. Alam, K. A. Shahriar, L. Xu, G. Vall-Llosera, B. Dortschy, P. J. Urban, F. Cavaliere, S. Lessard, and D. V. Plant, "25 and 50 Gb/s/ λ PAM-4 transmission over 43 and 21 km using a simplified coherent receiver on SOI," *IEEE Photonics Technology Letters*, vol. 31, no. 10, pp. 799–802, 2019.
- [104] "Applied Nanotools Inc. Nano SOI process," <https://www.appliednt.com/nanosoi/>, Applied Nanotools Inc., 2017.
- [105] L. Liao, A. Liu, S. Pang, and M. J. Paniccia, "Tunable Bragg grating filters in SOI waveguides," in *Integrated Photonics Research*. Optical Society of America, 2004, p. IThE2.
- [106] Q. Fang, J. F. Song, X. Tu, L. Jia, X. Luo, M. B. Yu, and G. Q. Lo, "Carrier-induced silicon Bragg grating filters with a pin junction," *IEEE Photonics Technology Letters*, vol. 25, no. 9, pp. 810–812, 2013.

-
- [107] S. Homampour, M. P. Bulk, P. E. Jessop, and A. P. Knights, "Thermal tuning of planar Bragg gratings in silicon-on-insulator rib waveguides," *Physica Status Solidi C*, vol. 6, no. S1 1, pp. S240–S243, 2009.
- [108] L. B. Soldano and E. C. Pennings, "Optical multi-mode interference devices based on self-imaging: principles and applications," *Journal of Lightwave Technology*, vol. 13, no. 4, pp. 615–627, 1995.
- [109] T. Koonen, "Fiber to the Home/Fiber to the premises: what, where, and when?" *Proceedings of the IEEE*, vol. 94, no. 5, pp. 911–934, 2006.
- [110] L. G. Kazovsky, N. Cheng, W.-T. Shaw, D. Gutierrez, and S.-W. Wong, *Broadband Optical Access Networks*. John Wiley & Sons, 2011.
- [111] Y. Ota, R. G. Swartz, V. D. Archer, S. K. Korotky, M. Banu, and A. E. Dunlop, "High-speed, burst-mode, packet-capable optical receiver and instantaneous clock recovery for optical bus operation," *Journal of Lightwave Technology*, vol. 12, no. 2, pp. 325–331, 1994.
- [112] T. Kodama, N. Wada, G. Cincotti, and K.-i. Kitayama, "Asynchronous OCDM-based 10 G-PON using cascaded multiport E/Ds to suppress MAI noise," *Journal of Lightwave Technology*, vol. 31, no. 20, pp. 3258–3266, 2013.
- [113] C.-W. Chow, C.-H. Yeh, C. Wang, C. Wu, S. Chi, and C. Lin, "Studies of OFDM signal for broadband optical access networks," *IEEE Journal on Selected Areas in Communications*, vol. 28, no. 6, 2010.
- [114] M. S. Erkılınç, D. Lavery, K. Shi, B. C. Thomsen, R. I. Killey, S. J. Savory, and P. Bayvel, "Comparison of low complexity coherent receivers for UDWDM-PONs (λ -to-the-user)," *Journal of Lightwave Technology*, vol. 36, no. 16, pp. 3453–3464, 2018.
- [115] E. Harstead, D. van Veen, V. Houtsma, and P. Dom, "Technology roadmap for time-division multiplexed passive optical networks (TDM PONs)," *Journal of Lightwave Technology*, vol. 37, no. 2, pp. 657–664, 2019.
- [116] D. Faulkner, R. Mistry, T. Rowbotham, K. Okada, W. Warzanskyj, A. Zylbersztejn, and Y. Picault, "The full services access networks initiative," *IEEE Communications Magazine*, vol. 35, no. 4, pp. 58–68, 1997.
- [117] P. W. Shumate, "Fiber-to-the-home: 1977–2007," *Journal of Lightwave Technology*, vol. 26, no. 9, pp. 1093–1103, 2008.

-
- [118] “Memorandum of Understanding (MoU) and Cooperation Agreements [MoU between ITU-T and IEEE Communications Society (ComSoc)],” <https://www.itu.int/en/ITU-T/extcoop/Documents/mou/itu-t-ieee-mou.pdf>, 2008.
- [119] “IEEE P802.3ca 50G-EPON Task Force,” <http://www.ieee802.org/3/ca/>, 2016.
- [120] V. Houtsma, D. van Veen, and E. Harstead, “Recent progress on standardization of next-generation 25, 50, and 100G EPON,” *Journal of Lightwave Technology*, vol. 35, no. 6, pp. 1228–1234, 2017.
- [121] K. Zhang, Q. Zhuge, H. Xin, Z. Xing, M. Xiang, S. Fan, L. Yi, W. Hu, and D. V. Plant, “Demonstration of 50Gb/s/ λ symmetric PAM4 TDM-PON with 10G-class optics and DSP-free ONUs in the O-band,” in *2018 Optical Fiber Communications Conference and Exposition (OFC)*. IEEE, 2018, pp. 1–3.
- [122] J. Zhang, J. S. Wey, J. Yu, Z. Tu, B. Yang, W. Yang, Y. Guo, X. Huang, and Z. Ma, “Symmetrical 50-Gb/s/ λ PAM-4 TDM-PON in O-band with DSP and semiconductor optical amplifier supporting PR-30 link loss budget,” in *Optical Fiber Communication Conference*. Optical Society of America, 2018, pp. M1B–4.
- [123] X. Tang, Y. Qiao, J. Zhou, M. Guo, J. Qi, S. Liu, X. Xu, and Y. Lu, “Equalization scheme of C-band PAM4 signal for optical amplified 50-Gb/s PON,” *Optics Express*, vol. 26, no. 25, pp. 33 418–33 427, 2018.
- [124] G. T. Reed, *Silicon Photonics: The State of The Art*. John Wiley & Sons, 2008.
- [125] “Lumerical Interconnect,” <https://www.lumerical.com/tcad-products/interconnect/>.
- [126] “Si-EPIC Ebeam PDK,” https://github.com/lukasc-ubc/SiEPIC_EBeam_PDK.
- [127] R. J. Bojko, J. Li, L. He, T. Baehr-Jones, M. Hochberg, and Y. Aida, “Electron beam lithography writing strategies for low loss, high confinement silicon optical waveguides,” *Journal of Vacuum Science & Technology B, Nanotechnology and Microelectronics: Materials, Processing, Measurement, and Phenomena*, vol. 29, no. 6, p. 06F309, 2011.
- [128] Y. Wang, X. Wang, J. Flueckiger, H. Yun, W. Shi, R. Bojko, N. A. Jaeger, and L. Chrostowski, “Focusing sub-wavelength grating couplers with low back reflections for rapid prototyping of silicon photonic circuits,” *Optics Express*, vol. 22, no. 17, pp. 20 652–20 662, 2014.
- [129] A. D. Simard, N. Belhadj, Y. Painchaud, and S. LaRochelle, “Apodized silicon-on-insulator Bragg gratings,” *IEEE Photonics Technology Letters*, vol. 24, no. 12, pp. 1033–1035, 2012.

-
- [130] J.-W. Hoste, S. Werquin, T. Claes, and P. Bienstman, "Conformational analysis of proteins with a dual polarisation silicon microring," *Optics Express*, vol. 22, no. 3, pp. 2807–2820, 2014.
- [131] Y. Liu, Y. Hsu, C.-W. Chow, L.-G. Yang, C.-H. Yeh, Y.-C. Lai, and H.-K. Tsang, "110 GHz hybrid mode-locked fiber laser with enhanced extinction ratio based on nonlinear silicon-on-insulator micro-ring-resonator (SOI MRR)," *Laser Physics Letters*, vol. 13, no. 3, p. 035101, 2016.
- [132] A. M. Armani and K. J. Vahala, "Heavy water detection using ultra-high-Q microcavities," *Optics Letters*, vol. 31, no. 12, pp. 1896–1898, 2006.
- [133] B. G. Lee, B. A. Small, K. Bergman, Q. Xu, and M. Lipson, "Transmission of high-data-rate optical signals through a micrometer-scale silicon ring resonator," *Optics Letters*, vol. 31, no. 18, pp. 2701–2703, 2006.
- [134] S. Xiao, M. H. Khan, H. Shen, and M. Qi, "A highly compact third-order silicon microring add-drop filter with a very large free spectral range, a flat passband and a low delay dispersion," *Optics Express*, vol. 15, no. 22, pp. 14765–14771, 2007.
- [135] W. Urquhart, M. Brierley, C. Millar, and S. Mallinson, "Transversely coupled fiber resonators," in *Conference on Lasers and Electro-Optics*. Optical Society of America, 1986, p. FN2.
- [136] M. Brierley and P. Urquhart, "Transversely coupled fiber Fabry-Perot resonators: performance characteristics," *Applied Optics*, vol. 26, no. 22, pp. 4841–4845, 1987.
- [137] P. Barnsley, P. Urquhart, C. Millar, and M. Brierley, "Fiber Fox-Smith resonators: application to single-longitudinal-mode operation of fiber lasers," *Journal of Optical Society of America A*, vol. 5, no. 8, pp. 1339–1346, 1988.
- [138] P. Urquhart, "Transversely coupled fiber Fabry-Perot resonator: theory," *Applied Optics*, vol. 26, no. 3, pp. 456–463, 1987.
- [139] C. Ciminelli, F. Dell'Olivo, D. Conteduca, C. Campanella, and M. Armenise, "High performance SOI microring resonator for biochemical sensing," *Optics & Laser Technology*, vol. 59, pp. 60–67, 2014.
- [140] Y. Wang, W. Shi, X. Wang, Z. Lu, M. Caverley, R. Bojko, L. Chrostowski, and N. A. Jaeger, "Design of broadband subwavelength grating couplers with low back reflection," *Optics Letters*, vol. 40, no. 20, pp. 4647–4650, 2015.

-
- [141] Z. Lu, H. Yun, Y. Wang, Z. Chen, F. Zhang, N. A. Jaeger, and L. Chrostowski, "Broadband silicon photonic directional coupler using asymmetric-waveguide based phase control," *Optics Express*, vol. 23, no. 3, pp. 3795–3808, 2015.
- [142] V. Donzella, A. Sherwali, J. Flueckiger, S. M. Grist, S. T. Fard, and L. Chrostowski, "Design and fabrication of soi micro-ring resonators based on sub-wavelength grating waveguides," *Optics Express*, vol. 23, no. 4, pp. 4791–4803, 2015.
- [143] X. Jiang, Y. Yang, H. Zhang, J. Peng, Y. Zhang, C. Qiu, and Y. Su, "Design and experimental demonstration of a compact silicon photonic interleaver based on an interfering loop with wide spectral range," *Journal of Lightwave Technology*, vol. 35, no. 17, pp. 3765–3771, 2017.
- [144] M. Ren, J. Pu, V. Krishnamurthy, L. Gonzaga, Y. Toh, F. Tjiptoharsono, Y. Yang, K. Ng, and Q. Wang, "A theoretical and experimental study of silicon Y-branch micro-loop reflectors," *IEEE Photonics Technology Letters*, vol. 28, no. 24, pp. 2811–2814, 2016.
- [145] A. Delâge, D.-X. Xu, R. W. McKinnon, E. Post, P. Waldron, J. Lapointe, C. Storey, A. Densmore, S. Janz, B. Lamontagne, P. Cheben, and J. H. Schmid, "Wavelength-dependent model of a ring resonator sensor excited by a directional coupler," *Journal of Lightwave Technology*, vol. 27, no. 9, pp. 1172–1180, 2009.
- [146] W. McKinnon, D.-X. Xu, C. Storey, E. Post, A. Densmore, A. Delâge, P. Waldron, J. Schmid, and S. Janz, "Extracting coupling and loss coefficients from a ring resonator," *Optics Express*, vol. 17, no. 21, pp. 18971–18982, 2009.
- [147] "Propagation loss of fully-etched 220 nm SOI devices," <https://www.appliednt.com/nanosoi/>, Applied Nanotools Inc., 2017.
- [148] S. J. Savory, "Digital filters for coherent optical receivers," *Optics Express*, vol. 16, no. 2, pp. 804–817, 2008.
- [149] E. Ip, A. P. T. Lau, D. J. Barros, and J. M. Kahn, "Coherent detection in optical fiber systems," *Optics Express*, vol. 16, no. 2, pp. 753–791, 2008.
- [150] J. M. Kahn and K.-P. Ho, "Spectral efficiency limits and modulation/detection techniques for DWDM systems," *IEEE Journal of Selected Topics in Quantum Electronics*, vol. 10, no. 2, pp. 259–272, 2004.
- [151] J. M. Kahn and D. A. Miller, "Communications expands its space," *Nature Photonics*, vol. 11, no. 1, pp. 5–8, 2017.

-
- [152] M. Morsy-Osman, M. Sowailem, E. El-Fiky, T. Goodwill, T. Hoang, S. Lessard, and D. V. Plant, "DSP-free coherent-lite transceiver for next generation single wavelength optical intra-datacenter interconnects," *Optics Express*, vol. 26, no. 7, pp. 8890–8903, 2018.
- [153] P. Reyes-Iglesias, I. Molina-Fernández, A. Moscoso-Mártir, and A. Ortega-Moñux, "High-performance monolithically integrated 120° downconverter with relaxed hardware constraints," *Optics Express*, vol. 20, no. 5, pp. 5725–5741, 2012.
- [154] P. A. Besse, M. Bachmann, H. Melchior, L. B. Soldano, and M. K. Smit, "Optical bandwidth and fabrication tolerances of multimode interference couplers," *Journal of Lightwave Technology*, vol. 12, no. 6, pp. 1004–1009, 1994.
- [155] "Lumerical MODE solutions," <https://www.lumerical.com/tcad-products/mode/EME>, 2016.
- [156] W. H. De Krom, "Sensitivity degradation of an optical (2×2) and a (3×3) phase diversity ASK receiver due to gain imbalance and nonideal phase relations of the optical hybrid," *Journal of Lightwave Technology*, vol. 9, no. 11, pp. 1593–1601, 1991.
- [157] Y. A. Vlasov, "Silicon CMOS-integrated nano-photonics for computer and data communications beyond 100G," *IEEE Communications Magazine*, vol. 50, no. 2, pp. 567–572, 2012.
- [158] D. Dai, L. Liu, S. Gao, D.-X. Xu, and S. He, "Polarization management for silicon photonic integrated circuits," *Laser & Photonics Reviews*, vol. 7, no. 3, pp. 303–328, 2013.
- [159] T. Barwicz, M. R. Watts, M. A. Popović, P. T. Rakich, L. Socci, F. X. Kärtner, E. P. Ippen, and H. I. Smith, "Polarization-transparent microphotonic devices in the strong confinement limit," *Nature Photonics*, vol. 1, no. 1, pp. 57–60, 2007.
- [160] N. Abadía, X. Dai, Q. Lu, W.-H. Guo, D. Patel, D. V. Plant, and J. F. Donegan, "Highly fabrication tolerant InP based polarization beam splitter based on pin structure," *Optics Express*, vol. 25, no. 9, pp. 10 070–10 077, 2017.
- [161] E. Elfiky, A. Samani, D. Patel, and D. Plant, "A high extinction ratio, broadband, and compact polarization beam splitter enabled by cascaded MMIs on silicon-on-insulator," in *Optical Fiber Communication Conference*. Optical Society of America, 2016, pp. W2A–8.
- [162] W. D. Sacher, T. Barwicz, B. J. Taylor, and J. K. Poon, "Polarization rotator-splitters in standard active silicon photonics platforms," *Optics Express*, vol. 22, no. 4, pp. 3777–3786, 2014.

-
- [163] Y. Huang, S. Zhu, H. Zhang, T.-Y. Liow, and G.-Q. Lo, "CMOS compatible horizontal nanoplasmonic slot waveguides TE-pass polarizer on silicon-on-insulator platform," *Optics Express*, vol. 21, no. 10, pp. 12 790–12 796, 2013.
- [164] M. Alam, J. S. Aitchison, and M. Mojahedi, "Compact hybrid TM-pass polarizer for silicon-on-insulator platform," *Applied Optics*, vol. 50, no. 15, pp. 2294–2298, 2011.
- [165] M. Alam, J. S. Aitchison, and M. Mojahedi, "Compact and silicon-on-insulator-compatible hybrid plasmonic TE-pass polarizer," *Optics Letters*, vol. 37, no. 1, pp. 55–57, 2012.
- [166] D. Dai, Z. Wang, N. Julian, and J. E. Bowers, "Compact broadband polarizer based on shallowly-etched silicon-on-insulator ridge optical waveguides," *Optics Express*, vol. 18, no. 26, pp. 27 404–27 415, 2010.
- [167] Y. Xiong, D.-X. Xu, J. H. Schmid, P. Cheben, and N. Y. Winnie, "High extinction ratio and broadband silicon TE-pass polarizer using subwavelength grating index engineering," *IEEE Photonics Journal*, vol. 7, no. 5, pp. 1–7, 2015.
- [168] X. Yin, X. Ke, L. Chen, T. Zhang, J. Li, Z. Zhu, and X. Li, "Ultra-broadband TE-pass polarizer using a cascade of multiple few-layer graphene embedded silicon waveguides," *Journal of Lightwave Technology*, vol. 34, no. 13, pp. 3181–3187, 2016.
- [169] M. G. Saber and R. H. Sagor, "Characteristics of symmetric surface plasmon polariton mode in glass–metal–glass waveguide," *Plasmonics*, vol. 8, no. 4, pp. 1621–1625, 2013.
- [170] M. G. Saber, R. H. Sagor, A. Al Noor, and M. T. Al-Amin, "Numerical investigation of SPP propagation at the nano-scale MDM waveguides with a combiner," *Photonics Letters of Poland*, vol. 5, no. 3, pp. 115–117, 2013.
- [171] X. Sun, M. Mojahedi, and J. S. Aitchison, "Low insertion loss hybrid plasmonic TE-pass polarizer," in *Lasers and Electro-Optics (CLEO), 2016 Conference on*. IEEE, 2016, pp. 1–2.
- [172] D.-X. Xu, J. H. Schmid, G. T. Reed, G. Z. Mashanovich, D. J. Thomson, M. Nedeljkovic, X. Chen, D. Van Thourhout, S. Keyvaninia, and S. K. Selvaraja, "Silicon photonic integration platform: Have we found the sweet spot?" *IEEE Journal of Selected Topics in Quantum Electronics*, vol. 20, no. 4, pp. 189–205, 2014.
- [173] X. Xiao, H. Xu, X. Li, Z. Li, T. Chu, Y. Yu, and J. Yu, "High-speed, low-loss silicon mach-zehnder modulators with doping optimization," *Optics Express*, vol. 21, no. 4, pp. 4116–4125, 2013.

-
- [174] S. Keyvaninia, G. Roelkens, D. Van Thourhout, C. Jany, M. Lamponi, A. Le Liepvre, F. Lelarge, D. Make, G.-H. Duan, D. Bordel, and J.-M. Fedeli, "Demonstration of a heterogeneously integrated III-V/SOI single wavelength tunable laser," *Optics Express*, vol. 21, no. 3, pp. 3784–3792, 2013.
- [175] L. Liu, Q. Deng, and Z. Zhou, "Manipulation of beat length and wavelength dependence of a polarization beam splitter using a subwavelength grating," *Optics Letters*, vol. 41, no. 21, pp. 5126–5129, 2016.
- [176] Y. Huang, Z. Tu, H. Yi, Y. Li, X. Wang, and W. Hu, "Polarization beam splitter based on cascaded step-size multimode interference coupler," *Optical Engineering*, vol. 52, no. 7, pp. 077 103–077 103, 2013.
- [177] C. Li and D. Dai, "Compact polarization beam splitter for silicon photonic integrated circuits with a 340-nm-thick silicon core layer," *Optics Letters*, vol. 42, no. 21, pp. 4243–4246, 2017.
- [178] M.-S. Rouified, C. G. Littlejohns, G. X. Tina, Q. Haodong, T. Hu, Z. Zhang, C. Liu, G. T. Reed, and H. Wang, "Low loss SOI waveguides and MMIs at the MIR wavelength of 2 μm ," *IEEE Photonics Technology Letters*, vol. 28, no. 24, pp. 2827–2829, 2016.
- [179] G. V. Naik, V. M. Shalaev, and A. Boltasseva, "Alternative plasmonic materials: beyond gold and silver," *Advanced Materials*, vol. 25, no. 24, pp. 3264–3294, 2013.
- [180] D. Linaschke, N. Schilling, I. Dani, U. Klotzbach, and C. Leyens, "Highly n-doped surfaces on n-type silicon wafers by laser-chemical processes," *Energy Procedia*, vol. 55, pp. 247–254, 2014.
- [181] R. A. Soref and B. R. Bennett, "Electrooptical effects in silicon," *IEEE Journal of Quantum Electronics*, vol. 23, no. 1, pp. 123–129, 1987.
- [182] S. A. Maier, *Plasmonics: Fundamentals and Applications*. Springer Science & Business Media, 2007.
- [183] Z. Qi, G. Hu, L. Li, B. Yun, R. Zhang, and Y. Cui, "Design and analysis of a compact SOI-based aluminum/highly doped p-type silicon hybrid plasmonic modulator," *IEEE Photonics Journal*, vol. 8, no. 3, pp. 1–11, 2016.
- [184] W. Choyke and E. D. Palik, "Handbook of optical constants of solids," *Palik (ed.), Academic Press, Inc*, vol. 587, 1985.

-
- [185] “Lumerical FDTD solutions,” <https://www.lumerical.com/tcad-products/fdtd/>, 2017.
- [186] “Lumerical FDTD solutions (integrated MODE source),” https://kb.lumerical.com/en/ref_sim_obj_sources_integrated_mode_source.html, 2017.
- [187] K.-W. Chang and C.-C. Huang, “Ultrashort broadband polarization beam splitter based on a combined hybrid plasmonic waveguide,” *Scientific Reports*, vol. 6, p. 19609, 2016.
- [188] N. Abadía, T. Bernadin, P. Chaisakul, S. Olivier, D. Marris-Morini, R. E. de Lamaestre, J. Weeber, and L. Vivien, “Low-power consumption Franz-Keldysh effect plasmonic modulator,” *Optics Express*, vol. 22, no. 9, pp. 11 236–11 243, 2014.
- [189] Q. Wang and S.-T. Ho, “Ultracompact TM-pass silicon nanophotonic waveguide polarizer and design,” *IEEE Photonics Journal*, vol. 2, no. 1, pp. 49–56, 2010.
- [190] R. Li, D. Patel, E. El-Fiky, A. Samani, Z. Xing, Y. Wang, and D. V. Plant, “Silicon photonic dual-drive MIM based 56 Gb/s DAC-less and DSP-free PAM-4 transmission,” *Optics Express*, vol. 26, no. 5, pp. 5395–5407, 2018.
- [191] S. K. Selvaraja, “Wafer-scale fabrication technology for silicon photonic integrated circuits,” Ph.D. dissertation, Ghent University, 2011.
- [192] Y. Tanushi, T. Kita, M. Toyama, M. Seki, K. Koshino, N. Yokoyama, M. Ohtsuka, A. Sugiyama, E. Ishitsuka, T. Sano, T. Horikawa, and Y. Hirohito, “Uniform characteristics of Si-wire waveguide devices fabricated on 300 mm SOI wafers by using ArF immersion lithography,” in *Group IV Photonics (GFP), 2013 IEEE 10th International Conference on*. IEEE, 2013, pp. 105–106.
- [193] S. K. Selvaraja, W. Bogaerts, P. Dumon, D. Van Thourhout, and R. Baets, “Subnanometer linewidth uniformity in silicon nanophotonic waveguide devices using CMOS fabrication technology,” *IEEE Journal of Selected Topics in Quantum Electronics*, vol. 16, no. 1, pp. 316–324, 2010.
- [194] S. Yuan, Y. Wang, Q. Huang, J. Xia, and J. Yu, “Ultracompact TM-pass/TE-reflected integrated polarizer based on a hybrid plasmonic waveguide for silicon photonics,” in *Group IV Photonics (GFP), 2014 IEEE 11th International Conference on*. IEEE, 2014, pp. 183–184.
- [195] S. I. Azzam and S. S. Obayya, “Ultra-compact resonant tunneling-based TE-pass and TM-pass polarizers for SOI platform,” *Optics Letters*, vol. 40, no. 6, pp. 1061–1064, 2015.

-
- [196] S. I. Azzam and S. Obayya, "Titanium nitride-based CMOS-compatible TE-pass and TM-pass plasmonic polarizers," *IEEE Photonics Technology Letters*, vol. 28, no. 3, pp. 367–370, 2016.
- [197] J. Zhang, J. Yang, L. Liang, and W. Wu, "Broadband TM-mode-pass polarizer and polarization beam splitter using asymmetrical directional couplers based on silicon subwavelength grating," *Optics Communications*, vol. 407, pp. 46–50, 2018.
- [198] A. E.-S. Abd-Elkader, M. F. O. Hameed, N. F. Areed, H. E.-D. Mostafa, and S. S. Obayya, "Ultracompact AZO-based TE-pass and TM-pass hybrid plasmonic polarizers," *Journal of the Optical Society of America B*, vol. 36, no. 3, pp. 652–661, 2019.
- [199] G.sup.HSP, "Supplement to ITU-T G-series recommendations PON transmission technologies above 10 Gb/s per wavelength," <https://www.itu.int/ITU-T/workprog/wp-item.aspx?isn=13463>, September, 2017.
- [200] V. Houtsma and D. van Veen, "Bi-directional 25G/50G TDM-PON with extended power budget using 25G APD and coherent detection," *Journal of Lightwave Technology*, vol. 36, no. 1, pp. 122–127, 2018.
- [201] A. D'Errico and G. Contestabile, "Next generation terabit transponder," in *Optical Fiber Communications Conference and Exhibition (OFC), 2016*. IEEE, 2016, pp. 1–3.
- [202] E. Ciaramella, "Polarization-independent receivers for low-cost coherent OOK systems," *IEEE Photonics Technology Letters*, vol. 26, no. 6, pp. 548–551, 2014.
- [203] R. Corsini, M. Presi, M. Artiglia, and E. Ciaramella, "10-Gb/s long-reach PON system with low-complexity dispersion-managed coherent receiver," *IEEE Photonics Journal*, vol. 7, no. 5, pp. 1–8, 2015.
- [204] M. Rannello, M. Presi, and E. Ciaramella, "Optical vs. electrical duobinary coding for 25 Gb/s PONs based on DSP-free coherent envelope detection," in *Optical Fiber Communication Conference*. Optical Society of America, 2018, pp. M1B–6.
- [205] D. van Veen and V. Houtsma, "50 Gbps low complex burst mode coherent detection for time-division multiplexed passive optical networks," in *Optical Communication (ECOC), 2018 European Conference on*. IEEE, 2018, pp. 1–3.
- [206] J. Zhang, J. S. Wey, J. Shi, and J. Yu, "Single-wavelength 100-Gb/s PAM-4 TDM-PON achieving over 32-dB power budget using simplified and phase insensitive coherent de-

- tection," in *Optical Communication (ECOC), 2018 European Conference on*. IEEE, 2018, pp. 1–3.
- [207] R. Urata, H. Liu, C. Lam, P. Dashti, and C. Johnson, "Silicon photonics for optical access networks," in *Group IV Photonics (GFP), 2012 IEEE 9th International Conference on*. IEEE, 2012, pp. 207–209.
- [208] J. Orcutt, D. M. Gill, J. E. Proesel, J. Ellis-Monaghan, F. Horst, T. Barwicz, C. Xiong, F. G. Anderson, A. Agrawal, Y. Martin, C. W. Baks, M. Khater, J. C. Rosenberg, W. D. Sacher, J. Hofrichter, E. Kiewra, A. D. Stricker, F. Libsch, B. Offrein, M. Meghelli, N. B. Feilchenfeld, W. Haensch, and W. M. J. Green, "Monolithic silicon photonics at 25Gb/s," in *Optical Fiber Communication Conference*. Optical Society of America, 2016, pp. Th4H-1.
- [209] W. Sacher, T. Barwicz, and J. K. Poon, "Silicon-on-insulator polarization splitter-rotator based on TM₀-TE₁ mode conversion in a bi-level taper," in *CLEO: Science and Innovations*. Optical Society of America, 2013, pp. CTu3F-3.
- [210] A. Novack, M. Gould, Y. Yang, Z. Xuan, M. Streshinsky, Y. Liu, G. Capellini, A. E.-J. Lim, G.-Q. Lo, T. Baehr-Jones, and M. Hochberg, "Germanium photodetector with 60 GHz bandwidth using inductive gain peaking," *Optics Express*, vol. 21, no. 23, pp. 28 387–28 393, 2013.
- [211] P. Cheben, J. H. Schmid, S. Wang, D.-X. Xu, M. Vachon, S. Janz, J. Lapointe, Y. Painchaud, and M.-J. Picard, "Broadband polarization independent nanophotonic coupler for silicon waveguides with ultra-high efficiency," *Optics Express*, vol. 23, no. 17, pp. 22 553–22 563, 2015.
- [212] "IEEE P802.3ca 50G-EPON Task Force: LDPC FEC Gain Downstream," http://www.ieee802.org/3/ca/public/meeting_archive/2018/01/powell.3ca_1a_0118.pdf, 2018.
- [213] Z. Huang, "Germanium photodetector integrated with silicon-based optical receivers," Ph.D. dissertation, University of Texas at Austin, 2006.
- [214] R. F. Potter, "Germanium (Ge)," in *Handbook of optical constants of solids*. Elsevier, 1997, pp. 465–478.
- [215] H. Subbaraman, X. Xu, A. Hosseini, X. Zhang, Y. Zhang, D. Kwong, and R. T. Chen, "Recent advances in silicon-based passive and active optical interconnects," *Optics Express*, vol. 23, no. 3, pp. 2487–2511, 2015.

-
- [216] F. Testa, C. J. Oton, C. Kopp, J.-M. Lee, R. Ortuño, R. Enne, S. Tondini, G. Chiaretti, A. Bianchi, P. Pintus, M.-S. Kim, D. Fowler, J. Á. Ayúcar, M. Hofbauer, M. Mancinell, M. Fournier, G. B. Preve, N. Zecevic, C. L. Manganelli, C. Castellan, G. Parès, O. Lemonnier, F. Gambini, P. Labeye, M. Romagnoli, L. Pavesi, H. Zimmermann, F. D. Pasquale, and S. Stracca, "Design and implementation of an integrated reconfigurable silicon photonics switch matrix in IRIS project," *IEEE Journal of Selected Topics in Quantum Electronics*, vol. 22, no. 6, pp. 155–168, 2016.
- [217] A. Samani, D. Patel, M. Chagnon, E. El-Fiky, R. Li, M. Jacques, N. Abadía, V. Veerasubramanian, and D. V. Plant, "Experimental parametric study of 128 Gb/s PAM-4 transmission system using a multi-electrode silicon photonic Mach Zehnder modulator," *Optics Express*, vol. 25, no. 12, pp. 13 252–13 262, 2017.
- [218] D. Patel, S. Ghosh, M. Chagnon, A. Samani, V. Veerasubramanian, M. Osman, and D. V. Plant, "Design, analysis, and transmission system performance of a 41 GHz silicon photonic modulator," *Optics Express*, vol. 23, no. 11, pp. 14 263–14 287, 2015.
- [219] F. Fresi, A. Malacarne, V. Sorianello, G. Meloni, P. Velha, M. Midrio, V. Toccafondo, S. Faralli, M. Romagnoli, and L. Potì, "Reconfigurable silicon photonics integrated 16-QAM modulator driven by binary electronics," *IEEE Journal of Selected Topics in Quantum Electronics*, vol. 22, no. 6, pp. 334–343, 2016.
- [220] M. Geng, L. Jia, L. Zhang, L. Yang, P. Chen, T. Wang, and Y. Liu, "Four-channel reconfigurable optical add-drop multiplexer based on photonic wire waveguide," *Optics Express*, vol. 17, no. 7, pp. 5502–5516, 2009.
- [221] R. Moreira, S. Gundavarapu, and D. J. Blumenthal, "Programmable eye-opener lattice filter for multi-channel dispersion compensation using an integrated compact low-loss silicon nitride platform," *Optics Express*, vol. 24, no. 15, pp. 16 732–16 742, 2016.
- [222] C. Roeloffzen, L. Zhuang, R. Heideman, A. Borreman, and W. Van Etten, "Ring resonator-based tunable optical delay line in LPCVD waveguide technology," in *Proc. 9th IEEE/LEOS Symp. Benelux*, 2005, pp. 79–82.
- [223] H. Yun, Z. Lu, Y. Wang, W. Shi, L. Chrostowski, and N. A. Jaeger, "2×2 broadband adiabatic 3-dB couplers on SOI strip waveguides for TE and TM modes," in *CLEO: Science and Innovations*. Optical Society of America, 2015, pp. STh1F–8.

- [224] Y. Ja, "Analysis of four-port optical fiber ring and loop resonators using a 3×3 fiber coupler and degenerate two-wave mixing," *IEEE Journal of Quantum Electronics*, vol. 28, no. 12, pp. 2749–2757, 1992.